ISSN 0911-5730
UVSOR-33
June 2007

UVSOR ACTIVITY REPORT 2006

APPLE-II type undulator

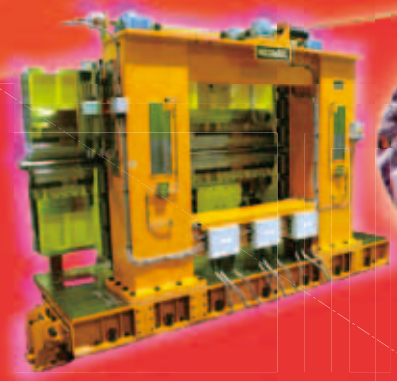

UVSOR II since 2003

BL7U

Wadswarth-type VUV NIM

Three-dimensional angle-resolved photoemission

UVSOR Facility
Institute for Molecular Science
National Institutes of Natural Sciences

UVSOR
ACTIVITY REPORT
2006

edited by
H. Hagiwara, T. Ito, A. Mochihashi

Preface

This Activity Report covers the research activities carried out at the UVSOR facility in FY2006 (April 2006-March 2007). This is the fourth volume in the new series for the third decade of UVSOR, corresponding to the fourth year of the use of the low-emittance UVSOR-II storage ring. The UVSOR-II ring has been stable in operation at the initial beam current of 350 mA for every 6-hour injection and the beam emittance of 27 nm-rad for these two years. We increased the beam energy of the booster synchrotron from 0.6 GeV to 0.75 GeV to realize the full energy injection and reinforced the radiation shield wall surrounding the storage ring of 53 m in circumference. Most upgrade plans to realize the top-up operation in the UVSOR-II ring have been completed. We hope we will succeed in it within FY2007.

The Ministry of Education, Culture, Sports, Science and Technology (MEXT) has been supporting SPring-8, Photon Factory, and UVSOR as three major facilities in Japan, where UVSOR is exclusively responsible for the high-brilliant VUV light source as a low-energy third generation ring. To enhance advanced VUV and soft X-ray study, some beamline upgrade projects were completed in FY2006. One of the highlights is BL7U, where we installed a new long undulator and a high-resolution normal incidence monochromator and now high-resolution VUV photoemission study is ongoing. In addition, we have started design of the surface chemistry and physics beamline BL6U using the short in-vacuum undulator previously installed at BL7U. Our final goal is to have 6 insertion device beamlines for the four 4 m-long and two 1.5 m-long straight sections and 8 limited dipole beamlines for the 8 bending magnets on the UVSOR-II ring.

IMS has reconstructed its organization this April. Now the UVSOR and Laser Research Center belong to the same research department, Department of Photo-Molecular Science, together with four research divisions I-IV. This Department is devoted to cultivating interdisciplinary Photo-Molecular Science in areas of the chemical, physical and life sciences. Furthermore, Dr. Masahito Hosaka, who is a key person in upgrade of our storage-ring FEL was promoted to associate professor of Nagoya University in November 2006. We hope strong collaboration with the Laser Research Center and Nagoya University will accelerate development of new light sources at the UVSOR, e.g. storage-ring FEL, Terahertz (THz) coherent synchrotron radiation (CSR), and coherent harmonic generation (CHG), and ensure more exciting activities at the UVSOR in the coming years.

April, 2007

Nobuhiro Kosugi
Director of UVSOR

Organization and Staff List

UVSOR Organization (2007/4/1)

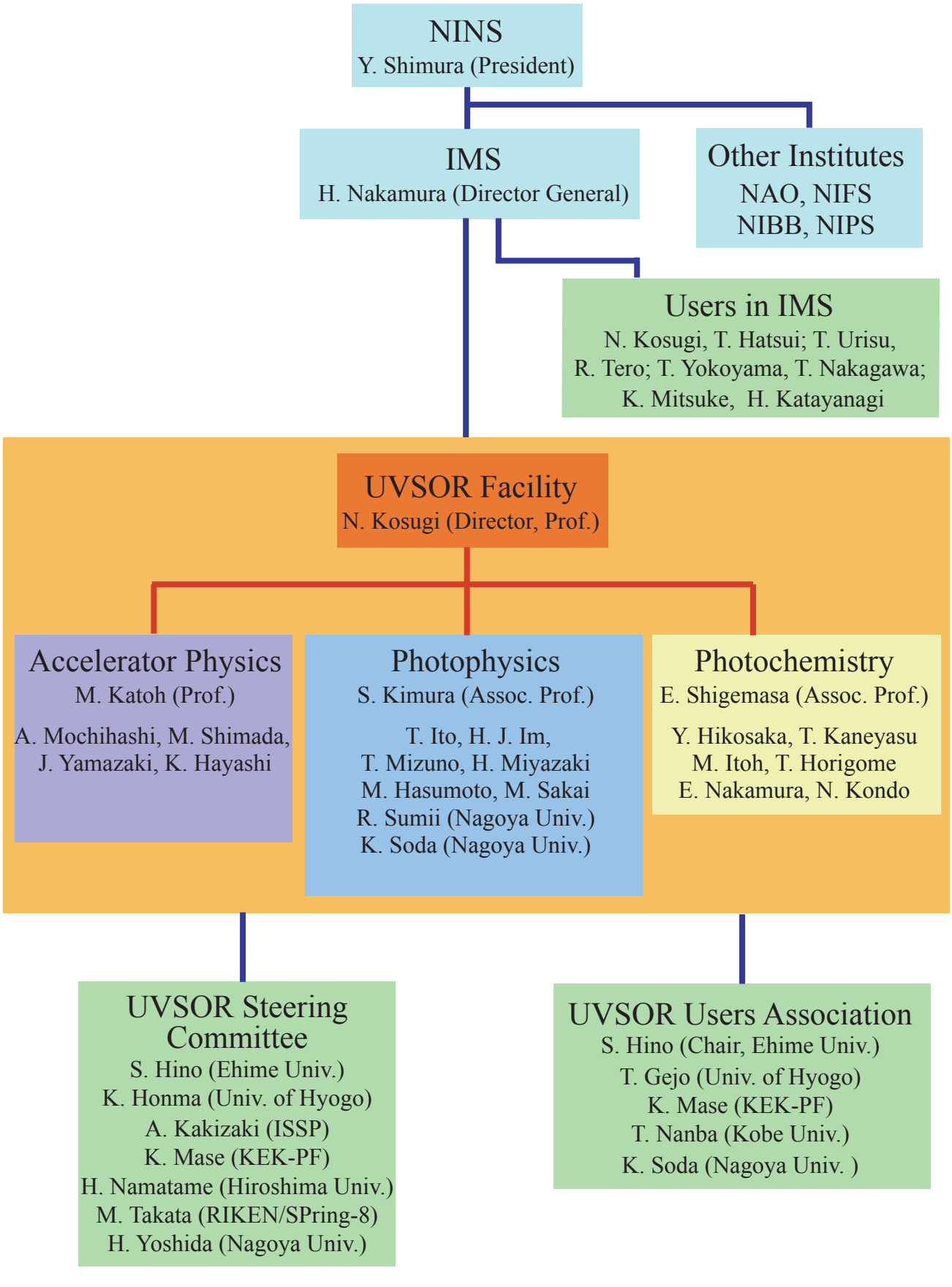

UVSOR Staff

Director

KOSUGI, Nobuhiro	Professor	kosugi@ims.ac.jp	

Light Source Division (Accelerator Physics)

KATOH, Masahiro	Professor	mkatoh@ims.ac.jp	
HOSAKA, Masahito	Research Associate	hosaka@ims.ac.jp	(until Oct. 2006)
MOCHIHASHI, Akira	Research Associate	mochi@ims.ac.jp	
YAMAZAKI, Jun-ichiro	Unit Chief Engineer	yamazaki@ims.ac.jp	
HAYASHI, Kenji	Engineer	h-kenji@ims.ac.jp	
MATSUO, Suekichi	Supporting Engineer	matsuo@ims.ac.jp	
HARA, Toru	Guest Associate Professor		(until Mar. 2007)
SHIMADA, Miho	Post-Doctoral Fellow	shimada@ims.ac.jp	

Beamline Division (Photophysics)

KIMURA, Shin-ichi	Associate Professor	kimura@ims.ac.jp	
ITO, Takahiro	Research Associate	tito@ims.ac.jp	
HASUMOTO, Masami	Unit Chief Engineer	hasumoto@ims.ac.jp	
SAKAI, Masahiro	Engineer	sakai@ims.ac.jp	
SAKURAI, Yoko	Post-Doctoral Fellow	sakurai@ims.ac.jp	(until Mar. 2007)
SUMII, Ryohei	Guest Researcher	sumii@ims.ac.jp	
SODA, Kazuo	Guest Professor		
IM, Hojun	Guest Researcher	hojun@ims.ac.jp	(since Oct. 2006)

Beamline Division (Photochemistry)

SHIGEMASA, Eiji	Associate Professor	sigemasa@ims.ac.jp	
HIKOSAKA, Yasumasa	Research Associate	hikosaka@ims.ac.jp	
HORIGOME, Toshio	Facility Chief Engineer	horigome@ims.ac.jp	
NAKAMURA, Eiken	Unit Chief Engineer	eiken@ims.ac.jp	
KONDO, Naonori	Engineer	nkondo@ims.ac.jp	
KANEYASU, Tatsuo	Post-Doctoral Fellow	kaneyasu@ims.ac.jp	

Secretary

HAGIWARA, Hisayo		hagiwara@ims.ac.jp	

Graduate Students

IM, Hojun	Grad. Univ. Adv. Studies	hojun@ims.ac.jp	(until Sept. 2006)
MIZUNO, Takafumi	Grad. Univ. Adv. Studies	tmizuno@ims.ac.jp	
MIYAZAKI , Hidetoshi	Nagoya Univ.	hmiyazak@ims.ac.jp	
MIZUNUMA, Tatsuro	Meiji Univ.	mizunuma@ims.ac.jp	(until Mar. 2007)
OTA, Shunji	Nagoya Univ.	shunota@ims.ac.jp	(until Sept. 2006)
SUZUMURA, Kosuke	Nagoya Univ.	suzumura@ims.ac.jp	(until Mar. 2007)
ITO, Masahiro	Niigata Univ.		

Visiting Scientists

COUPRIE, Marie-Emmanuelle	CEA, France	(Mar. 2007)
LAMBERT, Guillaume	CEA, France	(Jun. 2006, Mar. 2007)
LABAT, Marie	CEA, France	(Jun. 2006, Mar. 2007)
BIELAWSKI, Serge	Lille Univ., France	(Nov.-Dec. 2006)
SZWAJ, Christophe	Lille Univ., France	(Nov.-Dec. 2006)
EVAIN, Clement	Lille Univ., France	(Nov.-Dec. 2006)
KWON, Yong-seung	Sungkyunkwan Univ., Korea	(Jul. 2006, Jan. 2007)
LEE, Kyeng Eun	Sungkyunkwan Univ., Korea	(Jul. 2006, Jan. 2007)
YOON, Hee	Sungkyunkwan Univ., Korea	(Jul. 2006)
EUN, Kyeng	Sungkyunkwan Univ., Korea	(Jan. 2007)
SICHELSCHMIDT, Joerg	MPI-CPfS, Germany	(Aug. 2006)
MARUTZKY, Michael	MPI-CPfS, Germany	(Feb. 2007)

UVSOR Steering Committee (FY2005-2006)

KOSUGI, Nobuhiro	UVSOR, IMS	Chair
KIMURA, Shin-ichi	UVSOR, IMS	
KATOH, Masahiro	UVSOR, IMS	
SHIGEMASA, Eiji	UVSOR, IMS	
HARA, Toru	UVSOR, IMS	(Guest Associate Professor from RIKEN, since Apr. 2005)
YOKOYAMA, Toshihiko	IMS	
MATSUMOTO, Yoshiyasu	IMS	
OGAWA, Takuji	IMS	
MITSUKE, Koichiro	IMS	
KAKIZAKI, Akito	Univ. of Tokyo	
MASE, Kazuhiko	KEK-PF	
YOSHIDA, Hisao	Nagoya Univ.	
OSHIMA, Masaharu	Univ. of Tokyo	
SODA, Kazuo	Nagoya Univ.	
NAMBA, Hidetoshi	Ritsumeikan Univ.	
HIRAYA, Atsunari	Hiroshima Univ.	

Current Status of Light Source and Beamlines

Light Source in 2006

Masahiro KATOH

UVSOR Facility, Institute for Molecular Science

1. Status of UVSOR-II

In the fiscal year 2006, we have operated the UVSOR-II accelerators from April ’06 to March ’07. We had one 9 week shut-down period in July and August ’06 and two 2 week ones in October and March ’07. The long shut down in summer was to replace the magnet power supply of the booster synchrotron and to install a new beam duct at a straight section between B6 and B7 for new undulator. Construction of new radiation shield wall was also done during this period. The short shut down in October was to install a new variably polarized undulator. The shut down in March is to replace the bending magnet power supply of the beam transport line, preparing for full energy injection. We also stopped the operation for one week in the holiday week of May and for two weeks around the New Years day.

Fortunately, we had very few troubles on the accelerators during FY2006. We only had a few minor troubles on a kicker magnet power supply of the storage ring and the RF amplifier of the linear accelerator. All of them did not affect the operation schedule.

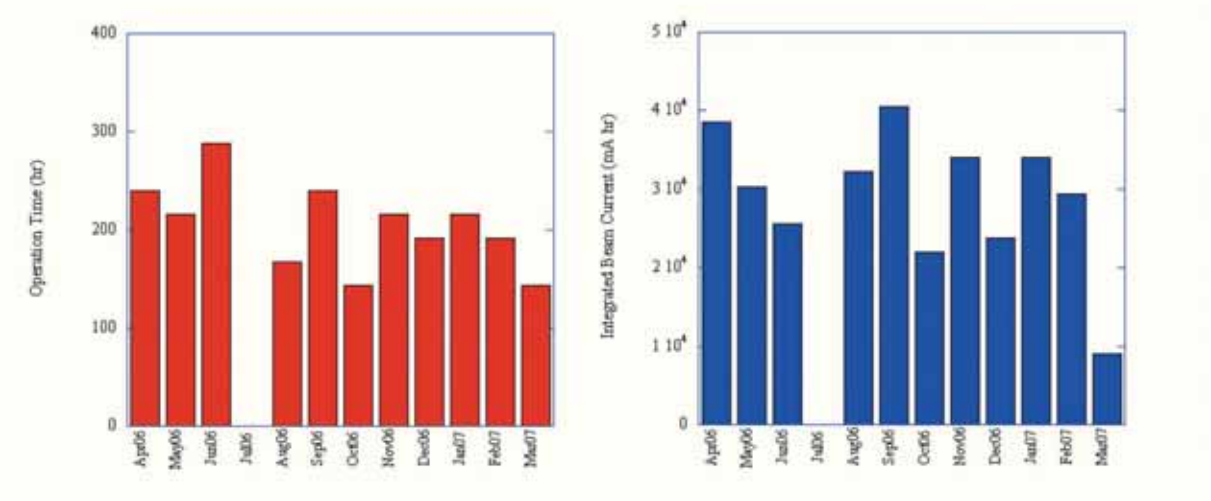

Figure 1 Monthly statistics of the operation time (left) and of the integrated beam current (right).

We had totally 31 weeks for the users operation, 29 weeks in multi-bunch mode and two weeks in single bunch mode. We had five weeks dedicated for machine studies. The monthly statistics of the operation time and the integrated beam current are shown in Figures 1. The normal operation pattern in a week is as follows. From Tuesday to Friday, the machine is operated for users. The beam injection is twice a day, at 9:00 and 15:00. The initial beam current of each run is 350 mA in multi-bunch mode and 100 mA in single bunch mode. On Monday, the machine is operated for machine studies.

2. Improvements

Commissioning of New Magnet Power Supplies for Booster Synchrotron

The magnet power supplies of the booster synchrotron had been working for more than twenty years. In these years, we had a few very serious troubles on then. In July, 2006, these power supplies were finally replaced. New power supplies have capability of accelerating the electron beam up to the full energy of the storage ring, 750 MeV. In August, we have commissioned the power supplies with the 600 MeV acceleration mode. In March, the power supply for the bending magnets of the beam transport line has been replaced. New power supply is compatible with the full energy injection. In April, 2007, the full energy acceleration, transportation and injection will be started.

Figure 2 New Magnet Power Supplies for Booster Synchrotron

Progress in Orbit Stabilization

The electron orbit of UVSOR-II shows drift motion of a few hundred microns with a time scale of hours. To suppress the orbit drift, a feedback system is under development. As the first step, a sub-system has been constructed to correct the orbit displacement in the horizontal plane automatically by controlling the RF frequency [1]. This system has been successfully commissioned and the orbit drift in the horizontal plane is reduced significantly. The system has been working for about one year and the change of the RF frequency has been recorded, which is strongly correlated with the temperature of the storage ring room floor [1].

As the second step, a sub-system to monitor the positions of the beam position monitors has been developed and tested [2]. The synchrotron irradiation cause thermal deformation of the beam ducts, which results in displacements of the beam position monitors mounted on them. The measurement shows that most of the beam position monitors show the displacements of a few tens of microns. So at present, this is not a serious problem but, in future, when we try to stabilize the orbit within ten microns, it should be considered.

New Undulator for BL7U

A new undulator was installed in the straight section between B6 and B7 in October. This undulator will provide VUV light of linear polarization in both horizontal and vertical planes. It can also provide circular polarized

VUV light. The configuration of the magnet array is of APPLE-II type [3]. The main parameters are shown in Table 1. The undulator is now under commissioning and partly opened for users.

Before installing the new undulator, another undulator of in-vacuum type, which had occupied a part of the straight section, was moved to another short straight section between B5 and B6. It will provide soft X-rays to BL6U, which is now under designing.

Figure 3 New APPLE-II undulator for BL7U (upper) and In-vacuum undulator for BL6U (lower)

3. Researches and Developments

Free Electron Laser

In FY2006, one watt lasing in deep UV region (230nm) was successfully demonstrated [4]. The lower emittance and the higher peak current of the electron beam in UVSOR-II made this possible. Several user experiments have been started. On example is related to the magnet circular dichroism which is described in these reports [5].

Coherent harmonic generation (CHG) is a method to produce coherent radiation in shorter wavelength region where no good mirror is available for the optical cavity. By using the Ti:Sa laser introduced for the bunch slicing experiment, the CHG was successfully demonstrated in collaboration with French group [6]. Coherent third harmonics of the injected laser was clearly observed.

Laser Bunch Slicing

By using a TiSa laser of 1 kHz repetition rate and 2.5 mJ pulse energy, we have succeeded in producing intense coherent terahertz radiation [7]. The short pulse laser interacts only with a part of the electron bunch inside an undulator. There is produced strong energy modulation at the interacting part. As the electron bunch is proceeding in the storage ring, the modulated part is separated from the bunch and there is created a dip on the

bunch. This fine structure on the longitudinal density distribution is the origin of the intense coherent radiation.

[1] K. Suzumura et al., in this report

[2] K. Suzumura et al., in this report

[3] S. Sasaki, Nucl. Instr. Meth. A347 (1994) 83

[4] M. Hosaka et al., in this report

[5] T. Nakagawa, T. Yokoyama, M. Hosaka, M. Katoh, in this report

[6] M. Labat et al., in this report

[7] M. Shimada et al., in this report

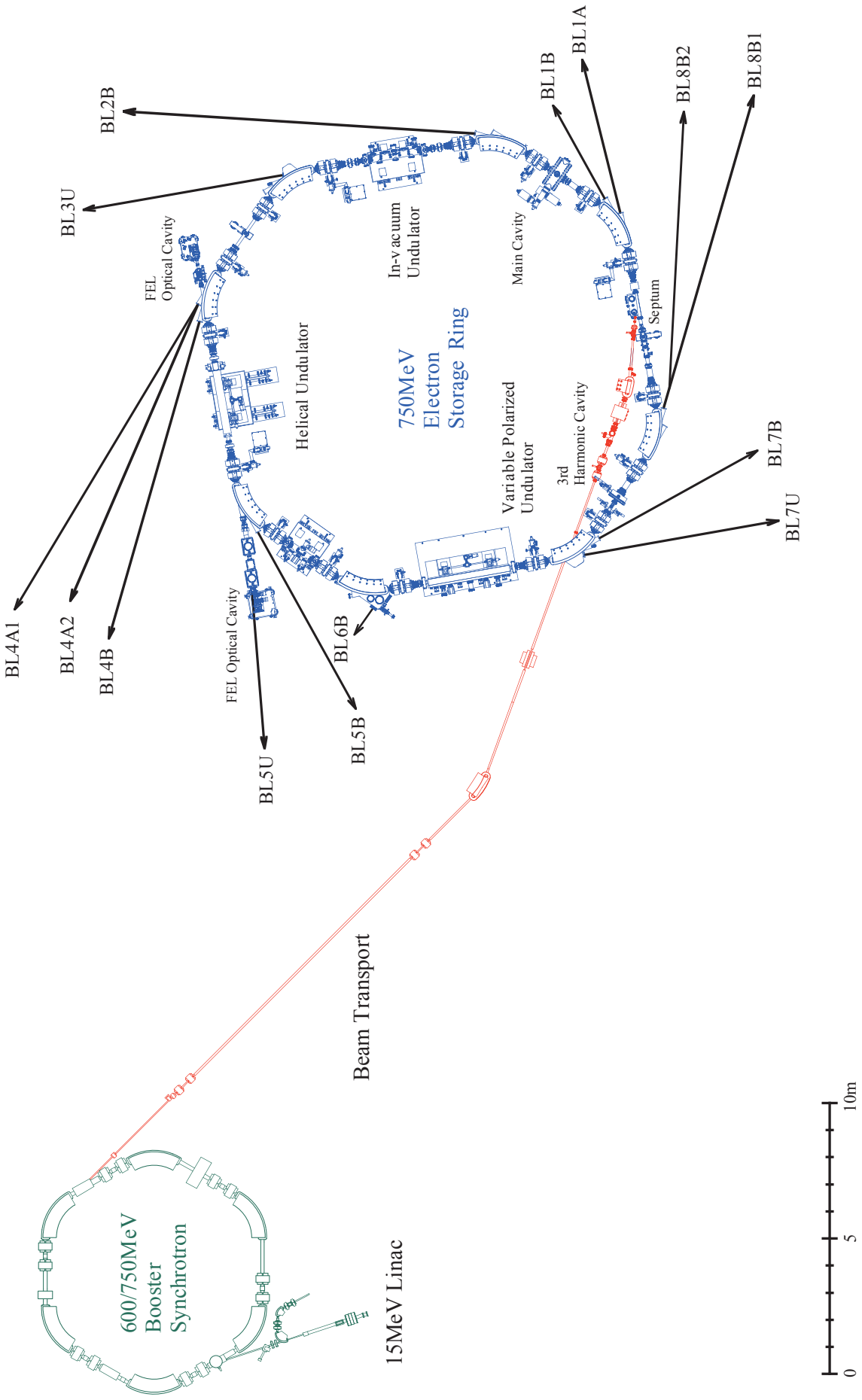
BL2B
BL3U
BL4A1
BL4A2
BL4B
BL5U
BL5B
BL6B
BL7U
BL7B
BL8B1
BL8B2
BL1A
BL1B
FEL Optical Cavity
Helical Undulator
In-vacuum Undulator
Main Cavity
Septum
750MeV Electron Storage Ring
Variable Polarized Undulator
3rd Harmonic Cavity
FEL Optical Cavity
Beam Transport
600/750MeV Booster Synchrotron
15MeV Linac
0
5
10m

Parameters of Injection Linear Accelerator

Energy	15 MeV
Length	2.5 m
Frequency	2856 MHz
Accelerating RF Field	2π/3 Traveling Wave
Klystron Power	1.8 MW
Energy Spread	~ 1.6 MeV
Repetition Rate	2.6 Hz

Parameters of Booster Synchrotron

Energy	600 / 750 MeV
Injection Energy	15 MeV
Beam Current	32 mA (uniform filling)
Circumference	26.6 m
RF Frequency	90.1 MHz
Harmonic Number	8
Bending Radius	1.8 m
Lattice	FODO × 8
Betatron Tune	
Horizontal	2.25
Vertical	1.25
Momentum Compaction	0.138
Repetition Rate	2.6 / 1 Hz (600 / 750 MeV)

Parameters of UVSOR-II Storage Ring

Energy	750 MeV
Injection Energy	600 / 750 MeV
Maximum Stored Current	500 mA (multi bunch) 100 mA (single bunch)
Natural Emittance	27.4 nm-rad
Circumference	53.2 m
RF Frequency	90.1 MHz
Harmonic Number	16
Bending Radius	2.2 m
Lattice	Extended DBA × 4
Straight Section	(4 m × 4) + (1.5 m × 4)
RF Voltage	100 kV
Betatron Tune	
Horizontal	3.75
Vertical	3.20
Momentum Compaction	0.028
Natural Chromaticity	
Horizontal	-8.1
Vertical	-7.3
Energy Spread	4.2×10^{-4}
Natural Bunch Length	108 ps

Electron Beam Optics of UVSOR-II Storage Ring

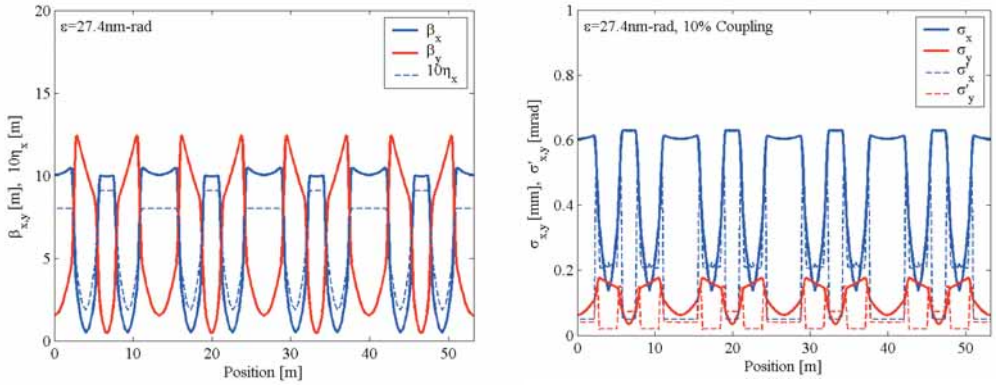

Horizontal/vertical betatron functions and dispersion function (left), and horizontal/vertical electron beam sizes and beam divergences (right) of UVSOR-II

Parameters of the insertion devices

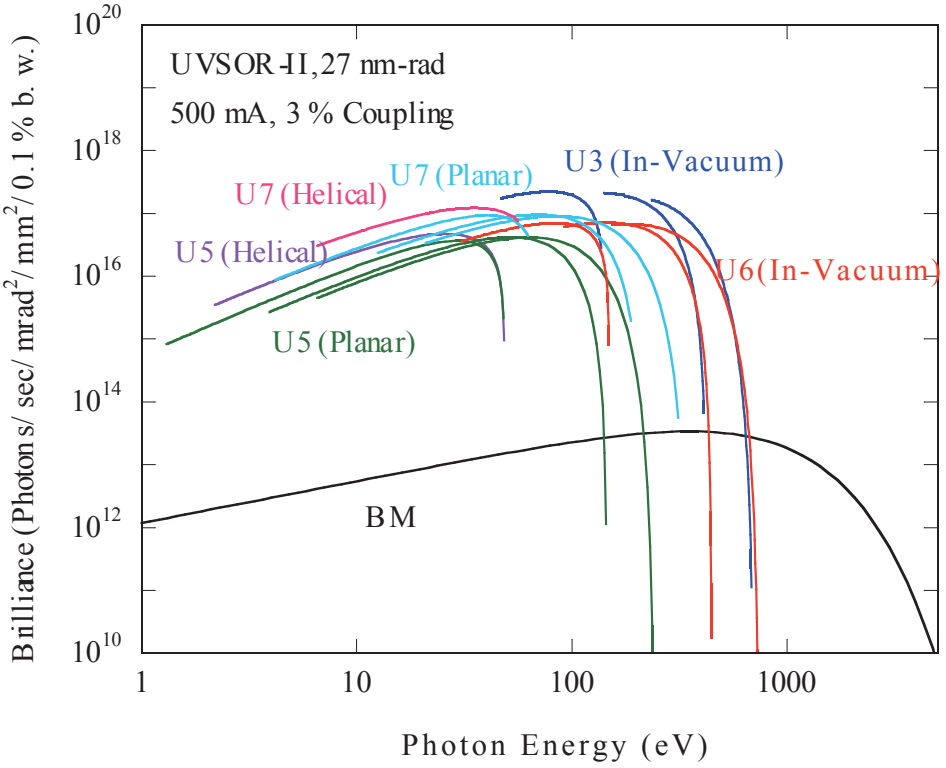

Brilliance of radiation from the insertion devices (U3, U5, U6 and U7) and a bending magnet of UVSOR-II

BL3U In-vacuum Undulator

Number of Periods	50
Period Length	38 mm
Pole Length	1.9 m
Pole Gap	15~40mm
Deflection Parameter	2.00~0.24

BL6U In-vacuum Undulator

Number of Periods	26
Period Length	36 mm
Pole Length	0.94 m
Pole Gap	15~40 mm
Deflection Parameter	1.78~0.19

BL5U Helical Undulator / Optical Klystron

Number of Periods	21 / 9+9(Opt. Kly.)
Period Length	110mm
Pole Length	2.35 m
Pole Gap	30~150 mm
Deflection Parameter	4.6~0.07(Helical) 8.5~0.15(Linear)

BL7U Apple-II variable polarization undulator

Number of Periods	40
Period Length	76mm
Pole Length	3.04 m
Pole Gap	24~200 mm
Deflection Parameter	5.4 (max. horizontal) 3.6 (max. vertical) 3.0 (max. helical)

Bending Magnets

Bending Radius	2.2 m
Critical Energy	425 eV

Beamlines in 2006

Eiji SHIGEMASA

UVSOR Facility, Institute for Molecular Science

Eight bending magnets and three insertion devices are available for utilizing synchrotron radiation at UVSOR. There is a total of thirteen operational beamlines in 2006, which are classified into two categories. Eight of them are so-called "Open beamlines", which are open to scientists of universities and research institutes belonging to the government, public organizations, private enterprises and those of foreign countries. The rest of the five beamlines are so-called "In-house beamlines", and are dedicated to the use of research groups within IMS. We have one soft X-rays station equipped with a double-crystal monochromator, seven extreme ultraviolet and soft X-rays stations with a grazing incidence monochromator, three vacuum ultraviolet stations with a normal incidence monochromator, one infrared (IR) station equipped with Fourier-Transform interferometers, one station with a multi-layer monochromator, and three non-monochromatized stations for irradiation of white-light, as shown in the appended table for all available beamlines at UVSOR.

The upgrade project of the UVSOR storage ring, in which the creation of four new straight sections and the achievement of much smaller emittance (27 nm-rad) were planned, has been approved in the fiscal year of 2002 and has been accomplished on schedule. Keeping pace with the upgrade project, the improvements and upgrades of the beamlines at UVSOR have been continuously discussed with users in a series of UVSOR workshops. From a viewpoint of the radiation safety, the experiments carried out at the experimental stations on the second floor such as BL3B and BL7B, and the fine tunings of the laser system installed inside the shield walls during the machine study, seem to become quite risky due to the introduction in the near future of the so-called top-up operation of the UVSOR storage ring. Accordingly we have decided to put two old beamlines, BL8A and BL3B, out of service until the middle of March 2006. In order to transfer the experimental endstation for BL7B to the space after the removal of BL8A, the optical path downstream the exit slit has been changed and a new refocusing mirror system has been installed. It was found through the alignment work at BL7B that the first mirror with a torodial shape had been misaligned seriously, which essentially degrades the performance of the monochromator. It may take several weeks to accomplish the alignment of this mirror, since the change of the position of the first mirror leads to the realignment of all the optical elements of the beamline. We have planned to make the realignment of BL7B in April and May of 2007. The laser system has been moved to the empty lot of BL3B by the machine group.

Regarding the utilization for the long straight section between B06 and B07, a UVSOR workshop has been held in March 2005. A high resolution and high flux variable polarization beamline for spectroscopy in the VUV range has been proposed and possible scientific cases performed on this beamline have been discussed there. The construction of the new beamline BL7U has been completed during the regular summer shutdown in 2006 as had planned. BL7U is composed of a modified Wadsworth-type monochromator with three interchangeable spherical gratings (R=10 m; 1200, 2400, and 3600 lines/mm), and a hemispherical photoelectron analyzer, where high-resolution angle-resolved photoemission experiments can be performed. A new APPLE-II type undulator for the light source of BL7U has successfully been installed at the end of October 2006. It has been confirmed that the total performance of BL7U, after careful tunings of the monochromator and the analyzer, nearly reaches the theoretically expected level. Concerning the utilization of the first in-vacuum type undulator, which has been relocated from the long straight section U7 to the short one between B05 and B06, a new project for constructing the undulator beamline BL6U is just beginning execution. A preliminary design study for the

monochromator at BL6U has been terminated, thanks to the collaboration with KEK-PF. The monochromator will cover the photon energy range from 30 to 500 eV, with the resolving power higher than 10000 and the photon flux more than 10^{10} photons/sec. The construction of BL6U is expected to start from the spring of 2008. Further serious discussion toward utilizing the available straight sections most effectively and formulating a basic plan on the beamline construction, will be continued.

All users are required to refer to the beamline manuals and the UVSOR guidebook (latest revision in 1999), on the occasion of conducting actual experimental procedures. Those wishing to use the open and in-house beamlines are recommended to contact the stationmaster/supervisor and the representative, respectively. For updated information of UVSOR, http://www.uvsor.ims.ac.jp/.

Station Masters and Supervisors of Open Beamlines in FY2006

Beamline	Station Master	Sub Master	Supervisor
1A	N. Kondo	E. Shigemasa	E. Shigemasa
1B	M. Hasumoto	S. Kimura	S. Kimura
5U	T. Ito	S. Kimura	S. Kimura
5B	M. Hasumoto	E. Nakamura	E. Shigemasa
6B	S. Kimura	E. Nakamura	S. Kimura
7B	M. Hasumoto	S. Kimura	S. Kimura
8B1	Y. Hikosaka	E. Nakamura	E. Shigemasa
8B2	R. Sumii	E. Nakamura	S. Kimura

Station Masters and Supervisors of In-House Beamlines in FY2006

Beamline	Representative	Affiliation
2B	K. Mitsuke	Dep. VUV Photoscience
3U	N. Kosugi	Dep. VUV Photoscience
4A1/4A2	T. Urisu	Dep. VUV Photoscience
4B	E. Shigemasa	UVSOR

Beamlines at UVSOR-II

Beam-line	Monochromator, Spectrometer	Energy Region (eV)	Experiments	Beamline master
1A	Double-Crystal	600 eV – 4 keV	Solid (Absorption)	N. Kondo nkondo@ims.ac.jp
1B	1m Seya-Namioka	1.9 eV – 40 eV	Solid (Reflection, Absorption)	M. Hasumoto hasumoto@ims.ac.jp
2B	18m Spherical Grating (Dragon)	20 eV – 200 eV	Gas (Photoionization, Photodissociation)	K. Mitsuke mitsuke@ims.ac.jp
3U	Varied-Line-Spacing Plane Grating (Monk-Gillieson)	40 eV – 600 eV	Gas (Photoionization, Photodissociation) Solid (Photoemission)	T. Hatsui hatsui@ims.ac.jp
4A1	Multi-Layered-Mirror	50 eV – 95 eV	Irradiation	T. Urisu urisu@ims.ac.jp
4A2	None		Irradiation	T. Urisu urisu@ims.ac.jp
4B	Varied-Line-Spacing Plane Grating (Monk-Gillieson)	25 eV – 800 eV	Gas (Photoionization, Photodissociation) Solid (Photoemission)	E. Shigemasa sigemasa@ims.ac.jp
5U (FEL)	None (Optical Klystron)		Free Electron Laser	J. Yamazaki yamazaki@ims.ac.jp
5U	Spherical Grating (SGM-TRAIN*)	5 eV – 250 eV	Solid (Photoemission)	T. Ito tito@ims.ac.jp
5B	Plane Grating	5 eV – 600 eV	Calibration Solid (Absorption)	M. Hasumoto hasumoto@ims.ac.jp
6B (IR)	Martin-Puplett FT-FIR Michelson FT-IR	0.25 meV – 2.5 eV	Solid (Reflection, Absorption)	S. Kimura kimura@ims.ac.jp
7U	10m Normal Incidence (Modified Wadsworth)	6 eV – 40 eV	Solid (Photoemission)	S. Kimura kimura@ims.ac.jp
7B	3m Normal Incidence	1.2 eV – 30 eV	Solid (Reflection, Absorption)	M. Hasumoto hasumoto@ims.ac.jp
8B1	15m Constant Deviation Grazing Incidence	30 eV – 600 eV	Solid (Absorption)	Y. Hikosaka hikosaka@ims.ac.jp
8B2	Plane Grating	1.9 eV – 150 eV	Solid (Photoemission)	R. Sumii sumii@ims.ac.jp

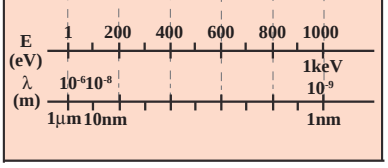

* Spherical Grating Monochromator with Translating and Rotating Assembly Including Normal incidence mount

BL1A

Soft X-Ray Beamline for Photoabsorption Spectroscopy

BL1A is a soft X-ray beamline for photoabsorption spectroscopy. The beamline is equipped with a focusing premirror and a double crystal monochromator [1]. The monochromator serves soft X-rays in the energy region from 585 to 4000 eV by using several kinds of single crystals such as β-Al_2O_3, beryl, KTP ($KTiOPO_4$), quartz, InSb, and Ge. The throughput spectra measured by a Si photodiode (AXUV-100, IRD Inc.) are shown in Fig. 1. Typical energy resolution (E/ΔE) of the monochromator is about 1500 for beryl and InSb. There are no experimental setups specific of this beamline, except for a small vacuum chamber equipped with an electron multiplier (EM) detector. Photoabsorption spectra for powdery samples are usually measured in a total electron yield mode, with the use of the EM detector.

[1] Hiraya at al, Rev. Sci. Instrum. **63** (1992) 1264.

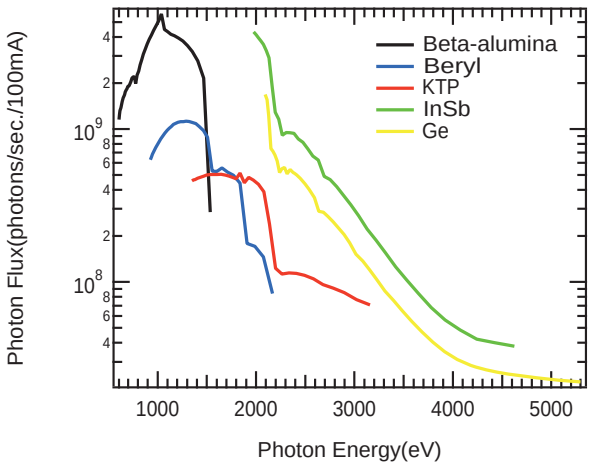

Fig. 1 Throughput spectra of the double crystal monochromator at BL1A.

Fig. 2 A side view of BL1A.

Beamline Specifications

Monochromator	Double crystal monochromator
Monochromator crystals: (2d value, energy range)	β-Al_2O_3 (22.53 Å, 585-1609 eV), beryl (15.965 Å, 826-2271 eV), KTP (10.95 Å, 1205-3310 eV), quartz (8.512 Å, 1550-4000 eV), InSb (7.481 Å, 1764-4000 eV), Ge (6.532 Å, 2094-4000 eV)
Resolution	E/ΔE = 1500 for beryl and InSb
Experiments	Photoabsorption spectroscopy

BL1B

Seya-Namioka Monochromator for General Purposes

BL1B has been constructed to perform various spectroscopic investigations such as absorption, reflectivity, and luminescence in condensed matters. This beamline consists of a pre-focusing mirror, a 1-m Seya-Namioka type monochromator, and post-focusing mirrors with different focal lengths. Three gratings of 600, 1200, and 2400 l/mm can cover the wavelength region ranging from 40 to 650 nm ($h\nu$ = 2 – 30 eV). The post mirror with a longer focal length is usually used with an LiF window to separate the vacuum condition of the monochromator from a main experimental station, which make experiments for liquids and bio-specimens possible, while the other is mainly utilized for solid-state spectroscopy. The output flux from this monochromator is about 10^{10} photons/sec. around 200 nm with 0.1 mm slit openings. The spectral distributions for two gratings measured by a conventional photomultiplyer are shown in Fig. 1. A second monochromator (Spex 270M) and a LN-cooled CCD detector (Princeton Inc.) are available for luminescence measurements, together with a liquid helium-flow type cryostat. To perform time-resolved experiments, a TAC system is also available.

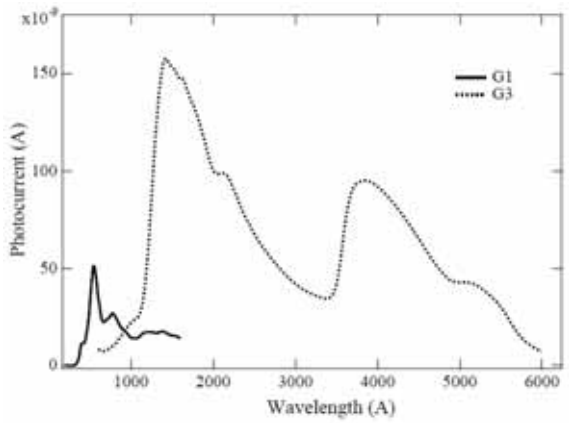

Fig. 1 Photocurrent at the sample position at BL1B.

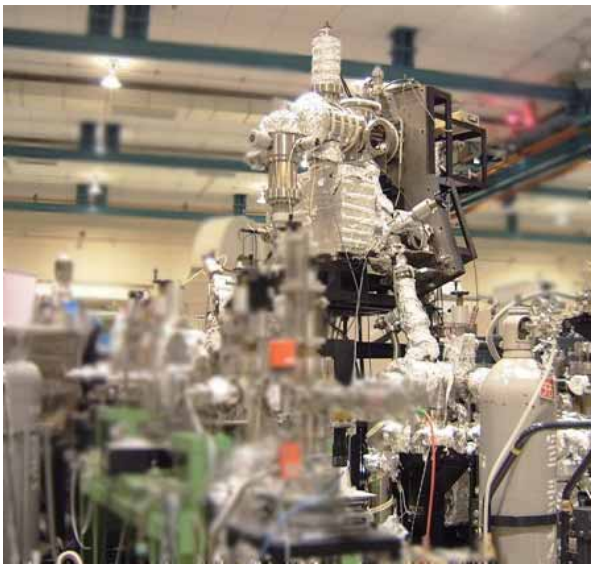

Fig. 2 Photo of BL1B.

Beamline Specifications

Monochromator	1-m Seya-Namioka type
Wavelength Range	40 to 600 nm (2-30 eV)
Resolution	E/ΔE~1000 at 100 nm (10 eV)
Experiment	Absorption, reflection, luminescence spectroscopy for solids

BL2B

Beamline for Gas Phase Photoionization and Reaction Dynamics

This beamline has been developed for the purpose of studying ionization, excitation and decay dynamics involving inner-valence electrons, 2*p* electrons of the third row atoms, and 4d electrons of the lanthanides. The monochromator is a spherical grating Dragon-type with 18-m focal length. High throughput (1×10^{10} photons s^{-1}) and high resolution ($E/\Delta E$ = 2000 - 8000) are achieved simultaneously under the condition of the ring current of 100 mA [1]. The optical system consists of two prefocusing mirrors, an entrance slit, three spherical gratings (G1 - G3), two folding mirrors, a movable exit slit and a refocusing mirror [2]. The monochromator is designed to cover the energy range of 23 - 205 eV with the three gratings: G1 (2400 lines mm^{-1}, R = 18 m) at 80 - 205 eV; G2 (1200 lines mm^{-1}, R = 18 m) at 40 - 100 eV; G3 (2400 lines mm^{-1}, R = 9.25 m) at 23 - 50 eV. The percentage of the second-order light contamination at $h\nu$ = 45.6 eV is 23 % for G2 or 7 % for G3.

We have been taking the yield curves of various fullerene ions [3]. Geometrical structures and electronic properties of fullerenes have attracted widespread attention because of their novel structures, novel reactivity, and novel catalytic behaviors as typical nanometer-size materials. However, spectroscopic information was very limited in the extreme UV region, owing to difficulties in acquiring enough amount of sample. This situation has been rapidly changed since the start of this century, because the techniques of syntheses, isolation, and purification have been advanced so rapidly that appreciable amount of fullerenes can be readily obtained.

Fig .1 18-m spherical grating monochromator at BL2B.

Fig. 2 End station of BL2B for gas phase spectroscopy of refractory materials.

[1] M. Ono, H. Yoshida, H. Hattori and K. Mitsuke, Nucl. Instrum. Meth. Phys. Res. A **467-468**, 577 (2001).
[2] H. Yoshida and K. Mitsuke, J. Synchrotron Radiation **5** (1998) 774.
[3] J. Kou, T. Mori, Y. Kubozono and K. Mitsuke, Phys. Chem. Chem. Phys. **7** (2005) 119.

Beamline Specifications

Monochromator	18-m spherical grating Dragon-type
Wavelength Range	6 – 55 nm
Resolution	2000-8000
Experiment	Mass spectrom.; Photoelectron spectrosc.

BL3U

Varied-line-spacing Plane Grating Monochromator

for Molecular Soft X-ray Spectroscopy

The beamline BL3U is equipped with an in-vaccum undulator composed of 50 periods of 3.8 cm period length. The emitted photons are monochromatized by the varied-line-spacing plane grating monochromator (VLS-PGM) designed for various spectroscopic investigations in the soft x-ray range including soft x-ray emission studies. Three holographically ruled laminar profile plane gratings are designed to cover the photon energy range from 60 eV to 800 eV. The beamline has two endstations, namely XES setup and Multi-purpose setup. The XES setup is used for soft x-ray emission spectroscopy. The beam is horizontally focused onto the sample position by plane-elliptical mirror, M2X. In the Multi-purpose setup, the beam is focused by the toroidal mirror M2. Between the sample position and M2, the differential pumping is placed.

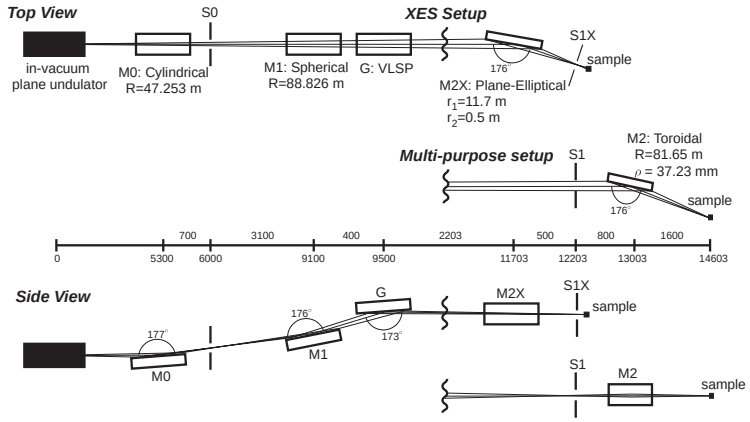

Fig. 1. Schematic layout (left) and the photography (right) of the BL3U. The distances along the beam from the center of the in-vacuum plane undulator are shown in mm. S1X and M2X can be replaced with the other exit slit S1 so that experiments can be carried out at either the XES or multi-purpose endstation. In the XES setup, the sample is placed at 5-10 mm downstream of S1X.

Beamline Specifications

Monochromator	Varied-line-spacing plane grating monochromator
Energy Range	60-800 eV
Resolution	E/ΔE > 10 000
Experiment	Soft X-ray spectroscopy (XPS, XES, XAS)
Beam Size (XES Endstation)	Gaussian shape Vertical 5-20 μm; Horizontal 41 μm (FWHM)

BL4A1

Irradiation Desorption on XeF_2 Gas Etching

BL4A1 has been constructed to perform the synchrotron radiation induced etching of Si and SiO_2 using XeF_2 as an etching gas. This beam-line is composed of a multilayered mirror (MLM) monochromator, a beam condenser system, and a differential pump system. The XeF_2 pressure during the etching will reach to 0.5 Torr, so a differential pump apparatus is installed in the vacuum system and the etching chamber as shown in Fig. 1. The etching chamber is evacuated independently and is designed to achieve high pressure (0.5 Torr) keeping other vacuum system at low pressure (< 10^{-5} Torr) by an aperture flange and a sequence of pressure stages. The condenser mirror focuses the divergent radiation onto the sample surface in the etching chamber, and obtains an extreme higher photon flux can be obtained.

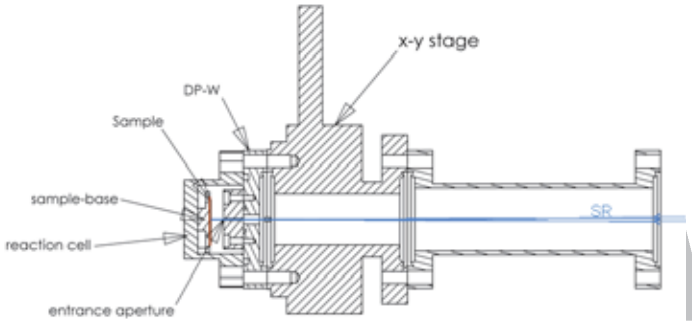

Fig. 1 Section view of differential pump apparatus installed in the etching chamber (reaction cell) and the entrance of beam.

Fig.2 A side view of the end-station at BL4A1.

Beamline Specifications

Monochromator	Multilayered mirror monochromator
Wavelength Range	13.3 ~ 22.5 nm
Resolution	5 ~ 9 eV (FWHM)
Experiment	Irradiation
Miscellaneous	Not-in-use for SR users

BL4A2

SR-induced Photo Etching and CVD Beam Line

This beam line is used for synchrotron radiation (SR)-induced photo-etching and chemical vapor deposition (CVD) experiments. The beam line has no monochromator for high photon flux to irradiate and consists of only two mirrors. One is for focusing and the other is for branching. At the beam line, the gas supply and extinction system is equipped for using legally controlled high pressure gasses such as SiH_4, Si_2H_6 and GeH_4. They are commonly used to CVD of semiconductor crystals.

The SR-CVD and photo-etching chambers are connected to the beam line as shown in Fig. 1. In those chambers, infrared reflection absorption spectroscopy (IRRAS) system is installed to study the surface photochemistry on Si surfaces modified with various kinds of molecules.

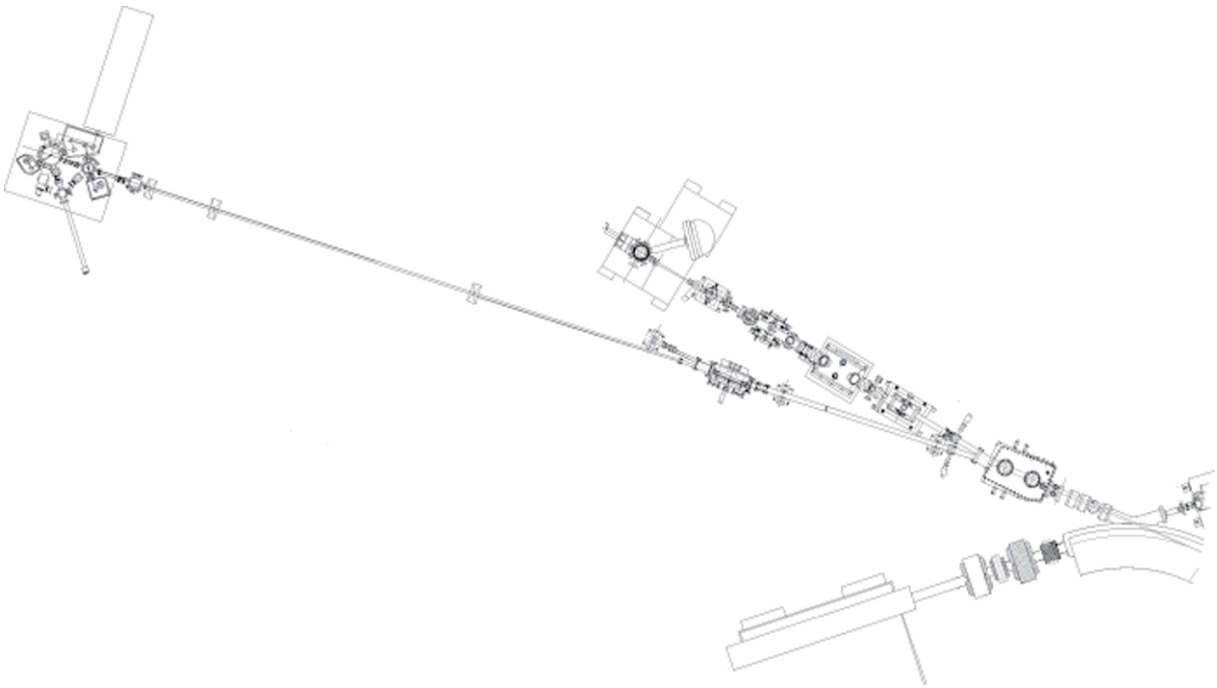

Figure 1 Top view of BL4A2

Specifications

Spectral range: whole range of synchrotron radiation from UVSOR

BL4B

Varied-line-spacing Plane Grating Monochromator for Molecular Soft X-ray Spectroscopy

The beamline BL4B equipped with a varied-line-spacing plane grating monochromator (VLS-PGM) was constructed for various spectroscopic investigations in a gas phase and/or on solids in the soft X-ray range. Three holographically ruled laminar profile plane gratings with SiO_2 substrates are designed to cover the photon energy range from 25 eV to 800 eV. The gratings with the groove densities of 100, 267, and 800 l/mm cover the spectral ranges of 25-100, 60-300, and 200-1000 eV, respectively, and are interchangeable without breaking the vacuum. Fig. 1 shows the absolute photon flux for each grating measured by a Si photodiode (IRD Inc.), with the entrance- and exit-slit openings set at 50 and 50 μm, respectively. The maximum resolving power (E/ΔE) achieved for each grating is more than 5000.

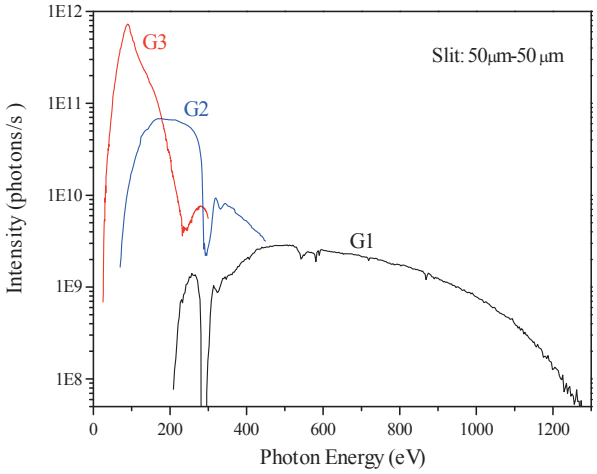

Fig. 1 Throughput from the VLS-PGM monochromator on BL4B.

Fig. 2 Photo of BL4B.

Beamline Specifications

Monochromator	Varied-line-spacing Plane Grating Monochromator
Energy range	25-1000 eV
Resolution	E/ΔE > 5000 (at maximum)
Experiments	Soft X-ray spectroscopy (mainly, angle-resolved photoion spectroscopy for gaseous targets and photoelectron spectroscopy for gaseous and solid targets)

BL5U

Photoemission Spectroscopy of Solids and Surfaces

This beamline is designed for a high-resolution angle-resolved photoemission study on solids and surfaces with horizontal-linearly and circularly (CW, CCW) polarized synchrotron radiation from a helical undulator. The beamline consists of a Spherical Grating Monochromator with Translational and Rotational Assembly Including a Normal incidence mount (SGM-TRAIN), and a high-resolution angle-resolved photoemission spectrometer.

The SGM-TRAIN is an improved version of a constant-length SGM to aim the following points; (1) covering the wide energy range of 5-250 eV, (2) high energy resolving power, (3) use of linearly and circularly polarized undulator light, (4) reduction of higher order light, and (5) two driving modes (rotation and translation of gratings) by computer control. The second-order light is well suppressed by using laminar profile gratings and combinations of mirrors and gratings.

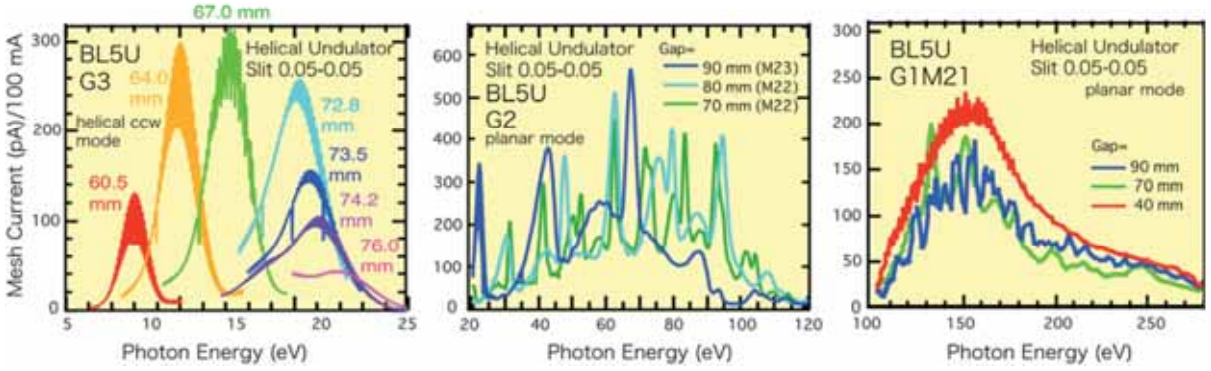

Fig. 1. Throughput spectra from the SGM-TRAIN monochromator at BL5U.

Beamline Specifications

Monochromator	SGM-TRAIN
Energy Range	5-250 eV
Resolution	$h\nu/\Delta E$ >2,000 for < 40μm slits
Experiment	ARPES, AIPES, XAS
Flux	$<10^{11}$ photons/s for < 40μm slits (at the sample position)
Main Instruments	Hemispherical photoelectron analyzer (MBS-Toyama 'Peter' A-1), LEED of reverse type (OMICRON), Liq-He flow cryostat (5 – 400 K)

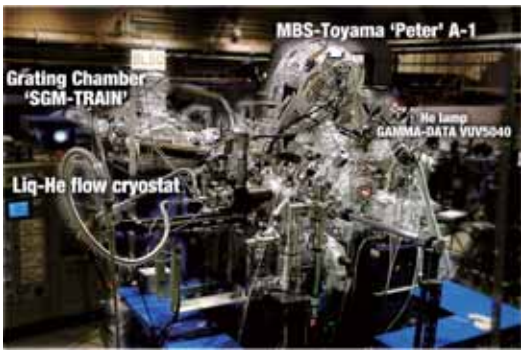

Fig. 2. High-resolution angle-resolved photoemission apparatus at BL5U

BL5B

Calibration Apparatus for Optical Elements and Detectors

BL5B has been constructed to perform calibration measurements for optical elements and detectors. This beamline is composed of a plane grating monochromator (PGM) and three end stations in tandem. The most upstream station is used for calibration measurements of optical elements, the middle one for optical measurements for solids and the last for photo-stimulated desorption experiments. The experimental chamber at the most downstream station is sometimes changed to a chamber for photoemission spectroscopy.

The calibration chamber shown in Fig. 2 is equipped with a goniometer for the characterization of optical elements, which has six-degree-of-freedom; X-Y translation of a sample, and interchange of samples and filters. These are driven by pulse motors in vacuum. Since the polarization of synchrotron radiation is essential for such measurements, the rotation axis can be made in either horizontal or vertical direction (s- or p-polarization).

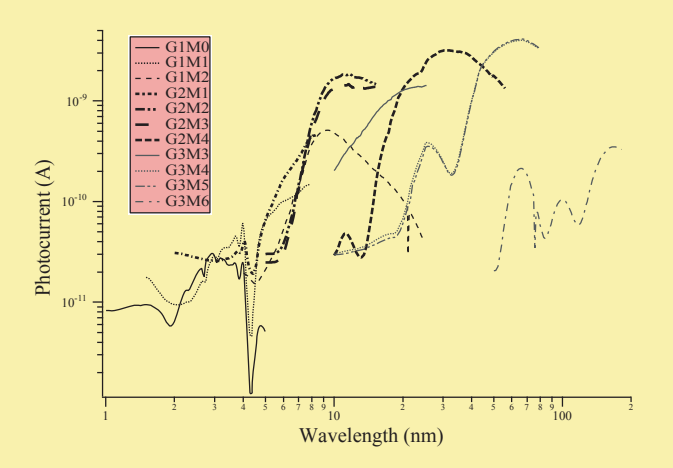

Fig. 1 Throughput spectra for possible combinations of gratings and mirrors at BL5B measured by a gold mesh.

Fig. 2 A side view of the experimental chamber for calibration measurements.

Beamline Specifications

Monochromator	Plane Grating Monochromator
Energy range	6-600 eV (2-200 nm)
Resolution	E/ΔE ~ 500
Experiments	Calibration of optical elements, absorption of solids, photo-stimulated desorption from rare gas solids

BL6B (IR)

Infrared and Terahertz Spectroscopy of Solids

SR has a good performance (high brilliance and high flux) not only in VUV and SX regions but also in IR and terahertz regions. This beamline covers in the IR and terahertz regions. The previous beamline BL6A1 that has been constructed in 1985 is the pioneer of the infrared SR research. The beamline was upgraded in the spring of 2004 and the name was changed to be BL6B (IR). The front-end part including the bending duct #6 was replaced to a new one with higher acceptance angle using a magic mirror as shown in Fig. 1.

The beamline is equipped with two interferometers, one is Michelson-type (Bruker IFS-66v) and the other Martin-Puplett-type (JASCO FARIS-1), for the wide spectral region from several to 20,000 cm^{-1} ($h\nu$ = several 100 μeV – 2.5 eV) as shown in Fig. 2. The experimental chamber in which users bring can be equipped at the free port. In the near future, an IR microscope covering down to terahertz region will be set up.

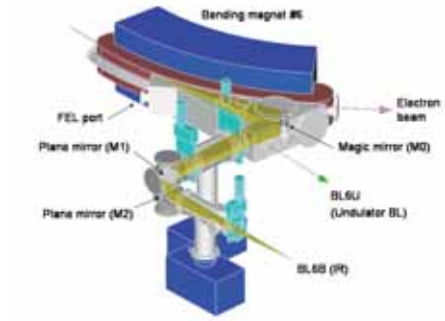

Fig. 1 The design of optics and front end of BL6B.

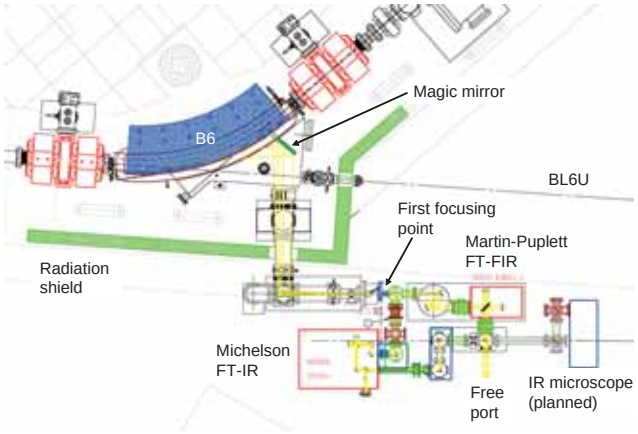

Fig. 2 Schematic figure of top view of BL6B.

Beamline Specifications

Interferometer	Michelson (Bruker IFS66v), Martin-Puplett (JASCO FARIS-1)
Wavenumber Range (Energy range)	several – 20,000 cm^{-1}, (several 100 μeV – 2.5 eV)
Resolution in cm^{-1}	0.1cm^{-1} for IFS66v, 0.25cm^{-1} for FARIS-1
Experiments	Reflectivity and transmission, Magneto-optics (Microspectroscopy)
Miscellaneous	Users can bring their experimental system in this beamline.

BL7U

Angle-resolved Photoemission of Solids in the VUV region

The beamline 7U is constructed to provide the photon flux with high energy resolution and high flux mainly for high-resolution angle-resolved photoemission spectroscopy of solids. An APPLE-II-type variable polarization undulator is equipped for the light source. The undulator can make high intense VUV light with horizontal/vertical linear and right/left circular polarization. The undulator light is monochromatized by the modified Wadsworth-type monochromator with three gratings (R = 10 m; 1200, 2400 and 3600 lines/mm optimized at $h\nu$ = 10, 20, and 33 eV). The energy resolution of light ($h\nu/\Delta h\nu$) is more than 10^4 with the photon flux of more than 10^{11} ~ 10^{12} ph/s on samples in the whole energy region.

The beamline has a photoemission end station which equips a 200-mm-radius hemispherical photoelectron analyzer (MB Scientific AB, A-l analyzer) and a liquid-helium-cooled cryostat with a 6-axes pulse motor control (A-VC Co. Ltd., i-GONIO). The main purpose is to determine the three-dimensional Fermi surface and electronic structure of solids at low temperatures and their temperature dependence to reveal the origin of the physical properties.

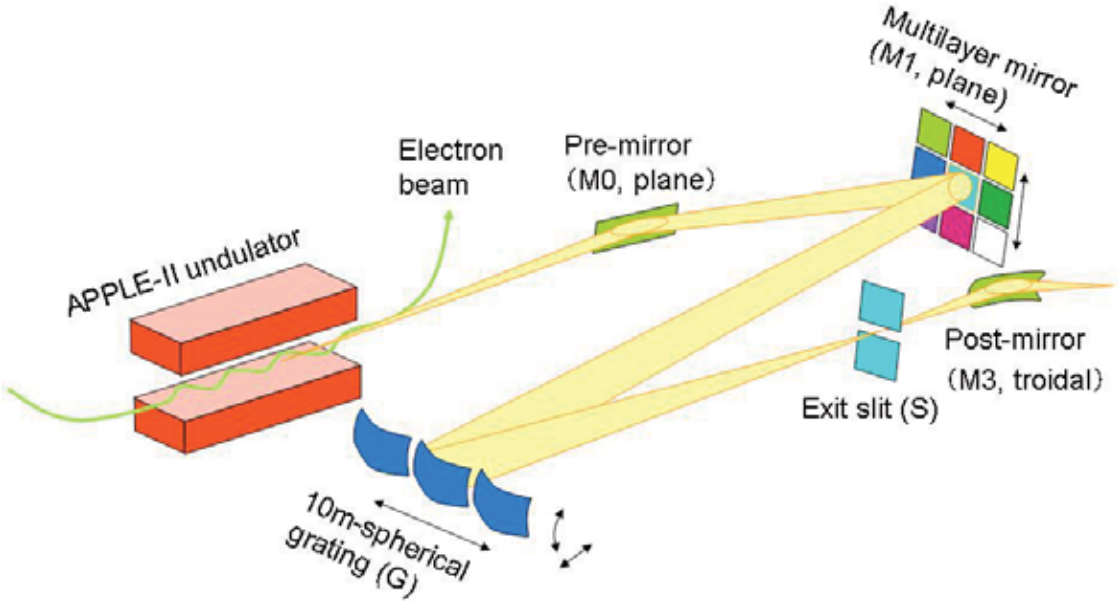

Fig.1. Schematic figure of BL7U.

Beamline Specifications

Light source	APPLE-II type undulator (λ_u = 76mm, N = 36)
Monochromator	10-m Normal Incidence Monochromator (modified Wadsworth-type)
Photon energy range	6 ~ 40 eV (λ = 30 ~ 200 nm)
Resolution ($h\nu/\Delta h\nu$)	1×10^4 ~ 5×10^4
Photon flux on sample	$\geq10^{12}$ ~ 10^{11} ph/s (depend on $h\nu$)
Beam size on sample	200(H)×50(V) μm^2
Experiments	Angle-resolved photoemission of solids (MB Scientific A-1 analyzer)

BL8B1

Spherical Grating Monochromatorfor Soft X-Ray Spectroscopic Studies on Solids and Surfaces

The beamline BL8B1 equipped with a constant-deviation constant-length spherical grating monochromator [1] provides soft X-ray photons in the energy range 30-800 eV with medium energy resolution. The photon energy range is covered by using three gratings (R=15 m; 1080 l/mm, R=15 m; 540l/m, and R=7.5m; 360 l/mm) which are interchangeable in vacuum. Figure 1 shows a throughput spectrum measured with the entrance- and exit-slit openings of 10 μm. Under this condition, the achievable resolving power is about 4000 at 400 eV and 3000 at 245 eV, respectively.

An experimental chamber is equipped for conventional measurements of electron yield spectra, or pseudo-photoabsorption spectra, under a ~1×10^{-6} Torr vacuum condition.

[1] Hiraya et al., Rev. Sci. Instrum. **66** (1995) 2104.

Fig. 1 Photo of BL8B1.

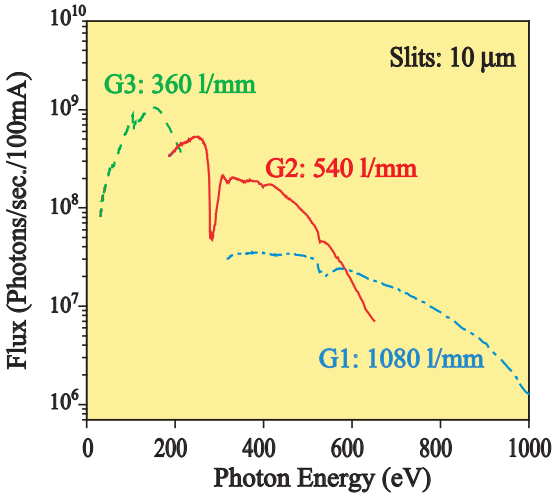

Fig. 2 Throughput of the monochromator at BL8B1.

Beamline Specifications

Monochromator	Constant-deviation constant-length spherical grating type
Energy range	30-800 eV
Resolution	E/ΔE = 4000 at 400 eV and 3000 at 245 eV
Experiments	Photoabsorption spectroscopy, electron spectroscopy and electron-ion coincidence spectroscopy for solids and surfaces

BL8B2

Angle-Resolved Ultraviolet Photoelectron Spectrometer for Solids

BL8B2 is a beamline for angle-resolved ultraviolet photoemission spectroscopy (ARUPS) system which is designed for measuring various organic solids such as molecular crystals, organic semiconductors, and conducting polymers. This beamline consists of a plane-grating monochromator (PGM), a sample preparation chamber with a fast entry Load-Lock chamber, a measurement chamber with an accurate for temperature dependence (base pressure 1×10^{-10}Torr), a cleaning chamber (base pressure 1×10^{-10}Torr), and a sample evaporation chamber (base pressure 3×10^{-10}Torr). The cleaning chamber is equipped with a back-view LEED/AUGER, an ion gun for Ar^+ sputtering, and an infrared heating unit. The PGM consists of premirrors, a plane grating, focusing mirror, and a post-mirror, with an exit slit. It covers the wide range from 2 to 130eV with exchanging two gratings (G1: 1200l/mm, G2: 450l/mm) and five cylindrical mirrors. The toroidal mirror focuses the divergent radiation onto the sample in the measurement chamber. The spot size of the zeroth-order visible light at the sample surface is about $1\times1mm^2$. Figure 1 shows the throughput spectra of PGM (slit=100μm). The energy resolution at a slit width of 100μm was found to be E/ΔE = 1000 in the wavelength range from 2 to 130eV. A hemi-spherical electron energy analyzer of 75mm mean radius with an angular resolution less than 2° can be rotated around vertical and horizontal axes. The sample mounted on a manipulator can be also rotated around two axes.

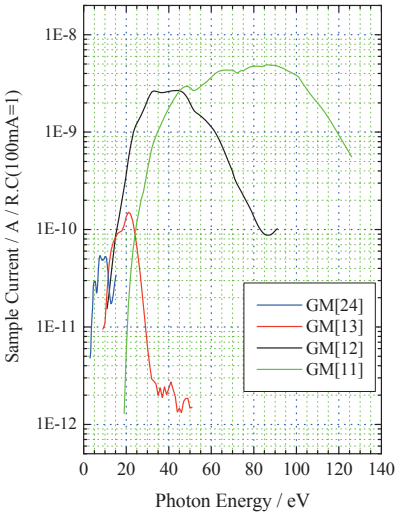

Fig. 1 Throughput spectra of plane-grating monochromator at BL8B2 (slit=100μm).

Fig. 2 A photo of BL8B2.

Beamline Specifications

Monochromator	Plane-grating monochromator
Wavelength Range	9- 600nm
Resolution	E/ΔE = 1000
Experiment	Angle-resolved ultraviolet photoemission spectroscopy

1
Accelerators and beam physics

Observation of Intense Terahertz Synchrotron Radiation Produced by Laser Bunch Slicing at UVSOR-II

M. Shimada[1], M. Katoh[1,2], A. Mochihashi[1], S. Kimura[1], T. Hara[1]*, M. Hosaka[2], Y. Takashima[2], T. Takahashi[3]

[1]*Institute for Molecular Science, Myodaiji-cho, Okazaki, 444-8585 Japan*
[2]*Nagoya University, Furo-cho, Chikusa-ku, 464-8603 Japan*
[3]*Kyoto University, Kumatori-cho, Sennan-gun, Osaka, 590-0494 Japan*

Coherent synchrotron radiation in terahertz region (THz CSR) can be produced from the sub-mm scale micro-structure on the longitudinal density distribution of the electron bunches. THz CSR is generated by the bunch instability [1] and the laser bunch slicing, which is a technique to produce the micro-structures on the electron bunches. In the laser bunch slicing, a femto-second ultra-short laser pulse interacts with an electron bunch in an undulator and induces the energy modulation in the bunch. As the bunch transports in the ring, the modulated electrons are separated from the bunch and a dip is created. We succeeded to observe high intensity THz CSR from the modulated electron bunch.

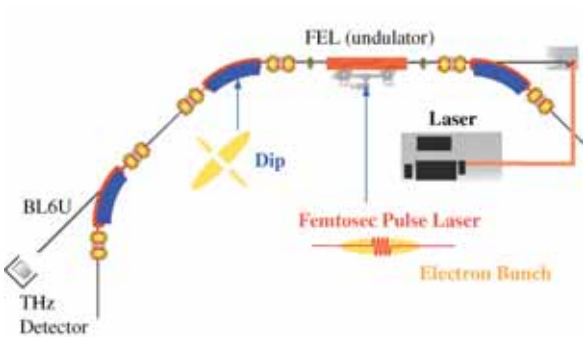

Fig. 1 Schematic of the laser bunch slicing system.

The laser system is composed of a mode-lock Ti:Sa laser and a regenerative amplifier as illustrated in Fig. 1. The former generates laser pulses synchronized with electron bunches and the latter generates intense ultra-short laser pulses with energy of 2.5 mJ/pulse and repetition rate of 1 kHz.

The laser pulses are introduced to the ring through a laser transport line conducted to the undulator in the free electron laser. The laser pulses and the electron bunches interact in the undulator polarized horizontally and tuned at the laser wavelength, 800 nm. The streak camera was used for spatial and temporal alignment between the laser beam and the electron beam.

The ring was operated in the single bunch mode at 600 MeV, which is suitable to tune the undulator at the laser wavelength, 800 nm. The THz CSR is observed at, BL6B, which is connected to the second bending magnet from the undulator section, and has a large solid angle, 215 mrad x 80 mrad [2]. The collected THz CSR is introduced to a liquid He cooled InSb bolometer, which is sensitive to the wavelength region between 0.2 mm to 3.0mm.

Intensity of the terahertz pulses generated by the laser bunch slicing is 10^4 – 10^5 times higher than that of the normal synchrotron radiation. The detector output for the individual pulse of THz CSR is also shown in Fig.2. The pulse width is a few micro-second, which is almost the same as the temporal resolution of the bolometer.

The intensity of the pulse of THz CSR was plotted as a function of the beam current in Fig. 3. The intensity is proportional to square of the peak current of the electron beam which was obtained experimentally by using a streak camera. This result clearly indicates that the observed THz radiation is coherent.

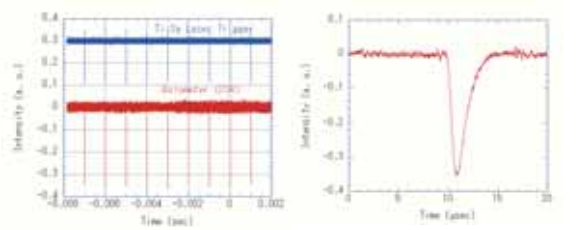

Fig. 2 (Left) terahertz pulses induced by the laser injection. (Right) detector output signal (negative) for individual terahertz pulse.

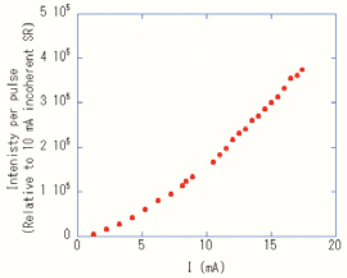

Fig. 3 Intensity of THz CSR versus peak current of electron bunch. The solid line is a best-fit square curve.

[1] Y. Takashima *et al*., Jpn. J. Appl. Phys. **44** (2005) 1131.
[2] S. Kimura *et al*., AIP Conf. Proc. **705** (2004) 416.

*Guest associate professor from RIKEN/SPring-8

BL5U (FEL)

Storage Ring FEL Exceeding 1 W in the Deep UV Region

M. Hosaka[1], M. Katoh[1,2], A. Mochihashi[1], M. Shimada[1], J. Yamazaki[1], K. Hayashi[1], Y. Takashima[2]

[1]*UVSOR Facility, Institute for Molecular Science, Okazaki 444-8585 Japan*

[2]*Depertment of Material Processing Engineering, Graduate School of Engineering, Nagoya University, Chikusa-ku, Nagoya 464-8603 Japan*

Thanks to a recent upgrade of the UVSOR-II storage ring (lower beam emittance and higher peak current), an FEL gain has been enhanced much and we have succeeded in high power lasing in deep UV region. In 2005 we replaced rf accelerating cavity system [1]. The aim is to improve lifetime of the electron beam with higher accelerating voltage. At the UVSOR, 90.1 MHz rf cavity had been operated with a 20 kW transmitter but the rf accelerating voltage (55 kV at maximum) was limited by low shunt impedance (1 MΩ) of the former cavity. Hence the new rf cavity was designed to have higher shunt impedance. The new cavity was installed in the spring of 2005 and the high cavity voltage of 150 kV was achieved. This upgrade is favourable to the FEL because higher accelerating voltage leads to shorter electron bunch and higher peak current.

The lasing experiment around 230 nm was planned oriented to users experiment [2]. Multi-layers of Al_2O_3/SiO_2 were also employed for cavity mirrors. Measured round-trip reflectivity and transmission were 98.8 % and 0.8%, respectively. The lasing experiment was carried out with an electron energy of 750 MeV. Former UVSOR FEL experiment had been made with an electron energy of 600 MeV. Recently we raised the electron energy from 600 MeV to 750 MeV, with which the storage ring is operated for SR use. According to the Renieri limit [3], the extracted FEL power is proportional to the total synchrotron radiation power per turn from electron beam. Since the total radiation power is proportional to the 4th power of the electron energy, higher extracted laser power is expected at 750 MeV. The measured threshold current for lasing is about 2 times higher than that in the case of 600 MeV. But a higher laser power is extracted. The observed maximum power reached 1.1 W at a beam current of 100 mA/bunch. During the experiment, drift of the laser power was observed especially at a high beam current as shown in the figure. The power could be recovered by adjusting the alignment with downstream mirror once again. Therefore the power drift can be explained by deformation of the cavity mirror due to heat-load from synchrotron radiation and from the FEL. The laser, however, became almost stable after about one hour exposure of synchrotron radiation. The FEL around 230 nm was applied to two experiments on surface physics and photo-electron spectroscopy. The FEL extracted from the upstream mirror was transported to the experimental stations by using aluminium mirrors and was focused on samples by lenses. In the experiments, they started the measurement after the laser became stable. The FEL power around 0.5 ~ 0.2 W was actually applied. Although the experiments were made in limited machine time, the users succeeded in obtaining primary results.

[1] A. Mochihashi *et al.*, UVSOR Activity Report 2005 (2006).
[2] T. Nakagawa *et al.*, UVSOR Activity Report 2006 (2007).
[3] A. Renieri, Nuovo Cimento **53** (1979) 160.

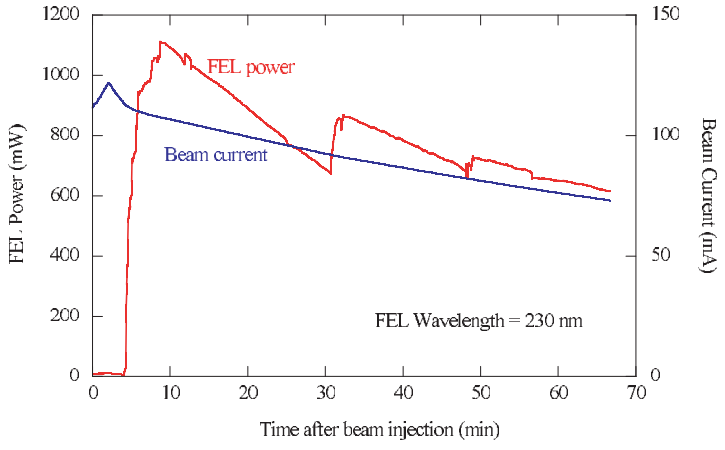

Fig. 1 Extracted FEL power and beam current as a function of time. The FEL wavelength is around 230 nm.

Coherent Harmonic Generation Experiment

M. Labat[1] , G. Lambert [1,2], M.E. Couprie [3], Y. Takashima [5], T. Hara [4], M. Hosaka [5], A. Mochihashi [6], J. Yamazaki [6], M. Shimada [6], M. Katoh [6]

[1] *CEA Saclay, 91 191 Gif-sur-Yvette France*

[2] *Synchrotron Soleil, Saint Aubin France*

[3] *Laboratoire Aimé Coton, Orsay France*

[4] *RIKEN SPring-8 Harima, Hyogo Japan*

[5] *Nagoya University, Nagoya Japan*

[6] *UVSOR Facility, Institute for Molecular Science, Okazaki 444-8585 Japan*

Coherent Harmonic Generation (CHG) is a seeded Free Electron Laser configuration based on storage ring [1]. A Ti:Sa laser is focused in the first part of the optical klystron (OK): the modulator, and synchronized with the circulating electron bunch. The electron beam is micro bunched at fundamental and sub harmonic wavelengths of the seeded laser. The light emission of the electrons is then enhanced in the second OK part, the radiator, at the third harmonic of the seed, i.e. 266 nm.

The intensity of the light emitted by a relativistic electron bunch in an optical klystron can be expressed as the sum of an incoherent and a coherent term. The coherent term equals zero for randomly distributed electronic phases. In the case of CHG process, the interaction between the electric field and the electrons induces a modulation of the distribution: the intensity of the coherent emission no longer averages to zero.

For CHG experiment, the machine is operated at 600 MeV in single bunch mode. The modulator and radiator of the BL5U OK are identical and separated by a dispersive section. The detection of the UV light is performed using a solar blind PhotoMultiplier. In order to observe the coherent emission at 1 kHz, among incoherent emission at 5.6 MHz, its signal is observed on an oscilloscope, triggered by the laser timing system. A streak camera (Hamamatsu, C5680) allows following the longitudinal distribution of the electron bunch. The seeding laser is high repetition rate (1 kHz), short pulse duration (150 fs to 1 ps) Ti:Sa with 800 nm wavelength.

The temporal overlap in the modulator for the micro bunching of the electronic distribution requires a precise synchronization of the laser pulse and the electron bunch, using a specific timing system. The condition of synchronization is observed with the streak camera, which temporal resolution reaches 10 ps. Spatial overlap is obtained adjusting the laser path on the electron orbit.

A picture of the PM signal is presented in Figure 1, illustrating the output radiation of the undulators. Central peak corresponds to the radiation of the laser heated electron bunch. The intensity at 266 nm is dramatically enhanced thanks to the coherent emission at the third harmonic of the seeding laser.

Fig. 1 Oscilloscope trace of the optical klystron out put radiation. Laser power=1.78 W, I=4.29mA. Time scale: 40 ns/division.

Figure 2 shows the streak camera image of CHG signal. This diagnostic confirms the enhancement of the intensity at 266 nm radiated by the heated electron bunches (see bright blue spots).

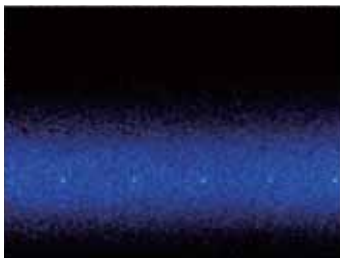

Fig. 2 Photograph of the streak camera image. Full scales are 85 ms for the horizontal and 700 ps for the vertical axis.

First results confirmed the expected quadratic dependency of the coherent emission with peak current. An optimum undulator gap for CHG emission was found at 40.8 mm and the signal vanishes for gaps below 39.7 and over 42.5 mm.

Using a 1 kHz Ti:Sa laser, a Coherent Harmonic Generation FEL configuration has been successfully set up at UVSOR-II facility. Short (below 2 ps), UV (266 nm), coherent laser pulses are delivered.

[1] R. Prazeres, J.M. Ortega, C. Bazin, M. Bergher, M. Billardon, M.E. Couprie, M. Velgue and Y. Petroff, Nucl. Inst. Meth. A **272** (1988) 68-72.

Variation of Circumference of UVSOR-II

K. Suzumura[1], M. Katoh[2,1], Y. Takashima[1], K. Hayashi[2], A. Mochihashi[2], J. Yamazaki[2], M. Hosaka[1], M. Shimada[2]

[1]*Graduate School of Engineering, Nagoya University, Chikusa-ku Nagoya 464-8603 Japan*

[2]*UVSOR Facility, Institute for Molecular Science, Okazaki 444-8585 Japan*

A drift of the electron orbit in a synchrotron light source causes a drift of the light source position, which makes harmful effects on the users experiments. Recently, we have developed a RF-FB system, to suppress orbit drift at UVSOR-II [1]. The system corrects automatically the drift by controlling the RF frequency, and its value is recorded during user operations. The system has been working successfully for about one year. By using the accumulated data, we can see the variation of the circumference of UVSOR-II in various time scales.

UVSOR-II is operated for users from Tuesday to Friday in a week, and from AM9:00 ~ PM9:00 in a day. Fig.1 shows variations of the RF frequency and of the floor temperature of the storage ring room during a week. During one day, the RF frequency decreases with time. The variation amplitudes during each day are about the same, but the absolute value decreases gradually throughout a week. On the other hand, the floor temperature increases with time during a day, and the absolute value increases throughout a week. As shown in Fig.1, the RF frequency shows strong correlation with the floor temperature. Fig.2 shows the variation of the RF frequency and the floor temperature during a year. The RF frequency varies through a year. It is higher in winter and lower in summer. The floor temperature also varies through a year. However, there can be seen no clear correlation with the RF frequency.

There can be seen a strong correlation between the RF frequency and the floor temperature during a day or during a week. This fact suggests that the variation of the circumference of the storage ring is mainly caused by thermal expansion of the floor. Because the storage ring components, such as magnets, are fixed rigidly to the floor, it is considered that the storage ring expands outward when the floor expands as its temperature increases.

We can quantitatively validate the assumption by comparing measured and theoretical values of the RF frequency using the measured floor temperature. The theoretical value can be calculated as following,

$$\Delta f_{RF} = -f_{RF} \cdot \alpha \cdot \Delta t ,$$

where f_{RF} the RF frequency, α the thermal expansion coefficient of the floor, and Δt the measured floor temperature variation. Each value is as following, f_{RF}=90.1MHz, α=1.0x10^{-5}/^{o}C for concrete and Δt=0.8^{o}C in a day. As assigning these values to the expression, the theoretical value of Δf_{RF} in a day becomes 0.72kHz. As shown fig.1, the measured value in a day is about 0.6kHz. The theoretical value is close to the actual measurement value. From this result, there is a high possibility that the main cause of the variation of the circumference is the thermal expansion of the floor.

It seems that there is no clear correlation between f_{RF} and Δt through a year, as shown in Fig. 2. However, it seems to have good correlation with the outdoor temperature. This point may be discussed after several year operation of the RF-FB system.

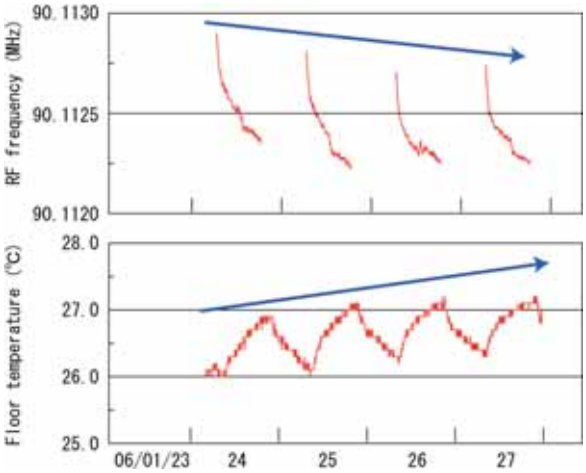

Fig.1 The variation of RF frequency and floor temperature of a week.

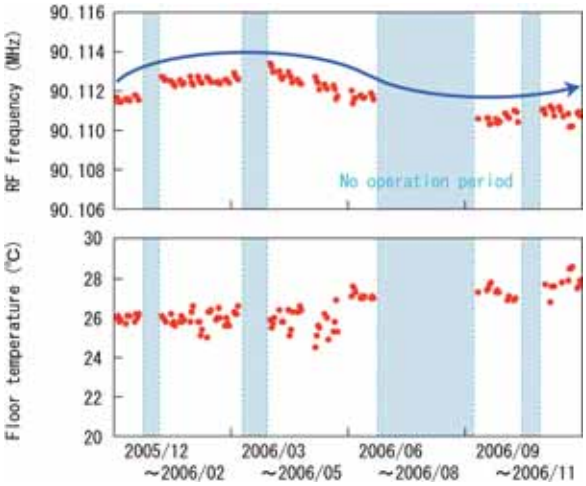

Fig.2 The variation of RF frequency and floor temperature of a year.

[1] K. Suzumura *et al.,* UVSOR Activity Report 2005 (2006), 39

Development of a BPM Displacement Measurement System at UVSOR-II

K. Suzumura[1], M. Katoh[2,1], Y. Takashima[1], K. Hayashi[2], A. Mochihashi[2], J. Yamazaki[2], M. Hosaka[1], M. Shimada[2]

[1]*Graduate School of Engineering, Nagoya University, Chikusa-ku Nagoya 464-8603 Japan*

[2]*UVSOR Facility, Institute for Molecular Science, Okazaki 444-8585 Japan*

The electron beam orbit of the UVSOR-II storage ring is measured by 24 BPMs (Beam Position Monitors), which are integrated on the beam ducts. Each BPM head consists of 4 electrodes, and detects the orbit by comparing the induced electric voltages on the electrodes. The data are used to correct the orbit. However, there is a possibility of measurement error caused by mechanical displacements of the BPM heads. We have developed a system to measure BPM displacement in real time.

The system we have developed is schematically shown in Fig.1. It consists of linear gauges, gauge counter, fixing clamps and PC for data logging. The read-out resolution of the linear gauges is one micron. The material of the fixing clamps is aluminum. They are fixed to iron cores of the bending magnet. With one fixing clamp, two linear gauges can be set to measure horizontal and vertical displacements at once. The data acquisition system on PC is developed by using LabVIEW7.0. The data are stored every 5 seconds.

The temperature of the storage ring room changes with time, because of the heats produced by the accelerator components, such as electric power supplies. We expected that the possibility of thermal deformation of the fixing jigs may cause measurement errors. We artificially changed the temperature of a jig using a heater, to see the effect of the thermal deformation. In the result, the error caused by the thermal deformation was less than ten microns for the temperature change in daily operation. So we disregard it in this research.

We measured BPM displacements during user operations. Fig.2 shows the BPM displacement and the orbit position measured at a BPM called No.2 during a user operation. At this BPM, the beam position shows a large motion of a few hundred microns. However, the BPM position also show quit similar motion. These data indicate that the beam position does not move but the BPM moves. In fact, the beam duct on which the BPM No.2 is installed has a trouble on the cooling water channel. The temperature of the beam duct is changed by the irradiation of SR light, as shown in Fig.3. BPM No.1 is installed on the same beam duct and its position shows similar motion.

Fig.4 shows a BPM displacement and a beam position at another BPM, called No.11. The BPM displacement is much smaller than that of BPM No.2. But, still we observed some displacement of a few 10 microns. The beam position movement is much larger than this. Thus, we can say that this orbit movement is real. It is similar at the other BPM on the beam ducts without water cooling trouble. However, when we try to stabilize the orbit movement less than 10 micron, we must consider the displacements of the BPMs. This measurement system will be integrated in the orbit correction system.

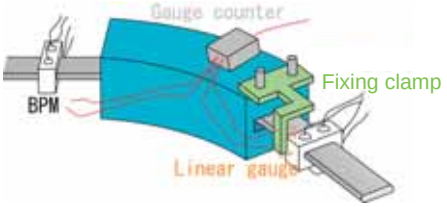

Fig.1 Schematic drawing of a BPM displacement measurement system.

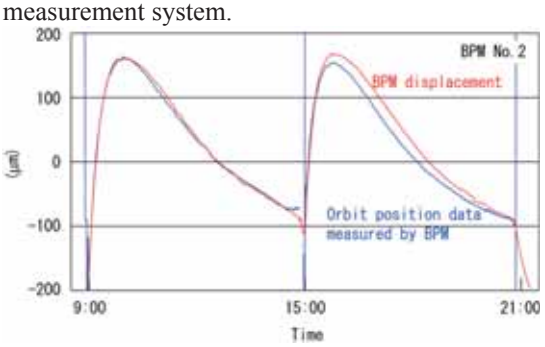

Fig.2 BPM displacement and orbit data measured by BPM during a user operation day at BPM2.

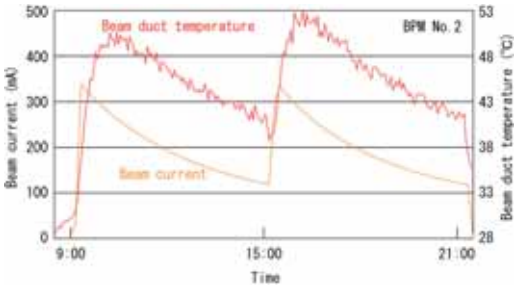

Fig.3 Beam current and beam duct temperature during a user operation day at BPM2.

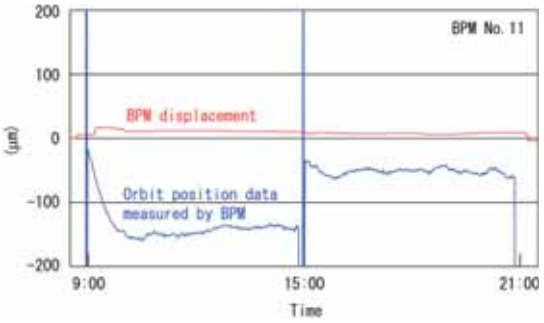

Fig.4 BPM displacement and orbit data measured by BPM during a user operation day at BPM11.

Touschek Lifetime Measurement with a Spurious Bunch in Single-bunch Operation in UVSOR-II Electron Storage Ring

A. Mochihashi[1], M. Katoh[1,2], M. Hosaka[2], Y. Takashima[2], Y. Hori[3]
[1]*UVSOR Facility, Institute for Molecular Science, Okazaki 444-8585 Japan*
[2]*Graduate School of Engineering, Nagoya University, Chikusa, Nagoya 464-8603 Japan*
[3]*High Energy Accelerator Research Organization (KEK) Oho, Tsukuba 305-0801 Japan*

We have developed a method to measure the Touschek beam lifetime of an electron storage ring using spurious bunches in single-bunch operation by measuring changes in the single-bunch impurity over time. To measure a spurious bunch and the main bunch simultaneously, we use a photon counting method with sufficient dynamic range and response time. We demonstrate the method by measuring the Touschek beam lifetime in the UVSOR-II electron storage ring. We find that the Touschek beam lifetime dominates the total beam lifetime in UVSOR-II in the usual vacuum condition. In SuperACO[1], a method to measure the Touschek lifetime by storing two bunches whose intensities are different has been developed. The 'two unequal bunches method' is very effective for measuring the Touschek lifetime if it is assumed that the Touschek lifetime is inversely proportional to the number of electrons in the bunch. The need for the assumption can be avoided by preparing two bunches with extremely different bunch charges. If the Touschek lifetime of the weaker bunch of the two is very long compared with that of the more intense bunch, it is possible to measure the Touschek lifetime of the intense bunch without making any assumption about the dependence of the Touschek lifetime on the bunch charge. However, it is difficult to make two bunches that have extremely different bunch charges when the bunch charge of the intense bunch is small. To make two bunches with extremely different bunch charges, with the more intense bunch having a small bunch charge, use can be made of the phenomenon in which extremely weak bunches compared with the main bunch can be generated automatically in single-bunch operation in electron storage rings [2,3]. The spurious bunch charge is extremely small compared with the main bunch regardless of the size of the main bunch charge, and can be generated automatically. Even though a spurious bunch can grow continuously during a measurement, it is possible to cancel the effects of the growth and measure the Touschek lifetime of the main bunch precisely using only the intensity of the main and spurious bunches, without requiring calculated beam or storage ring parameters. We consider the change with time in the number of electrons in a main bunch N_0 and that in the RF bucket immediately following the main bucket N_1. We assume the Touschek lifetime of the spurious bunch is much longer than that of the main bunch because of $N_0 >> N_1$. When the growth of the spurious bunch in one Touschek lifetime period of the main bunch $\tau_T(N_0)$ can be neglected compared with the single-bunch impurity N_1/N_0 the Touschek lifetime of the main bunch can simply be written as [4]

$$\frac{1}{\tau_T(N_0)} = \frac{d}{dt}\log\left(\frac{N_1}{N_0}\right). \quad (1)$$

If the assumption for the growth rate of the spurious bunch is not valid, it is still possible to measure the Touschek lifetime by repeating the measurement with a different spurious bunch charge with the same main bunch charge. For spurious bunch charges N_1 and N_1^* ($N_1 > N_1^*$) and main bunch charge N_0, $\tau_T(N_0)$ can also be written simply as

$$\frac{1}{\tau_T(N_0)} = \frac{d}{dt}\log\left(\frac{N_1 - N_1^*}{N_0}\right). \quad (2)$$

By considering the single-bunch impurity value in UVSOR-II, we adopted Eq.(2) to measure the Touschek lifetime in UVSOR-II. Figure 1 shows measured decay-rate and the Touschek beam lifetime in normal and poor vacuum conditions. To make the poor vacuum condition we turned off all of the ion pumps and heated a part of the beam ducts of the storage ring. In the figure, the decay-rate lifetime decreased in the poor vacuum condition but the Touschek lifetime still kept the same value as the normal vacuum condition. The vacuum pressure estimated from the beam lifetime agreed with the result from the vacuum gauge measurement.

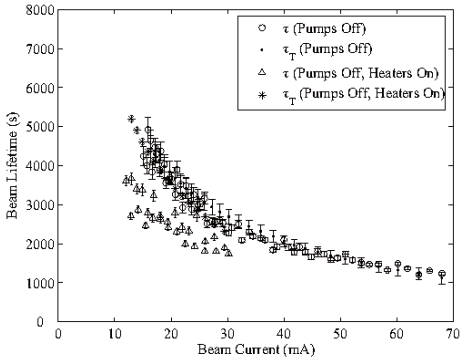

Fig.1 Measured decay-rate and Touschek lifetime in normal/poor vacuum condition in single-bunch operation.

[1] J. C. Besson *et al.*, Commissioning of SuperACO, ORSAY Report RT-88-01,(1988) 34.
[2]T. Kasuga *et al.*, Jpn. J. Appl. Phys. **28**(1989) 541.
[3]T. Obina *et al.*, Nucl. Instrum. Methods Phys. Res. A **354** (1995) 204.
[4]A. Mochihashi *et al.*, Nucl. Instrum. Methods Phys. Res. A **572** (2007) 1033.

2
Instrumental developments

High-Resolution Soft X-ray Emission Studies Using a Transmission-Grating Spectrometer

T. Hatsui[1,2,3], T. Horigome[1], H. Setoyama[4], N. Kosugi[1,2]
[1] *Institute for Molecular Science, Okazaki 444-8585 Japan*
[2] *Graduate University for Advanced Studies, Okazaki 444-8585 Japan*
[3] *PRESTO, JST, Kawaguchi, Saitama, 332-0012, Japan*
[4] *Kyushu Synchrotron Light Research Center, Tosu, Saga 841-0005, Japan*

Introduction

Soft x-ray emission studies in combination with synchrotron radiation sources have been a subject of increasing and broad interest as it provides information on the electronic structure on gas, liquid and solid materials. We have previously reported our new design of a transmission-grating spectrometer (TGS) for high resolution soft X-ray emission studies [1]. The optical design incorporates the basic concept for x-ray imaging and spectroscopy telescopes [2] into a compact and easy-to-use layout with higher energy resolving power. One of the advantage of the present TGS is its high light gathering capability without sacrificing the energy resolution, which is enabled by the introduction of the Wolter type-I mirror and the transmission grating (TG).

The present TGS is installed in the soft x-ray emission spectroscopy (XES) endstation of the undulator beamline BL3U of the UVSOR facility. In this report we describe the apparatus and its performance.

Optical Design and Apparatus

The present optical layout is a modification of the Rowland torus mount with facet gratings [1]. The design is adopted by Chandra x-ray satellite observatory. In the ideal Rowland torus mount, the facet TGs should be mounted onto Rowland torus while keeping their normal to point the focus of the incoming x-rays. In the present spectrometer, the facet TGs are positioned onto a single Si wafer. Such simplification may degradess optical properties. However, we demonstrated by ray-tracing simulations that the aberration in the geometry of the present spectrometer is small enough to realize the energy resolving power better than 5000 [2].

The TGS is pictured in Fig. 1. The soft x-rays emitted from the sample are collected by a type I Wolter mirror with a magnification of 10. The Wolter mirror is a tube-shaped composite mirror with hyperboloidal and elliptical inner-surfaces, which are 27 and 33 mm long, respectively. The incident anlge of 89 degree at the interconnection of the two mirror surfaces yields an acceptance angle as large as 1.5×10^{-3} sr. The slope error for each mirror estimated by the imaging property was better than 2.0 mrad rms [3]. The collected soft x-rays with a focus of 1500 mm downstream of the interconnection of the two mirror surfaces are dispersed by a transmission grating with a groove density of 6250 lines/mm. The transmission grating manufactured by NTT-ATN is made of silicon carbide and has a free-standing structure with a thickness of 800 nm. A detector together with the transmission grating and the focus of the 0^{th} order diffraction is positioned on a circle with a radius of 719.5 mm. The detector consists of a CCD (e2v CCD 42-40-A33) with a 2048 x 2048 pixel format with 13.5 x 13.5 mm and a preamplifier (Meisei Co.) inside the vacuum chamber. After the installation of the optical elements, the CCD chamber and the pipe between the CCD detector and the TG are baked at 100 °C. The pressure in the chamber is in the 10^{-7} Pa range.

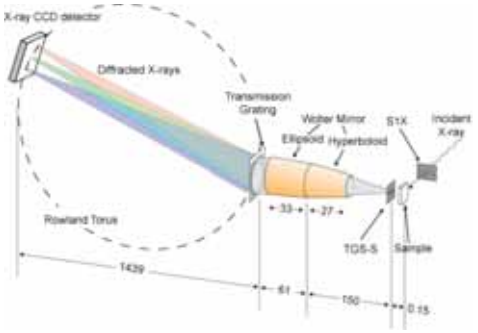

Fig. 1 Schematic layout of the transmission-grating spectrometer at the XES endstation of the undulator beamline BL3U.

The spectrometer is installed at the XES endstation of the undulator beamline BL3U. Schematic layout of the XES endstation of the undulator beamline BL3U is illustrated in Fig. 2 [4]. A soft x-ray emission spectrometer generally requires small beam size at the sample position, because a smaller opening of the spectrometer entrance slit is needed to achieve higher energy resolution. Beamline BL3U is designed to give small beam size of order of 10 x 40 μm^2 by placing sample 23 mm downstream of the beamline exit slit, S1X. This configuration is enabled by the constant exit-arm length of BL3U, where the x-rays from the undulator are dispersed by one of three plane varied-line-spacing grating, which have central groove densities of 240, 600, and 1200 lines/mm. The distance between the grating and the focal plane is 2703 mm. The slit opening as small as 10 μm diffracts soft x-ray significantly. The typical vertical beam size is 5-20 μm depending on the photon energy and the energy resolution of the incident x-rays. In the horizontal direction, the focusing mirror

M2X of the XES endstation images the undulator source with a demagnification of 23.4. Under operating condition, the horizontal beam profile has a gaussian profile with FWHM of 41.2 μm

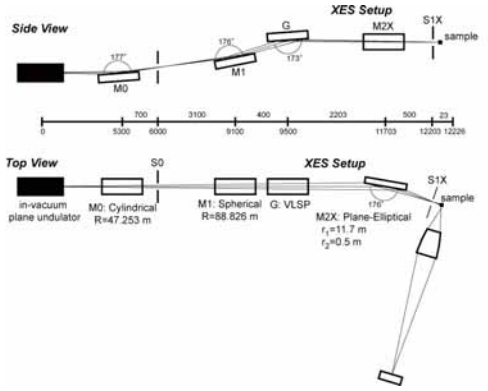

Fig. 2 Schematic Layout of XES endstation of the undulator beamline BL3U.

Results and Discussion

The stray light contamination is estimated by measuring the profile of the 0th order diffraction. Typically the stray light intensity is less than 1 % of the 1st diffraction order intensity. The energy resolution is estimated by measuring diffuse scattering from aluminum sample illuminated by 60 eV soft x-rays. Fig. 3 shows 1st order diffraction peak. The peak width was FWHM of 3 pixels, which corresponds to the energy resolving power of 4600. To our knowledge, the achieved resolving power by using TG is more than 4 times higher than the best record reported so far [5].

The spectrometer was employed to measure resonant XES spectra of a single crystal of silicon. The sample is illuminated with a grazing-angle of 20 degree. Fig. 4a shows the Si L-edge absorption spectrum of the sample together with the excitation energies. An image of the CCD detector taken by exciting at the resonance d is shown in Fig.4b. The vertically dispersed image where the lower direction corresponds to the higher photon energy clearly shows a sharp elastic peak with two bumped structure due to the x-ray emission. Horizontal length of the signal band is confined within about 1 mm, which is a magnified image of the sample area where the incident soft x-rays illuminated. Fig. 4c shows the XES spectra excited at the resonances, where each spectrum was taken within 30-120 min. with incident soft x-ray flux of 10^{11} photons/sec. The entrance slit opening was 20 μm. The spectrum clearly shows coherent and incoherent structure as reported in the previous work [6].

These results indicate that the present TGS is capable of carrying out high-resolution soft x-ray emission studies. Although rather low photon density is used in the current experiment, the results clearly show that the XES study is feasible with the present TGS. Large acceptance angle will give an advantage to the studies of organic samples where the sample damage is frequently problematic as well as the higher resolution studies which was out of the reach by using conventional x-ray emission spectrometers.

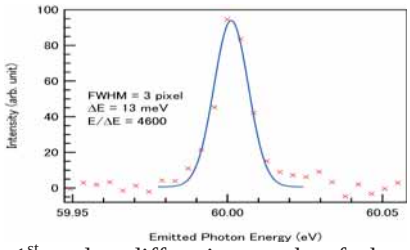

Fig. 3 1st order diffraction peak of the diffuse scattering from aluminum sample. Energy resolving power of 4600 is demonstrated.

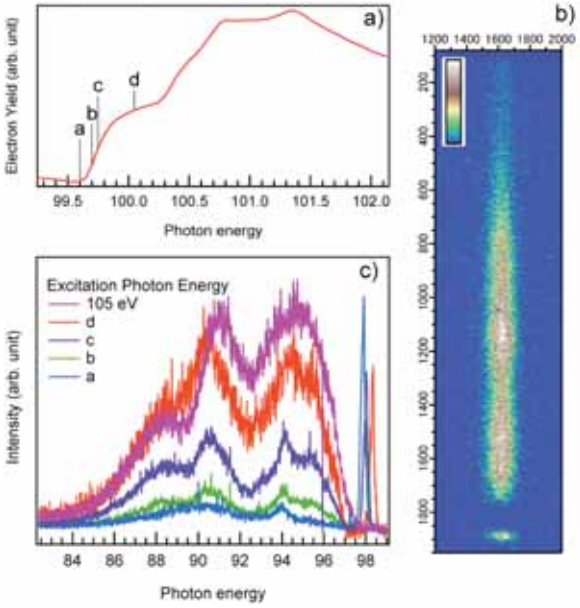

Fig. 4 Si L-edge Absorption spectra (a), and a CCD detector image when excitated at the resonance d.The labels a-d shows the excitation energies applied in resonant XES spectra (c).

Acknowledgements

The authors gratefully thank NTT-ATN, Hamamatsu Photonics, and Meisei Co. for the development of the TG and the Wolter mirror, and CCD electronics, respectively. This work is partly supported by the Japan Society for the Promotion of Science (JSPS), Special Coordination Funds for Promoting Science and Technology (MEXT), and International Collaboration Program (IMS).

[1] K.P. Beuermann, et.al., H. Bräuninger, J. Trümper, J. Applied Optics **17** (1978) 2304.

[2] T. Hatsui, E. Shigemasa, N. Kosugi, J. Electron Spectrosc. and Relat. Phenom., **144** (2005) 1059.

[3] A. Ohba, S. Onoda, Y. Sugiyama, private communication.

[4] T. Hatsui, E. Shigemasa, N. Kosugi, AIP Conf. Proc. **705** (2004) 921.

[5] C. R. Canizares, et.al., Publ. Astron. Soc. Pac. **117** (2005) 1144.

[6] S. Eisebitt, et.al., J. Electron Spectrosc. Relat. Phenom. **93** (1998) 245

BL2B

Construction of an End Station of BL2B to Study the Dissociative Photoionization of Fullerenes and VUV Spectroscopy of Ionic Liquids

H. Katayanagi[1,2], B. P. Kafle[2], S. I. Prodhan[2], H. Yagi[1], K. Mitsuke[1,2]

[1]Department of Vacuum UV Photo-Science, Institute for Molecular Science, Okazaki 444-8585 Japan

[2]Graduate University for Advanced Studies, Okazaki 444-8585 Japan

A new vacuum chamber for the end station of beam line 2B (BL2B) in UVSOR was constructed. The chamber was designed for the gas phase spectroscopy of refractory materials such as fullerenes, metallofullerenes and ionic liquids. The following three subjects are now under way: (1) the velocity map imaging of the ionic photofragments from fullerenes [1, 2], (2) threshold photoelectron – photoion coincidence measurements of the fullerenes, and (3) photoelectron and photoabsorption spectroscopy of ionic liquids.

Drawing of the chamber is shown in Fig. 1. The twofold μ-metal shield is put inside the chamber to prevent penetration of the geomagnetic field. The effective volume surrounded by the shield is five times as large as that of the previous chamber used at BL2B. The new chamber is equipped with 14 ports facing the ionization region, i.e. the focal point of the synchrotron radiation. This larger volume and versatile port arrangement enable us to incorporate many complicated devices. We designed this chamber to adapt not only to BL2B but also to BL7U. In order to compensate the difference of the heights of optical axes, we placed a stage of 50 cm in height at BL2B and put the chamber on the stage. Additionally the chamber was mounted on a micromotion stage to align its optical axis readily with the beam lines when the chamber is relocated.

The installation of the chamber at BL2B was accomplished. We observed TOF spectra of fragments and parent ions produced by the dissociative photoionization of fullerenes (C_{60}). We have obtained spectra using the previous setup at BL2B. In comparison with signal intensities and resolutions of these spectra, we can examine the performance of the new setup. The TOF spectrum at the photon energy of 90 eV obtained by the new setup is shown in Fig. 2. Intense three peaks in the spectrum correspond to C_{60}^{+}, C_{60}^{2+} and C_{60}^{3+} parent ions. Progressions of small peaks in shorter TOF side of doubly and triply charged parent ion peaks are fragments which lost C_2 units successively. From these results, we concluded that we succeeded in reproducing the results obtained with the previous setup.

Using the chamber with small modifications of signal processing electronics, we can perform more quantitative experiments than those using the previous setup. Prior to the new subjects (1) - (3), we resumed quantitative comparison of photoion yield spectra between the fullerene and higher fullerenes (C_{70} [3], C_{84}). This will give us a clue to understand extraordinary stability of fullerenes. Moreover, in the energy range available using BL7U (6 – 40 eV), the fullerenes have strong absorption (> 100 Mb) associated with structures which originate from molecular nature of the fullerenes. Although a part of the structure was observed using BL2B, it is subtle because the structure is out of practical coverage of the monochromator of BL2B. Observation of the fullerene absorption spectra in the energy range of BL7U using the new chamber will enable us to understand the ionization mechanism of fullerenes.

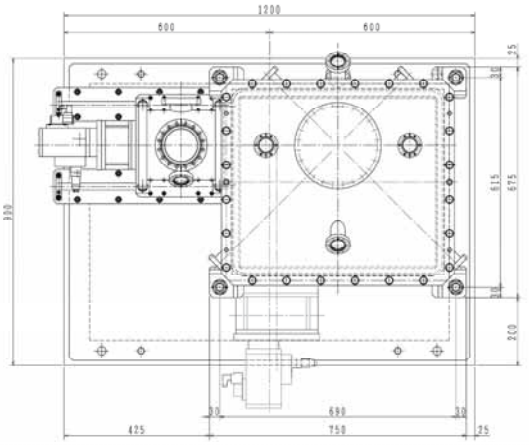

Fig. 1 Top view (drawing) of a new chamber for the end station of BL2B in UVSOR. Numbers in the figure are in mm.

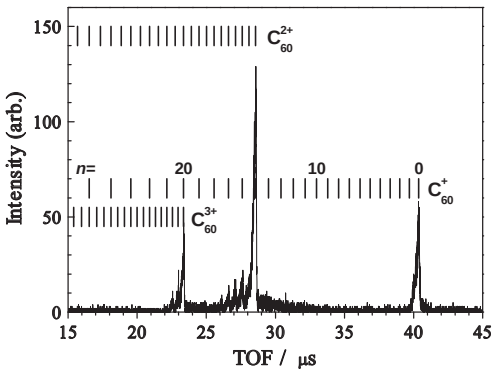

Fig. 2 TOF mass spectra of ions produced by the dissociative photoionization of the fullerene (C_{60})

[1] A. T. J. B. Eppink and D. H. Parker, Rev. Sci. Instrum. **69** (1997) 3477.
[2] B. P. Kafle *et al.,* AIP Conf. Proc. **879** (2007) 1809.
[3] J. Kou *et al.,* J. Chem. Phys. **120** (2004) 6005.

The Development of Sub-Pixel Spatial Resolution to Soft X-rays Using Electron-Multiplying CCD Detectors

T. Hatsui[1,2,3], N. Kosugi[1,2], A. Holland[4], R. Ingley[4], K. Holland[5]
[1] *Institute for Molecular Science, Okazaki 444-8585 Japan*
[2] *Graduate University for Advanced Studies, Okazaki 444-8585 Japan*
[3] *PRESTO, JST, Kawaguchi, Saitama, 332-0012, Japan*
[4] *Brunel University, Uxbridge, Middlesex,UB8 3PH, United Kingdom*
[5] *XCam Ltd, Northampton, NN3 7TG, United Kingdom*

Introduction

We have developed a transmission-grating spectrometer (TGS) for high-resolution soft-X-ray emission studies. This spectrometer is designed to realize a resolution E/ΔE beyond 5000 in the energy region of 50-600 eV with a high throughput. One of the key optical elements for this spectrometer is the charge-coupled device (CCD) detector. Here we report the development and performance of the CCD detector. The transmission grating has lower linear dispersion compared with reflection gratings. The detector is mounted in normal incidence geometry in order to obtain high quantum efficiency. These configurations demand the detector to have spatial resolution better than 5 μm. By measuring the center of the electron charge cloud generated in depletion layer of CCD, sub-pixel resolution detection was demonstrated for hard x-rays by Hiraga et.al [1]. In the case of soft X-rays, one photon produces a charge cloud, of which the total intensity is about 10 times weaker than hard x-rays (20-300 electrons). In order to analyze the centroid of the charge cloud, the intensity of the nearby pixels (1-10 electrons) must be accurately measured. This requirement is out of the reach of the conventional scientific CCD. In this study, we have introduced electron multiplying CCD technology in order to reduce the effective readout noise substantially lower than the intensity of the charge cloud tail, while increasing the readout rate as high as 400 kHz/pixel (10 frame/sec).

Experimental

The CCD detector is assembled with an un-coated back illuminated CCD sensor with L3Vision technology (CCD97-00) with 16 x 16 μm square pixels. The active area is 512 x 512 pixels (8.2 x 8.2 mm^2). The sensor is cooled by thermoelectric coolers and mounted on a conflat flange. The assembled and finely tuned CCD is illuminated by soft x-rays from the undulator beamline BL3U. The CCD detector is operated at 400 kHz/pixel (10 Hz/frame) readout rate with electron multiplication of about 100.

Results and Discussion

In the spectroscopic application, the one dimensional spatial resolution is of interest. Therefore, the CCD detector was operated in the binning mode of 4x1 pixels. The size of the charge clouds is evaluated by illuminating monochromatic soft x-rays from the undulator beamline BL3U. The spatial resolution has been estimated by measuring soft x-rays (380 eV) transmitted through 10 micron slit (Fig. 1a). Single pixel events are rejected as they originate from thermal electrons. Centroid in serial transfer direction (horizontal direction in Fig. 1) of all events that are spread over more than 2 pixels are analyzed. The resulting image is shown in Fig. 2b. The distance between the slit and the CCD sensor was 1.62 mm, which causes diffraction from the edge of the slit. The line profile across the slit image was simulated based on the Fresnel theory assuming the Gaussian profile of the point spread function (PSF) of the detector. By fitting the experimental results (Fig. 2), we obtained the PSF of the detector with FWHM of better than 3 μm, which represents 1/5th of a pixel resolution.

Acknowledgements

The authors gratefully thank Peter Pool (e2v) and e2v for the provision of the un-coated back-illuminated L3V sensors. This work is partly supported by Special Coordination Funds for Promoting Science and Technology (MEXT), and International Collaboration Program (IMS).

[1] J. Hiraga et.al., Jpn. J. Appl. Phys. **40** (2001)1493.

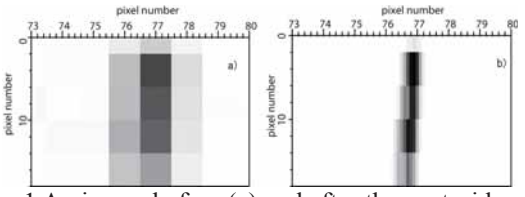

Fig. 1 An image before (a) and after the centroid analysis (b).

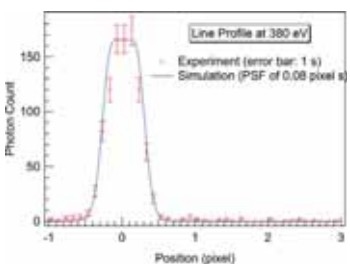

Fig. 2 Experimental line profile across the 10 μm slit image after the centroid analysis (+) and simulated line profile (blue line).

BL4B

Performance of the Double Toroidal Electron Analyzer for Electron-Ion Coincidence Experiments

T. Kaneyasu[1], M. Ito[1,2], Y. Hikosaka[1], E. Shigemasa[1]
[1]*UVSOR Facility, Institute for Molecular Science, Okazaki 444-8585 Japan*
[2]*Graduate School of Science and Technology, Niigata University, Niigata-shi 950-21 Japan*

A double toroidal electron analyzer (DTA) has been constructed for realizing electron-ion coincidence experiments. It has been planned to study the decay dynamics of core-excited or ionized molecules by using the DTA with an ion momentum imaging spectrometer. The molecule with a core hole is very unstable due to its high internal energy and subsequent electronic relaxation processes often lead to dissociation. A correlation analysis among the particles ejected during the relaxation process gives access to proper understanding on the decay dynamics. Detailed descriptions of the electron-ion coincidence spectrometer and the DTA had already been given elsewhere [1-3]. The DTA is suitable for electron-ion coincidence experiment because of its high angular acceptance (5% of 4π sr) and moderate energy resolution (less than 1% of the pass energy) for electron analysis. Additionally, the DTA allows the angular distribution measurement of electrons, with the use of a two-dimensional position sensitive detector (PSD: Roentdek DLD40).

Prior to the coincidence experiments [4], we have evaluated energy resolution achieved by the DTA under the present condition. The experiment was performed at soft x-ray beamline BL4B with an energy resolving power $E_{ph}/\Delta E_{ph}$~800 at 300 eV photon energy. We have detected Ne 2*s* photoelectrons for the performance test. The sample gas was effused through an aperture of 0.2 mm diameter on the repeller plate. The photoelectrons ejected at 54.7° with respect to the electric vector of the photon beam were analyzed in energy. The DTA pass energy E_{pass} was set to 200 eV which allows the simultaneous observation of electrons with the energy range of 248 - 270 eV. Photoelectron spectrum was deduced from the electrons' arrival positions on the PSD.

Figure 1(a) shows a Ne 2*s* photoelectron image obtained at 302.6 eV. A concentric circle on the image corresponds to the photoelectrons. The anisotropic intensity along the circumference of the circle results from the unevenness of the transmission efficiency. The radial intensity distribution corresponding to the photoelectron spectrum is shown in Fig. 1(b). A least square fit with a Gauss function gives the peak width of 1.34 eV (FWHM). Considering the monochromator bandwidth, the instrumental energy resolution is estimated to be ΔE=1.3 eV (FWHM), which corresponds to the resolving power of the DTA $E_{pass}/\Delta E$=154. We have measured Ne 2s photoelectron spectra by changing the photon energy and estimated the resolving power. In Fig. 2, the electron energy resolution and the resolving power are plotted as a function of the kinetic energy. The resolving power better than 100 is achieved within an energy range corresponding to 7% of the pass energy. For the lower/higher kinetic energy electrons, the resolving power is somewhat worse than that for 254.1 eV electrons, which results from an imperfection of the electric field at the exit plane of the toroidal surfaces.

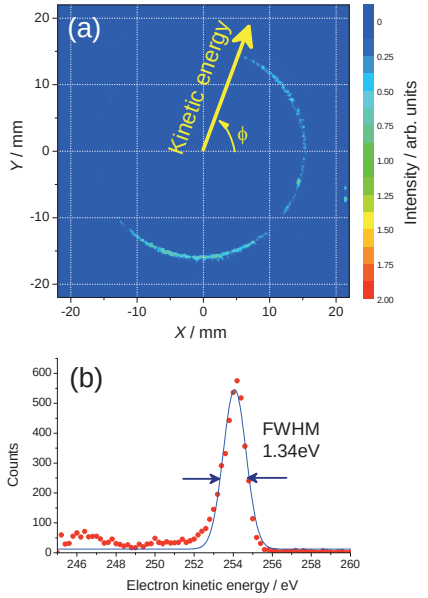

Fig. 1 (a) Two-dimensional image of Ne 2*s* photoelectrons measured at 302.6 eV photon energy. (b) Ne 2*s* photoelectron spectrum deduced from the image.

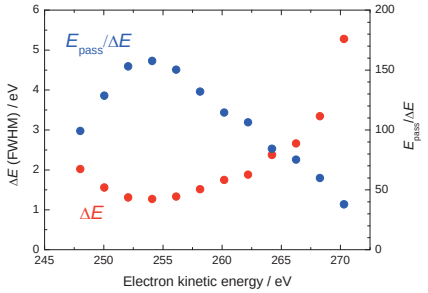

Fig. 2 The energy resolution and resolving power of the DTA plotted as a function of the kinetic energy.

[1] T. Kaneyasu *et al.*, AIP conf. proc. **978** (2007) 1793.
[2] T. Kaneyasu *et al.*, J. Electron Spectrosc. Relat. Phenom., in press.
[3] C. Miron *et al.*, Rev. Sci. Instrum. **68** (1997) 3728.
[4] T. Kaneyasu *et al.*, in this report.

BL5B

Measurement of Absolute Efficiency for Micro Channel Plates by Using Pure-Calibrated EUV Beam

G. Murakami[1], K. Yoshioka[1], K. Hikosaka[1], A. Yamazaki[2], I. Yoshikawa[1]
[1]*Department of Earth and Planetary Science, Graduate School of Science, The University of Tokyo, Tokyo 113-0033 Japan*
[2]*Institute of Space and Astronautical Science, Japan Aerospace Exploration Agency, Sagamihara, Kanagawa 229-8510 Japan*

Introduction

We study to optically observe the Earth's plasmasphere, which is filled with cold plasmas (mainly H^+, He^+, O^+ and electrons). The He^+ and O^+ ions have resonance scattering emission lines in the extreme ultraviolet (EUV) region, at 30.4nm (HeII) and 83.4nm (OII) respectively. The intensity of each emission is proportional to column density of each scattered particle under the assumption of the optically thin condition.

The SELenological and ENgineering Explorer (SELENE) satellite will be launched in 2007 and put into the orbit around the moon. The Telescope for EXtreme ultraviolet light (TEX) of the Upper atmosphere and Plasma Imager (UPI) onboard the SELENE satellite will observe the plasmasphere at 30.4nm and 83.4 nm lines from the lunar orbit. In this experiment, in order to calibrate the sensitivity of the UPI-TEX we measure the quantum efficiency of the micro channel plates (MCPs), which we use as the standard detector, at 30.4nm line.

Measurement and Result

We install an Al/Mg/Al (744Å/3958Å/747Å) filter on the entrance of the SOR beam to eliminate the multi-order lines from the 30.4nm line with PGM35. At first, we investigate the purity of the 30.4nm line through the Al/Mg/Al filter. We judge the purity from the consistency between the wavelength characteristics of an Al/C (1201Å/54Å) filter and an Al/Mg/Al (744Å/3958Å/747Å) filter for the particular lines at the EUV facilities of Institute of Space and Astronautical Science (ISAS) and those for the continuous lines at UVSOR. The former is measured for the emission lines of the gas (He, Ne) with the discharge light source. Fig. 1 shows the transmittances of the two filters measured at ISAS and UVSOR. It is clear that both profiles of each filter are consistent in the wavelength region of 25-50nm. We interpret from the result that the pure 30.4nm can be introduced through the Al/Mg/Al filter by using PGM35.

With the available pure 30.4nm line, then we measure the quantum efficiency of the MCPs. The quantum efficiency is calculated by the rate of the MCPs count to the electron yield of the photo diode which is absolutely calibrated. The result of the measurement shows that the quantum efficiency of the MCPs is 7.4% at 30.4nm line.

As the next step, in addition to the 30.4nm line, we plan to measure the quantum efficiency at the 83.4nm line, which is another observational object of UPI-TEX. Then the purity of 83.4nm line is essential, and must be investigated for the next machine time.

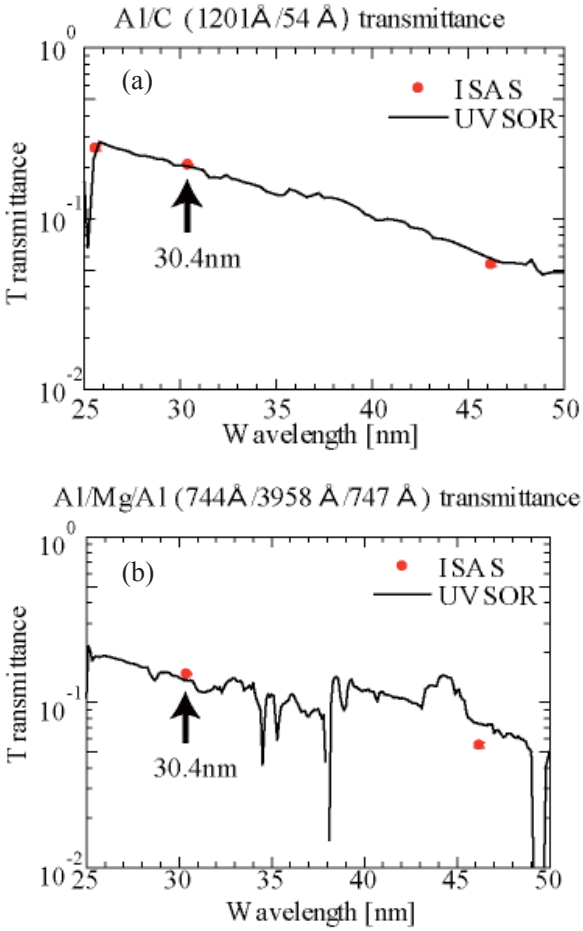

Fig. 1 The transmittances of (a) an Al/C (1201Å/54Å) filter and (b) an Al/Mg/Al (744Å/3958Å/747Å) filter. The red dots show the results of the measurements at the EUV facility of ISAS and the solid lines show those at UVSOR. The solid line in (b) is discrete at 38nm and 49nm because the incident beam introduced by PGM35 is weak at the wavelengths and the results have large error.

BL5B

Calibration of Optics for Extreme Ultra-Violet Region

M. Yamamoto, H. Habara, K. A. Tanaka
Graduate School of Engineering Osaka University, 2-1 Yamadaoka, Suita 565-0871, Japan

Introduction

We're developing a new spectrometer in order to measure the high-order harmonics in vacuum ultra-violet (VUV) and extreme ultra-violet (XUV) generated in ultra-intense laser-plasma interactions. Optical system of spectrometer for VUV/XUV light should compose of reflective optics which are spherical mirror (SM) and spherical grating mirror (GR) because the harmonics can not propagate in the transmittive optics for examples CaF_2 (cut-off 120 nm) and MgF_2 (cut-off 115 nm). We investigated the reflectivity of SM and the ±1st diffractivity of GR.

Experimental

We utilize SM (ACTON Research Corp. #1200-VUV coating) and GR (Horiba Jovin Yvon monochrometer concave grating) for the spectrometer. These properties are shown in Table 1 and Table 2. As varying the incident angle, the dependence of reflectivity of SM and the ±1st diffractivity of GR on pump wavelength were measured using s-polarization synchrotron radiation of multi-bunch operation at BL5B line with a photodiode (IRD AXUV-100). In the experiments, we measured the reflected light from spherical optics irradiating into the photodiode aperture monitoring maximum photodiode currents.

Table 1. Properties of spherical mirror [1].

Coating	Wavelength	Reflectivity
Al - MgF_2	115 – 300 nm	70 -90 %

Table 2. Properties of spherical grating mirror [2].

Coating	Groove density	Deviation
Al - MgF_2	1200 gr/mm	64 deg

Results and Discussion

Reflectivities of SM for the harmonics from 9th (@117 nm) to 15th (@70.2 nm) with s-polarization incidence are shown in Fig. 1. It is found that our results are significantly different from Ref. [1]. Also at the smaller incident angle, the difference of reflectivity becomes larger by the wavelength. In addition reflectivity of 9th is insensitive to the incident angle compared with 13th (@75.2 nm).

The ±1st diffractivities of GR for the 9th to 15th harmonics with s-polarization incidence are shown in Fig. 2 and Fig. 3. Only the +1st relative diffractivities from 100 to 300 nm were calculated and this calculation shows particularly decrease from 100 to 140 nm in Ref. [2]. Our experiment found that the ±1st difrractivity roughly increased with shorter wavelength.

The experiments were carried out using s-polarization light. However, it is well known that reflectivity and difrractivity hardly depend on polarization in VUV/XUV region light [3]. From the results, we can evaluate the total optical loss for the spectrometer.

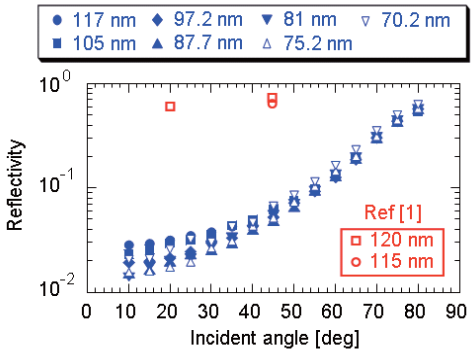

Fig. 1 The reflectivity of SM was measured using s-polarization synchrotron light.

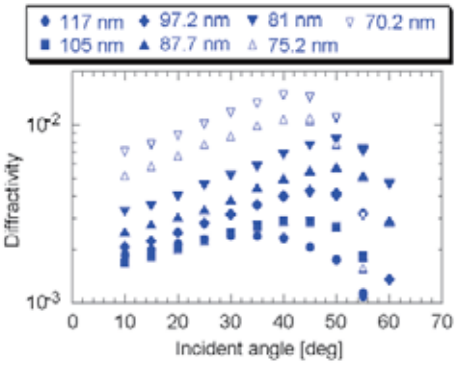

Fig. 2 The -1st diffractivity of GR was measured using s-polarization synchrotron light.

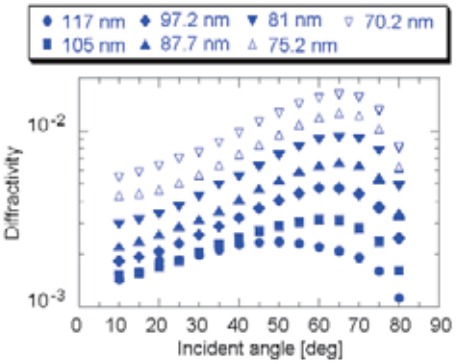

Fig. 3 The +1st diffractivity of GR was measured using s-polarization synchrotron light.

[1] Catalog, ACTON Research Corp.
[2] Catalog (Ref. 522 00 250), Horiba Jobin Yvon.
[3] C. Palmer, "Diffraction grating handbook (fifth edition)", Thermo RGL, 2002.

BL5B

Calibration of Phosphors for Extreme Ultra-Violet Region

M. Yamamoto, H. Habara, K. A. Tanaka
Graduate School of Engineering Osaka University, 2-1 Yamadaoka, Suita 565-0871, Japan

Introduction

We're developing a new spectrometer in order to measure the high-order harmonics in vacuum ultra-violet (VUV) and extreme ultra-violet (XUV) generated in ultra-intense laser-plasma interactions. Instead of expensive light detector such as a micro-channel plate (MCP) and a charge coupled device (CCD), we utilized phosphors (Zn_2SiO_4:Mn, $BaMgAl_{10}O_{17}$:Eu) for plasma display panel of that property is well known above VUV (λ>120 nm) region. We experimentally evaluated luminous fluorescent characteristics at the shorter wavelength from the rear side of the phosphor films in the condition of actual uses.

Experimental

The sample films on the glass plate are made by the coagulation sedimentation method. The properties are shown in Table 1. Measurements of luminous fluorescent spectra and quantum efficiency dependence on pump wavelength were measured using synchrotron radiation of multi-bunch operation at BL5B line. Each property was measured with a spectrometer (Jobin Yvon HR320) and a photodiode (IRD AXUV-100).

Table 1. Properties of phosphor sample films.

Sample	Thickness	Fluorescent center
Zn_2SiO_4:Mn	30 um	9.03 % (Mn)
$BaMgAl_{10}O_{17}$:Eu	50 um	9.31 % (Eu)

Results and Discussion

Luminous fluorescent spectra of phosphors were shown in Fig. 1 and Fig. 2. In spite of different pump wavelength, the luminous fluorescence spectra show no difference between VUV/XUV and over 120 nm [1]. It is clear that it is impossible to distinguish the pump wavelength from the spectra in uses an imaging detector for VUV/XUV region.

Luminous fluorescent quantum efficiency of phosphors excited by VUV/XUV light corresponding to the high order harmonics is shown in Fig. 3. T luminescent fluence for both phosphors is estimated by multiplying the simulation results of harmonics intensity at 20 J/ 10^{19}W/cm^2 laser (@1.05 um) light irradiated to a solid target [2], resulting that the luminescence of 210 mLux for 105 nm (10th harmonic) can be detected with 144 msr solid view angle. As the result, it experimentally examines that the harmonics could be measured with phosphors because a general astronomical CCD, which has more than a few mLux sensitivity, could detect the VUV/XUV harmonics.

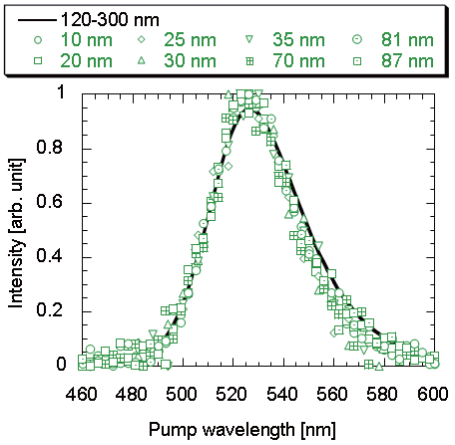

Fig. 1 Luminescence spectra of Zn_2SiO_4:Mn excited by VUV/XUV region light of synchrotron radiation.

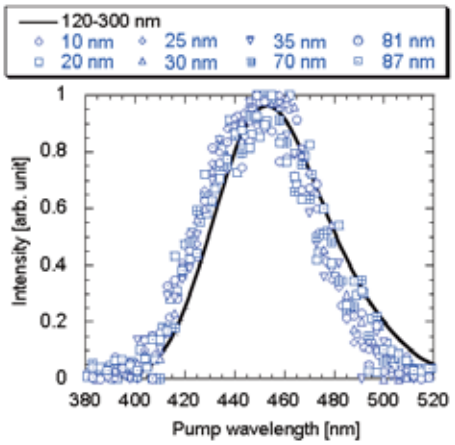

Fig. 2 Luminescence spectra of $BaMgAl_{10}O_{17}$:Eu excited by VUV/XUV region light of synchrotron radiation.

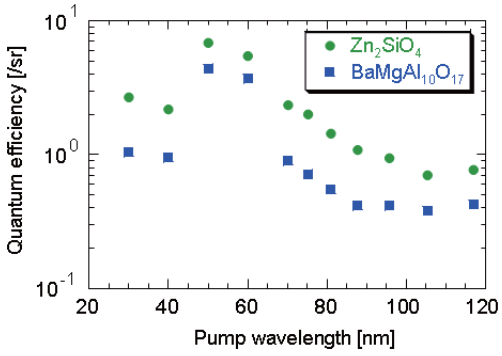

Fig. 3 Quantum efficiency of phosphors excited by VUV/XUV region light of synchrotron radiation.

[1] Catalog, Kasei Optonix LTD.
[2] P. Gibbon, Phys. Rev. Lett. **76** (1996) 50.

BL7U

Construction of a VUV Angle-Resolved Photoemission Beamline BL7U

S. Kimura[1,2], T. Ito[1,2], M. Sakai[1], E. Nakamura[1], N. Kondo[1], T. Horigome[1], M. Hosaka[1,3], A. Mochihashi[1,2], M. Katoh[1,2], T. Ejima[4], H.J. Im[1,5], H. Miyazaki[1,3], K. Soda[1,3]

[1]*UVSOR Facility, Institute for Molecular Science, Okazaki 444-8585, Japan*
[2]*School of Physical Sciences, The Graduate University for Advanced Studies (SOKENDAI), Okazaki 444-8585, Japan*
[3]*Graduate School of Engineering, Nagoya University Nagoya 464-8603, Japan*
[4]*IMRAM, Tohoku University, Sendai 980-8577, Japan*
[5]*Department of Physics, Sungkyunkwan University, Suwon 440-746, South Korea*

Recently, the energy resolution of photoemission experiments is drastically improved by using helium discharge lamps and VUV lasers. Due to the improvement, the thermodynamical properties of solids can be understood by the change of the electronic structure detected by photoemission. In the case of the angle-resolved photoemission spectroscopy (ARPES) using such light sources, the momentum along the normal direction of sample surface (k_z) cannot be set at a high symmetry point because the excitation photon energy that directly connects to k_z cannot be tuned. To determine the three-dimensional band structure at the high symmetry points by ARPES with tunable photons is important to compare with the band structure calculation. Since synchrotron radiation (SR) is suitable for the use of the various photon energies, some photoemission beamlines have been constructed in the world up to now. Because of the low photon flux of SR, however, the energy-resolution in ARPES was lower than the other sources mentioned above. Then we constructed a new undulator beamline in the VUV region at UVSOR-II for the purpose of the high-energy resolution ARPES with the total energy resolution less than 1 meV in the whole excitation energy of 6 - 40 eV and with the various (vertically / horizontally linear and circular) polarizations of photons.

We employed a various polarized APPLE-II-type undulator light source [1], a Wadsworth-type VUV monochromator [2] and a high-energy-resolution photoelectron analyzer with a liquid-He-cooled cryostat with 6-axes manipulator. Since the Wadsworth monochromator has no entrance slit and the light source size (2σ) of $0.04(H)\times1.2(H)$ mm^2 in the 1-% coupling machine operation of UVSOR-II [3], the VUV light with high photon flux and with high energy resolution can be obtained. The overall picture of the beamline is shown in Fig. 1. The undulator radiation is guided to 10-m-radius spherical gratings by two plane mirrors (M0, M1). The light is focused on the exit slit (S) by the spherical gratings. The monochromatized light is focused again on a sample by a toroidal mirror (M3). Because of no entrance slit, the photon flux on the sample becomes very high. However the near-normal incident mirror M1 reduces the photon flux in the higher energy region. Then we employed changeable nine mirrors including Mo/Si multilayer mirrors which have high reflectivity in the photon energy range of 30-40 eV to increase the photon flux [4].

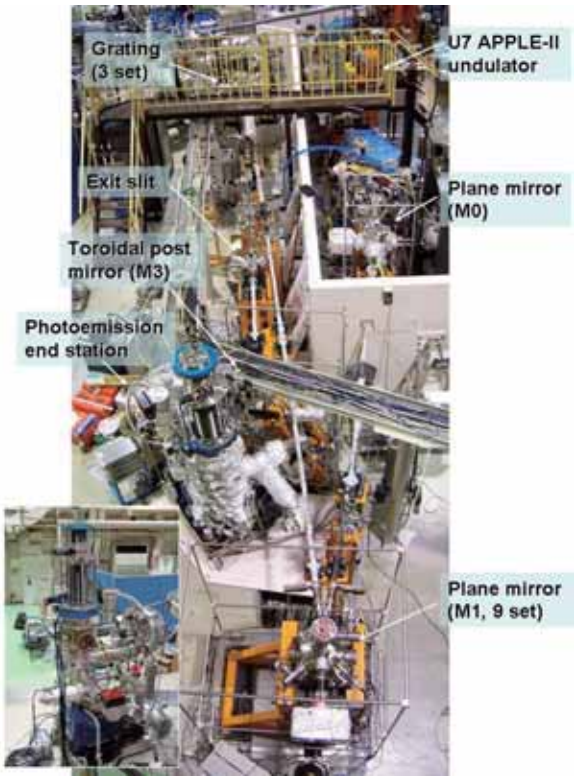

Fig. 1. Top view of the VUV photoemission beamline BL7U of UVSOR-II.

[1] S. Sasaki, K. Miyata, and T. Takada, Jpn. J. Appl. Phys. **31**, L1794 (1992).
[2] S. Kimura, T. Ito, E. Nakamura, M. Hosaka, and M. Katoh, AIP Conf. Proc. **879**, 527 (2007).
[3] M. Katoh, M. Hosaka, A. Mochihashi, J. Yamazaki, K. Hayashi, Y Hori, T. Honda, K. Haga, Y Takashima, T. Koseki, S. Koda, H. Kitamura, T. Hara, and T. Tanaka, AIP Conf. Proc. **705**, 49 (2004).
[4] T. Ejima, A. Yamazaki, T. Banse, K. Saito, Y Kondo, S. Ichimaru, and H. Takenaka, Appl. Opt. **44**, 5446 (2005).

Performance Test of The VUV Monochromator at BL7U

S. Kimura[1,2], M. Sakai[1], T. Ito[1,2]
[1]*UVSOR Facility, Institute for Molecular Science, Okazaki 444-8585, Japan*
[2]*School of Physical Sciences, The Graduate University for Advanced Studies (SOKENDAI), Okazaki 444-8585, Japan*

BL7U is a new VUV undulator beamline at UVSOR-II constructed in FY2006. The main purpose of the beamline is to elucidate the origin of the exotic physical properties of functional materials including strongly correlated electron systems by determination of the electronic structure by an angle-resolved photoemission experiment. To perform the experiment, both of the high energy resolution and high photon flux of the monochromatized light are simultaneously required. Then we checked the energy resolution and the photon flux at the same monochromator condition with the exit slit size of 100 μm.

The energy resolution is tested by using rare gases. The helium 1*s np* ($h\nu \sim 24.5$ eV) and argon $3s3p^6$ *np* ($h\nu \sim 29$ eV) absorption lines are shown in Figure 1. The helium absorption spectrum was recorded using the grating (3600 lines/mm) for the highest energy range. The energy resolution was evaluated to be $E/\Delta E > 19{,}000$. On the other hand, the argon spectrum was obtained by using the medium region grating (2400 lines/mm) and the energy resolution was $E/\Delta E > 9{,}000$.

The obtained and the geometrically calculated energy resolution are plotted in Figure 2. The energy resolution of this beamline depends on the electron beam parameter of the storage ring, particularly, the beam size at the emission point. At present, the storage ring is operated with 5-% coupling. The obtained energy resolutions at 24.5 and 29 eV are higher than the calculated lines. In the top-up operation, the coupling percentage will be reduced to 1 %. Then the energy resolution becomes 2.2 times higher than the 5-% coupling operation because of the reduction of the electron beam size.

With the same beamline parameter, the photon flux was obtained as shown in Figure 3. The spectra were recorded by using the different undulator gap size, two M1 mirrors, Au and SiC and different gratings. If the quantum efficiency of the gold film is assumed to be 5 %, the photon flux at $h\nu = 10$ - 22 eV is more than 10^{12} ph/sec at 200 mA beam current. In the energy region above 30 eV, the intensity rapidly decreases with increasing photon energy because of the poor reflectivity of gold. In the energy region, we will employ four Mg/SiC multilayer mirrors.[1] Since the reflectivity is about a few 10 times higher than that of a gold film, the photon flux in the energy region will recover to at least 10^{11} ph/s.

[1] T. Ejima et al., Appl. Opt. **44** (2005) 5446.

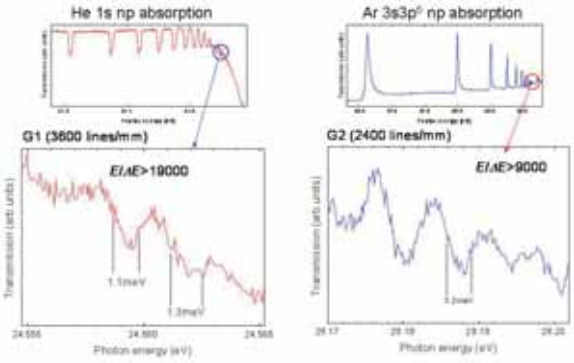

Fig. 1. Absorption spectra of helium and argon gases with the exit slit size of 100 μm. The narrowest width of the absorption lines is regarded as the energy resolution.

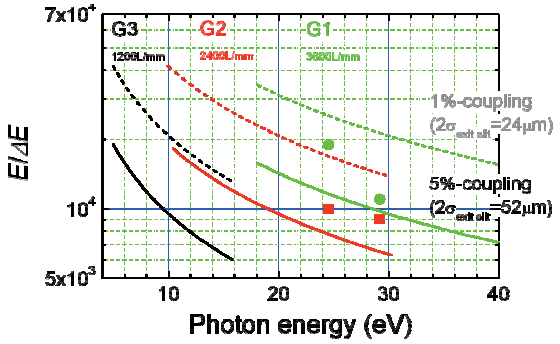

Fig.2. Experimentally evaluated (marks) and calculated (lines) energy resolution ($E/\Delta E$) of three installed gratings as a function of photon energy and the coupling of the electron beam. The present coupling is 5 %.

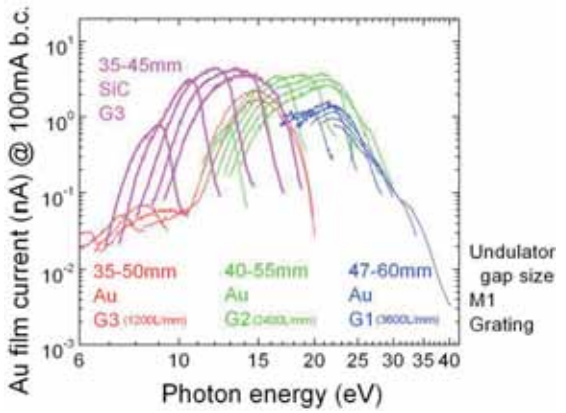

Fig. 3. The throughput spectra of BL7U detected by a drain current of a gold film. The undulator gap, M1 mirrors and gratings are changed. The exit slit size was 100 μm.

BL7U

Performance of the Three-Dimensional VUV Angle-Resolved Photoemission Apparatus at BL7U

T. Ito[1,2], S. Kimura[1,2], M. Sakai[1], N. Kondo[1], T. Horigome[1], H.J. Im[1,3], H. Miyazaki[1,4], K. Soda[1,4]

[1]*UVSOR Facility, Institute for Molecular Science, Okazaki 444-8585, Japan*

[2]*School of Physical Sciences, The Graduate University for Advanced Studies (SOKENDAI), Okazaki 444-8585, Japan*

[3]*Department of Physics, Sungkyunkwan University, Suwon 440-746, South Korea*

[4]*Graduate School of Engineering, Nagoya University Nagoya 464-8603, Japan*

The investigation of the anisotropic interaction at the Fermi surface (FS) of inter-metallic compounds, namely "Fermiology", is one of the most facilitating research field in recent days, since the interactions between carriers, local spins, and lattice vibrations play a dominant role for the functionality (superconductivity, magnetism, etc.) of materials. Angle-resolved photoemission (ARPES) spectroscopy is a powerful tool to observe the quasiparticles which form FS's. The recent technological innovation of synchrotron radiation instruments makes that it is possible to observe three-dimensional (3D) FS's [1]. However, there are few 3D-ARPES apparatuses meeting demands of high-energy/momentum resolution, enough bulk-sensitivity, and high-photon-flux in the world.

To investigate the anisotropic interaction at FS of solids, we have constructed a bulk-sensitive three-dimensional angle-resolved photoemission apparatus (Fig. 1) using VUV light with high-energy resolution and high photon flux from an undulator beamline BL7U at UVSOR-II [3]. The main part of the apparatus consists of a 200-mm-radius hemispherical photoelectron energy analyzer (MBScientific AB; 'Peter' A-1) and a liquid-helium flow cryostat with 6-axes manipulation system (R-dec Co. Ltd.; i-Gonio). To obtain ARPES spectra along high-symmetry lines of a sample, the sample manipulator is equipped with three-independent rolling mechanism; two of them are rotations (θx and θy) with respect to the sample surface normal and the other an in-plane rotation (ϕ). In addition, to be feasible to obtain a complete data set, not only of FS, but also of quasi-particle band dispersion within 12 hours (e.g., user beam operation time in a day), we will develop a computational multidimensional scanning system.

Finally, we briefly introduce the present performance of the PES measurement. From the energy-distribution-curve of evaporated gold at the Fermi level (Fig. 2(a)), the total energy resolution with the angle-integrated mode is about ΔE_{Total} = 1.5 meV with $h\nu$ = 10 eV photons at T = 15 K. The horizontal spot size on the sample estimated from the position distribution curve (Fig. 2(b)) is about 0.5 mm.

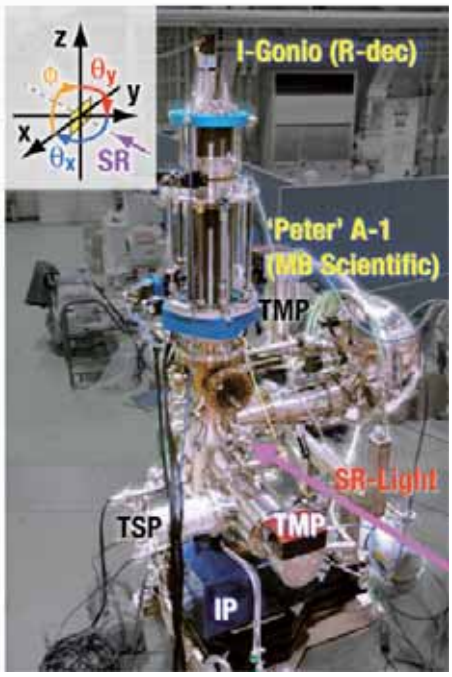

Fig. 1. Three-dimensional VUV angle-resolved photoemission apparatus at BL7U. Purple arrow indicates a path of SR light. Inset shows the definitions of 6-axes of the manipulater.

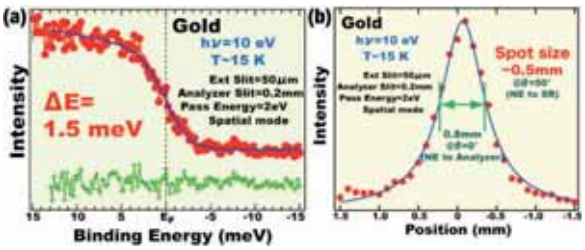

Fig. 2. Energy- (a) and position- (b) distribution curves of gold at the Fermi level at T = 15K obtained by using $h\nu$ = 10 eV photons.

[1] T. Ito *et al.*, J. Mag. Magn. Mater. **310**, 431 (2007).

[2] S. Kimura *et al.*, AIP Conf. Proc. **879**, 527 (2007).

3
Molecular spectroscopy and dynamics

BL2B

Formation Mechanism of Multilply-Charged Fullerene Ions

K. Mitsuke, H. Katayanagi, C. Huang, B.P. Kafle, M.S.I. Prodhan, H. Yagi
Division of Chemical. Dynamics and Grad. Univ. Adv. Studies, Inst. for Molec. Sci., Myodaiji, Okazaki 444-8585, Japan.

Formation mechanism of multiply-charged fullerene ions was discussed in terms of valence-electron excitation to antibonding unoccupied orbitals and/or spherical standing waves inside the cavity of fullerene. This excitation should be followed by Spectator Auger processes and transmission of the excess electronic energy among enormous vibrational degrees of freedom.

Colavita et al. have calculated the partial photoionization cross sections for valence electrons as a function of $h\nu$ using local density approximation Hamiltonian over an extended energy range. Hence we will discuss the formation mechanism of C_{60}^{2+} from C_{60} with the help of their results. Analogous mechanisms may hold for the formation of C_{70}^{2+} and C_{84}^{2+} from C_{70} and C_{84}, respectively. The partial photoionization cross sections of Colavita et al. were characterized by the presence of many resonances up to about 40 eV above the respective photoionization thresholds. Since the binding energies of five deepest valence orbitals of C_{60} range from -24.2 to -27.5 eV, one can expect that, below $h\nu$ ~ 65 eV, these resonances should participate in the formation of C_{60}^{2+}. Among the reported partial cross sections the curve of photoionization of the $3g_g$ and $5h_g$ orbitals demonstrates pronounced broad resonances at $h\nu$ = 37 and 50 eV. These resonances are considered to give rise to the peaks at 35 and 50 eV on the cross section curve for double photoionization of C_{60} if we take account of the broadening of the theoretical peaks by many electron or vibrational effects. Colavita et al. ascribed the resonances at $h\nu$ = 37 and 50 eV to promotion of the $3g_g$ and/or $5h_g$ electron to spherical standing waves inside the cavity of fullerene which have high angular momentum. The energies of the final orbitals are calculated from the binding energies (-22.42 and -22.89 eV) of the $3g_g$ and $5h_g$ orbitals to be ~ 14 and ~ 27 eV, corresponding to the resonances at $h\nu$ = 37 and 50 eV, respectively.

We can propose a possible pathway for the formation of C_{60}^{2+}, identifying the dominant features of the C_{60}^{2+} cross section curve with the above cavity resonances involving spherical standing waves (see Fig. 1). Let's assume that the cavity-resonance state is formed by promotion of the $3g_g$ or $5h_g$ electron when C_{60} absorbs a 50 eV photon. Then spectator Auger ionization leads to C_{60}^{+}* in which the excited electron is still trapped inside the cavity. This excited state undergoes multiple conversion to nearby cavity- or shape-resonance states by transmitting a part of the electronic energy to numerous vibrational modes. Such conversion may occur consecutively until the excited electron is stabilized down to one of low-lying unoccupied orbitals of antibonding σ* or π* character near the threshold. Thereby the excess energy of at most ~ 27 eV is dissipated in the fullerene cage. Finally C_{60}^{2+} is produced by tunneling of the electron in the antibonding orbital. We believe this mechanism is most plausible below $h\nu$ ~ 65 eV for the formation of C_{60}^{2+}.

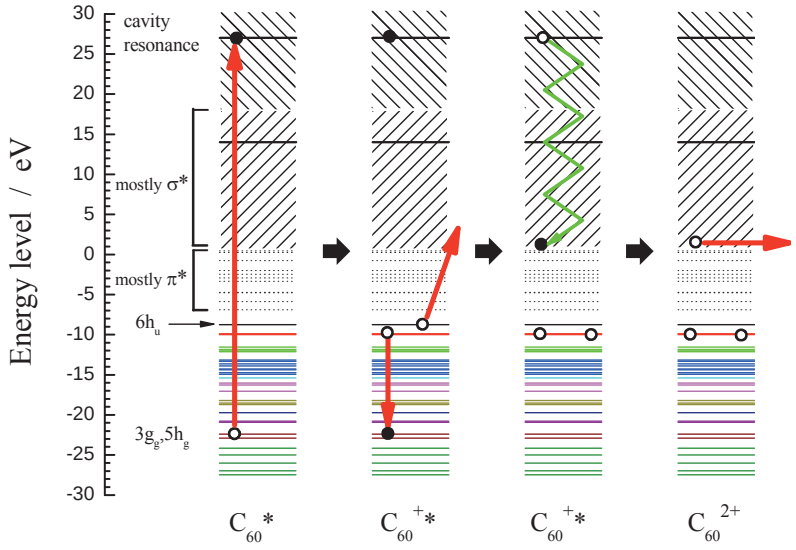

Fig. 1 Schematic picture illustrating the decay mechanism of the cavity-resonance state formed by excitation of the $3g_g$ electron of C_{60}. Vibrationally-excited C_{60}^{2+} can be produced by spectator Auger ionization, multiple internal conversion with intramolecular vibrational redistribution, and tunneling of the excited electron.

BL2B

Partial Cross Sections for Single and Multiple Photoionization of C_{60}

B.P. Kafle, H. Katayanagi, H. Yagi, M.S.I. Prodhan, C. Huang, K. Mitsuke
Division of Chemical Dynamics and Grad. Univ. Adv. Studies, Inst. for Molec. Sci., Myodaiji, Okazaki 444-8585, Japan

Partial cross sections for the photoion formation from C_{60} were determined from the yields of singly-, doubly- and triply-charged ions which were measured by mass spectrometry combined with tunable synchrotron radiation at $h\nu$ = 25 – 120 eV.

Open circles of Fig. 1 show the relative partial cross sections $\sigma(C_{60}^{+})$ and $\sigma(C_{60}^{2+})$ for the formation of C_{60}^{+} and C_{60}^{2+} from C_{60}. Each partial cross section includes the contribution of not only the parent but fragment ions produced by the C_2-loss processes, so that it is equal to the cross section involving all the ionic species in a particular charge state. The solid curves in Fig. 1 show partial cross sections for the formation of C_{60}^{+} and C_{60}^{2+} reported by Kou et al. [1], which will be referred to hereafter as $\sigma_{Kou}(C_{60}^{+})$ and $\sigma_{Kou}(C_{60}^{2+})$, respectively. The $\sigma_{Kou}(C_{60}^{+})$ is normalized to $\sigma(C_{60}^{+})$ at $h\nu$ = 100 eV. The $\sigma(C_{60}^{2+})$ curve makes a broad maximum at ~50 eV above which it monotonically descends, in consistent with $\sigma_{Kou}(C_{60}^{2+})$ [1]. Nonetheless, $\sigma(C_{60}^{2+})$ is about one third as large as $\sigma_{Kou}(C_{60}^{2+})$ at all photon energies, because, in the present study, we have taken into account the difference in the detection efficiency of C_{60}^{+} and C_{60}^{2+}. The $\sigma(C_{60}^{+})$ and $\sigma_{Kou}(C_{60}^{+})$ curves agree well between 60 and 120 eV. With decreasing $h\nu$ the former curve starts to deviate upwards from the latter curve and the ratio of $\sigma(C_{60}^{+})$ to $\sigma_{Kou}(C_{60}^{+})$ reaches ~2.5 at 25 eV. This discrepancy can be accounted for by that the $\sigma_{Kou}(C_{60}^{+})$ curve has a discontinuity between the $h\nu$ regions covered by grating G2 and that by G3. The contamination of the 2nd-order light of G2 at $h\nu$ = 40–50 eV brings about the discontinuity. In the present study correction of the $\sigma(C_{60}^{z+})$ has been performed carefully by estimating the percentage of the 2nd-order light.

Reliability of the present $\sigma(C_{60}^{z+})$ in Fig. 1 can be confirmed by comparing with previously published data of the total photoionization cross section σ_T of C_{60}. In Fig. 2 open circles indicate the sum of $\sigma(C_{60}^{+})$, $\sigma(C_{60}^{2+})$, and $\sigma(C_{60}^{3+})$, which is approximately equivalent to σ_T, while the dotted curve represent the σ_T curve observed by Reinköster et al. [2] and dashed curve does the total photoabsorption cross section calculated by Colavita et al. [3] These three curves are normalized at $h\nu$ = 100 eV. Our curve is in a fair agreement with the published curves over a whole energy range, which provides tangible evidence for the validity of our data analysis. Neglecting the *m/z*-dependence of the detection efficiency resulted in overestimation of $\sigma_{Kou}(C_{60}^{2+})$ and eventually rendered the sum of cross sections, ~$\sigma_{Kou}(C_{60}^{+})$+$\sigma_{Kou}(C_{60}^{2+})$ enhanced above 50 eV.

The fine structures observed in $\sigma_{Kou}(C_{60}^{+})$ reappeared in the present $\sigma(C_{60}^{+})$ curve: two peaks at 26 and 34 eV and flat area ranging 40 – 50 eV. The 34 eV peak was also discernible on the $\sigma(C_{60}^{2+})$ curve as a shoulder. These structures originate from ionization via the shape resonances as single-electron excitation to vacant orbitals. The curve of $\sigma(C_{60}^{3+})$ has an onset around 40 eV and steadily increases with $h\nu$. This onset energy is consistent with the published ionization potential of 35.6 [4] or 39.8 eV [5] for the formation of C_{60}^{3+} from C_{60}.

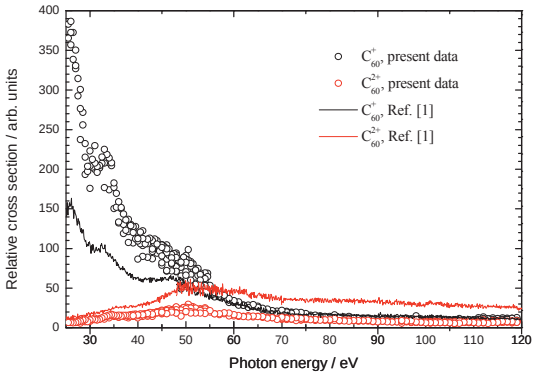

Fig.1 Partial cross sections for single and double photoionization of C_{60}.

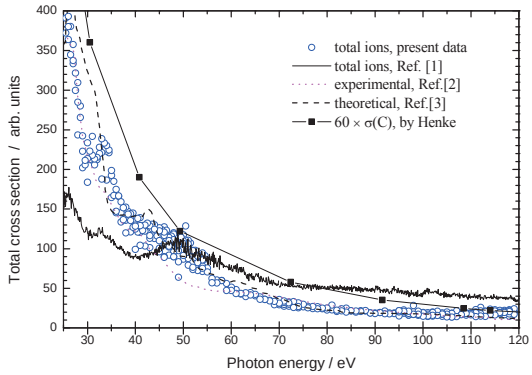

Fig.2 Total photoionization cross section of C_{60}. Comparison between the present and previous data in the literature is made.

[1] Kou et al., J. Chem. Phys. **120** (2004) 6005.
[2] Reinköster et al., J. Phys. B, **37** (2004) 2135.
[3] P. Colavita, et al., Phys. Chem. Chem. Phys. **3** (2001) 4481.
[4] P. Scheier et al., Int. J. Mass Spectrom. Ion Proc. **138** (1994) 77.
[5] Juranic et al., Phys. Rev. A **73** (2006) 04271.

BL2B

High Resolution Photoelectron Spectroscopy of Gaseous C_{60}

H. Yagi, C. Huang, S. I. Prodhan, B. P. Kafle, H. Katayanagi, K. Mitsuke
Division of Chemical Dynamics and Grad. Univ. Adv. Studies,
Institute for Molecular Science,Okazaki 444-8585 Japan

C_{60} has many degenerate bands in the 7-40 eV ionization energy range. To clarify its electronic structure, photoelectron spectroscopy (PES) studies of solid C_{60} have been made by several groups. However, the PES studies of gaseous C_{60} are few and the energy resolution was about 100 meV at the best, which was not enough to resolve closely spaced bands in detail. We are developing an apparatus of high-resolution angle-resolved PES. Our goal is to carry out PES of various kinds of gaseous fullerenes with a total energy resolution of ~20 meV.

At the beginning, we performed He I ($h\nu$=21.2 eV) PES of free C_{60} molecules. The experimental setup is illustrated in Fig. 1. Powder of C_{60} was loaded in a nickel sample holder, which was attached to a conical nozzle, and heated up to 800 K by a cartridge heater. The fullerene vapor was discharged from the nozzle and ionized by He I radiation. Electrons ejected at right angles to the direction of the photon beam were analyzed by the electron energy analyzer (AC-902, comstock). The flux of the fullerene beam was measured by a thickness monitor (XTM/2, Inficon). When the oven temperature was ~800 K, the mass deposition rate was ~16 ng/s. From these values, the number density of C_{60} at the photoionization region is estimated to be 1.2×10^{16} molecules/m^3. The total energy resolution of this apparatus at the pass energy of 3 eV is estimated to be ~50 meV from the peak width of O_2 spectra.

Figure 2 shows the photoelectron spectrum of C_{60} from which the background is already subtracted. The sharp peak at 12.62 eV is attributed to the water contained in the sample powder. Results and experimental conditions of other groups [1,2] are also shown for comparison. Although our data have large uncertainties above ~14 eV due to the large background at low electron kinetic energies, the peak structures below ~14 eV is reconciled well with those of the precedence research. However, in order to elucidate the fine electronic structure such as the Jahn-Teller splitting and the vibrational progressions of C_{60}^+ cations, a better signal to noise ratio is needed. We are now trying to improve S/N ratio by setting the oven unit closer to the ionization region and coating the inner wall of the analyzer by aerodag (a colloidal suspension of fine graphite particles).

As the next step, we plan to carry out PES study at BL2B in UVSOR using a Scienta SES-100 electron spectrometer, which will give higher intensity and better energy resolution. Using BL2B, the partial photoionization cross sections and anisotropy parameters of each band may be determined in the photon energy range of 25-150 eV. The partial cross sections of the HOMO and HOMO-1 orbitals were reported between 18 and 130 eV photon energies [3], but those of other orbitals are still unknown because their peaks are closely spaced and unresolved.

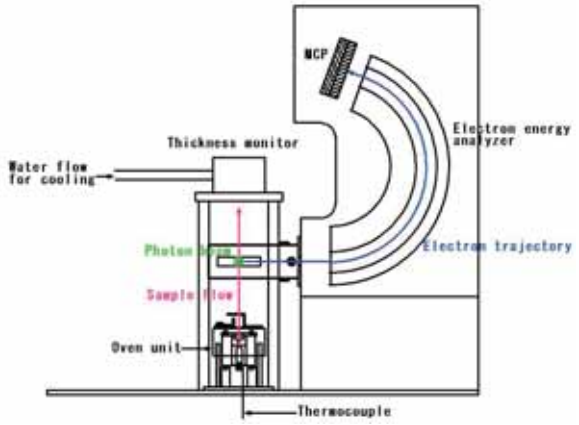

Fig. 1 Apparatus for the photoelectron spectroscopy of gaseous fullerenes. The direction of the photon beam is normal to the paper.

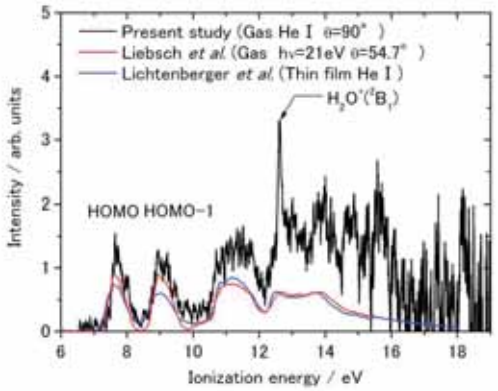

Fig. 2 Photoelectron spectra of C_{60}. The results of other groups are also plotted for comparison [1,2]. θ is the photoelectron sampling angle relative to the photon beam.

[1] T. Liebsch *et al*., J. Electron Spectrosc. Relat. Phenom. **79** (1996) 419.
[2] D. Lichtenberger *et al*., Chem. Phys. Lett. **176** (1991) 203.
[3] A. Rüdel *et al*., Phys. Rev. Lett. **89** (2002) 125503.

BL2B

Refinements on the Estimation Method of Photoabsorption Cross Sections of Metallofullerenes

H. Katayanagi[1,2], B. P. Kafle[2], T. Mori[1], J. Kou[1],
Y. Takabayashi[3], E. Kuwahara[3], Y. Kubozono[3], K. Mitsuke[1,2]
[1]*Department of Vacuum UV Photo-Science, Institute for Molecular Science, Okazaki 444-8585 Japan*
[2]*Graduate University for Advanced Studies, Okazaki 444-8585 Japan*
[3]*Department of Chemistry, Okayama University, Okayama 700-8530, Japan*

Endohedral metallofullerenes ($M@C_n$; M: metal, n = 60, 70, …) have a unique structure in which one or more metal atoms are encapsulated in a "nano-space" inside a fullerene cage. We carried out a systematic investigation of their absolute photoabsorption cross sections which are expected to be of fundamental importance in various contexts of science and application of metallofullerenes.

We have reported photoabsorption cross sections of several metallofullerenes ($Ce@C_{82}$ [1], $Dy@C_{82}$ [2] and $Pr@C_{82}$ [3]) in the photon energy range available with a monochromator at BL2B in UVSOR. We obtained the values by means of comparison between normalized count rates for the metallofullerenes and standard samples of which cross sections are well known. While the standard samples have much lower masses than those of the metallofullerenes, we did not correct the detection efficiency dependence of the time-of-flight (TOF) mass spectrometer on sample masses and charges at the time. Although the values obtained by our previous study might serve as the first estimate of the cross sections of metallofullerenes, we realized that it was a crude assumption. Accordingly we started an attempt to refine these cross sections.

In the present study, in order to compensate a mass dependence of the detection efficiency we adopted an empirical formula which has been proposed by Twerenbold et al. [4]. The formula gives relative detection efficiency of a Microchannel plate (MCP) detector, which mainly governs the overall detection efficiency of the TOF mass spectrometer. We verified the formula using rare gases (He, Ne, Ar, Kr and Xe) and confirmed that the formula is applicable to our experimental setup.

We applied the formula to our on-going study to evaluate the photoabsorption cross sections of $Pr@C_{82}$ at the outset. In this study, we found out in the photoabsorption spectra that the giant dipole resonance of praseodymium atoms survives regardless of the encapsulation. The refined values for $Pr@C_{82}$ at the on-resonance (130 eV) and off-resonance (110 eV) photon energies are shown in Table 1. In this evaluation we used C_{60} as a standard sample. The cross section at 110 eV agrees well with the cross section (33.5 Mb) 82 times as large as that of a carbon atom σ(C). In the previous evaluation without the efficiency correction, the off-resonance value was only approximately 60% of 82σ(C). Moreover we measured the phoion yield spectra of Xe in order to use Xe as another standard sample. The cross sections of $Pr@C_{82}$ using Xe as a standard agreed with those using C_{60} as a standard. This agreement shows that the efficiency dependence is fairly corrected.

Without correcting the detection efficiency, we had come to the conclusion that the giant resonance was weakened by the fullerene cage in $Pr@C_{82}$ as well as in $Ce@C_{82}$. In order to ascertain it, we again estimated an enhancement by the giant resonance from the difference between cross sections at 110 and 130 eV. The enhancement was thus 15 Mb, which agreed well with the previous value (16.5 Mb [3]). Similar enhancement by the giant resonance was also observed in $Ce@C_{82}$ [1] and its value was found to be 14.3 Mb. The refined value corroborated our statements that the giant resonance survives but is suppressed by the encapsulation and that it is not specific to $Ce@C_{82}$ but almost universal among metallofullerenes.

In the present study, we confirmed that the absolute values obtained by this method are reliable. Refinements of cross sections for other metallofullerenes as well as higher fullerenes such as C_{70} and C_{84} are also in progress using several standards and the Twerenbold's formula. Accurate determination of cross sections of fullerenes will allow us to assign structures appear in the photoabsorption spectra which arise from molecular nature of fullerenes.

Table 1 Refined cross sections of $Pr@C_{82}$ at the photon energy of 110 and 130 eV. All cross sections are in Mb. Numbers in parentheses show estimated errors.

Photon energy	cross section		
	$Pr@C_{82}^{+}$	$Pr@C_{82}^{2+}$	Total
110 eV (off-resonance)	22 (11)	15 (4)	37 (12)
130 eV (on-resonance)	28 (11)	24 (7)	52 (13)

[1] K. Mitsuke *et al.,* J. Chem. Phys. **122** (2005) 064304.
[2] K. Mitsuke *et al.,* Int. J. Mass Spectrosc. **243** (2005) 121.
[3] H. Katayanagi *et al.,* UVSOR Activity Report **32** (2006) 51.
[4] D. Twerenbold *et al.,* Proteomics **1** (2001) 66.

BL2B

Partial Cross Sections for Single and Multiple Photoionization of C_{84}

C. Huang[1], B.P. Kafle[1], H. Katayanagi[1], M.S.I. Prodhan[1], H. Yagi[1], Y. Kubozono[2], K. Mitsuke[1]

[1]*Division of Chemical Dynamics and Grad. Univ. Adv. Studies, Inst. for Molec. Sci., Myodaiji, Okazaki 444-8585, Japan*

[2]*Dept. of Chem., Okayama Univ., Okayama 700-8530, Japan*

Partial cross sections for the photoion formation from C_{84} were determined from the yields of singly-, doubly- and triply-charged ions which were measured by mass spectrometry combined with tunable synchrotron radiation at $h\nu$ = 50 – 120 eV.

The soot containing C_{84} was prepared by an arc-discharge of carbon graphite composite rods with Eu_2O_3. The C_{84} sample was purified by high performance liquid chromatography with toluene as eluent, after a Soxhlet-extraction of the soot. The laser-desorption mass spectrum of the purified sample exhibited only a single peak for C_{84}, and the purified C_{84} sample contains only isomer with D_2 symmetry. About 5 mg of C_{84} was produced with purity better than 99 % from 10 g of the soot.

Figure 1 shows the spectrum taken at $h\nu$ = 100 eV, the oven temperature T = 413 °C, and mass deposition rate D of 0.2 ng s^{-1}. Peaks of the parent ions C_{84}^{z+} are clearly observed. The shoulder in the smaller m/z side of the main peak of C_{84}^{2+} is ascribed to C_{82}^{2+} and other fragments produced by the C_2-loss processes from C_{84}^{2+}. We calculated the relative partial cross sections $\sigma(C_{84}^{z+})$ (z = 1 - 3) for the formation of C_{84}^{z+} from C_{84} in the gas phase that was calculated using

$$\sigma_{abs}(C_{84}^{z+}) \propto R(C_{84}^{z+})\, m\, \bar{v}^2 / \Phi D\, \eta(C_{84}^{z+})$$
$$\propto R(C_{84}^{z+})\, T / \Phi D\, \eta(C_{84}^{z+}) \equiv \sigma(C_{84}^{z+}),$$

where Φ is the photon flux of synchrotron radiation, and $\eta(C_{84}^{z+})$ is relative detection efficiency of the MCP. The net count rate $R(C_{84}^{z+})$ of the ion signal was computed by integrating the signal counts over each mass peak and then subtracting a uniform background. With increasing photon energy $\sigma(C_{84}^{+})$ shows a slow decrease, while the $\sigma(C_{84}^{3+})$ curve tends to increase gradually. Over the whole $h\nu$ range $\sigma(C_{84}^{2+})$ remains almost flat or slightly declines.

Figures 2 and 3 show the ratio between $\sigma(C_{84}^{2+})$ and $\sigma(C_{84}^{+})$ and that between $\sigma(C_{84}^{3+})$ and $\sigma(C_{84}^{+})$. The ratio $\sigma(C_{84}^{3+})/\sigma(C_{84}^{+})$ has a positive dependence on the photon energy and takes 0.16 at 100 eV. In contrast the $\sigma(C_{84}^{2+})/\sigma(C_{84}^{+})$ curve appears to reach a maximum value of 1.0 around 80 eV and thereafter slowly decreases. The ratios of the partial cross sections are compared with those for C_{60} and C_{70} evaluated at $h\nu$ ~ 100 eV. All these ratios can be arranged in descending order as

$\sigma(C_{70}^{2+})/\sigma(C_{70}^{+}) > \sigma(C_{84}^{2+})/\sigma(C_{84}^{+}) > \sigma(C_{60}^{2+})/\sigma(C_{60}^{+})$

and

$\sigma(C_{70}^{3+})/\sigma(C_{70}^{+}) > \sigma(C_{84}^{3+})/\sigma(C_{84}^{+}) > \sigma(C_{60}^{3+})/\sigma(C_{60}^{+})$.

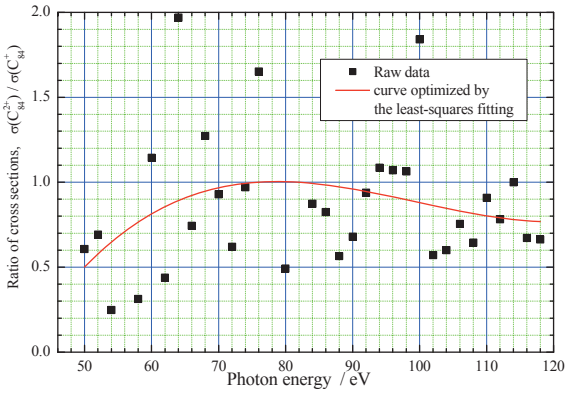

Fig. 2 Ratio between the cross sections for double and single photoionization.

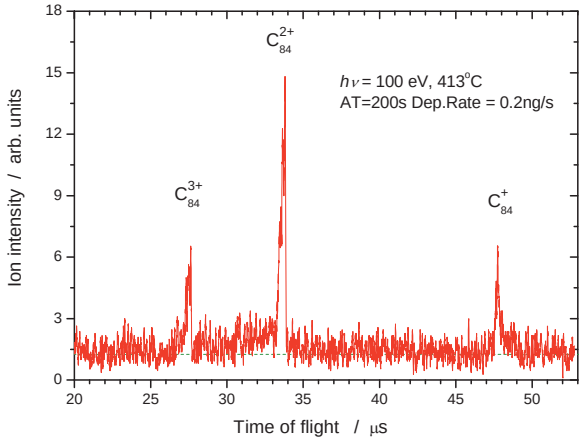

Fig. 1 Time-of-flight mass spectrum of C_{84}.

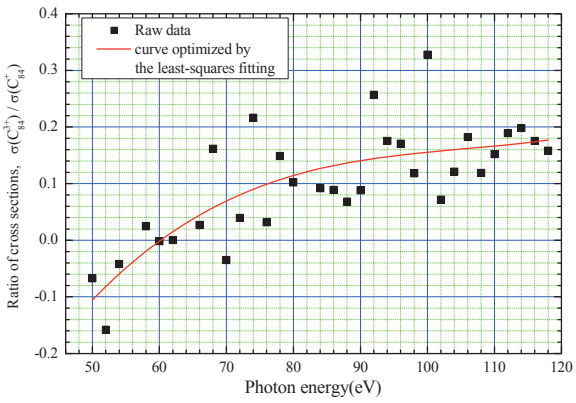

Fig. 3 Ratio between the cross sections for triple and single photoionization.

BL4B

Observation of Correlation Between Electron Emission and Dissocciation Following S *2p* Excitation of OCS

T. Kaneyasu[1], M. Ito[1,2], Y. Hikosaka[1], E. Shigemasa[1]

[1]*UVSOR Facility, Institute for Molecular Science, Okazaki 444-8585 Japan*

[2]*Graduate School of Science and Technology, Niigata University, Niigata-shi 950-21 Japan*

Coincidence detection and correlation analysis among the particles ejected during the relaxation processes of core-excited molecules bring a deeper insight into the molecular inner-shell processes. When both an Auger electron and fragment ions are analyzed in energy, one can give access to the state-to-state dissociation dynamics of the core-excited molecules. We have observed correlation between resonant Auger emission and subsequent molecular dissociation following S $2p_{3/2} \rightarrow \pi^*$ excitation of OCS molecules. In contrast to the dipole-allowed direct photoemission from the valence shells, it is expected to observe spin-forbidden states as the Auger final states [1], but their dissociation dynamics has not been revealed.

The experiment was performed on BL4B using the electron-ion coincidence spectrometer [2]. The monochromator bandwidth was set to $E_{ph}/\Delta E_{ph}$~1000 at $h\nu$=164 eV. The electrons ejected at 54.7° with respect to the electric vector of the light were analyzed in energy by the double toroidal electron analyzer, while ions were extracted from the interaction region into the momentum spectrometer by a pulsed electric field according to the electron detection. Arrival positions on the detector and time-of-flights (TOFs) of ions were recorded for every event. The pass energy of the DTA was set to 50 eV for observing resonant Auger electrons in a binding energy range from 14.5 to 19 eV. The resolving power of the DTA was estimated to be $E/\Delta E$~50. The coincidence data set was recorded at $h\nu$=164.3 eV, corresponding to S $2p_{3/2} \rightarrow \pi^*$ excitation.

Figure 1 shows a correlation between the resonant Auger final states and the TOFs of the fragments ions. Note that false coincidence events are subtracted. Due to the limited energy resolution in the present setup, the spin-forbidden states are hardly discernible in the electron spectrum. The two bands observed are assigned to the overlap of the $A^2\Pi$ and $B^2\Sigma$ states, and the $C^2\Sigma$ state as noticed in the spectrum. The A and B states are energetically capable to dissociate into S^+ + CO, while the C state can decay into both the S^+ + CO and S + CO^+ limits. This is roughly confirmed in Fig. 1(a), although the CO^+ fragment is hardly seen in the C state, which may arise from its low branching ratio [3] and the imperfection of the false coincidence subtraction.

We have deduced kinetic energy of the S^+ fragments formed through the dissociations from A, B and C states. In Fig. 2, the energy correlation between the Auger final states and S^+ ions is plotted. Three dissociation limits of $S^+(^4S)$ + $CO(X^1\Sigma)$, $S^+(^2D)$ + $CO(X^1\Sigma)$ and $S^+(^2P)$ + $CO(X^1\Sigma)$ are energetically accessible, and the limits are indicated by diagonal lines, neglecting the internal energy of CO fragment. The S^+ kinetic energy distributions are spread even to 0 eV, which are due to the vibrational and/or rotational excitations of the neutral CO fragment. The A and B states dissociate into $S^+(^4S, ^2D)$ + CO, while the C state decays into $S^+(^2D, ^2P)$ + CO. The present analysis demonstrates the direct observation of the correlation between the resonant Auger emission and molecular dissociation.

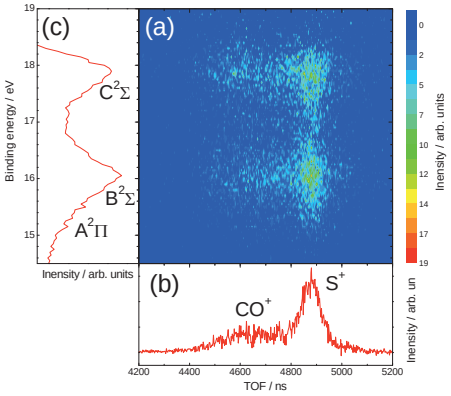

Fig. 1 (a) Correlation between the Auger final states and TOF of fragments. (b) TOF spectrum of fragments. (c) Resonant Auger spectrum.

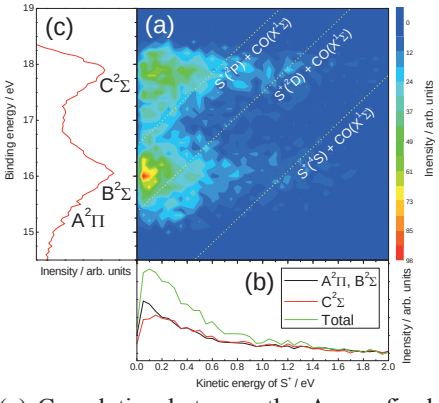

Fig. 2 (a) Correlation between the Auger final states and kinetic energies of S^+ fragments. (b) Kinetic energy distribution of S^+. (c) Resonant Auger spectrum.

[1] S. Masuda *et al*, J. Electron Spectrosc. Relat. Phenom., **137-140** (2004) 351.

[2] T. Kaneyasu *et al*, J. Electron Spectrosc. Relat. Phenom., in press.

[3] S. Morse *et al*., Int. J. Mass Spectrom., **184** (1999) 67.

BL4B

Three-dimensional Momentum Analyses in Ionic Fragmentations Following Inner-Shell Photoionization

T. Kaneyasu[1], M. Ito[1,2], Y. Hikosaka[1], E. Shigemasa[1]

[1]*UVSOR Facility, Institute for Molecular Science, Okazaki 444-8585 Japan*

[2]*Graduate School of Science and Technology, Niigata University, Niigata-shi 950-21 Japan*

Auger electron-ion coincidence is a powerful method for studying the decay dynamics of core-excited/ionized molecules produced by soft x-ray irradiation. In order to exert the full potential of this method, the spectrometer should be equipped with a performance realizing analyses of vector correlations among the momenta of all the particles emitted. Coincidence imaging spectrometers, which enable to measure three-dimensional momenta of both the electron and ions, have been widely used in the research field of atomic and molecular science. However it becomes difficult to observe fast Auger electrons with a sufficient energy resolution by the imaging technique. In this respect, a conventional electrostatic analyzer is suitable for observing the fast Auger electrons.

We have developed an Auger electron-ion coincidence spectrometer which consists of a double toroidal electron analyzer (DTA) and a three-dimensional ion momentum spectrometer [1,2]. We report on the three-dimensional momentum analysis for fragment ions following the C 1*s* photoionization of CO. The momentum, energy and angular resolutions for the fragment ions have been evaluated.

The experiment was carried out on BL4B. The DTA pass energy was set to 200 eV for observing the Auger electrons with the binding energy range of 40 – 55 eV. The pulsed electric field for ion extraction was adjusted to ensure the detection angle of 4π sr for ions with kinetic energies less than 6 eV. In this measurement, the arrival positions and time-of-flights (TOFs) of $C^+ + O^+$ ion-pairs were recorded in coincidence with the C 1*s* Auger spectrum at 334 eV photon energy. Three-dimensional momentum vectors of the ions $\mathbf{P}_1(C^+)$ and $\mathbf{P}_2(O^+)$ are derived from their arrival positions and time information. The momenta of each $C^+ + O^+$ pair should obey the momentum conservation on the two-body fragmentation: $\mathbf{P}_1 + \mathbf{P}_2 = 0$. Conversely, the values of $\mathbf{P}_1 + \mathbf{P}_2$ which are practically observed reflect the momentum resolution of the fragment ions measured by the present spectrometer. Figure 1(a) plots the correlation between $P_{X1} + P_{X2}$ and $P_{Y1} + P_{Y2}$. Here, the *x*-and *y*-axes are defined to be perpendicular to the TOF axis, while the *z*-axis corresponds to the TOF axis which is parallel to the electric vector of the radiation. The spot size on the map reflects the momentum resolution. In order to evaluate the momentum resolution, the sum-momentum distributions are derived by projecting the map onto each axis, which are shown in Figs. 1(b) and 1(c). The peak widths indicated by arrows in the distributions correspond to momentum resolutions $\sqrt{2}\,\Delta P_{X(Y)}$. As a result we have evaluated momentum resolutions as ΔP_X=11 au, ΔP_Y=17 au. Similarly ΔP_Z=38 au is determined from the $P_{Z1}+P_{Z2}$ distribution. The kinetic energy and angular resolutions are also estimated for the $C^+ + O^+$ events. Figure 2(a) represents the energy difference $3/4E_1 - E_2$. From the energy spread in the distribution, the energy resolution ΔE is estimated to be 1.3 eV. The angular distribution is analyzed in a similar way to the energy resolution, and the relative angle, $\theta_1 + \theta_2 - 180$, distribution is shown in Fig. 2(b). The emission angle θ is measured with respect to the TOF (electric vector) axis. The angular resolution obtained is better than 18°, which is sufficient to measure the emission angle of the fragment ions and to define initial molecular orientations when the axial-recoil approximation is valid.

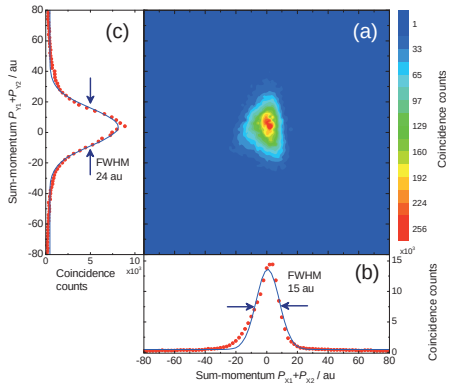

Fig. 1 (a) Contour plot of correlations between the sum-momenta $P_{X1}+P_{X2}$ and $P_{Y1}+P_{Y2}$. Projections of the intensities on the contour plot to (b) *x*-axis, and to (c) *y*-axis.

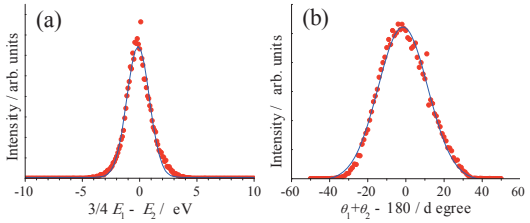

Fig. 2 (a) Energy difference distribution and (b) relative emission angle distribution for the $C^+ + O^+$ dissociation events.

[1] T. Kaneyasu *et al*, AIP conf. proc. **978**, (2007) 1793.

[2] T. Kaneyasu *et al*, J. Electron Spectrosc. Relat. Phenom., in press.

BL4B

Molecular Deformation of Core-Excited OCS Probed by a Momentum Imaging Method

M. Ito[1,2], T. Kaneyasu[1], Y. Hikosaka[1], K. Soejima[2], E. Shigemasa[1]

[1] *UVSOR Facility, Institute for Molecular Science, Okazaki 444-8585 Japan*

[2] *Graduate School of Science and Technology, Niigata University, Niigata 950-2181 Japan*

Interaction between molecules and soft X-rays is characterized by excitation and ionization of the core electrons. Core-excited molecules decay mostly via Auger electron emission, leading to multiply-charged ion states. The subsequent dissociation of the ion states often results in ionic fragmentations. The emission directions of the fragment ions reflect the molecular structures at the moment of dissociation. An ion momentum correlation measurement, therefore, enables us to determine the molecular structures at the dissociation, and further to discuss the molecular deformations of core-excited states.

In this work, we have studied molecular deformations of core-excited OCS, with an ion momentum spectrometer [1] followed by a position sensitive detector. Here, fragment ions were extracted from an interaction region by a DC electric field, and the momentum vector of each fragment ion was determined from the arrival position on the detector. We have accumulated a multi-ion coincidence dataset at a photon energy of 288 eV which corresponds to the C1s $\rightarrow \pi^*$ resonance. Only the triple coincidences due to the three-body dissociation of OCS^{3+} were used for the present analysis, because this choice enables us to determine directly the momentum vectors of all the fragment ions. The triple coincidences associated with the formation of O^++C^++S^+ can be deduced from the coincidence dataset, by using information on time-of-flight (TOF) differences between the three ion fragments. Fig.1 shows a two-dimensional plot of the numbers of the triple coincidence events, as a function of TOF difference between first hit and second hit (horizontal) and that between first hit and third hit (vertical). The triple coincidences for O^++C^++S^+ can be identified in the marked area.

Figure 2 shows momentum correlations among three ionic fragments included in the triple coincidences. Here, the relative momentum vectors of C^+ and S^+ are plotted, with normalizing the O^+ momentum vectors to (X,Y)=(-1,0). One can see in Fig. 2 that angles between O^+ and S^+ fragments are preferably around 150 degree, while the neutral ground state of OCS has a linear geometry. This observation implies that the molecular geometry is deformed after the inner-shell photoexcitation to OCS ($C1s^{-1}\pi^*$). Here, a significant molecular deformation is not expected on the OCS^{3+} potential energy surfaces in general, due to the fast dissociation which approximates to the Coulomb explosion. Therefore, the molecular deformation seems to be occurred at OCS ($C1s^{-1}\pi^*$). The degeneration of OCS ($C1s^{-1}\pi^*$) is dissolved by the Renner-Teller effect, and one of the OCS ($C1s^{-1}\pi^*$) states has a bent geometry. The observed molecular deformation shows a good correspondence to the Renner-Teller distortion at OCS ($C1s^{-1}\pi^*$).

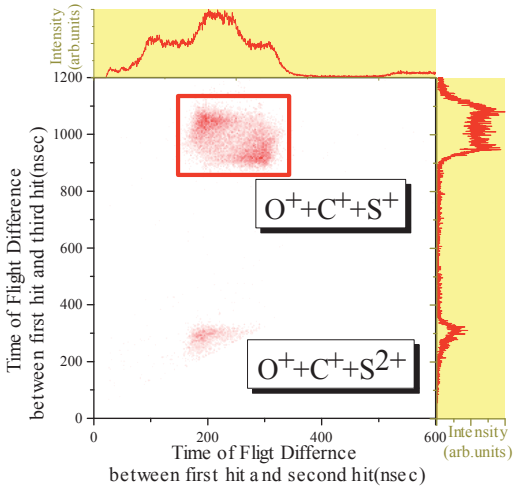

Fig. 1 Time-of-flight difference between first hit and second hit, and those between first hit and third hit. The marked area with a square shows triple coincidences associated with formation of O^++C^++S^+.

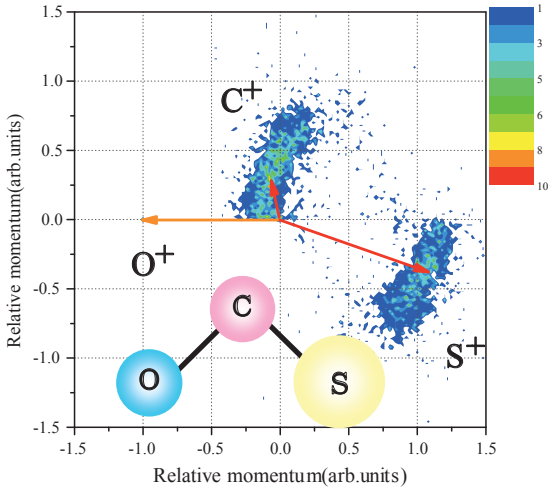

Fig. 2 Momentum correlation for three-body dissociation of OCS^{3+} formed by Auger decay from the C 1s$\rightarrow\pi^*$ resonance.

[1] T. Kaneyasu, Y. Hikosaka, E. Shigemasa, J. Electron. Spectrosc. Relat. Phenom, in press.

BL7B

Ion Pair Formation in the Vacuum Ultraviolet Region of NO

Y. Hikosaka, T. Kaneyasu, E. Shigemasa
UVSOR Facility, Institute for Molecular Science, Okazaki 444-8585 Japan

Pair formation of positive and negative fragment ions is one of the basic reaction processes induced by interaction between molecules and vacuum ultraviolet photons, though the cross section is highly unfavorable. The cross section of the ion pair formation is often enhanced at neutral excited states, reflecting predissociation of the neutral excited states into ion pair states. The predissociation rate relates to the electronic properties and the potential energy surfaces of the relevant states, and accordingly the neutral excited states which are hardly discernable in the total photoabsorption cross sections may appear remarkably in the cross section for the ion pair formation. Here, one can locate the neutral excited states without direct ionization background, because direct ionization does not contribute to the ion pair formation. The observation of the ion pair formation can be, therefore, a peculiar probe for neutral excited states.

In this work, we have studied the ion pair formation from NO by using a negative ion imaging spectrometer [1]. The advantages of the present imaging method [2] over ordinary mass spectrometry are (i) high collection efficiency (4π-sr. solid angle), and (ii) informativeness on the velocity vector distribution of negative fragment ions. The first useful information derived from the velocity vector distribution is the angular distribution of fragment ions with respect to the electric vector of the incident light. The angular distribution may imply the molecular alignment induced by photoexcitation, where the alignment reflects the symmetries of initially-formed excited states. The kinetic energy distribution of the negative fragment ions is the second useful information derived from the velocity vector distribution, and the internal states of negative and positive fragments are determinable from the kinetic energy distribution. The populations of the final fragment states closely relate to the reaction dynamics.

A negative ion yield curve of NO measured in the photon energy region of 19-25 eV is shown in Fig. 1, in a comparison with a positive ion yield curve. The negative ion yield curve shows much richer structures than the positive ion yield curve. This fact proves the spectroscopic usefulness of negative ion detection to the neutral excited states. Figure 2(a) shows a negative ion image measured at a photon energy of 22.01 eV, where the first two N^++O^- limits are accessible. The measured image corresponds to the projection of the three-dimensional velocity distributions for the O^- fragments, where the O^- fragments associated with each N^++O^- limit contributes to a circular pattern on the projection, with intensity concentrated around the circumference. The two rings on the image in Fig. 2(a), which show individual anisotropic intensity distributions with respect to the electric vector, are associated with the first two N^++O^- limits. Figure 2(b) shows a transformed image using an onion-peeling procedure. On the transformed image, obviously the two rings corresponding to the individual N^++O^- limits become clearer than those on the image in Fig. 2(a). The total intensity of each ring gives the population of the corresponding final N^++O^- pair, and the intensity distribution along the ring shows the angular distribution relative to the electric vector.

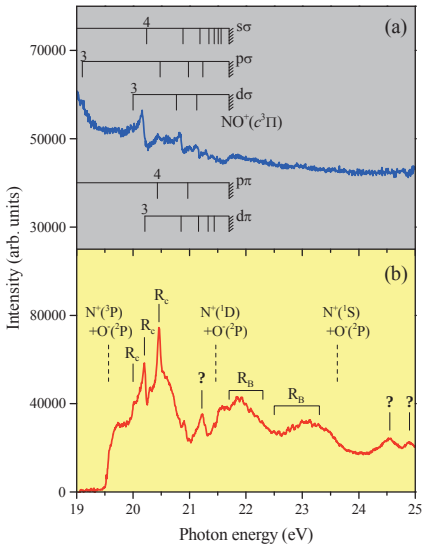

Fig. 1 (a) Positive ion yield curve and (b) negative ion yield curve of NO. R_c and R_B denote Rydberg states converging to $NO^+(c^3\Pi)$ and $NO^+(B^1\Pi)$, respectively.

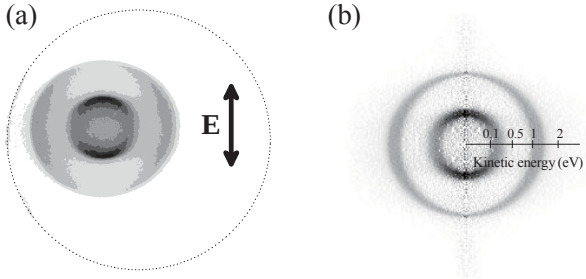

Fig. 2 (a) Negative ion image measured at a photon energy of 22.01 eV, where the first two ion pair limits are accessible. (b) Transformed image using an onion-peeling procedure.

[1] Y. Hikosaka, T. Kaneyasu and E. Shigemasa, J. Electron Spectrosc. Relat. Phenom. **154** (2007) 43.
[2] Y. Hikosaka and E. Shigemasa, J. Electron Spectrosc. Relat. Phenom. **148** (2005) 5.

4
Solid state spectroscopy I: IR and VUV

BL1B

Vacuum-ultra Violet Reflectance Spectroscopy of Strongly Correlated Electron System

J. Fujioka[1], S. Miyasaka[2], Y. Tokura[1,3,4]

[1]*Department of Applied Physics, University of Tokyo, Tokyo 113-8656 Japan*

[2]*Department of Physics, University of Osaka, 560-0043, Osaka Japan*

[3]*Correlated Electron Research Center (CERC), National Institute of Advance Industrial Science and Technology (AIST), Tsukuba 305-8562*

[4]*ERATO-SSS, Japan Science and Technology Agency (JST) Tsukuba 305-8562 Japan*

The spin, orbital and charge degrees of freedom in the correlated electron system have been attracting much attention. The interplay among them leads to the versatile magnetic and/or electronic structure, even though the crystal structure is nearly cubic. One interesting topic is the reconstruction of the electronic structure in the course of the insulator-metal transition, accompanying the spin/orbital ordering-disordering transition [1]. The investigation of the electronic structure over wide energy range by the measurements of the reflectivity spectra is indispensable to reveal the spin-orbital-charge coupled phenomena associated with the insulator to metal transition.

In this beamtime, we have measured the reflectivity spectra of the several transition metal oxides, including the V, Mn, Fe, Ni, and Cu ions, for an energy range between 4eV and 35eV at room temperature using the beam line BL1B. We connected the measured spectra to the low energy ones below 4 eV and calculated the optical conductivity spectra by the Kramers-Kronig analysis. As an example, we focus on the optical conductivity spectra of the single domain crystals of $Y_{1-x}Ca_xVO_3$ in this report.

The perovskite-type vanadium oxide YVO_3, which is known as the prototypical Mott-Hubbard insulator, has two valence electrons in the 3*d* orbital of the nominally trivalent V ion with the spin configuration of S=1. The orthorhombic crystal distortion splits the triply degenerate t_{2g} levels into the lower lying d_{xy} level and the higher lying doubly degenerate d_{yz} and d_{zx} ones. With lowering temperature, the Jahn-Teller distortion further lifts the degeneracy of the d_{zx} and d_{yz}, and the G-type orbital ordering (OO), where the occupied d_{zx} and d_{yz} orbitals are staggered in all (x, y, z) directions, appears at T_{OO1}=200K. Subsequently, the C-type spin ordering (SO) appears at T_{SO1}=116K, where spins align ferromagnetically along the c axis and antiferromagnetically in the ab plane. With further lowering the temperature, the C-type orbital and G-type spin ordered state appears at T_{SO2} ($=T_{OO2}$)=77K. Recent studies have revealed that the low temperature C-type orbital and G-type spin ordered phase is immediately suppressed by Ca doping, *i.e.* the hole doping as shown in fig. 1 (a).

In Fig. 1(b), we show the optical conductivity spectra of $Y_{1-x}Ca_xVO_3$ x=0 and x=0.10 for $E \parallel c$, which was measured at room temperature. In both

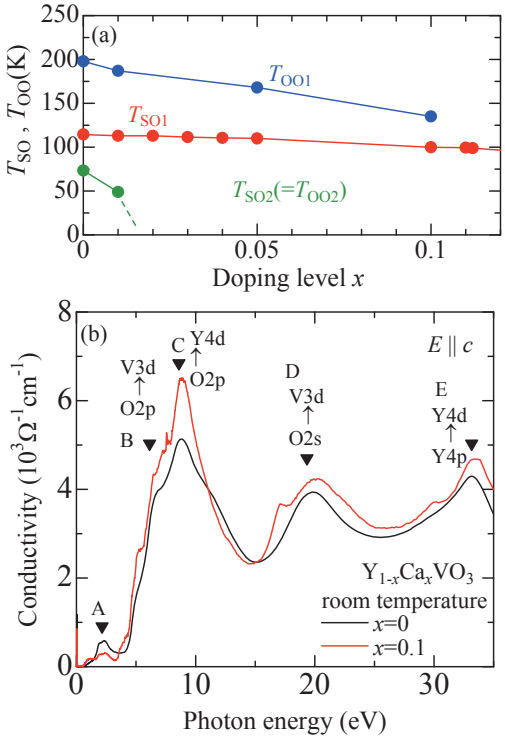

Fig. 1: (a) The spin-orbital phase diagram of $Y_{1-x}Ca_xVO_3$. (b)The optical conductivity spectra of $Y_{1-x}Ca_xVO_3$ x=0 (black line) and x=0.1 (red line), respectively.

spectra, several peaks are observed. We assigned the peak A around 2eV to the Mott-gap excitation. A more intense peak (B) is observed around 7 eV, which is assigned to the charge transfer excitation from O2*p* to V3*d* level. Above 7eV, three peaks (C, D, and E) are observed and we have assigned them to the excitations from O2*p* to Y4*d*, from O2*s* to V3*d*, and from Y4*p* to Y4*d*, respectively, according to Ref. [2]. To see the Mott gap excitation in more detail, in fig. 2, we show the magnified view of the optical conductivity spectra for YVO_3 in the low energy region. With lowering the temperature, the intensity of the Mott gap excitation for $E \parallel c$ spectra increases especially in the range of T_{SO2} ($=T_{OO2}$) < T < T_{OO1}, while that for $E \perp c$ shows minimal temperature dependence. Such an anisotropic charge dynamics is also observed in the similar system, $LaVO_3$, and is explained in terms of the quasi-one-dimensional orbital exchange interaction, which is characteristic in

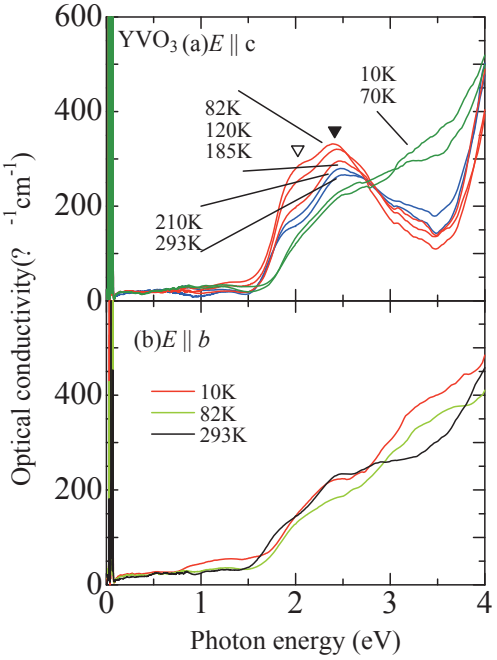

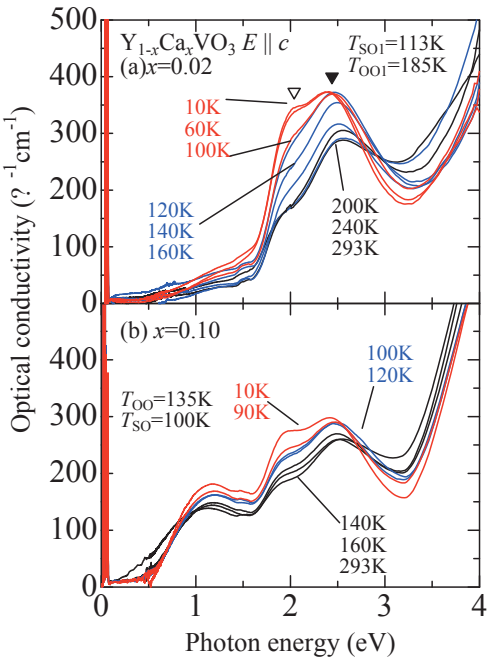

the C-type spin and G-type orbital ordered state [3,4,5]. According to the ref. [4], in the C-type spin and G-type orbital ordered phase, the Mott gap excitation is decomposed into the two components. The lower-lying band (mg1) is an allowed Mott-gap excitation along the ferromagnetic chain ($\|c$) in the C-type spin ordered state. The higher-lying band (mg2) is the nominally forbidden one, which is weakly allowed due to the imperfect spin-orbital polarization. For $T > T_{SO2}$ ($=T_{OO2}$), the intensity of mg2 seems to be larger than that of mg1, indicating the large spin and orbital fluctuation. Such kind of the large spin and orbital fluctuation in the C-type spin and G-type orbital ordered phase is also pointed out by the neutron scattering experiment [6]. On the other hand, for $T < T_{SO2}$ (T_{OO2}), the intense peak structure around 2eV disappears and the spectral weight is transferred to above 3eV. Concomitantly, the anisotropic feature of the Mott gap excitation also disappears. The disappearance of the anisotropic electronic structure may be explained in terms of the nearly isotropic orbital exchange interaction in the G-type spin and C-type orbital ordered phase.

For x=0.02, the ground state is the spin C-type / orbital G-type and the intensity of the Mott-gap excitation around 2eV in the $E\|c$ spectra increases monotonously with lowering the temperature as shown in fig. 3(a). In particular, the intensity of the mg1 continues to increase down to 10K, while there is still considerable contribution from that of mg2. This contrasts with the case of $LaVO_3$, where that of mg2 is much smaller at 10K [4]. One explanation may be that, for x=0.02, the spin and orbital quantum fluctuation is relatively enhanced compared to $LaVO_3$, since this system is located in the vicinity of the spin-orbital ordered phase boundary.

In the $E \| c$ spectra for x=0.10, the intensity of the Mott gap excitation is reduced and the additional bump structure (mid-IR peak) appears at ~1eV, which results from the incoherent motion of the doped hole as shown in fig. 3(b). The mid-IR peak for $E \| c$ spectra has larger spectral weight than that for $E \perp c$ and increases its intensity in the low temperature region, while that for $E \perp c$ shows minimal temperature dependence. Note that the spectral weight is a good measure for the kinetic energy of the electrons. For x=0.10, the orthorhombic crystal distortion is still robust and, hence, the d_{xy} level might be lower in energy than d_{yz} or d_{zx} level. Thus, as the explanation for the enhancement of the mid-IR peak for $E\|c$ spectra, it is expected that the doped holes mainly occupy the d_{yz} and d_{zx} orbitals and have a large kinetic energy along the c-axis, reflecting the quasi-one-dimensional orbital exchange interaction.

[1]M.Imada *et al.*, Rev. Mod. Phys. **70** (1998)1039.
[2] T. Arima *et al.*, J. Phys. Soc. Jpn. **64** (1995) 2488.
[3]Y. Motome *et al*, Phys. Rev. Lett. **90** (2003) 146602.
[4] S. Miyasaka *et al*, J. Phys. Soc. Jpn. **71** (2002) 2086.
[5]J. Fujioka *et al.*, Phys. Rev. Lett. **97** (2006) 196401.

BL5B

Phase Change of EUV Reflection Multilayer by Total Electron Yield and Reflection Spectra

T. Ejima, T. Harada, A. Yamazaki

Institute of Multidisciplinary Research for Advanced Materials, Tohoku University, Sendai 980-8577 Japan

In the extreme ultraviolet (EUV) wavelength region, normal incidence mirrors were made available through the use of reflection multilayers and are required to have extremely low aberrations [1]. To achieve the aberration-free multilayer mirrors, the technique of surface milling has been proposed as an accurate correction method of figure errors [2]. In order to make an accurate correction, it is important to first obtain information regarding the reflection phase in multilayer mirrors. In this study, reflection phase values for multilayer optics were obtained according to the formula derived from the total electron yield intensity and reflection in the multilayer. These phase values were found to change in accordance with increases in the thickness of the top layer.

Total electron yield (TEY) is a spectroscopic method used in X-ray regions for detecting the wavelength-dependence of the number of emitted electrons from a solid, and is proportional to the absorbed energy of the incident light in the EUV region [3]. The intensity of the photoelectrons emitted from a reflection multilayer is optically represented by three terms: incidence-, reflection-, and interference- terms [4]. When the attenuation length L of emitted photoelectrons from the top layer is smaller enough than the thickness d of the top layer, the TEY intensity $I_T(\lambda)$ is approximately represented by

$$I_T(\lambda) = I(\lambda)\left[1 + R(\lambda) + 2\sqrt{R(\lambda)}\cos\left(\delta - 2\xi(d+L)\right)\right], \quad (1)$$

where $I(\lambda)$ is a TEY spectrum of the top-layer material, R is the real part of the complex reflectance of the top layer, δ is the reflection phase at one layer below the top layer, and ξ is the real part of the top-layer's propagation-vector using angle of incidence θ, wavelength λ, and complex dielectric function ε of the top layer. The term ξ is represented as $\xi = 2\pi(\varepsilon - \sin^2\theta)/\lambda$. Equation (1) resembles the formula applied to analyze surface structures using X-ray standing waves generated by a single crystal in the hard X-ray region [5]. A phase term will be obtained on the basis of the relation to determine surface structures. As the same manner, the phase term in Eq. (1) can be represented by measurable quantities. When the phase term $\delta - 2\xi(d+L)$ is represented by Δ in Eq. (1), the cosine term difference between the thicknesses d and δd of the top layers can be obtained as

$$\cos(\Delta - 2\xi\cdot\delta d) - \cos\Delta = \left(\frac{I_T(\lambda) - I'_T(\lambda)}{I(\lambda)}\right) \Big/ 2\sqrt{R(\lambda)}. \quad (2)$$

Periodic [Mo 2.6nm/Si 4.1nm]×20 multilayers with different thicknesses of top Mo layer were fabricated on a same Si substrate. Thicknesses of the top Mo layer were accurately controlled by the shutter that was placed in front of the sample, and were deposited from 0.4nm to 3.2nm at 0.4nm intervals. A Mo single layer (d > 200nm) was also fabricated for normalization of the TEY spectra. TEY spectra of these aperiodic multilayers were measured with reflection spectra. In the measurement, a combination of the G2 grating and the M22 mirror was used for the 10-20 nm wavelength region. The incident wavelength was calibrated according to the position of the Si-$L_{2,3}$ absorption edge. The resolving power of the wavelength $\lambda/\Delta\lambda$ estimated from the width of the Si-$L_{2,3}$ absorption edge was 200. The incident light estimates include a higher order light component, with a 20% intensity component of first order light. The reflection and TEY spectra of the Mo/Si multilayer system were measured simultaneously at 10° to the normal angle of incidence.

TEY spectra of the aperiodic multilayers were normalized using the TEY spectrum of the Mo single layer. The TEY and reflection spectra are shown in Figure 1. In the TEY spectra, the main peak is observed clearly around 13.4 nm and the peak position shifts from 13.2 nm to 13.6 nm as the thickness of the top Mo layer increases. Smaller peaks are observed either side of the main peak, and the peak positions shift also to the longer wavelength region. In the reflection spectra, the series of peaks located at 13.4 nm, deviate little in their peak position despite increases in the thickness of the Mo layer.

To obtain the phase term differences, the normalized TEY spectra of each multilayer and the reflection spectra were substituted for $I_T(\lambda)/I(\lambda)$, $I'_T(\lambda)/I(\lambda)$, and $R(\lambda)$ in Eq. (2). In Figure 2, phase changes obtained experimentally are represented with those obtained numerically using the exact formula [4]. Here, the graph labels (+Mo xx nm) correspond to the top Mo layer thickness. In the calculation, the optical constants were taken from data compiled by Henke and Palik [6, 7]. The thicknesses of the periodic Mo (2.02 nm) and Si (4.76 nm) layers used

in reflection spectrum were determined by comparison of the X-ray diffraction data and fabrication conditions. The attenuation length was treated as the fitting parameter, based on NIST Standards [8]. The value of $2\xi L$ obtained from the fitting procedure was 0.3π.

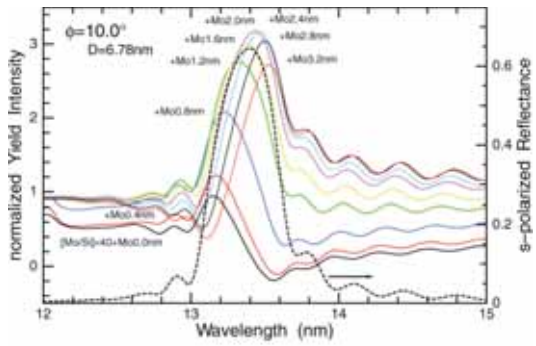

Fig. 1. Total electron yield (solid curves) and reflection (broken curve) spectra of Mo/Si multilayers with varying top Mo layer thicknesses.

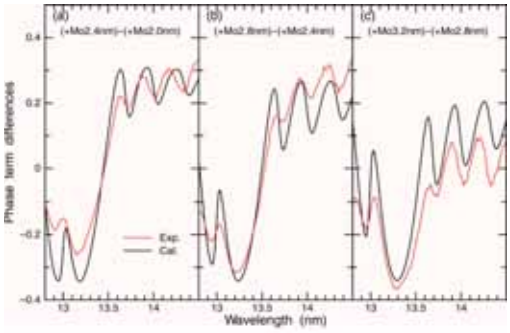

Fig. 2. Differences of the cos terms in Eq. (2). Red curves represent the experimental results and black curves, the calculation ones.

Experimental phase changes were reproduced well by the numerical simulations at that the thickness of the top Mo layer is more than 1.2nm. This result suggests that reflection phases of multilayer mirrors will be observed by both reflection and TEY spectra around reflection peaks. On the other hand, spectral shapes of the phases resemble to those of the calculation results but the values were disagreed at that the thickness of the top Mo layer is less than 1.2nm. This disagreement will be caused by overlap of photoelectrons emitted from the layers below the top layer. In other words, the assumption made on the derivation of Eq. (1), the photoelectrons are emitted from the top layer only, will not applicable in the thinner top layers.

Simultaneous reflection and TEY measurements have been obtained for aperiodic Mo/Si multilayers. The phase term differences obtained from the reflection and TEY spectra are in accordance with the change in thickness of the top Mo layer. This method will be applied to evaluate the phase information for accurate multilayer optics, for example microscopes, telescopes, and photo-masks, in the EUV region. Same phase information will be obtained from the Kramers-Kronig analysis of a reflection spectrum. The merit of this method is reliant on the TEY intensity, which can be easily measured in accordance with the corresponding reflection spectra, such that the associated phase information can be obtained for a given wavelength.

[1] For example, D. Attwood, Soft X-rays and extreme ultraviolet radiation, (Cambridge University Press, Cambridge, 2000) Chap. 4.
[2] M. Yamamoto, Nucl. Instrum. Meth. Phys. Res. A, **467-468** (2001) 1282.
[3] W. Gudat and C. Kunz, Phys. Rev. Lett., **29** (1972) 169.
[4] T. Ejima, Jpn J. Appl. Phys. **42** (2003) 6459.
[5] J. Zegenhagen, Surf. Sci. Reports, **18** (1993) 199.
[6] "Handbook of Optical Constants of Solids I, II, and III" ed. E. D. Palik, (Acad. Press. Inc., New York & London, 1985, 1991, and 1998).
[7] B. L. Henke, E. M. Gullikson, and J. C. Davis, At. Data Nucl. Data Tables 54, 181 (1993), at http://www.cxro.lbl.gov/optical_constants/.
[8] C. J. Powell and A. Jablonski, NIST Electron Effective-Attenuation-Length database, NIST standard reference database 82, (National Institute of Standards and Technology, Gaithersburg, 2001).

BL1B

Effect of Anionic Species in Ionic Liquids on Photostability

N. Inoue, M. Makita, T. Ishioka, A. Harata
Department of Molecular and Material Sciences, Kyushu University, Kasugakoen 6-1, Kasuga-shi, Fukuoka 816-8680, Japan

Photostability of ionic liquid compounds of 1-butyl-3-methylimidazolium salts was evaluated using synchrotron radiation. A remarkable change in ^{1}H-NMR and FT-IR spectra was observed for [bmim][PF_6] and [bmim][BF_4]. Production of methylimidazolium ionic liquids was confirmed. While no changes was observed for [bmim][Tf_2N]. It is suggested that photostability of ionic liquids are largely influenced by anionic species.

Introduction

Ionic liquids are defined as salts which are in the liquid state at room temperature. Ionic liquids are rapidly expanding topic of research because of their favorable properties such as negligible volatility; high chemical, thermal, and electrochemical stability; high ionic conductivity; and, in some case, hydrophobicity. These properties make them highly attractive candidates for the use in solvent for chemical reactions such as photochemistry, organic synthesis, and photocatalysis. Especially, in photochemical reaction, it is known that ionic liquids act as an electron donor or an accepter. However, photochemical behavior and any potential toxicity issues for most ionic liquids are not known, particularly with respect to alkylimidazolium systems, and preliminary data is only now being determined.

Recently, researches on water stability and thermo stability are reported. Some ionic liquids possibly decompose under moisture and high temperature atmosphere. In the case of photoreactions, presence of decomposed products might cause lowered experimental accuracy and distorted results. It is important to investigate photostability of ionic liquids precisely.

In this report, photostability and photolysis of 1-butyl- 3-methylimidazolium hexafluorophosphate, tetrafluoroborate, bis(trifluoromethanesulfonyl)imide (abbreviated [bmim][PF_6], [bmim][BF4], [bmim][Tf_2N], respectively) were investigated using synchrotron irradiation.

Experimental

The 0-th order diffraction of Seya-Namioka monochromator (10eV>) was obtained from BL1B at the UVSOR facility. The light was emitted from the chamber to a He-purged cell through an MgF_2 window. The emitted light was reflected with an Al mirror and vertically irradiated on the [bmim][PF_6] surface for 30 minutes.

These kinds of ionic liquids ([bmim][PF_6], [bmim][BF_4], [bmim][Tf_2N] (Figure 1)) were synthesized according to the literature [1-3].

Results and Discussion

In ^{1}H-NMR spectra of [bmim][PF_6], new peaks appeared at 7.5ppm (d, C-H), 7.0ppm (d, C-H), and 3.6ppm (s, N-CH_3) after SR light irradiation. These chemical shifts show that compounds like methylimidazole are formed. Similar changes were observed in [bmim][BF_4]. Figure 2 shows IR spectra of [bmim][PF_6]. New absorption peaks appeared at 1230cm^{-1}, 1285cm^{-1}, 1525cm^{-1}. These are assigned to N-CH_3 stretching vibration, N-CH_3 stretching vibration, imidazolium ring asymmetric stretching vibration, respectively. Similar changes were observed in [bmim][BF_4]. Compared to the IR spectra of methylimidazole, the products of the photolysis are assigned to methylimidazolium hexafluorophosphate ([mim][PF_6]), or methylmidazolium tetrafluoroborate ([mim][BF_4]). In contrast, [bmim][Tf_2N] did not show any change in ^{1}H-NMR and IR spectra.

It is considered that [bmim][PF_6]([bmim][BF_4]) photodecompose into [mim][PF_6]([mim][BF_4]), and 1-butene. However, no photolysis was observed in [bmim][Tf_2N]. Thus, it is apparent that photostability of ionic liquids are influenced largely by anionic species. It is considered that photolysis proceeds by nucleophilic reaction or abstraction reaction of proton. Further research including wavelength dependence will be needed.

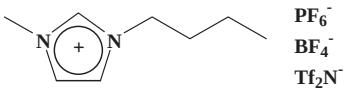

Fig. 1 Structure of [bmim][PF_6], [bmim][BF_4], and [bmim][Tf_2N].

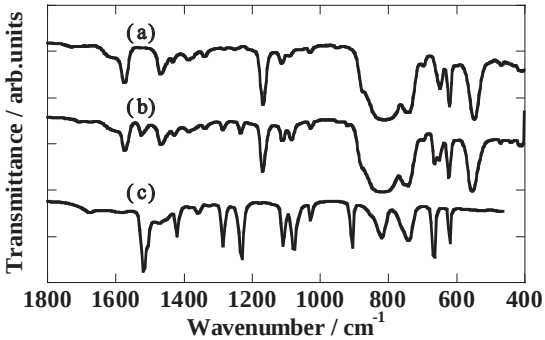

Fig. 2 IR spectra of (a) [bmim][PF_6], (b) [bmim] [PF_6] after SR light irradiation, and (c) methyl imidazole.

[1] J. G. Huddleston, R. D. Rogers, Chem. Commun (1998) 1765
[2] Rika. Hagiwara, Yasuhiko Ito, Journal of Fluorine Chemistry **105** (2000) 221
[3] M.J.Earle, C.M.Gordon, K.R.Seddon, Analytical Chemistry (2006) 6

BL1B

Photoluminescence from Localized Excitons in $PbCl_2$, $PbCl_2$:Br^- and $PbCl_2$:I^- Crystals

S. Izuhara[1], M. Kitaura[2], H. Nakagawa[1]
[1]*Dep. of Electrical & Electronics Engineering, Fukui University, Fukui, 910-8507*
[2]*Fukui National College of Technology, Sabae, 916-8507*

The excitonic states of lead halides are represented by the excited states of a Pb^{2+} ion in rough approximation. Indeed, since the optical properties are strongly dependent on halogen species, the excitonic states certainly include significant contribution from electronic orbitals of halogen. It has been accepted that the outermost p orbitals of halogen play an important role in self-trapping of excitons in PbX_2 (X=F, Cl, Br). As is well known, the information on absorption and luminescence of the halide crystal doped with other halogen ion impurity is indispensable to see the relaxed configuration of self-trapped excitons (STE's) in the host crystal. The purpose of the present study is to investigate the localized exciton luminescence of $PbCl_2$ crystals doped with a small amount of Br^- ions and I^- ions.

Special reagent grade powder of 99.99% purity of dehydrated $PbCl_2$, $PbBr_2$ and PbI_2 were purchased from Kojundo Chemical Laboraty. The single crystals of $PbCl_2$, $PbCl_2$:Br^- (0.01mol%) and $PbCl_2$:I^-(0.01mol%) were grown from melt in sealed quartz ampoules by the Bridgeman method. Samples were cut in the size of 5×5×5 mm^3 from crystal ingots with a razor blade. The mesurements of emission and excitation spectra were carried out at BL1B using a normal incidence monochromator. Photoluminescence from samples was guided into the incident slit of a grating monochromator by a optical fiber, and then detected by a CCD detector or a photomultiplier tube. The crystal samples were mounted on the copper holder of a closed-cycle He refigerator in order to perform measurements at 13K.

Figure 1 shows emission spectra of $PbCl_2$, $PbCl_2$:Br^-, and $PbCl_2$:I^- at 13K (black lines). The excitation spectra for the emission bands observed in the three samples are also indicated by red lines. In the crystal of $PbCl_2$, two emission bands are observed at 3.78eV (UV emission) and 2.89eV (B emission) under excitation at 4.6 eV. This spectrum is in agreement with the emission spectrum previously reported [1] .

In the crystal of $PbCl_2$:Br^-, three emission bands are observed at 3.1eV (V_1 emission), 2.32eV (G emission) and 1.75eV (R emission) by photostimulation at 4.3eV. The V_1 emission is strongly excited in the narrow energy region around 4.3eV (shaded area), which is located in the low energy tail of the fundamental abosrption in $PbCl_2$.

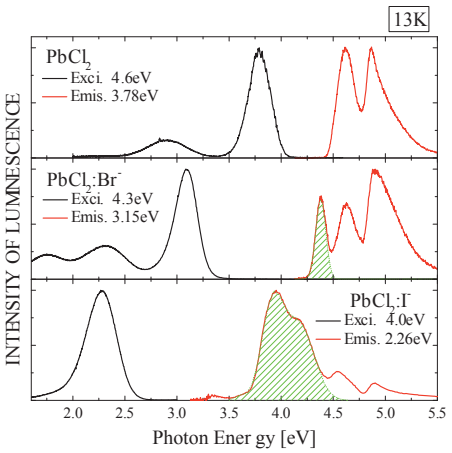

Fig.1 Emission spectra (black lines) and excitation spectra (red lines) of $PbCl_2$, $PbCl_2$:Br^-, and $PbCl_2$:I^- .

In the crystal of $PbCl_2$:I^-, an emission band appears at 2.26eV (Y emission) when the excitation photon energy is adjusted at 4.0 eV. The Y emission is also excited in the limited energy region around 4.0eV (shaded area), which separates from the intrinsic absorption edge.

It seems that the V_1 emission in $PbCl_2$:Br^- and Y emission in $PbCl_2$:I^- are similar to the luminescence from localized excitons in Br^- or I^- doped alkali chlorides, in the sense that the excitation for the emission takes place in the energy region below the excitonic absorption band of the host lattice. They are assigned to the luminescence from localized excitons.

According to the cluster calculation, the excitonic states of lead halide are described by a complex molecule of lead and halogen ions. We expect that the wave function of an electron is localized on a lead ion while that of a hole is distributed on the adjacent halogen ions in $PbCl_2$:Br^- and $PbCl_2$:I^-. The cluster calculation by the DV-Xα method is now under proceeding to make sure of our expectation.

[1] M.Kitaura *et al*., J. Phys. Soc. Jpn. **70** (2001) 2462.

BL1B

Luminescence and Excitation Properties of Host Lattice and Eu^{2+} Ions in $BaMgAl_{10}O_{17}$:Eu Phosphor

H. Yoshida[1,2], H. Kai[1], S. Watanabe[1], K. Ogasawara[1]

[1]*Department of Chemistry, Kwansei Gakuin University, 2-1 Gakuen, Sanda, 669-1337, Japan*

[2]*Research and Development Division, NEC Lighting, Ltd., 3-1 Nichiden, Minakuchi-cho, Koka, 528-8501, Japan*

From the view points of the importance as an efficient blue-emitting phosphor, $Ba_{1-x}Eu_xMgAl_{10}O_{17}$ (BAM:Eu) is a material of great interest in the recent research of phosphor. It is well known that BAM:Eu phosphor used for 3-band fluorescent lamps (FLs) and color plasma displays (PDPs) exhibit a decrease of luminescence and color shift due to thermal and discharge damage. Therefore, their products have been many issues in using it.

The blue emission in BAM:Eu is due to the $4f^65d^1 \rightarrow 4f^7$ transition of Eu^{2+} ions. As substituted location of Eu^{2+} ions, three sites are generally considered in the host lattice. The Beevers-Ross(BR) site is originally located to the Ba^{2+} site, while the anti-Beevers-Ross (aBR) and the mid-oxygen (mO) sites are in the interstitial positions[1]. According to recent reports, the most dominant site of Eu^{2+} ions in BAM is considered to be aBR[2-5]. However, this problem is still in controversy.

In this report, we have investigated the excitation properties of host lattice and Eu^{2+} ions in BAM:Eu phosphor by using the technique of vacuum ultraviolet measurements by synchrotron radiation light and first-principles molecular orbital calculation method developed for rare earth ions.

The luminescence bands at about 258 nm and 450 nm, which originate from the host lattice and the Eu^{2+} ions in BAM:Eu respectively, are observed. Figure 1 shows normalized excitation spectra of BAM:Eu. For x = 0, two excitation peaks at 160 nm and 175 nm are observed. They are considered to be due to the O 2p → Ba 5d transitions and the O 2p → Al 3d transitions within spinel block, respectively [6]. The excitation spectra at 450-nm emission band show a significant absorption band at 200 nm as well as the two main structures peaking at 310 nm and 250 nm. It is well known that the excitation band between 220 nm and 380 nm clearly increases with an increase of the amount of Eu^{2+} ions, which is due to $4f^7 \rightarrow 4f^65d^1$ transitions of Eu^{2+} ions. It is also found that the absorption edge of host lattice at 190 nm is unchanged with increase of Eu content, which indicates that the absorption of Eu activator center in BAM does not overlap that of the host lattice. On the other hand, in the luminescence spectrum under the excitation at 200 nm, the 388-nm emission band with an extrinsic characteristic was strongly observed, while the electronic state calculation of Eu^{2+} site in BAM:Eu suggested a possible contribution of the mid-oxygen sites in BAM:Eu [4,5] to this 200-nm structure. Therefore, in addition to the mO site, the present results indicate that some kind of defects or impurities also contribute to the 200-nm structure.

[1] N. Iyi, Z. Inoue and S. Kimura, J. Solid State Chem. **61** (1986) 236.

[2] K. C. Mishra, M. Raukas, A. Ellens and K. H. Jhonson, J. Lumin. **96** (2002) 95.

[3] M. Stephan, P.C.schmidt, K.C. Mishra, MRaukas, A. Ellens and P. Boolchand, Z. Phys. Chem. **215** (2001) 1397.

[4] H. Toyoshima, S. Watanabe, k. Ogasawara and H. Yoshida, J. Lumin. **122-123** (2007) 104.

[5] H. Yoshida, T. Yamazaki, H. Toyoshima, S. Watanabe, K. Ogasawara and H. Yamamoto, J. Electrochem. Soc., submitted.

[6] B. Howe and A.L. Diaz, J. Lumin. **109** (2004) 51.

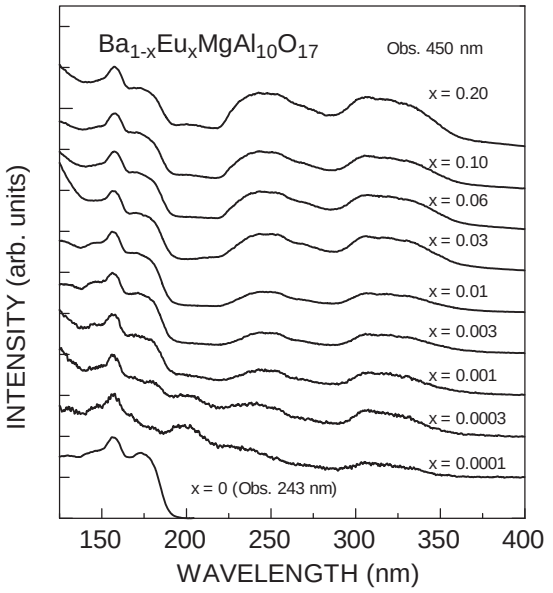

Fig. 1 Excitation spectra of $Ba_{1-x}Eu_xMgAl_{10}O_{17}$ (x = 0.0001, 0.0003, 0.001, 0.003, 0.01, 0.03, 0.06, 0.1, 0.2) observed at 450-nm emission band. As reference, an excitation spectrum of the 243-nm emission in x = 0 is also shown.

BL1B

Excitation Energy Transfer in CeF_3 Crystals Heavily Doped with Sr^{2+} Ions

Y. Tani, T. Katagiri, D. Iri, M. Itoh, M. Fujita[1], A. Yoshikawa[2], K. Aoki[3]
Department of Electrical and Electronic Engineering, Shinshu University, Nagano 380-8553
[1]Japan Coast Guard Academy, Kure 737-8512
[2]Institute of Multidiscriplinary Research for Advanced Materials, Tohoku University, Sendai 980-8577
[3]Stella Chemifa Corporation, 1-41 Rinkai-cho, Izumiootsu, Osaka 595-0075

Among single-component fluorides such as BaF_2, CaF_2, CeF_3, etc., CeF_3 is one of the most commonly used crystalline scintillating materials with fast decaying luminescence. In the present paper, excitation energy transfer in CeF_3 crystals doped with Sr^{2+} ions is discussed.

Experiment

CeF_3 single crystals heavily doped with Sr^{2+} ions (3 mol%) were grown by the micro-pulling-down (μ-PD) method [1]. Three dimensional emission (λ_{em})-excitation (λ_{ex}) spectra were measured using a SpectraPro-300i monochromator equipped with an LN/CCD camera. The decay kinetics of luminescence was detected by an MCP with use of a time-correlated single-photon counting technique when the UVSOR storage ring was operating in single-bunch mode (pulse width: 1.3 ns; pulse interval: 177.6 ns).

Results and Discussion

Figure 1 shows the contour plots of emission-excitation spectra of CeF_3:Sr at (a) 8 K and (b) 300 K. In Fig. 1(a) an emission band peaking around 330 nm is excited with UV light at $\lambda_{ex} < 290$ nm. This band somewhat red-shifts relative to the Ce^{3+} 5d → 4f luminescence (287 and 304 nm) in pure CeF_3. The excitation threshold (290 nm) is also lowered as compared to that (260 nm) for the intrinsic Ce^{3+} luminescence. These facts suggest that the 330 nm band is ascribed to Ce^{3+} ions perturbed by nearby Sr^{2+} ions. The intrinsic Ce^{3+} luminescence locating on the short-wavelength side of the main band at 330 nm is very weak in intensity due to heavy doping.

In Fig. 1(b) an emission band appears at around 400 nm at the expense of the 330 nm band. The 400 nm band, which is excited at $\lambda_{ex} < 295$ nm, is probably attributed to some defect that was introduced by Sr^{2+} doping. Therefore, it is supposed that excitation energy is efficiently transferred from Ce^{3+} sites to defect sites when the CeF_3:Sr crystal is warmed from 8 to 300 K.

Figure 2 shows the decay behaviors of (a) the 330 nm luminescence at 8 K and (b) the 400 nm luminescence at 300 K, both being excited at $\lambda_{ex} = 266$ nm. The two bands exhibit a single exponetial decay over two decades. The decay times of the 330 and 400 nm bands are 26 and 40 ns, respectively. These values are comparable with the decay time (17 ns at 8 K) of the intrinsic Ce^{3+} luminescence.

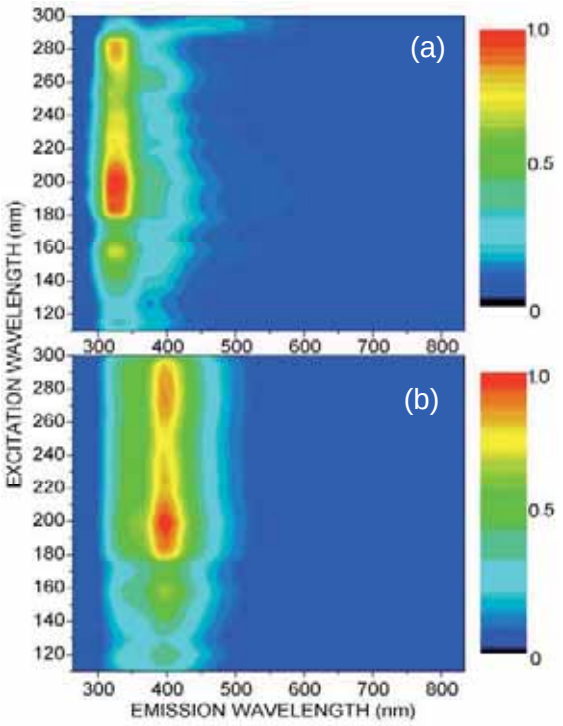

Fig. 1. Contour plots of the emission-excitation spectra of CeF_3:Sr at (a) 8 K and (b) 300 K.

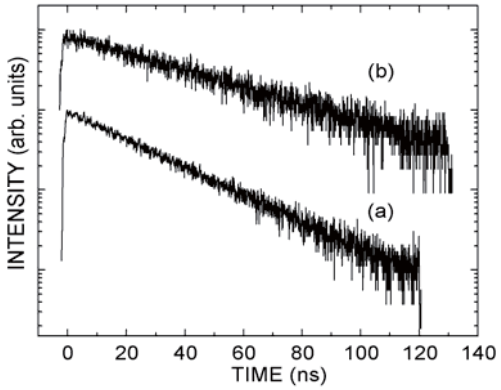

Fig. 2. Decay curves of (a) the 330 nm luminescence at 8 K and (b) the 400 nm luminescence at 300 K.

[1] A. Yoshikawa, et al.: J. Cryst. Growth **270** (2004) 427.

BL1B

Energy Transfer to Pr^{3+} Ions in LuAG:Pr Crystals

T. Katagiri, D. Iri, M. Itoh, M. Fujita[1], A. Yoshikawa[2], H. Ogino[2], K. Kamada[2]

Department of Electrical and Electronic Engineering, Shinshu University, Nagano 380-8553
[1]Japan Coast Guard Academy, Kure 737-8512
[2]Institute of Multidiscriplinary Research for Advanced Materials, Tohoku University, Sendai 980-8577

In the last decade, $Lu_3Al_5O_{12}$ (LuAG) garnet doped with rare-earth ions attracts much attention as an effective scintillating material. Pr^{3+}-doped $Lu_3Al_5O_{12}$ is a newly-grown crystal in the LuAG family. Therefore, a search for its luminescence properties is very interesting. In this work, we have investigated three dimensional (3-D) emission-excitation spectra and luminescence decay kinetics of LuAG:Pr crystals.

Experiment

Single crystals of LuAG:Pr (0.3 mol%) were grown by the micro-pulling-down (μ-PD) method [1]. The 3-D emission (λ_{em})-excitation (λ_{ex}) spectra were measured by using an Acton SpectraPro-300i monochromator equipped with a camera (Roper Scientific LN/CCD-100EB-GI). Luminescence decay kinetics was detected by an MCP (Hamamatsu R3809U-52) with use of a time-correlated single-photon counting technique under the single-bunch operation of the UVSOR ring (duration: 1.3 ns; interval: 177.6 ns).

Results and Discussion

Figure 1 shows the 3-D spectrum of LuAG:Pr at 8 K. Three broad emission bands are observed at 260, 310 and 370 nm. The 260 nm band is the intrinsic luminescence of LuAG, because it is excited with UV light above the fundamental absorption edge (λ_{ex} < 172 nm). The 310 and 370 nm bands are ascribed to the 5d → 4f transitions of Pr^{3+} ions. In the region at λ_{em} > 400 nm, several weak emission lines are seen and attributed to the 4f → 4f transitions of Pr^{3+} ions.

The decay behaviors of the 310 nm luminescence excited at 280 and 170 nm are shown in Figs. 2(a) and 2(b), respectively. Under the direct 4f → 5d excitaion of Pr^{3+} ions (a), the emission intensity decays single-exponentially over two orders of magnitude, with a lifetime of 18.4 ns. When the host crystal is photoexcited (b), two remarkable changes take place in the decay kinetics. One is that a rise componet appears in the initial stage at t = 0, as seen from the insets of Fig. 2. The other is that a piled-up component apparently increases in intensity.

The above facts strongly suggest that there are two kinds of energy transfer mechanisms from the host LuAG crystal to the Pr^{3+} ions; a fast process with a transfer time τ_T of nanoseconds or less and a slow process with τ_T > 1 μs. These transfer processes are not so sensitive to the temperature, because the decay behaviors at 300 K are almost the same as Fig. 2.

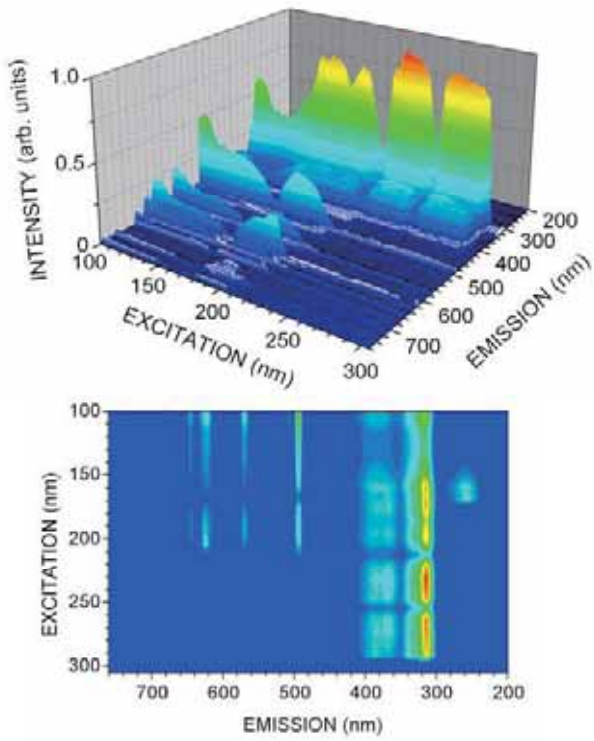

Fig. 1. 3-D emission-excitation spectrum of LuAG:Pr at 8 K, together with the contour plot of the upper spectrum in the (λ_{em}, λ_{ex}) plane.

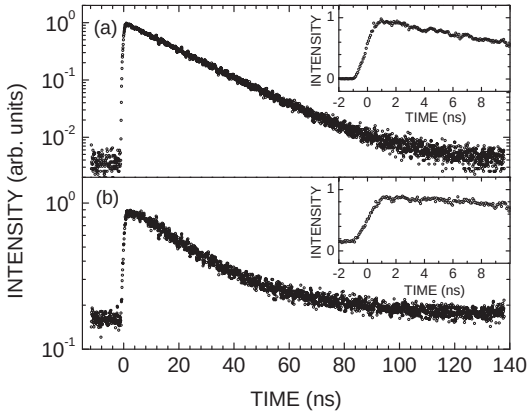

Fig. 2. Decay behaviors of the 310 nm luminescence of LuAG:Pr excited at (a) 280 and (b) 170 nm at 8 K.

[1] H. Ogino, A. Yoshikawa, et al., J. Cryst. Growth **287** (2006) 335.

Luminescence Properties of Heavily Doped CsI:Tl$^+$ Crystals

T. Kawai[1], T. Hirai[2], N. Ohno[2,3]

[1]*Graduate School of Science, Osaka Prefecture University, Sakai 590-0035, Japan*
[2]*Academic Frontier Promotion Center, Osaka Electro-Communication University*
[3]*Graduate School of Engineering, Osaka Electro-Communication University, Neyagawa 572-8530, Japan*

CsI crystals doped with Tl^+ ions exhibit complicated luminescence properties in the different way from the Tl^+ centers doped in NaCl-type alkali halides. The two UV bands are attributed to intra transition of the Tl^+ ion. The two visible-light bands are considered to originate from the Tl^+ perturbed self-trapped excitons [1]. In order to determine the characteristics of the complicated luminescence and their origin, the luminescence properties of CsI:Tl^+ crystals with various Tl^+ concentrations have been studied [2]. In the present study, we have investigated luminescence properties of the heavily doped CsI:Tl^+ crystals in order to clarify an influence of the Tl^+ concentration on the luminescence characteristics.

Single crystals of the heavily doped CsI:Tl^+ were grown from a starting material with the concentration of 1.0 mol% TlI by Bridgmann method. Luminescence and excitation spectra of the CsI:Tl^+ crystals were measured at the BL-1B beam line of UVSOR.

Figure 1 shows the luminescence spectra of the heavily doped CsI:Tl^+ crystal at 10K under the excitation on 4.30 and 4.00 eV. Under the excitation on 4.30 eV, which corresponds to the peak energy of the A absorption band of CsI:Tl^+, the luminescence bands are observed around 2.21, 2.52, and 3.05 eV. The bands are the same ones of the CsI:Tl^+ crystals with the concentration of less than 10^{-3}mol%. When the concentration of the Tl^+ ions is 1.0 mol%, the absorption intensity around the energy region below 4.30 eV increases remarkably. In the heavily doped CsI:Tl^+ crystal, the 4.00 eV excitation causes the new luminescence bands peaking at 2.05, 2.31 and 2.73 eV.

Figure 2 shows the excitation spectra 2.03 and 2.25 eV of the heavily doped CsI:Tl^+ crystal. The excitation spectrum for 2.25 eV is similar to that of the CsI:Tl^+ crystals with the concentration of less than 10^{-3}mol%. On the other hand, the excitation spectrum for 2.03 eV exhibits the strong response at 4.10 eV, which corresponds to the energy region below the A absorption band.

In general, as the concentration of the Tl^+ ions increases beyond 10^{-2} mol%, aggregate centers such as dimer are created [3]. The absorption bands due to the aggregate centers are observed in the energy region below the A absorption band. Since the 2.05 eV luminescence band in the heavily doped CsI:Tl^+ crystal has the strong response in the lower energy region than the A band, the 2.05 eV band should be attributed to the aggregate centers of the Tl^+ ions. The aggregate centers would exhibit the different characteristics of the luminescence from the isolated Tl^+ centers.

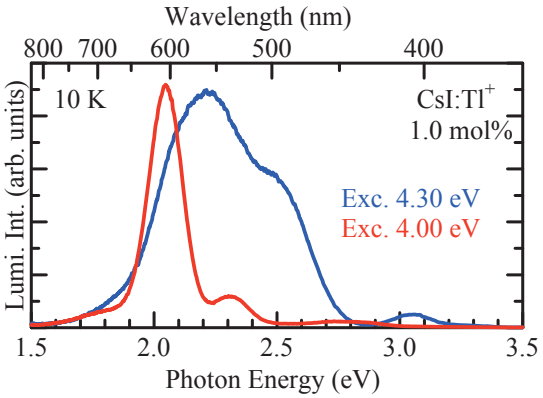

Fig. 1. Luminescence spectra of the heavily doped CsI:Tl^+ crystal under the excitation on 4.00 eV (red curve) and 4.30 eV (blue curve).

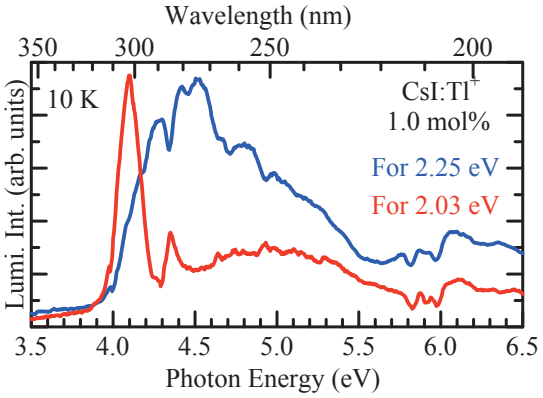

Fig. 2. Excitation spectra for 2.03 eV (red curve) and 2.25 eV (blue curve) of the heavily doped CsI:Tl^+ crystal.

[1] V. Nagirnyi, S. Zazubovich, V. Zepelin, M. Nikl and G. P. Pazzi, Chem. Phys. Lett. **227** (1994) 533.
[2] V. Babin, A. Krasnikov, H. Wieczorek and S. Zazubovich, Nucl. Instr. and Meth. in Phys. Res. A **486** (2002) 486.
[3] T.Tsuboi and P.W.M.Jacobs, J. Phys. Chem. Solids **52** (1991) 69.

BL1B

Luminescence Properties of $YPO_4:Bi^{3+}$

N. Ohno, T. Hirai

Academic Frontier Promotion Center,
Osaka Electro-Communication University, Neyagawa, Osaka 572-8530, Japan

Metal ions with s^2 electronic configurations doped in wide-gap materials such as alkali halides, which are called Tl^+-type ions, show several strong absorption bands due to $s^2 \rightarrow sp$ transitions. Since these optical transitions are dipole-allowed, the absorption is expected to be much stronger than that due to the dipole-forbidden *f-f* transitions in rare-earth ions.

Xe dimer (Xe_2) discharge fluorescent lamp is one of the candidates for alternative lighting sources to a conventional Hg discharge fluorescent lamp. New phosphors suitable for the conversion of vacuum ultraviolet (VUV) light into visible light are quite desired at present. In the Xe_2 discharge florescent lamps, phosphors are excited by VUV light of 7.2 and 8.4 eV. Most fluoride and phosphate hosts are transparent up to ~ 10 eV, so that the VUV light can directly excite impurity activators in these hosts. The strong absorption would give efficient conversion of the VUV light from the Xe_2 discharge fluorescent lamps.

In the present study, luminescence properties of trivalent Tl^+-type Bi^{3+} centers in phosphate and fluoride hosts have been studied in the UV and VUV region. The $YPO_4:Bi^{3+}$ and $YF_3:Bi^{3+}$ phosphors were prepared by amounts of the appropriate starting compound powders of YPO_4 and YF_3 adding BiF_3 (~ 2 mol %), mixing and firing in a carbon crucible at 900ºC in argon atmosphere. Impurity Bi^{3+} ions would be expected to be substituted for Y^{3+} ions in the host lattices.

Figure 1 shows luminescence (blue curve) and photo-excitation (red curve) spectra of $YPO_4:Bi^{3+}$ measured at room temperature. Luminescence peaks located at 3.1 eV and 3.6 eV and a small hump at 4.9 eV are observed for the excitation of VUV light at 7.8 eV. The 3.1 and 3.6 eV luminescence is excited with photons of 5.4 eV and the luminescence energies of Xe discharge lamp in the VUV region. These excitation peaks are located at lower energies than the absorption edge of the host YPO_4 (~ 12 eV). Therefore, the observed luminescence bands of $YPO_4:Bi^{3+}$ would be responsible for intra-ionic transitions in impurity Bi^{3+} ions.

Tl^+-type ions doped in alkali-halide crystals with a high symmetry crystal structure exhibit three characteristic absorption bands arising from the $s^2 \rightarrow sp$ transitions, namely, A, B and C bands [1]. These absorption bands have been attributed to the optical transition from the $^1S_0$ ground state to $^3P_1$, $^3P_2$, and $^1P_1$ excited states, respectively. Kang *et al*. have reported that the A and C bands appear at 3.7 and ~ 6.0 eV, respectively, in the absorption spectrum of $KCl:Bi^{3+}$ at low temperatures [2].

In Bi^{3+} ions doped in phosphate and fluoride hosts, the absorption bands would shift to the higher energy side, as compared to those in chloride hosts. In $YPO_4:Bi^{3+}$ crystals, the excitation band appearing at 5.4 eV is tentatively assigned as the A band nature due to $^1S_0 \rightarrow {}^3P_1$ transition in Bi^{3+} ions. The excitation bands at 6.5–10 eV show composite structures, which is a common feature of the C band of Tl^+-type ions. Therefore, these structures in the VUV region is ascribed to the C band origin ascribed to $^1S_0 \rightarrow {}^1P_1$ transitions in Bi^{3+} ions.

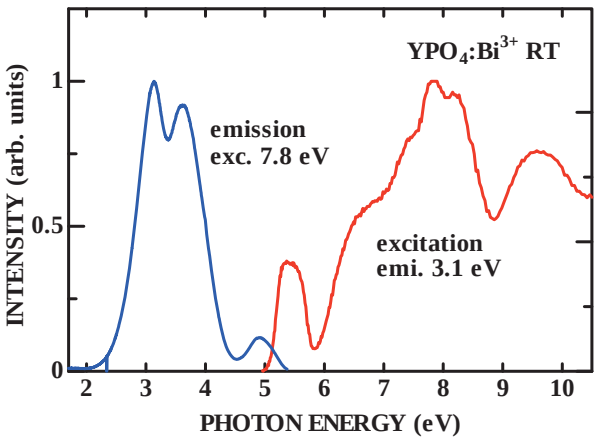

Fig. 1. Luminescence (blue curve) and excitation (red curve) spectra of $YPO_4:Bi^{3+}$ at room temperature.

[1] W.B. Fowler, *Physics of Color Centers,* Academic Press Inc., New York, 1968.
[2] J.G. Kang, H.M. Yoon, G.M. Chun, Y.D. Kim and T. Tsuboi, J. Phys.: Condens. Matter **6** (1994) 2101.

BL1B

Photoluminescence of Hydroxyapatite Irradiated by Ultraviolet Synchrotron Orbital Radiation Light (3)

M. Ohta

Department of Material Science and Technology, Faculty of Engineering, Niigata University, 8050 Ikarashi 2-no-cho, Niigata 950-2181, Japan

It was known that rare earth ions dosed for oral administration to mouse and rat are transferred to blood vessel through the ileum and deposited its teeth and bone, which mainly consists of hydroxyapatite ($Ca_{10}(PO_4)_6(OH)_2$) [1-2]. Recently, rare earth is also useful as a contrast medium for magnetic resonance imaging, restriction enzyme, biocatalyst, and so on in fields of biochemistry, physiology, medicine, etc. However, the behavior of rare earth in the living body system remains an open question until now. We have found that Eu ion substituted Ba ion in Eu doped $Ba_{10}(PO_4)_6Cl_2$ phosphor, which matrix is apatite structure[3]. The rare earth ion is also found to substitute easily for calcium ion in hydroxyapatite which is soaked in rare earth chloride aqueous solution, and to play on emission center.

In this study, hydroxyapatite samples doped with rare earth phosphate were prepared in order to apply to phosphor. Their characteristics were investigated by photoluminescent property of rare earth ion-doped hydoxyapatite samples excited by ultraviolet synchrotron orbital radiation light.

Eu-doped hydroxyapatite and Gd-doped hydroxyapatite samples were prepared as follows: hydroxyapatite was added with $EuPO_4$ or $GdPO_4$ and mixed homogeneously, and then heated at 1373K for 1 hr. $EuPO_4$ or $GdPO_4$ was prepared by reaction of $GdCl_3$ or $YbCl_3$ and $Na_3PO_4 \cdot 12H_2O$ and then fired at 1373K for 1 hr. $GdCl_3$ or $YbCl_3$ was prepared by reaction of Eu_2O_3 or Gd_2O_3 and HCl.

The photoluminescent property of each sample exited by ultraviolet synchrotron orbital radiation light (BL-1B) was detected by using with a multi-channel analyzer.

Figure 1 shows photoluminescence spectra of rare earth ion-doped hydroxyapatite samples excited by BL-1B.

The data of X-ray powder diffraction indicated that the rare earth ion substituted for calcium ion in hydroxyapatite.

Figure 1 shows the photoluminescent spectra of rare earth ion-doped hydroxyapatite samples excited by ultraviolet synchrotron orbital radiation light. In Eu ion-doped sample, 4 peaks due to $^5D_0 \rightarrow {}^7F_1$ (595nm), $^5D_0 \rightarrow {}^7F_2$ (612nm), $^5D_0 \rightarrow {}^7F_3$ (654nm), and $^5D_0 \rightarrow {}^7F_4$ (700nm) of Eu^{3+}, and 3 broad peaks (at near 330nm, 430nm and 580nm) due to hydroxyapatite matrix. The emission intensity of Eu^{3+} ion was very weak.

In Gd ion-doped sample, a peak due to $^6P_{7/2} \rightarrow {}^8S$ (320nm) and 3 broad peaks (at near 330nm, 430nm and 580nm) due to hydroxyapatite matrix.

[1] S. Hirano, K. T. Suzuki, Environ. Health Perspect. **104** (Supplement 1) (1996) 85.
[2] K. Kostial, B. Kargacin, M. Lendeka, Int. J. Radiat. Biol. Relat. Stud. Phys. Chem. Med. **51** (1987) 139.
[3] M. Sato, T. Tanaka, M. Ohta, J. Electrochem. Soc.,**141** (1994) 1851.

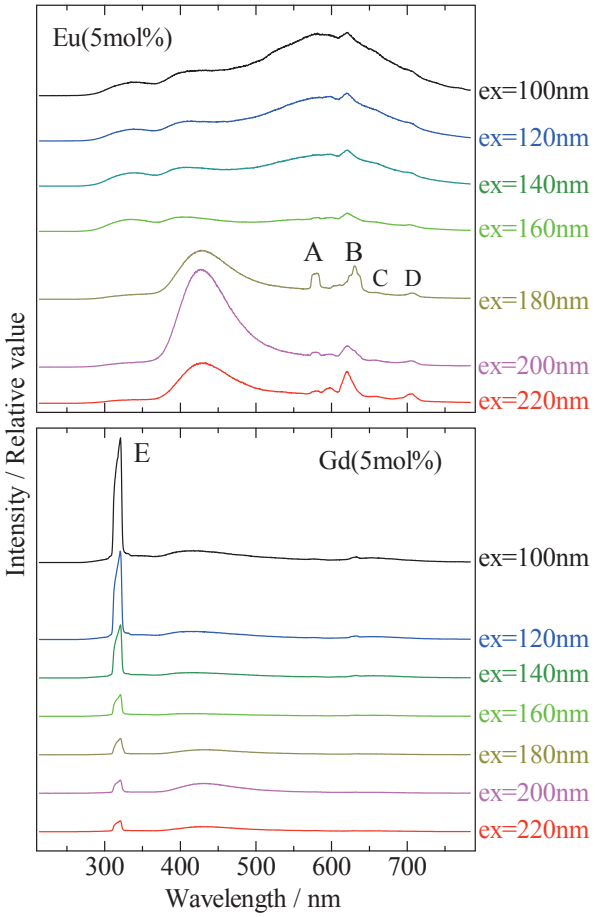

Fig. 1 Photoluminescent spectra of rare earth ion-doped hydroxyapatite samples excited by ultraviolet synchrotron orbital radiation light.

Eu^{3+}:

A: $^5D_0 \rightarrow {}^7F_1$, B: $^5D_0 \rightarrow {}^7F_2$

C: $^5D_0 \rightarrow {}^7F_3$, D: $^5D_0 \rightarrow {}^7F_4$

Gd^{3+}:

E: $^6P_{7/2} \rightarrow {}^8S$

BL1B

Temperature Dependence of Absorption Spectra for Pr^{3+} in $LiYF_4$

S. Watanabe[1], H. Kai[1], H. Yoshida[1,2], K. Ogasawara[1]

[1]*Department of Chemistry, Kwansei Gakuin University, 2-1 Gakuen, Sanda 669-1337 Japan*

[2]*Research and Development Division, NEC Lighting, Ltd., 3-1 Nichiden, Minakuchi-cho, koka, 528-8501, Japan*

The trivalent or divalent lanthanides in crystals and glasses have drawn attentions due to their application for luminescent materials in UV and VUV regions such as tunable solid-state lasers or phosphors. In those materials, transitions between the multiplet energy levels were used. In case of trivalent praseodymium ion (Pr^{3+}) in various host crystals, the $4f^2$-$4f^15d^1$ transitions lie in UV and VUV regions. Therefore, Pr^{3+} in host crystals or glasses hold the promise of good luminescent materials in UV or VUV regions.

The excitation spectrum for Pr^{3+} in $LiYF_4$ was reported by Pieterson et al [1]. They measured the excitation spectrum at 6 K using the DESY synchrotron facility. According to their report, 3 main peaks and 2 sub-peaks were observed in the excitation spectrum.

In this report, we have investigated the temperature dependence of absorption spectra for Pr^{3+} in $LiYF_4$. And we also analyzed the spectra based on the first-principles calculation for multiplet energy and absorption spectrum using the 4-component relativistic configuration interaction (CI) method [2]. This calculation method has been successfully applied to calculation of the multiplet energy levels and optical absorption spectrum between multiples for impurity ions in host crystals [3]. By measurements of the absorption spectrum at low temperature, we could directly compare the theoretical absorption spectrum to that obtained by the first-principles calculation. Therefore, the combination of measurements of the absorption spectrum at low temperature and first-principles calculations is very effective procedure for analysis of optical properties.

The $LiYF_4$ single crystal doped with Pr^{3+} were grown by Bridgeman-Stockbarger method. The concentration of Pr^{3+} ion in the sample was 0.3 mol%.

Fig. 1 shows the temperature dependence of absorption spectra for Pr^{3+} in $LiYF_4$. The absorption spectra were measured at 10, 50, 100, 150, 200 and 300 K. The 3 main peaks, A, B, C, were observed in each spectrum at 5.8, 6.7 and 7.6 eV. The first-principles relativistic CI calculation indicates that the splitting of those 3 peaks A, B, C is due to the crystal field splitting of Pr-5*d* levels. On the other hand, the 2 sub-peaks, A', B', were observed in spectrum at 10, 50, 100 and 150 K at about 6.0 and 7.2 eV. The first-principles relativistic calculation indicates that the splitting between peak A and A' and that between peak B and B' are due to the spin-orbit interaction of Pr-4*f* levels. These splittings are observed only in the spectra measured at low temperature measurements. We should point out that observation of peaks A' and B' originating form spin-orbit interaction also significantly depend on the Pr^{3+} concentration.

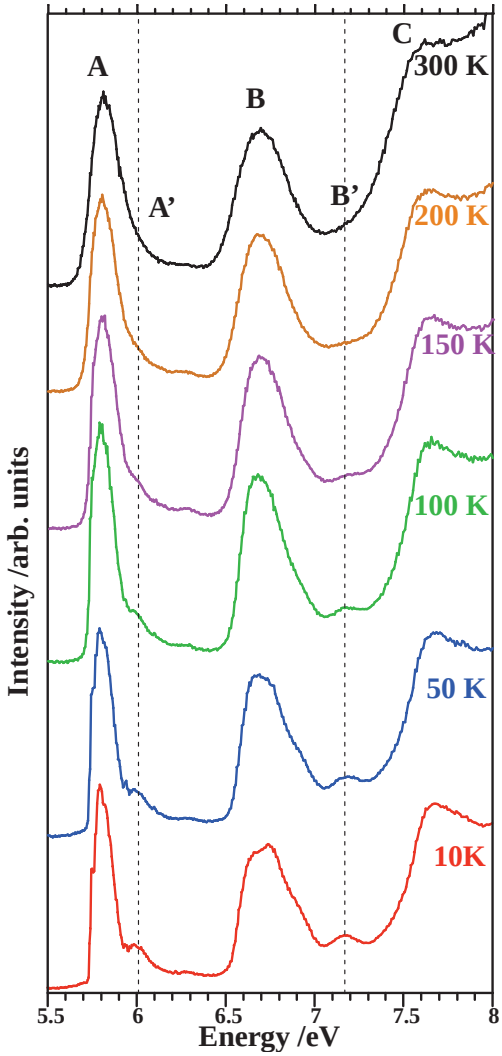

Fig. 1 The temperature dependence of absorption spectra for Pr^{3+} in $LiYF_4$. The concentration of Pr^{3+} ion is 0.3 mol%.

[1] L. van Pieterson, M. F. Reid, R. T. Wegh, S. Soverna and A. Meijerink, Phys. Rev. **B65** (2002) 045113.

[2] K. Ogasawara, T. Iwata, Y. Koyama, T. Ishii, I. Tanaka and H. Adachi, Phys. Rev. **B64** (2001) 143.

[3] K. Ogasawara, S. Watanabe, H. Toyoshima, T. Ishii, M. G. Brik, H. Ikeno and I Tanaka, J. Sol.Stat.Chem. **178** (2005) 412

BL1B

Optical Spectroscopy of Ce-doped Oxides

Y. Ohsumi, M. Yoshida, T. Hasegawa, M. Yamaga,
Faculty of Engineering, Gifu University, Gifu 501-1193 Japan

Ce^{3+}-doped crystals are attractive for applications to lasers, scintillators, and phosphors. The 4f ↔ 5d transitions of Ce^{3+} are parity- and spin-allowed so that the transition probabilities are very large. The lifetimes of Ce^{3+} in crystals are in the range of 10-60 ns [1-3]. Recently, Lu_2SiO_5 (LSO) doped with Ce^{3+} was developed as a new scintillator with high conversion efficiency from high energy to visible light. However, when there are deficits in the crystal, the emission efficiency is degraded. In addition, the afterglow is observed. This report describes optical spectra of LSO and $CaYAl_3O_7$ (CYAM) single crystals doped with Ce^{3+}, which were grown using the Czochralski method.

Figure 1 shows the vacuum ultraviolet (VUV) and UV absorption/excitation and visible fluorescence spectra in CYAM:Ce^{3+} and LSO:Ce^{3+} crystals. The optical absorption spectra of Ce^{3+} consist of five broadbands due to the transitions from the 4f ground state to the five 5d excited states. However, the absorption spectra could not be resolved because of strong absorption coefficient. Although CYAM and LSO have different crystal structure, the peak wavelengths of the fluorescence bands are about 440 nm. These fluorescence spectra have large Stokes shift. On the other hand, both excitation spectra consist of two groups: one is in the range of 200-400 nm and the other is in the range of 100-200 nm. The former corresponds to the five absorption bands of Ce^{3+}, whereas the latter may be due to band-to-band transitions with band edges around 200 nm.

The decay curves of the Ce^{3+} fluorescence in CYAM and LSO fit single exponential curves with lifetimes of about 40 ns. However, the fluorescence spectra have background intensities, which are drastically enhanced with an increase of temperature. This is called as afterglow.

Figure 2 shows the decay curve of the long-lasting phosphorescence in CYAM:Ce^{3+} at 300 K in the time range of 1-300 s in log-log scales. The decay curve does not fit a single exponential curve, but a function of t^{-n} ($n \approx 1$). In order to examine a radiative process of the phosphorescence, it is very useful to measure the excitation spectra of the phosphorescence in the VUV region. The excitation spectra for CYAM and LSO have peaks around 200 nm as the same as those of the fluorescence in Fig.1. The wavelength of 200 nm in Fig. 1 is corresponding to the band edge energy. This result suggests that electron-hole pairs produced by VUV/UV light are trapped at deficits in the crystals, such as color centers, and recombine radiatively when temperature is elevated up to room temperature.

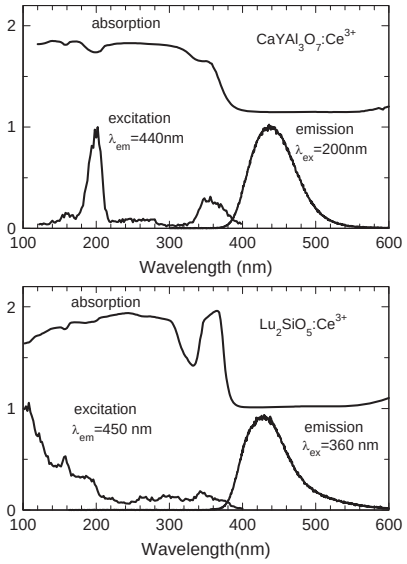

Fig. 1. Absorption, excitation and emission spectra in $CaYAl_3O_7:Ce^{3+}$ and $Lu_2SiO_5:Ce^{3+}$ measured at 17K.

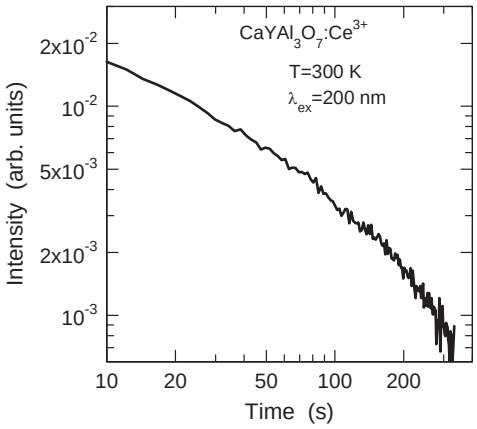

Fig. 2. Decay curve of the phosphorescence in $CaYAl_3O_7:Ce^{3+}$ measured at 300 K.

[1] E. Hayashi, K. Ito, S. Yabashi, M. Yamaga, N. Kodama, S. Ono, N. Sarukura, J. Lumin. **119-120** (2006) 67.
[2] E. Hayashi, K. Ito, S. Yabashi, M. Yamaga, N. Kodama, S. Ono, N. Sarukura, J. Alloys and Compounds **408-412** (2006) 883.
[3] M. Yamaga, E. Hayashi, N. Kodama, K. Itoh, S. Yabashi, Y. Masui, S. Ono, N. Sarukura, T.P.J. Han, H.G. Gallagher, J. Phys. Condens. Matter **18** (2006) 6033.

BL4B, BL1A

Excitation Energy Dependence of Time Resolved Decay Curves in AlGaN Alloys

T.Sakai[1], S.Suzuki[1], N.Nakagawa[1], K.Fukui[1], S.Naoe[2], H.Miyake[3], K.Hiramatsu[3]
[1]*Research Center for Development of Far-Infrared Region, University of Fukui, Fukui910-8507, Japan*
[2]*Faculty of Engineering, Kanazawa University, Kanazawa 920-1192, Japan*
[3]*Faculty of Engineering, Mie University, Mie 514-8507, Japan*

The III-V nitride semiconductors are promising materials for visible-UV opto electronic devices, such as LEDs, LDs and photo detectors. To expand the operation wavelength of LEDs and LDs into ultraviolet (UV) regions, research efforts are being made for the growth of device quality AlGaN alloys, since their band gaps spread from 3.39eV (GaN) to 6.2 eV (AlN). However, investigations into the mechanisms of near band-edge photoluminescence (PL) in AlGaN alloys are also hardly adequate. We have been measuring PL, photoluminescence excitation (PLE) and time resolved decay (TRD) curves at the excitation energy of not only near band-gap but also high photon energy up to 1.5 keV to investigate the effects of both core electron excitation and multi-electron excitation. Since all of TRD curves can be fitted as the sum of three different single exponential components (fast, middle and slow components in the order corresponding to their lifetime), we have been considering that three components suggest the existence of three energetically adjacent decay processes. In this report, we present TRD curves and their excitation energy dependence from 30 eV to 1 keV.

$Al_xGa_{1-x}N$ (x=0.34 - 0.76) samples have been made by MOVPE method at Mie University. The thicknesses of AlGaN thin films are about 1μm on 1μm AlN single crystal films with Al_2O_3 substrates. The measurement was performed in BL4B at the time of single bunch operation. A conventional 30cm VIS-UV monochromator with liquid N_2 cooled CCD detector is used for PL measurements of all samples.

Figure 1 shows time integrated PL intensity ratios among three decay components of $Al_{0.76}Ga_{0.24}N$. Measurement temperature is 9.9 K and excitation photon energy is 85 eV. The vertical line at 5.27 eV indicates the PL peak position. Below this photon energy, the contribution of LO phonon replica bands becomes dominant relative to the main PL band. It is clear that slow component is dominant and stable in the replica band region, in other words, decay process of LO phonon replicas mainly consists of slow component. However, in the main band region, intensity ratios are continuously shifted. This probably reflects inhomogeneity of cation distribution. These behaviors are similar to those results under near band-edge excitation.

Figure 2 shows TRD curves of $Al_{0.76}Ga_{0.24}N$ at various excitation energies. Measurement temperature is 9.9 K and emission photon energy is 5.27 eV. The contribution of fast component which is shown in fig. 2 as a sharp peak at 2 ns becomes large with increasing excitation photon energy. This tendency is also observed near 1.5 keV excitation. Even though the contribution of fast component becomes large, this contribution smoothly depends on the excitation photon energy and shows no drastic changes between below and above core levels. It is probably indicated that the main effect of the high energy excitation photons is multi electron-hole pair creation effect.

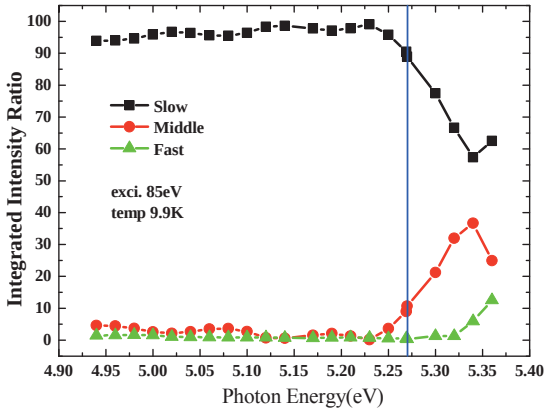

Fig. 1 Integrated intensity ratio of $Al_{0.76}Ga_{0.24}N$ at 9.9K

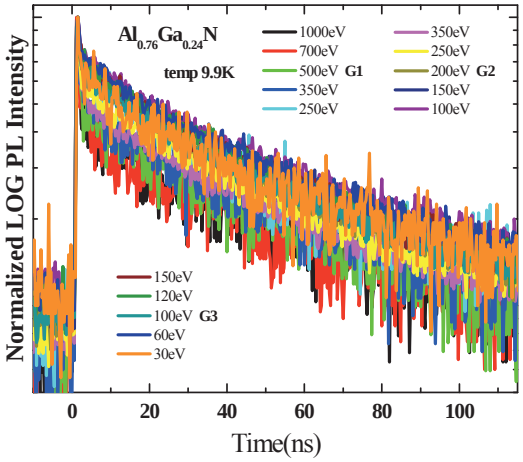

Fig.2 Time resolved decay curves of $Al_{0.76}Ga_{0.24}N$ at various excitation energies.

BL5B

Vacuum Ultraviolet Transmission Spectra of Substrate-Free Evaporated Amorphous Thin Films

K. Hayashi, K. Kimata

Department of Electrical and Electronic Engineering, Gifu University, Gifu 501-1193, Japan

Introduction

Amorphous semiconductor materials are very expected as a potential material for optoelectronic devices because these materials are very sensitive to the light and show a variety of photoinduced phenomena [1-3]. For the device application, it is necessary to sufficiently understand the physical property of these materials. Although a large number of studies have been done on the photoinduced phenomena of these materials, little is known about the details of these mechanisms. These phenomena were studied by exciting outer core electrons with the irradiation of light with the energy corresponding to the optical bandgap or sub-bandgap. The interest has been attracted for the change of the optical properties in the energy region of the visible light. We are interesting for the change of the optical properties in the higher energy region. To obtain a wide knowledge of the photoinduced phenomena, it is necessary to investigate to the photoinduced effects on wide energy region. In previous reports, we reported the photoinduced change at the VUV reflection spectra of the amorphous chalcogenide semiconductor films induced by bandgap light [4]. Recently, we measure the VUV transmission spectra of amorphous thin films prepared onto polymer membrane substrates [5]. In present work, we report the VUV transmission spectra of substrate-free evaporated amorphous thin films.

Until now, we have measured the transmission spectrum by using amorphous thin film which evaporated on the ultrathin polymer membrane substrate. However, there are some problems in this method. For example, the problems are effective decreases of the transmitted light intensity by the absorption of the polymer membrane and uncertainty of the thickness of the polymer membrane. The detection accuracy in the measurement becomes bad, when the transmitted light intensity decreases. And, it is not possible to obtain true transmission spectrum of the sample, when the thickness of polymer membrane can not be accurately measured. Then, we thought out the method for removing the polymer from the sample of the amorphous thin film which evaporated on the polymer membrane substrate.

Experimental

The ultrathin polymer membranes were prepared onto stainless steel metal plates in which two pinholes of the 1.0mm diameter opened. Thin films of amorphous chalcogenide semiconductor (a-As_2S_3 and a-As_2Se_3) were prepared onto the ultrathin polymer membranes by conventional evaporation technique. The removal of the polymer membrane tried two kinds of methods of a thermal method and a method by organic solvent. The measurement of the VUV transmission spectra were carried out at room temperature at the BL5B beam line of the UVSOR facility of the Institute for Molecular Science. And the spectrum was measured by using the silicon photodiode as a detector. To eliminate the higher order light from the monochromator, an aluminum thin film was inserted between the monochromator and sample.

Results and Discussion

Figure 1 shows the spectra of the incident light (without polymer) and the transmitted light of the polymer membrane (with polymer). As shown in the figure, the intensity of the incident light decreases under the half by the polymer membrane. Therefore, it seems to be possible to obtain the two times the signal intensity by removing the polymer membrane. Actually, it was possible to obtain the result along the expectation.

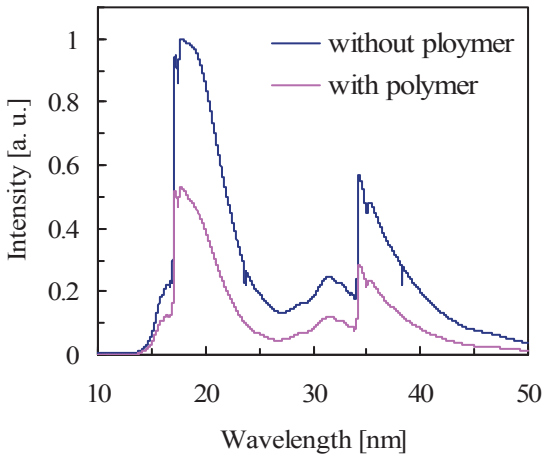

Fig. 1 Spectra of the incident light (without polymer) and the transmitted light of the polymer membrane (with polymer).

[1] Ke. Tanaka, Rev. Solid State Sci. **4** (1990) 641.
[2] K. Shimakawa, A.Kolobov, and S. R. Elliott, Adv. Phys., **44** (1995) 475.
[3] Ke. Tanaka, Encyclopedia of Nanoscience and Nanotechnology, **7** (2004) 629.
[4] K. Hayashi, UVSOR Activity Report **2001** (2002) 126.
[5] K. Hayashi, UVSOR Activity Report **2004** (2005) 79.

BL6B&7B

Optical Response of a New Type of $CaRh_2O_4$ & $NaRh_2O_4$

T.Iizuka, K.Iizuka,A.Irisawa, T.Nanba, [1]K.Yamaura
Kobe University, nada-ku, Kobe 657-8501, Japan
[1] National Research Institute for Metals, 1-2-1 Sengen, Tsukuba, 305-0047, Japan

Introduction

Recently, $CaRh_2O_4$ & $NaRh_2O_4$ have been newly synthesized by a high-pressure method in Tsukuba [1]. The oxides crystallize in a $CaFe_2O_4$-type structure. The recent electrical resistivity experiment revealed that at atmospheric pressure, $NaRh_2O_4$ exhibits a metallic property ($Rh^{3.5+}$;$Rh^{4+}(t_{2g}^5)$ and Rh^{3+} (t_{2g}^6)) but $CaRh_2O_4$ is an insulating and non-magnetic material (Rh^{3+};t_{2g}^6). Up to now, there exist no optical study except macroscopic studies such as specific heat and electrical resistivity. To study its fundamental electronic states close to the Fermi level at ambient pressure, we measured the temperature dependence of optical reflectivity spectra $R(\omega)$ of $NaRh_2O_4$ & $CaRh_2O_4$.

Experimental

The optical reflectivity spectra $R(\omega)$ at ambient pressure were measured in the wide photon energy range from 7 meV to 30 eV in the temperature range of 8-300 K. The measurements were performed using a Fourier-transform interferometer combined with a thermal light source and synchrotron radiation source at the beam line BL6B & 7B of UVSOR. The optical conductivity $\sigma_1(\omega)$and complex dielectric function $\varepsilon_1(\omega)$ were obtained from a standard Kramers-Kronig (K-K) transformation of the measured reflectivity(R) spectrum.

Results and Discussions

Fig.1 shows the temperature dependence of the R-spectra of $NaRh_2O_4$. The spectra in the low energy region exhibit a strong Drude component due to the free conduction electrons which grows with cooling. The peaks at 2.6, 6.0 and 15 and 20 eV from a visible to vacuum ultraviolet originate to the electronic interband transition.

Fig.2 shows the temperature dependence of the R-spectra of $CaRh_2O_4$.The whole spectra exhibits an insulating property. In the low energy part of the R-spectra, twelve distinct peaks were resolved which correspond to the phonon bands. They have a very weak temperature dependence. The structure in the higher energy region corresponds to the electronic interband transitions of which spectral profile is similar with $NaRh_2O_4$ but shows an additional fine structure superposed on the main peaks. Such fine structure might result from the super lattice structure due to the charge ordering states between $Rh^{4+}(t_{2g}^5)$ and Rh^{3+} (t_{2g}^6). The analysis is now on progress.

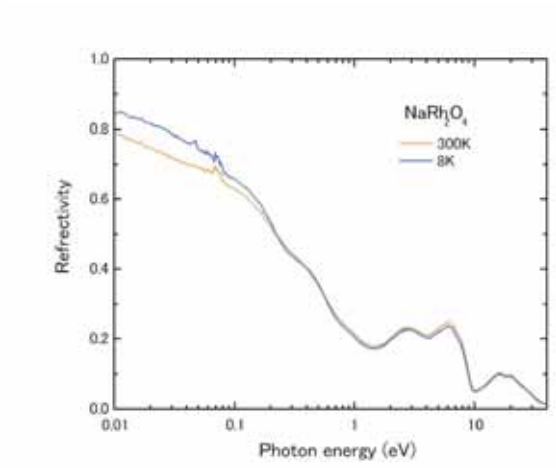

Fig.1 Temperature dependence of R-spectra of $NaRh_2O_4$ at 300 & 8 K.

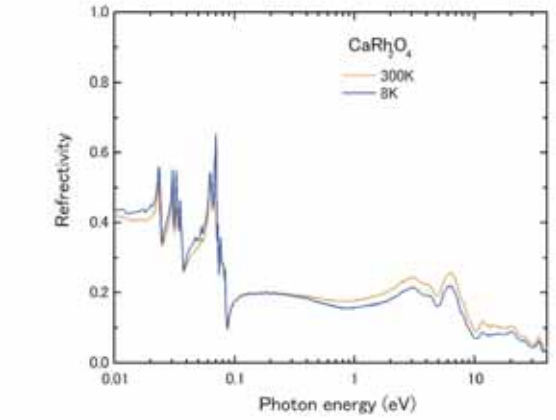

Fig.2 Temperature dependence of R-spectra of $CaRh_2O_4$ at 300 & 8 K.

[1] K.Yamaura *et al.,* Chem.Mater. **17** (2005) 359.

BL6B

Far-infrared Spectroscopy of Iodides Doped Silver Phosphate Superionic Conducting Glasses

T. Awano

Department of Electronic Engineering, Tohoku Gakuin University, Tagajo 985-8537, Japan

Enhancement of ionic conductivity by doping of PbI_2 in $AgPO_3$ glass was reported previously. Swenson et al. investigated mechanism of the enhancement on the PbI_2-$AgPO_3$ glass by diffraction measurements and reverse Monte Carlo simulation[1]. They explained the increase of ionic conductivity by that the doped Pb^{2+} substitute Ag^+ which was connected with non-bonding oxygen and the released Ag^+ contribute to ionic conduction.

The enhancement of ionic conductivity by metal iodide doping has also been reported on BiI_3, CdI_2 and other metal iodides[2]. The increase of ionic conductivity is proportional to dopant concentration and valence number of the metal ion. This abstract reports results of far-infrared spectra of high-density metal iodides doped silver phosphate glasses to investigate correlation effect of released silver ion on the enhancement of ionic conductivity, besides the above mentioned model.

Fig. 1 shows absorption spectra obtained by Kramers-Kronig analysis from the reflectivity spectra of $(AgI)_{0.5}(AgPO_3)_{0.5}$, $(BiI_3)_{0.03}(AgPO_3)_{0.97}$ and $(CdI_2)_{0.1}(AgPO_3)_{0.9}$ glasses. As previously reported, Ag-O vibration absorption in $AgPO_3$ glass is observed at 135cm^{-1}. In iodides doped glasses, it was observed at different position with different band strength. In $(CdI_2)_{0.1}(AgPO_3)_{0.9}$, the peak was at 128 cm^{-1} and shift slightly toward low wave number. In $(BiI_3)_{0.03}(AgPO_3)_{0.97}$, the strength is more than that in $(CdI_2)_{0.1}(AgPO_3)_{0.9}$ as shown in fig. 1. In $(AgI)_{0.5}(AgPO_3)_{0.5}$, the peak was at 115 cm^{-1} which is rather lower than that in $AgPO_3$.

In the above mentioned model of structural change of the glass, the number of the released silver ions is proportional to the dopant concentration and also the valence number of the doped metal ion. Therefore intensities of newly induced absorption band by Ag-I is expected to proportional to the product of the dopant concentration and the valence number. On the other hand, intensities of newly induced absorption band by Cd- or Bi-O is expected to proportional only to the dopant concentration. The intensity of Ag-O vibration should also decrease with the product of the dopant concentration and the valence number. The simulation curves in fig. 1 shows the sum of each Gaussian component of Ag-O, Ag-I and Cd- or Bi-O vibration, which are centered at 135, 100 and 165 cm^{-1}[3]. The intensity of each band is added or subtracted as above mentioned. Net absorption spectra by these component bands are shown by dashed lines in fig. 1. These simulation spectra well agree with the observed one.

The far-infrared spectral change showed the mechanism of the enhancement of ionic conductivity in iodides doped silver phosphate glasses. A doped metal ion substitutes a silver ion which is connected with a non-bonding oxygen. The released silver ion is coordinated weakly with an iodine ion and conducts easily. This mechanism is the same as that in PbI_2-$AgPO_3$ glass. The correlation effect seems to exist in lower wave number region.

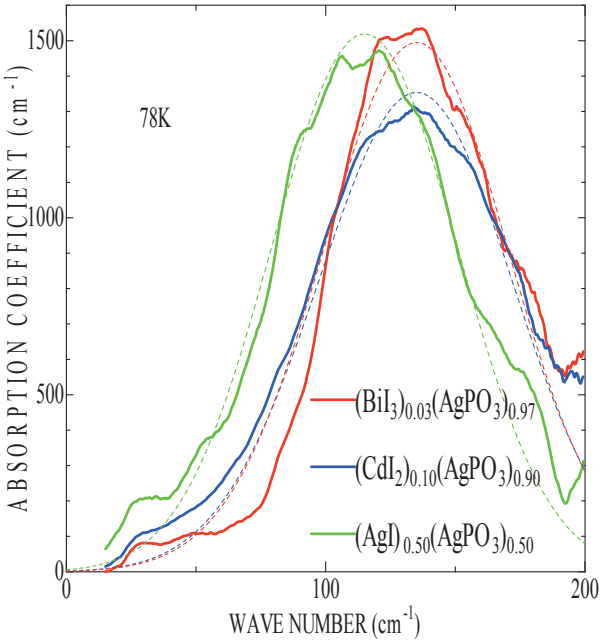

Fig. 1. Absorption spectra of iodides doped silver phosphate glasses. Absorption coefficients were obtained from reflectivity spectra by K-K transformation. Simulation curves (thin lines) by Gaussian components of Ag-I, Ag-O and Bi- or Cd-O vibration were drawn as described in the text.

[1] J. Swenson, A. Matic, C. Gejke, L. Boerjesson, W. S. Howells and M. J. Capitan, Phys. Rev. B **60** (1999) 12023.

[2] H. Takahashi, H. Nakanii and T. Sakuma, Solid State Ionics **176** (2005) 1067.

[3] B. N. Nelson and G. J. Exarhos, J. Chem. Phys. **71** (1979) 2739.

BL6B

Terahertz Spectroscopy of SmS under Pressures

T. Mizuno[1], S. Kimura[2,1], K. Matsubayashi[3], K. Imura[3], H.S. Suzuki[4], N.K. Sato[3]
[1]*School of Physical Sciences, The Graduate University for Advanced Studies (SOKENDAI), Okazaki 444-8585, Japan*
[2]*UVSOR Facility, Institute for Molecular Science, Okazaki 444-8585, Japan*
[3] *Department of Physics, Nagoya University Nagoya 464-8602, Japan*
4 National Institute for Materials Science, Tsukuba 305-0047, Japan

Introduction

SmS is a strongly correlated insulator (namely "black phase") with the gap size of 1000 K at ambient pressure.[1] Above about 0.7 GPa, the sample color changes to golden-yellow (golden phase) and the Sm-ion changes from the divalence to mixed valence.[2] To investigate the mechanism of the black-golden phase transition, we developed the terahertz (THz) reflection spectroscopic method under pressures and applied to this material.

Experimental

The THz reflection spectroscopy under pressures was performed at the THz microspectroscopy end station of BL6B. A membrane-type diamond anvil cell was employed to produce high pressures to samples. The pressure applied to samples is controlled by the helium gas pressure filled in the membrane. Since the areas of the culet plane of diamond and of the membrane are 1.13 mm^2 and 10^3 mm^2, respectively, the pressure of samples is about 10^3 times larger than the helium gas pressure. The sample with a typical size of 0.4×0.4×0.05 mm^3 was set in a diamond anvil cell with Apiezon-N grease as the pressure medium and with a gold film as a reference and ruby tips as for a pressure reference. The pressure was calibrated by a ruby fluorescence measurement.

Results and Discussion

The obtained reflectivity spectrum [$R(\omega)$] of SmS at 300 K as a function of pressure are shown by thick lines in Fig. 1(a). At the ambient pressure, the spectrum indicates the insulating character because the low energy limit does not approach to unity and a clear large peak due to the TO-phonon between Sm^{2+} and S^{2-} ions appears. When pressures were applied, the background intensity increases with increasing pressure. The background that originates from the Drude component indicates the existence of carriers. Therefore the carrier density increases with increasing pressure. The fitting curve of the combination of a Drude and a Lorentz functions is shown by thin solid lines in the same figure. The Lorentz function was set to reproduce the TO-phonon absorption. To fit the obtained spectra, the N_{eff} in the Drude function is only changed and the other parameters (the relaxation time in the Drude function and all parameters in the Lorentz function) are fixed. The obtained N_{eff} is plotted in Fig. 1(b). The logN_{eff} is proportional to the pressure up to 0.65 GPa. The pressure dependence indicates that the energy gap closes with increasing pressure. The energy gap size (2Δ) at the ambient pressure was evaluated to be about 1000 K [3]. By evaluating the gap size from N_{eff}, the energy gap at the black-golden phase boundary is 850 K and then the gap suddenly closes to 100 K in the golden phase by the first order transition. This result indicates that the charge instability occurs at the phase boundary with the gap size of 850 K.

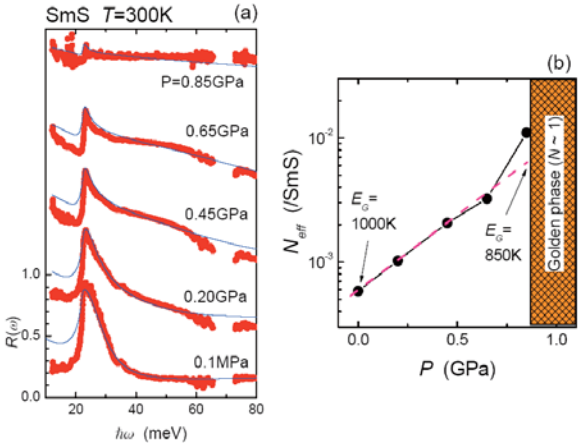

Fig.1. (a) Pressure dependence of reflectivity spectrum [$R(\omega)$] of SmS (thick lines) in the black phase at 300 K. The fitting curve of the combination of a Drude and a Lorentz functions are also plotted by thin solid lines. Successive curves are offset by 0.5 for clarity. (b) Pressure dependence of energy gap evaluated by the Drude and Lorentz fitting of $R(\omega)$ spectra.

[1] K. Matsubayashi, K. Imura, H.S. Suzuki, T. Mizuno, S. Kimura, T. Nishioka, K. Kodama, and N.K. Sato, J. Phys. Soc. Jpn. (2007) in press.
[2] J.L. Kirk, K. Vedam, V. Narayanamurti, A. Jayaraman, and E. Bucher, Phys. Rev. B **6** (1972) 3023.
[3] T. Mizuno, S. Kimura, K. Matsubayashi, K. Imura, H.S. Suzuki, and N.K. Sato, submitted.

BL6B(IR)

Dielectric Spectroscopy of $Ba_4R_{9.33}Ti_{18}O_{54}$ (R=La and Sm) Ceramics

K. Wada, Y. Yamada, I. Kagomiya, K. Kakimoto, H. Ohsato
Graduate School of Engineering, Nagoya Institute of Technology, Gokiso-cho, Showa-ku, Nagoya 466-8555 Japan

$Ba_4R_{9.33}Ti_{18}O_{54}$ is a paraelectric material with tungsten-bronze-like crystal structure. Characteristics of $Ba_4R_{9.33}Ti_{18}O_{54}$-based material with both high permittivity (ε_r) and the temperature stability at GHz frequency range are proper to a resonator or filter application for the wireless telecommunication devices. In general, temperature coefficient of permittivity (τ_ε) of high-permittivity paraelectric material shows large negative value, e.g. $SrTiO_3$ (ε_r = 304, $\tau_\varepsilon \approx$ -3200 ppm/°C), $CaTiO_3$ (ε_r = 162, $\tau_\varepsilon \approx$ -1700 ppm/°C) and TiO_2 (ε_r = 104, $\tau_\varepsilon \approx$ -900 ppm/°C). On the other hand, the τ_ε of $Ba_4R_{9.33}Ti_{18}O_{54}$ strongly depends on the R species in spite of the crystal symmetry retention. $Ba_4La_{9.33}Ti_{18}O_{54}$ (ε_r = 114; BLaT) shows τ_ε of about -800 ppm/°C whereas $Ba_4Sm_{9.33}Ti_{18}O_{54}$ (ε_r = 78; BSmT) demonstrates τ_ε of almost zero. Understanding of this difference is not sufficient despite much investigation for the development of dielectric property has been performed.

IR reflectivity spectra give us useful information, i.e. the lattice vibration, which essentially correlates to the dielectric behavior at high frequency. Dielectric spectroscopy at the frequency range from sub-millimeter to THz can be obtained by the analysis of IR reflectivity. In this study, we measured the reflectivity spectra of BLaT and BSmT to examine the dielectricity of $Ba_4R_{9.33}Ti_{18}O_{54}$.

Reflectivity spectra of BLaT and BSmT dense ceramics were obtained in the temperature range of 10-300 K at the BL6B beam line of UVSOR. The spectra below 150 cm^{-1} were corrected by Martin-Puplett interferometer (JASCO, FARIS-1) and synchrotron radiation source. Measurement at higher frequency range (>150 cm^{-1}) was carried out using Michelson interferometer (Bruker, IFS66v) and glow-bar source. Each peak of the imaginary part of dielectric spectroscopy obtained from Kramers-Kronig transformation of experimental spectra was used as an initial parameter (TO mode) for the fitting. Then, the experimental spectra were fitted by Drude-Lorentz model.

Fig.1 shows far-infrared reflectivity spectra (circle) and their fits (solid line) of BLaT and BSmT at 300 and 10 K, respectively. Observed spectra are similar to that of Pr-analogy reported in the literature [1]. The portion of the spectra above 1000 cm^{-1} is not shown since no reflection bands were observed. Because of the complexity of the crystal structure in BLaT and BSmT, the spectra showed much dip resulted from the many vibration modes. From the factor group analysis based on the crystal structure data, BLaT and BSmT have 203 IR active modes. Actually, fitting was carried out by use of less than 30 modes because small number of strong modes and/or bundled modes can represent the dielectric behavior approximately. The fitted spectra are good agreements with the observed ones. Usually, low-frequency modes in high-permittivity paraelectric material show softening toward to the Currie temperature. However, in this study, the softening was not confirmed for the less change in the spectra of BLaT and BSmT. The lack of distinct changes in the spectra suggests that no ferroelectric phase transition occurs in both materials at least down to 10 K. Fig. 2 shows real part of permittivity obtained from the fitting of spectra of BLaT. Although BLaT shows large temperature dependence of permittivity below at several GHz ranges [2], the permittivity obtained from IR reflectivity exhibits small temperature dependence. These phenomena can be well connected if BLaT has broad dielectric dispersion. Therefore, $Ba_4R_{9.33}Ti_{18}O_{54}$ probably belongs not to normal paraelectrics but to relaxor dielectrics with broad dielectric dispersion.

[1] K. Fukuda, R. Kitoh and I. Awai, J. Mater. Sci. **30** (1995) 1209.
[2] A. Belous, O. Ovchar, M. Valant and D. Suvorov, J. Appl. Phys. **92** (2002) 3917.

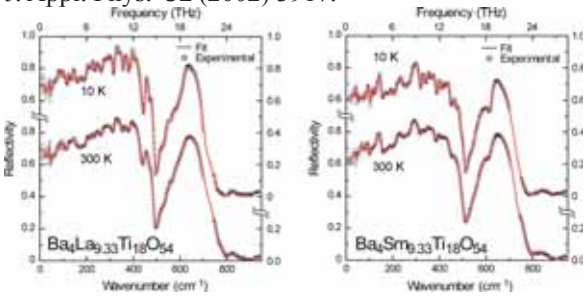

Fig. 1. Far-infrared reflectivity spectra together with their fits of $Ba_4La_{9.33}Ti_{18}O_{54}$ and $Ba_4Sm_{9.33}Ti_{18}O_{54}$ ceramics at 10 and 300 K.

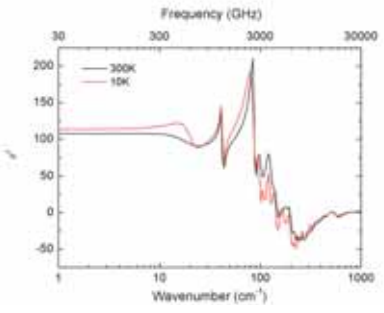

BL6B(IR)

Optical Properties of Bismuth Clusters

S. Yoshida, A. Goyo, H. Ikemoto
Faculty of Science, University of Toyama, Gofuku 3190, Toyama 930-8555, Japan

It is well known that small clusters of atoms will have a local structure and a property different from their elemental crystalline equilibrium.

Raman-scattaring measurements of cluster of Bi exhibit phase transition from rhomdohedral Bi nanocrystalline to amorphouselike clusters depending on cluster size[1]. They also suggest that amorphous clusters are semiconducting and covalent interactions increase with decreasing size.

The Raman studies are good tools but indirect evidences for the transition. So it is very important to investigate the optical property directly to reveal the mechanism of the phase transition. In the present study we report results of optical absorption coefficients for Bi clusters.

Experimental

Bismuth of 99.999 % purity was slowly deposited onto the substrates from a melting crucible. The Bi film was discontinuous with isolated island formation. Then, KBr of 99.99 % purity was deposited to cover the Bi islands. By repeating these procedures, a sample of Bi clusters isolated in a KBr matrix was obtained. The size of the islands was adjusted by controlling the thickness deposited on the substrates, which was monitored with a quartz oscillator. The thickness ratio of the Bi and the matrix is about 1:20. As mentioned above the Bi clusters are formed in thin films, and samples are represented by their average thickness of the Bi thin films in this paper. The measurements of reflectivity and transmissivity were performed in the energy range of 0.05~0.8 eV with the rapid-scan Michelson interferometer (Bruker, IFS-66v) and a HgCdTe detector at the UVSOR. All measurements were performed at room temperature.

Results and Discussion

Figure 1 shows the measured transmittance spectra of the Bi 10nm thick films with comparison with those calculated by two models. In a multilayer(ML) model the layers of Bi and KBr are assumed to be uniform respectively. In an effective medium(EM) model it is assumed that there is a single layer composed of mixture of Bi clusters and KBr matrix, and optical constants of the layer are mixed optical constants of Bi[2] and those of KBr[3] are mixed in the ratio of the thickness. The EM model is better than that the ML models for 10nm thick films.

The absorption coefficients are calculated by Hong's expression[4]. The absorption coefficients of 10nm thick films are close to those of crystalline Bi, suggesting that 10nm thick films are semimetal. Meanwhile the absorption coefficients of the 2nm and 0.5nm thick films are smaller than those of bulk Bi. These results suggest the semimetal-semiconductor transition of Bi clusters.

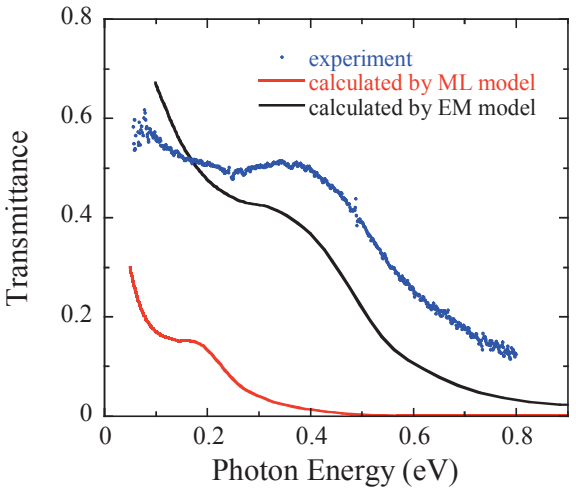

Fig. 1. Transmittance of the 10 nm-thick films. Measured transmittance (blue), transmittances calculated by ML models(black) and EM model(red).

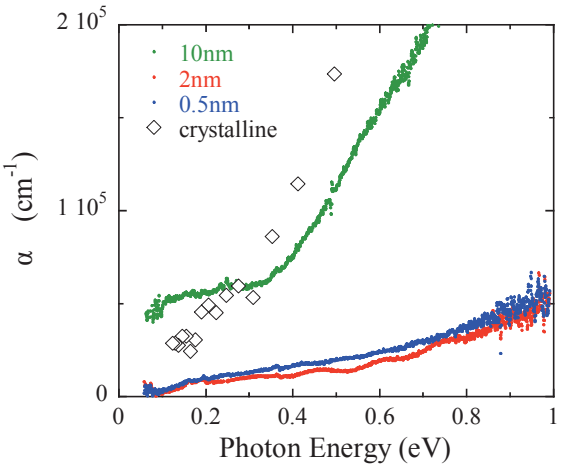

Fig. 2. Variations in optical absorption coefficients of the as-deposited Bi clusters for different thickness. Open circles denote those of polycrystalline [2].

[1] M. G. Mitch, S.J.Chase, J Fortner, R.Q. Yu, and J. S. Lannin, Phys. Rev. Lett. **67** (1991) 875-878.
[2] A.D.Lenham,et al. J.Opt.Soc.Am.**55** (1965) 1072.
[3] Handbook of optical constants of solids II. Academic Press (1991).
[4] W.Q.Hong, J.Phys.D:Appl.Phys.**22**(1989)1384.

BL6B

Infrared Reflection Absorption Spectroscopy of Potassium Doped Alq_3 Thin Film Using Synchrotron Radiation

Y. Sakurai[1], S. Kimura[1,2], K. Seki[3]

[1]*UVSOR Facility, Institute for Molecular Science, Okazaki 444-8585 Japan*

[2]*School of Physical Sciences, Graduate University for Advanced Studies, Okazaki 444-8585 Japan*

[3]*Department of Chemistry, Graduate School of Science, Nagoya University, 464-8602 Japan*

Tris-(8-hydroxyquinoline) aluminum (Alq_3) (figure 1) is most widely used as the electron transport/light emitting layer in organic light emitting diodes (OLEDs). A typical OLED consists of indium tin oxide (ITO) as the anode on which organic thin films are sequentially deposited, with low work function metals finally deposited as the cathode. The property of the interface between cathode metals and Alq_3 affect the performance of the devices. Doping is on way to modify the electronic property of the interface.

Infrared reflection absorption spectroscopy (IRAS) is a powerful probe for the structure and chemistry of a surface and interface. Al-N and Al-O vibrational modes of Alq_3 which are expected to be significantly affected by alkali metals appear in the wavenumber region lower than 600 cm^{-1}. Since a conventional FTIR system using a globar light source cannot cover the wavenumber region because of its low brilliance, we have performed IRAS measurement of potassium doped Alq_3 thin film using a high brilliant synchrotron radiation, UVSOR-II, in the region between 300 and 500 cm^{-1}. The change of the Al-N stretching mode with the potassium doping was observed [1]. In this study, we measured IRAS spectra in the region between 400 and 700 cm^{-1} to observe Al-N and Al-O stretching modes.

Experiments including the sample preparation and measurement were performed in an ultrahigh vacuum chamber specially designed for this experiment [2]. Alq_3 films were prepared by vacuum evaporation onto Ag films deposited on Si substrates. Potassium was evaporated on the Alq_3 films from SAES getter sources. IRAS spectra were obtained with the SR light through CsI windows at the incident angle of 80° relative to the surface normal. The reflected light was detected by a liquid-helium-cooled Si bolometer.

Figure 2 shows the potassium doping dependence of the IRAS spectra of an Alq_3 film of 20 nm thickness in the wavenumber region between 400 and 700 cm^{-1}. In the pristine Alq_3 spectrum, four strong peaks at 422, 458, 552 and 655 cm^{-1} are observed. These peaks are assigned to Al-N stretching, pyramidalization modes of the nitrogen atom, Al-O stretching and pyramidalization modes, respectively, as previously assigned by absorption spectra of powder Alq_3 samples [3]. The intensity of these peaks gradually decreases and new peaks additionally appeare around 440 and 502 cm^{-1} with increasing potassium evaporation amount. These new peaks are assigned to Al-N and Al-O stretching modes, respectively, by comparing with calculated vibrational modes. Therefore the frequency of Al-N stretching mode changed to higher frequency, and that of Al-O stretching mode changed to lower frequency, i.e., the Al-N bond strengthens and the Al-O bond weakens by the potassium doping. These changes are believed to be caused by the charge transfer from the potassium atom to the Alq_3 molecule which is predicted by theoretical investigation.

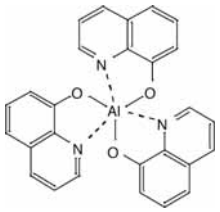

Fig. 1 The chemical structure of Alq_3.

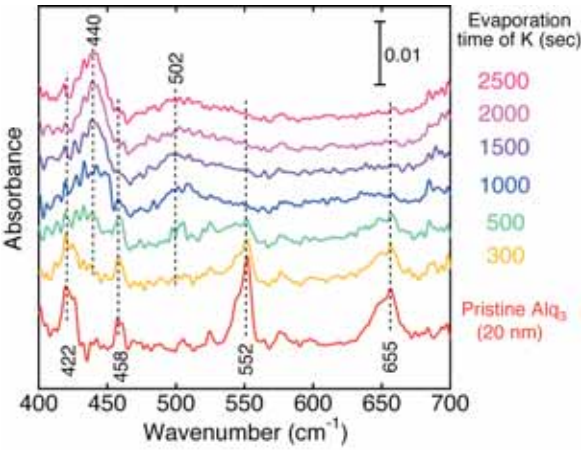

Fig. 2 The potassium doping dependence of the IRAS spectra of an Alq_3 film.

[1] Y. Sakurai, S. Kimura and K. Seki, UVSOR Activity Report 2005 (2006) 81.

[2] S. Kimura, Y. Sakurai, E. Nakamura and T. Mizuno, AIP Conf. Proc. **879** (2007) 595.

[3] M. Cölle, S. Forero-Lenger, J. Gmeiner and W. Brütting: Phys. Chem. Chem. Phys., **5** (2003) 2958

BL7B

Reflectivity of $YbAl_2$ in Visible to VUV Regions

H. Okamura[1], S. Nagano[1], T. Nanba[1], M. Kosaka[2]
[1]*Graduate School of Science and Technology, Kobe University, Kobe 657-8501, Japan.*
[2] *Department of Physics, Saitama University, Saitama, Japan.*

At ambient pressure, the average 4*f* electron configuration of Yb in $YbAl_2$ is $(4f)^{13.8}$, hence the average valence of Yb is 2.2. It has been shown that $YbAl_2$ undergoes a valence crossover under external pressure, from 2.2 at ambient pressure to nearly 3 at 16 GPa [1]. When the valence of Yb is 3+, it has a hole within the 4*f* shell; hence it possesses a localized magnetic moment. Namely, as the applied pressure is increased, the number of localized 4*f* holes increases. This can be viewed as a pressure-induced crossover from itinerant to localized character of the 4*f* electrons through the electron-hole symmetry. Associated with this crossover, there should be also changes in the strength of the hybridization between the conduction and 4f electron (*c-f* hybridization). This is an interesting system where the degree of f electron localization can be tuned continuously by the applied pressure. We are planning an infrared study of $YbAl_2$ under pressure, to explore the crossover of electronic states under pressure. To do so, it is important to measure its optical spectra in detail at ambient pressure in a wide photon energy range. As a part of this, we have carried out reflectivity measurements of $YbAl_2$ at BL7B from visible to vacuum UV regions.

Fig. 1 shows the measured reflectivity spectrum of $YbAl_2$ single crystal. It is seen that the reflectivity decreases rapidly above 2 eV, reaching a minimum (plasma edge) at 8 eV. We are also measuring the reflectivity in the infrared region, so the spectrum in the entire region can be analyzed via the Kramers-Kronig analysis to obtain the optical conductivity spectrum of $YbAl_2$.

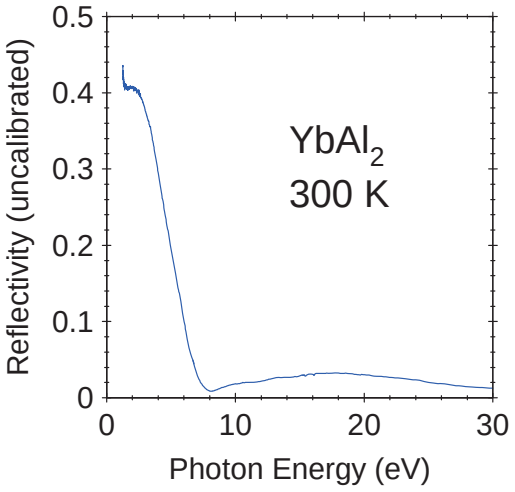

Fig. 1. Reflectivity spectrum of $YbAl_2$ at room temperature. Note that since the sample size was smaller than the SR beam spot size on the sample, the absolute value of the reflectivity is not correct (uncalibrated).

[1] C. Dallera et al., Phys. Rev. B **68** (2003) 245114.

BL7B

Reflection Spectra of Polyimide (CBDA/BAPP) Films Exposed to Polarized UV Radiation

T. Mizunuma, K. Nakagawa, T. Tsuda, S. Matsumoto
School of Science and Technology, Meiji University, Kawasaki 214-8571 Japan

Polyimides compounds based on aromatic dianhydrides and diamines are widely used as base materials for electronic devices, becouse of their thermal stability and chemical resistance. Recently it has been reported that polyimide films exposed to linearly polarized Ultraviolet (UV) radiation are capable of aligning liquid crystal(LC) molecules on their surface. This technique, named photo alignment, is remarkable for fabricating Liquid Crystal Displays (LCD's). But the detailed mechanism of photo alignment of LC molecules has not been clear. Optical spectra of polyimide films in the UV-VIS and IR regions give important clues to infer the photo alignment mechanism[1][2][3]. But few spectroscopic investigation has been made about higher energy regions such as vacuum ultraviolet (VUV) region. In this paper, we report VUV reflection spectra of polyimide (CBDA/BAPP) films exposed to linearly polarized UV radiation.

Experimental

An amic acid form of CBDA/BAPP from Nissan chemical Industries, Ltd was used and suitable concentrations of the poly (amic acid) (PAA) form was spin coated on quartz substrates. Spin condition was 3500 rpm for 40 s and film thickness was about 50 nm. They were soft baked for 10 min at 100 ^{o}C to remove the solvents and hard baked 250 ^{o}C in a convection oven to accomplish imidization for 2 hours. UV irradiation was accomplished using a He-Xe lamp based irradiator. The intensity of the UV radiation was about 5.5 mW/cm^2 around 365 nm. Reflection spectra of polyimide (CBDA/BAPP) films exposed and without exposed to linearly polarized UV radiation were measured in the vacuum ultraviolet region up to 25.0 eV with the 3-m normal incident type monochromator (grating: G1 and G2) at BL-7B of UVSOR-II.

Results and Discussion

Figure 1 shows the reflection spectra of polyimide (CBDA/BAPP) films exposed to linearly polarized UV radiation compared with that of no exposed film. Peaks in the figure are named as indicated for convenience. In the reflection spectra, five peaks named as A, B, C, D and E were observed at about 6.0 eV, 9.5 eV, 13.0 eV, 16.0eV and 20.0eV, respectively. Therefore both reflection spectra show some remarkable peaks at same energies. But peak intensities of spectrum exposed to UV radiation becomes stronger than that of without exposed except peak A. It is considered that molecular reorienteation occurred by linearly polarized UV radiation. To analysis of spectra changes caused by exposed to linearly UV radiation, DV-Xα molecular orbital calculation was performed. Figure 2 shows Density of State (DOS) spectra calculated. Peak A has been reported to π-π* transition on a benzene ring. And it is already known that n-π* transitions is dominant for alicylic polyimides, which implies the peaks B, C, D and E may be attributed to n-π* transitions of carbonyl groups contained in CBDA/BAPP as drawn in Fig 2.

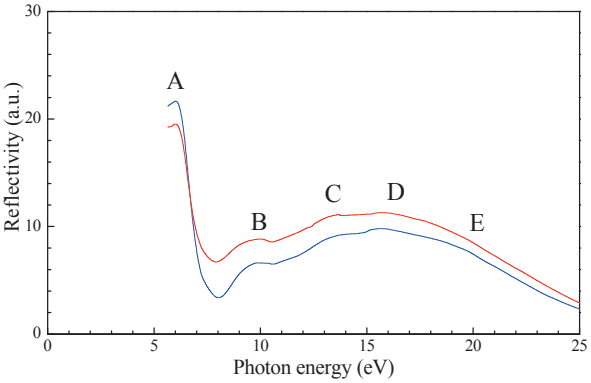

Fig. 1 Reflection spectra of polyimide (CBDA/BAPP) films exposed (red line) and without exposed (blue line) to linearly polarized UV radiation.

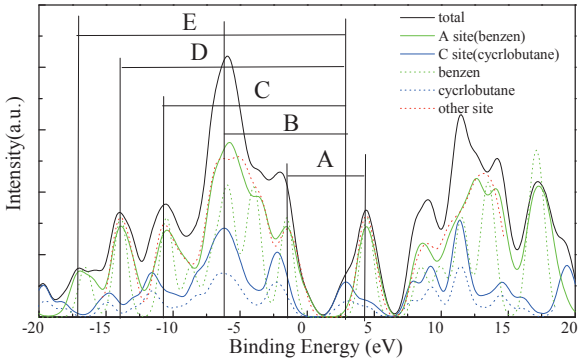

Fig. 2 DOS spectra of polyimide (CBDA/BAPP) calculated by DV-Xα method.

Acknowledgements

The authors would like to thank H. Shitomi of AIST for his support.

[1] H. Endo, T. Shinozuka, H. Fukuro, Y. Imura and S. Kobayashi, AM-LCD(1996)341.
[2] H. Shitomi, T. Ibuki, S. Matsumoto and H. Onuki, Jpn.J.Appl.Phys. **38** (1999)176.
[3] K. Sakamoto, K. Usami, T. Araya and S. Ushioda, Jpn.J.Appl.Phys. **38** (1999)1435.

Optical Investigation of the Charge Gap Opening in $FeSb_2$

M. Marutzky, S. Kimura[1], J. Sichelschmidt, A. Bentien, F. Steglich
Max-Planck Institut für Chemische Physik fester Stoffe, Dresden, Germany
[1]UVSOR Facility, Institute for Molecular Science, Okazaki 444-8585, Japan

Introduction

$FeSb_2$ is characterized as a Kondo-insulator with similar physical properties to FeSi [1, 2]. It shows a crossover from a diamagnetic to a paramagnetic state around 100 K [3, 4]. In the literature, a semiconducting behaviour for two crystal axes and a metal-semiconductor crossover for the third axis was reported [3]. We have grown single crystals and found a semiconducting behaviour for all three axis and a colossal Seebeck coefficient [2]. In order to study the correlation effects in $FeSb_2$, we started an optical investigation over a large energy range from the FIR (3meV) to the VUV (30 eV).

Experimental

Single crystals of $FeSb_2$ were grown by flux method. The optical anisotropic crystals have a large [110] surface which was polished in order to allow optical measurements with the E vector parallel and perpendicular to the c-axis. Michelson- and Martin-Puplett Fourier transform spectroscopy was used in the IR where the contribution of the conduction carriers to the optical properties can be observed. Additionally, reflectivity measurements were made from 1 to 30 eV at BL7B of the UVSOR which was necessary in order to investigate the interband transitions and to enable an exact Kramers-Kronig transformation (KKT) of the reflectivity. The latter is needed to calculate the complex optical conductivity.

Results and Discussion

In Figure 1 the reflectivity of $FeSb_2$ with $E \parallel c$ from 3 meV to 30 eV is depicted at various temperatures. At 300 K, the reflectivity in the FIR is predominant metal-like. Remarkable is the fact that at 24 meV a peak is visible arising from phonon absorption which is unusual for a metal. At 50 K, the reflectivity has changed dramatically and dropped from approx. 0.9 at 300K down to 0.7. This is similar to the situation in FeSi where a charge excitation gap opens [5]. Very distinctive phonon structures appear with a minimum reflectivity of 0.1 at 10 K. The drastic depletion of the reflectivity and the absorptive part of the optical conductivity was also observed in [6]. Qualitatively the same behaviour occurs for $E \perp c$, not shown here. A quantitative analysis of these optical spectra will help to answer the question if the intriguing physical properties of $FeSb_2$ can be understood in the framework of a Kondo model.

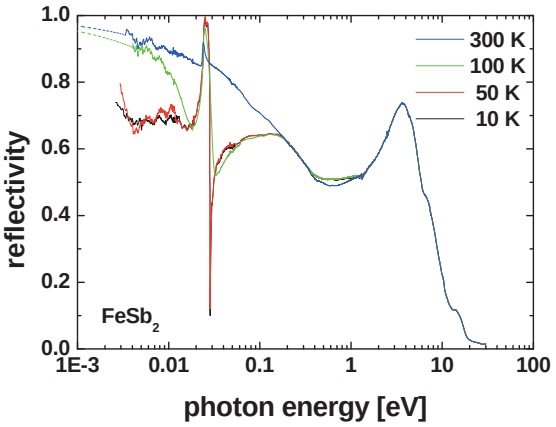

Fig. 1 Reflectivity of single crystalline $FeSb_2$ with E parallel to the c-axis in the [110] plane. For 100 and 300 K, the reflectivity was extrapolated down to zero with the Hagen-Rubens relation in order to enable a KKT. Above 30 eV, $R \sim \omega^{-4}$ was used for extrapolation.

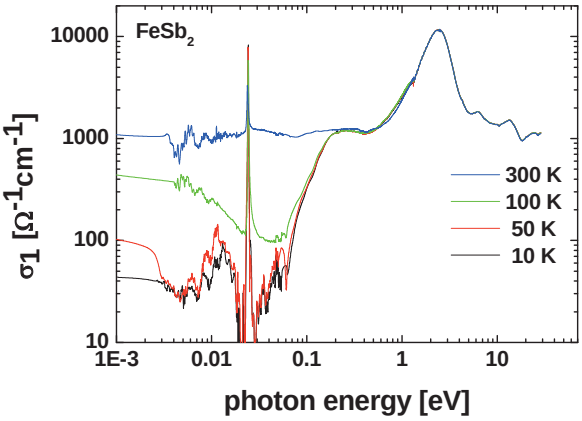

Fig.2 Real part of the optical conductivity, obtained by Kramers-Kronig transformation of the reflectivity data in Fig. 1.

[1] C. Petrovic et al., Phys. Rev. B **72** (2005) 045103.
[2] A. Bentien et al., submitted to Nature Physics
[3] C. Petrovic et al., Phys. Rev. B **67** (2003) 155205.
[4] Ronwei Hu et al., Phys. Rev B **74** (2006) 195130.
[5] Z. Schlesinger et al., Phys. Rev. Lett. **71** (1993) 1748.
[6] A. Perucchi et al, Eur. Phys. J. B **54** (2006) 175-183.

BL7B

Temperature Dependence of Time Resolved Decay Curves in AlGaN Alloys

M.Suzuki[1], T.Sakai[1], N.Nakagawa[1], K.Fukui[1], S.Naoe[2], H.Miyake[3], K.Hiramatsu[3]

[1]*Research Center for Development of Far-Infrared Region, University of Fukui, Fukui910-8507, Japan*

[2]*Faculty of Engineering, Kanazawa University, Kanazawa 920-1192, Japan*

[3]*Faculty of Engineering, Mie University, Mie 514-8507, Japan*

AlGaN alloys have a great potential for UV opt-electronic devices, because AlGaN alloys can cover their band gap energies from 3.39 to 6.2 eV by changing a compositional rate of Al and Ga. Then, to understand the decay processes of near band edge ultraviolet (UV) photo luminescence (PL) in AlGaN, we have been performing the measurement of the time resolved decay (TRD) curves of AlGaN alloys. In this report, temperature dependence of TRD curves in AlGaN alloys is presented.

All samples are made by the MOVPE method. The thicknesses of AlGaN thin films are about 1μm on 1μm AlN single crystal thin films with Al_2O_3 substrates. The all measurements were carried out at BL7B under single-bunch operations. A optical fiber is used for guiding PL in the vacuum sample chamber to a spectrometer with CCD. Time resolved decay curve measurements are carried out by using time correlated single photon counting (TCSPC) method.

Figure 1 shows TRD curves at various temperatures (from 10 to 170 K) of $Al_{0.67}Ga_{0.33}N$. Excitation energy is 5.01 eV where PL excitation spectrum becomes maximum intensity. As shown in fig. 1, these curves can not be analyzed as a single exponential decay process. We have been considering that TRD curves consist of three different single exponential decay components. Decay times of first, middle and slow components are less than 1 ns (less than resolution limit of TCSPC), order of ns ~ 10 ns, and order of 10 ns ~ 100 ns, respectively. Decay time of each component also decreases with increasing temperature as shown in fig. 1. Time integrated PL intensity of each component is calculated from the product of decay time with initial intensity, and fig. 2 shows normalized time integrated PL intensity of each component which is derived from the analyzed results of TRD curves shown in fig. 1. The curve labeled as 'total' in fig. 2, which represents simple sum of three components, is in good agreement with temperature dependence of PL intensity obtained from time integrated PL measurement at 5.01 eV. The temperature dependence of slow component indicates that the decay process corresponds to the slow component is dominant process at low temperature and this decay process basically shows temperature quenching; there are potential barriers which connect another processes, and the role of the radiative process by slow component decreases with increasing temperature. One of 'another processes' is a non-radiative process, but the temperature dependence of middle component clearly suggests that the other 'another process' is the radiative process by middle component. Similar intensity exchange is also found between middle and fast components.

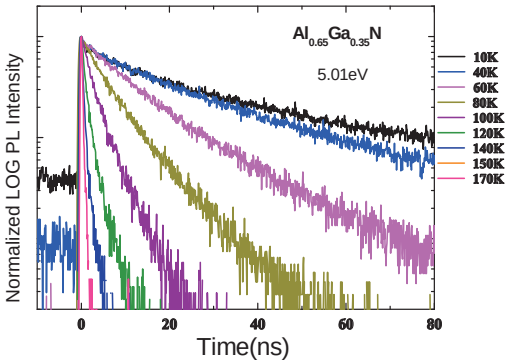

Fig.1 Time resolved decay curves of $Al_{0.67}Ga_{0.33}N$ at 5.01eV

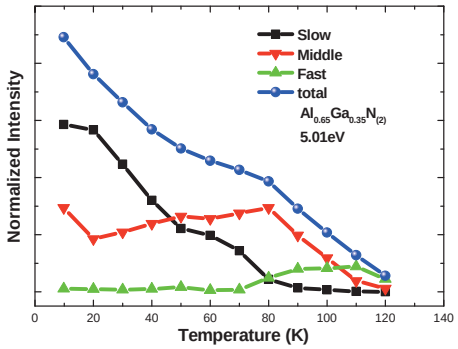

Fig.2 Temperature dependence of area strength at PL energy peak position(5.01eV)

BL7B

Angle Dependence of Polarized Reflectance Spectra in AlN

F.Suzuki[1], M.Kishida[1], K.Fukui[1]

[1]*Research Center for Development of Far-Infrared Region, University of Fukui, Fukui910-8507, Japan*

AlN has a large bandgap of about 6 eV and a high thermal resistance, and is expected in fields such as lasers and LED in the ultraviolet and the deep ultraviolet. Usually, high quality AlN single crystal is fabricated as a thin film by MOCVD method. AlN thin film has the wurtzite structure and *c*-axis is perpendicular to the surface. In this restriction, reflectance measurements are usually carried out under $\boldsymbol{E} \perp c$ condition, where $\boldsymbol{E}$ represents the electric field of incident light. In this condition, optical transition which corresponds to the minimum bandgap becomes forbidden transition due to the selection rule, and first allowed transition is observed at 6.2 eV. For this reason, the true bandgap has been reported using unobtainable bulk crystals even though crystal quality of the bulk sample is lower than that of thin film. However, it is possible to investigate optical properties around true bandgap of high quality AlN thin film by using the reflectance spectra with incidence angle dependency and high linear polarization incident light. In this report, we present angle dependence of polarized reflectance spectra in AlN by using BL7B.

High quality AlN thin film has a wurtzite structure which is evaporated on the sapphire substrate by MOVPE method. Thickness of AlN film is 1μm. Reflectance measurement at 10 K has been carried out in the range between 5.8-7eV, and the incidence angles to the surface normal are 6, 15, 30, 45, and 60 degrees.

Figure 1 shows the reflectance spectra of AlN at 6, 15, 30, 45, and 60 degrees. In all spectra, wave-like features by interference are shown in the transparance region (below 6.2eV), and the peak with dip structures due to exciton absorption are also seen near 6.2 eV. However, wave-like features become discontinuous near 6.0 eV with increasing incidence angle. This is caused by the exciton absorption at minimum bandgap, since $\boldsymbol{E}$ // c component of incident light becomes increasing with increasing incidence angle. Although band edge absorption begins at 6.0 eV by $\boldsymbol{E}$ // c component of incident light, AlN is still transparance under $\boldsymbol{E} \perp c$ condition. Then, wave-like features still exist up to 6.2 eV with its intensity decreasing.

Figure 2 shows the refractive index *n* and the extinction coefficient *k* derived from reflectance spectra shown in Fig. 1 by using the characteristic matrix of the single-layer thin film model. Clear jumps of *k* which corresponds to optical absorption can be seen in not only ~ 6.2 eV but also ~ 6.0 eV at grazing incidence conditions.

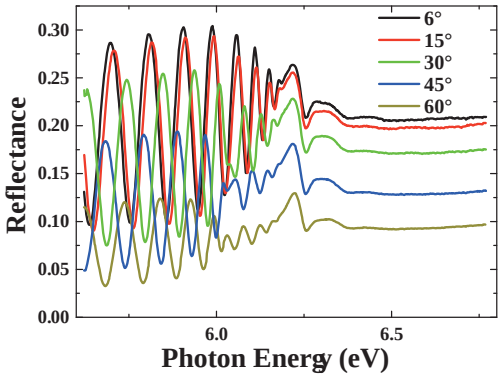

Fig. 1 Reflectance spectra of AlN of 6, 15, 30, 45, and 60 degrees

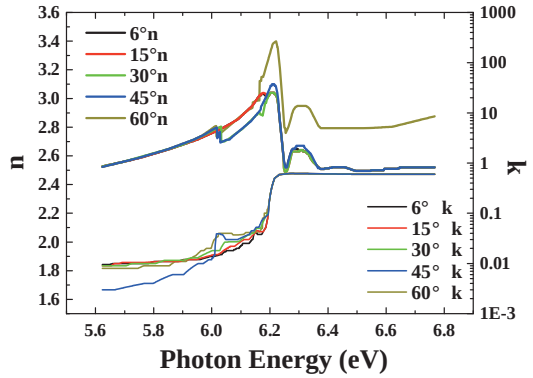

Fig. 2 Optical constant n and k to each incidence angle

BL7B

Photoluminescence of Forsterite Single Crystals Excited by Vacuum Ultraviolet Radiation

M. Kitaura[1], S.Izuhara[2], H.Nakagawa[2], A.Ohnishi[3]
[1]*Fukui National College of Technology, Sabae, 916-8507, Japan*
[2]*Dept. of Electrical and Electronics Engineering, Fukui University, Fukui, 910-8507,Japan*
[3]*Deparment of Physics, Yamagata University, yamagata, 990-8560, Japan*

Magnesium silicate (Mg_2SiO_4) is orthorhombic at normal condition, which is named forsterite. This material has been used as the host of radiation dosimeter. The application of it extends to the other optical materials, e.g., laser, phosphor and so on. Because of its industrial importance, most of the studies concentrate in optical properties of activator ions. There are few reports on optical properties of forsterite, except for our optical constant data [1]. It seems valuable to investigate the optical properties of forsterite from the viewpoint of fundamentals and applications.

In the present experiment, we have measured the emission spectra of forsterite single crystals under excitation with synchrotron radiation at low temperatures. In addition, excitation spectra were also measured for the observed emission peaks. The correction for the distribution of excitation light source was carried out for the excitation spectra observed.

Figures 1(a) and 1(b) show the emission spectra at 10K and 150K, respectively. In Fig.1(a), one can see the two emission peaks at around 2.60 eV and 2.82 eV. Since the 2.60 eV peak begins to quench thermally even at 10K, it cannot be found in Fig.1(b). The 2.82 eV peak is clearly observed at 300K. The other peaks below 2 eV may be connected to extrinsic origin, because their features vary for each sample. The excitation spectra for the 2.60 eV and 2.82 eV emission peaks are presented in Fig.2, together with the absorption tail spectrum. The threshold of excitation for the 2.60 eV peak is in good agreement with the fundamental absorption edge. This result indicates that the 2.60 eV peak is of an intrinsic of forsterite. The 2.82 eV peak is stimulated with ultraviolet photons below the fundamental absorption edge, and thus it originates in lattice imperfections. It is to be noted that both spectra resemble each other in the energy above 10 eV. This fact is explained as follows. The energetic *e-h* pairs produced by vacuum ultraviolet photons immediately relax into excitonic states. Excitons will migrate to be trapped at the sites of lattice imperfection. As a result, the 2.82 eV emission peak originates from the lattice imperfections excited. We thus suppose that the excitation of lattice imperfections by the inelastic scattering of hot photoelectrons is negligible in the energy region investigated here.

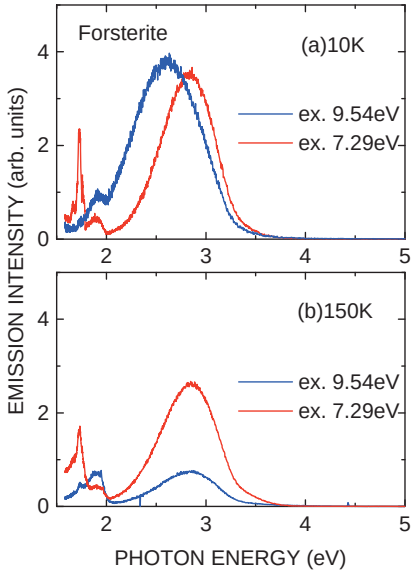

Fig.1: Emission spectra of forsterite at (a) 10K and (b) 150K. The red and blue lines correspond to the emission spectra measured under excitation below and above the fundamental absorption edge, respectively.

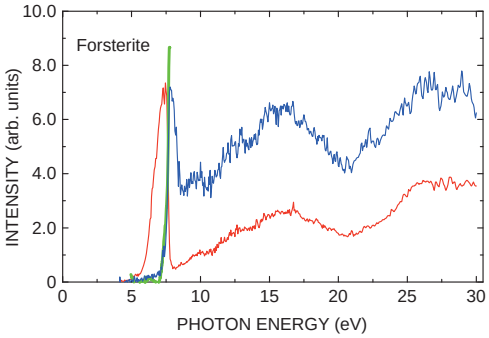

Fig.2: Excitation spectra for 2.60 eV emission peak at 10K (Blue line) and 2.82 eV one at 150 K (red line). The absorption tail spectrum at 10K is also presented by a green line for comparison.

[1] M. Kitaura *et al.*, J. Phys. Soc. Jpn. **71** (2002) 2736.

5
Solid state spectroscopy II: XAFS and PES

BL5U

Angle-resolved Photoemission Study of $CeCoGe_{1.2}Si_{0.8}$ in the Three-dimensional Momentum Space

H.J. Im[1,2], T. Ito[2,3], S. Kimura[2,3], J.B. Hong[1], Y.S. Kwon[1]

[1]*BK21 Physics Research Division and Institute of Basic Science, Sungkyunkwan University, Suwon 440-746, Korea*

[2]*UVSOR Facility, Institute for Molecular Science, Okazaki 444-8585, Japan*

[3]*School of Physical Sciences, The Graduate University for Advanced Studies, Okazaki 444-8585, Japan*

Recently, $CeTX_2$ systems (T = transition metals, X = semiconducting elements) have intensively studied because of several intriguing phenomena such as heavy fermion behavior with J = 5/2 in $CeCoGe_2$ [1], valence fluctuation in $CeNiSi_2$ [2], and strongly anisotropic magnetic and transport properties in $CeNiGe_2$ [3]. Hybridization of localized *f*-electrons with conduction electrons (*f-d* hybridization) plays an important role to derive the above properties. In order to understand these interesting physical properties, it is important to clarify the electronic structure of this system. Therefore, we have performed the angle-resolved photoemission spectroscopy (ARPES) on $CeCoGe_{1.2}Si_{0.8}$ with large *f-d* hybridization strength in the three-dimensional momentum (*k*-) space at BL5U.

Figure 1(a) shows the energy distribution curves (EDCs) measured at T = 10 K and θ = 0° (normal emission) with changing the photon energy ($h\nu$) from 48 to 88 eV. Peak positions represent the band dispersion along the k_y-direction. We can recognize that there are two weakly dispersed bands around E_B = 0.4 and 1.2 eV with the bottom and top at $h\nu$ = 66 eV, respectively. This indicates that $h\nu$ = 66 eV is a symmetry point in the k_y-direction, and is found to correspond to the Γ-point with inner potential, V_0 = 15.8 eV.

Figure 2(a) shows the Fermi surface (FS) in the k_{zx}-k_y plane as depicted by the shaded plane in Fig. 1(b), mapped with the energy window from E_B = 100 to -100 meV. There are two kinds of FS: One is a large FS, which is continuously formed along k_y-direction in the range of from $k_{zx} \approx 0.5$ to 0.7 Å^{-1} as guided by a dashed line. Other FS inside large FS also seems to open along k_y-direction. In comparison to band dispersions around Γ and Y-points as shown in Fig. 2(b) and (c), respectively, the opened large FS consists of bands which cross E_F at around k_{zx} = 0.6 Å^{-1} ,forming hole pockets.

As a result, the large hole FS that opens along the k_y-direction indicates the quasi-two-dimensional electronic structure. This is consistent with the results of transport experiments (large anisotropy of electrical resistivity, $\rho_c/\rho_{ab} \approx 700$ [4]) and suggests that the *f-d* hybridization strength has anisotropy due to two-dimensionality.

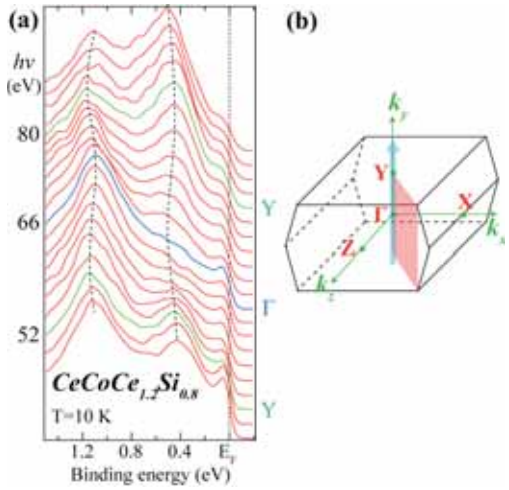

Fig. 1. (a) EDCs of $CeCoGe_{1.75}Si_{1.25}$ observed by $h\nu$-dependent ARPES. The dashed lines are guides to the eye. (b) Brillouin zone of the single-faced orthorhombic structure. The bold arrow and shade plane stand for the measurement path and plane, respectively.

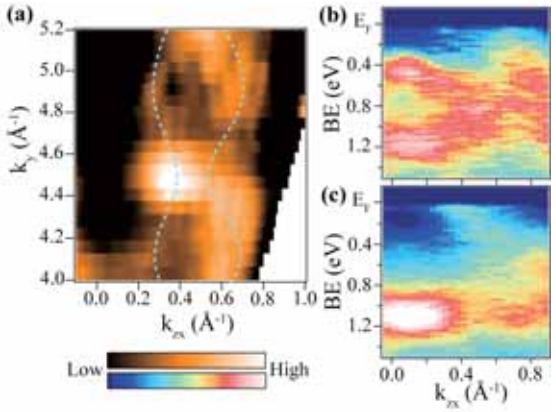

Fig. 2. (a) FS mapping of $CeCoGe_{1.75}Si_{1.25}$ in the k_{zx}-k_y plane as depicted by the shaded plane in Fig 1(b). ARPES intensity plot representing the band dispersions along k_{zx}-direction at around Y- (k_y = 4.89 Å^{-1}, b) and Γ- (k_y = 4.52 Å^{-1}, c) points, respectively.

[1] E.D. Mun *et al*., Phys. Rev. B **69** (2004) 085113.
[2] E.D. Mun *et al*., Phys. Rev. B **67** (2003) 033103.
[3] M.H. Jung *et al*., Phys. Rev. B **66** (2002) 054420.
[4] Y.S. Kwon et al., private communication (2007).

BL1A

Local Structure Analysis of Aluminum Compounds by an XAFS Method

T. Kurisaki[1], Y. Inoue[1], H. Wakita[1,2]

[1]*Department of Chemistry, Faculty of Science, Fukuoka University, Nanakuma, Jonan-ku, Fukuoka 814-0180, Japan*

[2]*Advanced Materials Institute, Fukuoka University, Nanakuma, Jonan-ku, Fukuoka 814-0180, Japan*

Aluminum compounds collected much interest because of their ability to act as catalysts, and functional materials. The function of aluminum compound is concerned closely with that coordination structure. For various aluminum compounds, we have studied the electronic structure by X-ray absorption spectroscopy [1, 2]. This result suggested that there is correlation in the form of XANES spectrum and the local structure

In this work, we applied the x-ray absorption near edge structure (XANES) spectroscopy to aluminum compounds combined with oxygen atoms. The results of the measurement indicate unoccupied and occupied electronic structure of aluminum compounds. The X-ray absorption spectra were measured at BL1A of the UVSOR in the Institute of Molecular Science, Okazaki [2]. The ring energy of the UVSOR storage ring was 750MeV and the stored current was 110-230 mA. Al K-edge absorption spectra were recorded in the regions of 1620-1750eV by use of two KTP(011) crystals. The absorption was monitored by the total electron yield using a photomultiplier. The samples were spread into the carbon tape on the first photodynode made of CuBe of the photomultiplier.

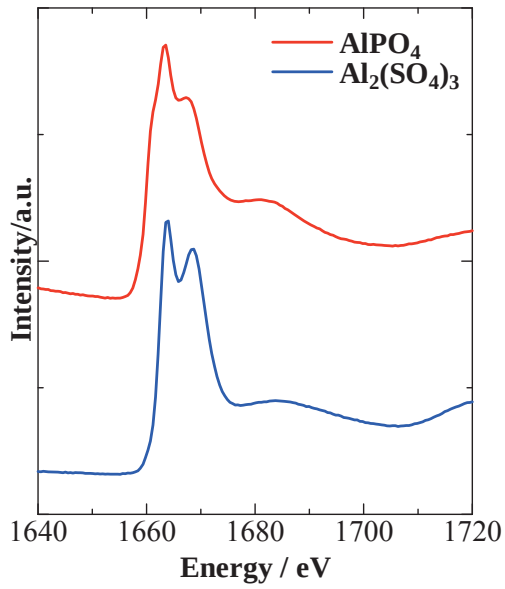

Fig. 1 Observed Al K-edge XANES spectra of aluminum phosphate and aluminum sulfate

The Al K-edge XANES spectra for the aluminum phosphate and aluminum sulfate are shown in Fig. 1. A remarkable change of the spectral patterns was observed for the aluminum phosphate and aluminum sulfate. This result showed that the two aluminum compounds have different electronic state. We are going to try to analyzed this change from comparison of Al K edge XANES and calculated spectra by DV-Xα molecular orbital calculations.

[1] H. Ichihashi, T. Kurisaki, T. Yamaguchi, T. Yokoyama, and H. Wakita, Jpn. J. Appl. Phys. Part 1, **38**(suppl.) (1999) 101.

S. Matsuo, K. Shirouzu, Y. Tateishi and H. Wakita, Adv. Quan. Chem. **42** (2002) 407.

[3] S. Murata, T. Matsukawa, S. Naoè, T. Horigome, O. Matsuodo, and M. Watatabe, Rev. Sci. Instrum. **63** (1992) 1309.

BL1A

Characterization of Aluminum Naphthalocyanine Complexes by an XAFS Method

T. Kurisaki[1], Y. Inoue[1], H. Wakita[1,2]

[1]*Department of Chemistry, Faculty of Science, Fukuoka University, Nanakuma, Jonan-ku, Fukuoka 814-0180, Japan*

[2]*Advanced Materials Institute, Fukuoka University, Nanakuma, Jonan-ku, Fukuoka 814-0180, Japan*

Phtalocyanines (PC) and their derivatives are of particular interest due to many possible applications, such as catalyst, medical supply, semiconductor, and high sensitivity colorimetric regent. Naphthalocyanine (NPC) has a largely p-conjugated. In order to elucidate the effect of the axial ligand, it is necessary to determine their electronic structure [1]. But the electronic structure of naphthalocyanine is not well known.

In this work, we applied the x-ray absorption near edge structure (XANES) spectroscopy to analyze the structure of AlNPC-Cl. The results of the measurement indicate unoccupied and occupied electronic structure of AlNPC-Cl complex. The X-ray absorption spectra were measured at BL1A of the UVSOR in the Institute of Molecular Science, Okazaki [2]. The ring energy of the UVSOR storage ring was 750MeV and the stored current was 110-230 mA. Cl K-edge absorption spectra were recorded in the regions of 3000-3285eV by use of two InSb(111) crystals. The absorption was monitored by the total electron yield using a photomultiplier.

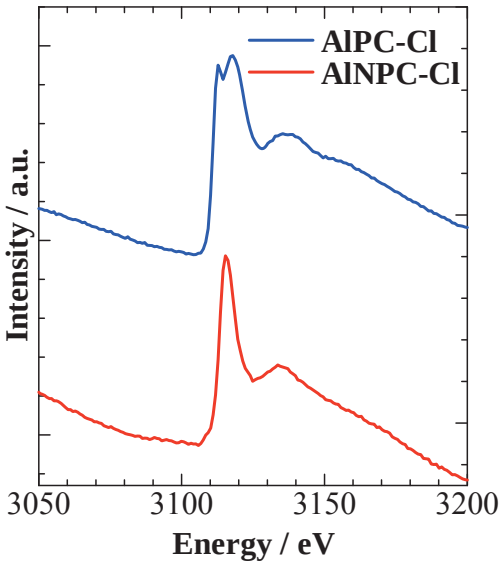

Fig. 1 Observed Cl K-edge XANES spectra of AlNPC-Cl and AlPC-Cl

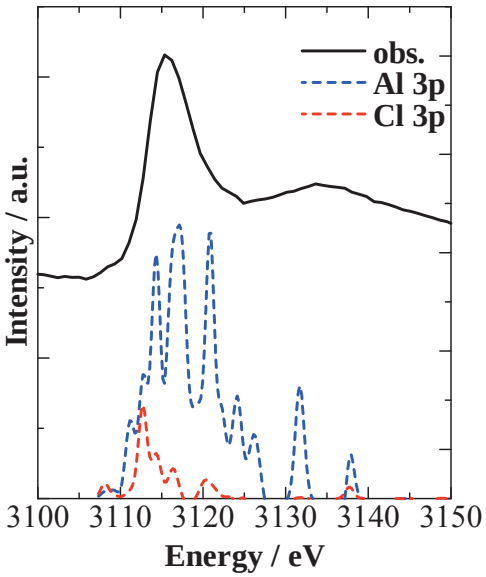

Fig. 2 Observed and calculated Cl K-edge XANES spectra of AlNPC-Cl.

The Cl K-edge XANES spectra for AlNPC-Cl and AlPC-Cl are shown in Figs. 1. A remarkable change of the spectral patterns was observed for AlNPC-Cl and AlPC-Cl. The observed and calculated Cl K XANES spectra for AlNPC-Cl are shown in Fig. 2. Comparison of observed and calculated spectra revealed that aluminum 3p and chloride 3p orbits contribute to the first peak. However, AlNPC-Cl did not contain the contribution from the N 2p and Al 3d orbits.

[1] J. Simon F. Tournilhaec and J. –J. André, Nouv. J. Chim. **10** (1986) 295.

[2] S. Murata, T. Matsukawa, S. Naoè, T. Horigome, O. Matsuodo, and M. Watatabe, Rev. Sci. Instrum. **63**, (1992) 1309.

BL1A

Study of Local Structure of Al-*K* Edge for Modified Hydrotalcite (Layered Double Hydroxide)

A. Nakahira[1], H. Murase[1], H. Nagata[1], S. Nakamura[1], T. Kubo[1], H. Aritani[2]
[1]*Faculty of Engineering, Osaka Prefecture University, Gakuencho, Sakai 599-8531, Japan*
[2]*Saitama Institute of Technology, Fukaya 369-0293, Japan*

Introduction

Layered double hydroxide (LDH) is a clay mineral with a layered structure, in which its composition formula is $[M(II)_{1-x}\ M(III)_x(OH)_2]^{x+}\cdot[A^{n-}_{x/n}\cdot YH_2O]$. M(II), M(III) and exchangeable anions in LDH are able to substitute to various cations and anions. In the present study, we focus on the structure evaluation of basic LDH composed of Mg^{2+} and Al^{3+}, which is called hydrotalcite, MgAl-LDH. Furthermore, it is known that various mixed oxide was generated by calcination of LDH. Obtained mixed oxide is expected to be applicable to many fields such as adsorption and ion exchange materials, magnetic materials, catalysis, and environmental purification materials since it has high specific surface area and unique rehydration behaviors. However, it is not clarified about he structure evaluation of basic LDH and the detailed structure of mixed oxides generated of LDH from 300 to 500°C.

In the present study, the structure evaluation of basic LDH composed of Mg^{2+} and Al^{3+}, which is called hydrotalcite, and mixed oxide obtained by calcination of MgAl-LDH at 300 to 500°C were performed.

Experiments

Mixing solution was adjusted by mixing 0.2 mol/dm^3 $MgCl_2$ aqueous solution and 0.1 mol/dm^3 $AlCl_3$ aqueous solution. MgAl-LDH with M^{2+}/M^{3+} =2 were synthesized by adding mixing solution into 0.05 mol/dm^3 $NaHCO_3$ at room temperature. 1 mol/dm^3 NaOH was simultaneously added into the aqueous solution in order to keep pH 10. After precipitation was finished, products for MgAl-LDH were aged at room temperature for 2 hours. They were separated from liquid phase and sufficiently washed by deionized water and finally air-dried at 110°C for 24 hours.

Mixed oxides were obtained by calcination at 200, 300, 400, and 500°C for 2 hours of MgAl-LDH. The local structures around Al were characterized by measuring X-ray adsorption near edge structure (XANES) at BL1A in UVSOR with KTP.

Results and Discussion

Products prepared by co-precipitation method identified to be layered double hydroxide consisted of Mg^{2+} and Al^{3+} by powder X-ray diffraction analysis. Then, it was suggested that mixed oxide generated by calcination of obtained MgAl-LDH had broad peaks derived from rock salt structure from XRD results.

Figure 1 shows the results of XANES of Al-*K* edge of some mixed oxides. All were different from oxides like α and γ-Al_2O_3 and a hydroxide like $Al(OH)_3$. The spectrum of mixed oxide obtained at 200°C corresponded approximately to that of MgAl-LDH. It was elucidated that Al-K edge XANES spectra of mixed oxides generated at 300, 400, and 500°C was similar to that of MgAl-LDH, although peaks was broad with temperature.

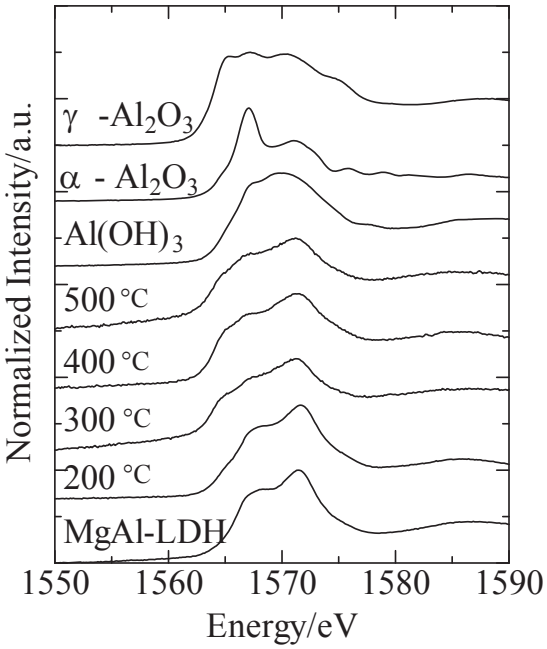

Fig. 1 Al-*K* XANES of MgAl-LDH products and samples obtained by calcination of MgAl-LDH at various temperatures. α-Al_2O_3 and γ-Al_2O_3 are reference materials.

BL1A

Study of Si K-edge of Local Structure in Mesoporous Silica Bulk Prepared by Hydrothermal Hot-pressing

A. Nakahira[1], H. Nagata[1], M. Takimura[2], S. Nakamura[1], T. Kubo[1], H. Aritani[3]
[1]*Faculty of Engineering, Osaka Prefecture University, Gakuencho, Sakai 599-8531, Japan*
[2]*Faculty of Engineering, Kyoto Institute of Tech, Matsugasaki, Kyoto 605-8585, Japan*
[3]*Saitama Institute of Technology, Fukaya 369-0293, Japan*

Mesoporous silica MCM-41 have attracted much attention because of their possible uses as supports for catalysts, a host for nanosize materials and adsorption. However, since bulks of mesoporous structure could not be obtained by conventional solidified methods such as sintering, the application of mesoporous materials is limited. Nakahira et al reported that densified bulky MCM-41 was successfully synthesized using hydrothermal hot-pressing (HHP) method [1]. Therefore, we attemped to exmine the local structure around Si of MCM-41 bulk by XANES spectra.

MCM-41 powder was prepared as a starting material [2]. Mixture of powder and water was heated at 150°C with uniaxial pressing under 40MPa and kept constant for 2 hours. Obtained bulks were identified by XRD. Si K-edge XANES spectra were obtained in a total electron yield mode at room temperature using a KTP double–crystal monochrometer at BL01A of the UVSOR. The spectra were collected in the photon energy range from 1700 to 1925 eV atintervals of 0.05 eV with a dwell time of 1 s.

XRD results showed that MCM-41 bulk was also retained the mesopores after HHP. Figure 1 shows the results of Si K-edge XANES of MCM-41 bulk and starting material powder ((a) and (b)). Silicagel (c) was used as a reference material of amorphous silica with coordiation number 4. The spectrum of HHP bulk was significantly similar to those of starting powder and silicagel. Hence, there is no apparent change in the relative intensity nor the width of these spectra. These results of XANES spectra revealed that the local structure around Si enviroment was almost unchanged before or after HHP treatment.

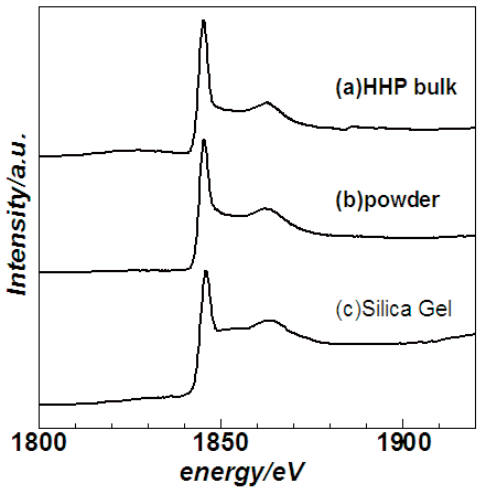

Fig. 1 Si K-edge XANES spectra of MCM-41 bulk prepared by HHP.

[1] H. Nagata, M. Takimura, Y. Yamasaki and A. Nakahira, Materials Transactions, **47** (08) (2006) 2103-2105
[2] H. P. Lin and C. Y. Mou, Science, **273** (1996) 765-768.

BL1A

Measurement of X-ray Excited Optical Luminescence from a Silica Glass

T. Yoshida[1], T. Tanabe[2], H. Yoshida[3]
[1]*Department of Materials, Physics and Energy Engineering, Nagoya University, Furo-cho, Chikusa-ku, Nagoya 464-8603*
[2]*Department of Advanced Energy Engineering Science, Interdisciplinary Graduate School of Engineering Science,Kyushu University6-10-1, Hakozaki, Higashi-ku, Fukuoka 812-8581*
[3]*EcoTopia Science Institute, Nagoya University, Furo-cho, Chikusa-ku, Nagoya 464-8603*

Introduction

Radiation effects on silica glasses are one of the main concerns for their application as optical windows, insulators and optical fibers under fusion and fission environments. Although the radiation damage of silica glass has been extensively studied, the detailed damaging processes and/or radiation effects are not yet fully understood.

In the present study, we have utilized soft X-ray as a radiation source. Since the energy region of the soft X-ray covers the *K*- and *L*-edges of silicon and oxygen, it enables us to study the effects of preferential excitations of inner-shell electrons on the defect production and/or annihilation. We thus examined the changes in X-ray excited optical luminescence (XEOL) of a silica glass with respect to excitation X-ray energy near the threshold of the Si *K*-edge, irradiation time and temperature.

Experimental

The sample used in this study was a low-OH fused silica glass (T-2030) disc produced by Toshiba Ceramics, Japan. The diameter and thickness of the sample were 13 mm and 2 mm, respectively. XEOL of the silica glass by X-ray energy between 1.8 and 1.9 keV was measured between 50 K and 300 K on the beam line 1A at UVSOR-II, Institute for Molecular Science. The luminescence was collected and guided by a lens in a UHV chamber to the monochromator (CP-200, JOBIN YVON) and detected by a multi-channel analyser (OMAIII, EG&G PRINCETON APPLIED RESEARCH), which covers the photon energies from ca. 1.5 eV to 4 eV.

Results and Discussion

We selected three excitation X-ray energies of 1834 eV (just below the Si *K*-edge), 1848 eV (on the white line) and 1858 eV (well above the threshold). Fig. 1(a) shows observed XEOL spectra from the sample excited by the three different energies, measured at room temperature. An intense emission band peaked around 3.1 eV is observed in each spectrum. The previous studies assigned the origin of the 3.1 eV band to the intrinsic $B_{2\beta}$ center [1,2]. We reported previously that in-reactor or UV irradiation on silica glasses induced similar emission bands, and this emission band can be induced also by the soft X-ray irradiation, presumably by exciting the electrons trapped at the oxygen-deficient sites.

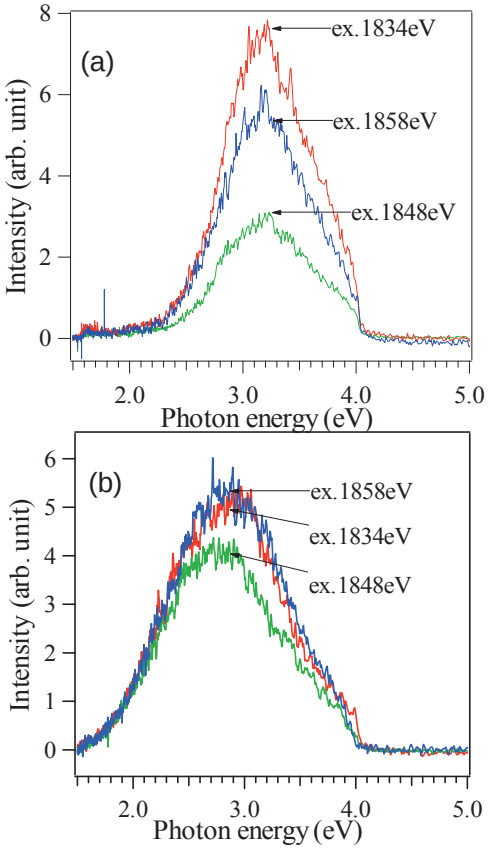

Fig. 1 Optical luminescence spectra of a fused silica glass excited by X-rays with the energies of 1834, 1848 and 1858 eV at (a) 300 K and (b) 50K. Solid curves are two Gaussians peaked at 2.6 and 3.1 eV, resulting from the peak fit for the profile at 1848 eV.

We also measured XEOL at lower temperatures, and found the broadening of the emission band below 100 K. Fig. 2(b) shows XEOL of the same sample measured at 50 K. A peak position is shifted to the lower energy side, because an additional emission band appears around 2.6 eV, revealed by the peak fit, as shown in Fig.2 (b). This additional emission band occurs, presumably because the excited electrons survive longer at lower temperatures until relaxed to the corresponding energy level(s).

[1] R. Tohmon, H. Mizuno, Y. Ohki, K. Sasagane, K. Nagasawa, Y. Hama, Phys. Rev. B **55** (1989) 1337.
[2] S. Agnello, R. Boscaino, M. Cannas, F. M. Gelardi, J. Non-cryst. Solids **232-234** (1998) 323.

BL1A

Atomic Structure of Supersaturated ZnO-Al_2O_3 Solid Solutions

I. Tanaka, S. Yoshioka, F. Oba, T. Yamamoto
Department of Materials Science and Engineering, Kyoto University, Kyoto 606-8501, Japan

X-ray absorption near-edge structure (XANES) is known to be a powerful tool to probe local electronic structure because of its sensitivity to change in chemical environment. It allows us to access the local structure of dopants, utilizing the element selectivity. In the present study, we investigate the local structure of Al solute atoms in ZnO by XANES. Samples are supersaturated solid solution synthesized by pulsed laser deposition (PLD) technique. First-principles calculations are systematically made to evaluate the local atomic structures and energetics. Theoretical XANES is also obtained by first-principles calculations to interpret the experimental spectra.

Experimental and Computational Procedures

Thin film samples were prepared by PLD technique using an excimer KrF* laser source (λ= 248 nm, τ = 25 ns, Lambda physik COMPex205). Laser frequency was kept at 10 Hz. The ceramic samples were used for targets of PLD. Laser power was approximately 3×10^4 J/m^2. All PLD experiments were made in oxygen backfill pressure of p_{O2}=0.3Pa. High purity SiO_2 glass plates were used as substrates. Substrate temperature was 600 ºC. High-resolution X-ray absorption spectra at the Al K-edge were measured using the BL1A beamline at UVSOR. The XANES spectra were collected by the total electron yield (TEY) method. The incident photon beam was monochromatized using a KTP ($2d_{011}$=10.954Å) double-crystal monochromator. Samples were mounted using adhesive carbon tapes. No surface coating to avoid charging was found to be necessary.

In order to reproduce XANES by theoretical calculations, it is necessary to take into account the correlation between the core-hole and the excited electron. [1] It can be evaluated in a straightforward way using all-electron methods. Therefore, first-principles all-electron calculations based on orthogonalized linear combination of atomic orbitals (OLCAO) method [2] were employed in the present study. Theoretical XANES spectra were obtained within the electronic-dipole transitions. The core-hole effects were fully taken into account by removing one electron on Al 1*s* orbital and putting one additional electron at the bottom of the conduction band. In order to avoid the artificial interactions among core-holes, supercells composed of more than 100 atoms were chosen on the basis of test calculations. Transition energies were obtained as the difference in total energy between the ground and core-hole states. More details of the XANES calculation and its application to dopant characterization can be found elsewhere. [1, 3]

Results and Discussion

X-ray diffraction (XRD) analysis found that ZnO:Al films with Al concentration of less than 19 cation% are composed of a single crystalline phase. It can be assigned as a wurtzite phase with an abnormal expansion in lattice constant *c* by 1.5%. Experimental and calculated XANES are shown in Fig 1. The spectral features of experimental thin film sample are different from those of the reference compound, $ZnAl_2O_4$ having spinel structure. The spectrum is closer to the theoretical spectrum for Al_{Zn} model where Al is located at the substitutional Zn site of wurtzite ZnO. However, this model is found to be inconsistent to the XRD results revealing lattice expansion in the *c* direction. Systematic evaluation of theoretical lattice constants and XANES spectra for models with miscoordinated Al indicates that partial contribution of such Al can provide a consistent explanation of the structural and spectral features.

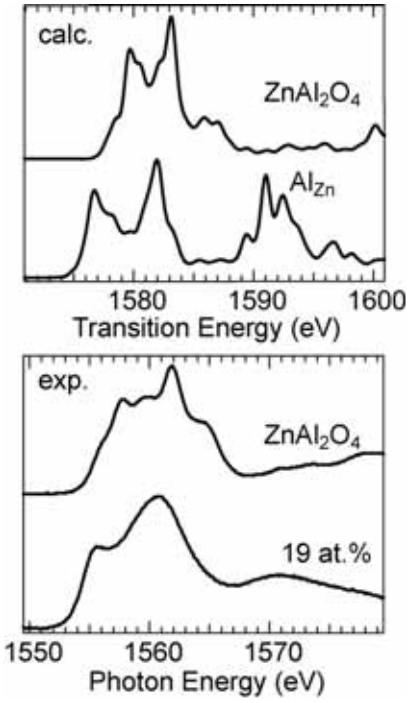

Fig. 1. Theoretical and experimental Al K-edge XANES spectra for $ZnAl_2O_4$ and Al-doped ZnO.

[1] I. Tanaka, T. Mizoguchi, and T. Yamamoto, J. Am. Ceram. Soc. **88** (2005) 2013.
[2] W. Y. Ching, J. Am. Ceram. Soc. **73**, 3135 (1990).
[3] I. Tanaka *et al.*, Nature Mater. **2** (2003) 541.

BL1A

Structural Analysis of Active Mo species on H-MFI for Methane Dehydroaromatization with Hydrogen

H. Aritani[1], N. Naijo[1], K. Takanashi[1], H. Orihara[1], A. Nakahira[2]
[1]*Faculty of Engineering, Saitama Institute of Technology, Fukaya 369-0293, Japan*
[2]*Graduate School of Engineering, Osaka Prefecture Universitty, Sakai 599-8531, Japan*

Supported Mo catalysts on H-MFI zeolites show noted high and selective activity to convert methane to benzene. Because the catalytic process, so-called "GTL (Gas to Liquid)" one, is conventional and quite selective for liquefaction of natural gases, catalysts with high and durable activity have been called for. However, design of the catalysts with durable activity for methane dehydroaromatization is very difficult because of carbon deposition and/or grafting during the reaction. For MoO_3/H-MFI, Mo species are reduced to form several types of carbide species (Mo^{2+} mainly) in the initial reaction step (at above 973 K), and the carbide species play a role for methane activation to form CH_x intermediates. At the same time, H_2 is outgassed. On H-MFI support, oligomerization of CHx intermediates assist to form benzene. Selectivity of benzene formation is based on the sieving by microporous structure of H-MFI. Therefore, relation between the H-MFI support (with surface acidity) and active Mo species formed in the reaction is thus important to clarify the formation process and its stability of highly active Mo.[1,2] In this study, Mo L_{III}-edge XANES is applied to characterize the Mo species on H-MFI with various SiO_2/Al_2O_3 ratios.

All the catalysts were prepared by impregnation of each silica-alumina support with ammonium heptamolybdate solution (7.5wt% loading as MoO_3), and followed by drying and calcination at 773 K for 3 h. H-MFI (Si/Al_2=40, 72, 90, and 1880) supports were synthesized hydrothermally at 443 K for 7 days, and followed by ion-exchange (NH_4^+) treatment and calcination at 773 K. Mo L_{III}-edge XANES spectra were measured in BL1A of UVSOR-IMS in total-electron yield mode at ambient temperature.

For evaluation of catalytic activitty for methane dehydroaromatization at 973 K, it is concluded that MoO_3/H-MFI(Si/Al_2=40) in low Mo contents (2.5-5.0 wt% as MoO_3) shows the maximun benzene yield in an initial streaming range. In this case, deactivation due to carbon deposition can not be avoided. It is definitely that rate of deactivation becomes low by coexistence of H_2 (CH_4/H_2=20) in the reaction. Figure 1 shows the L_{III}-edge XANES spectra of MoO_3(5.0wt%)/H-MFI(Si/Al_2=40) catalysts after methane dehydroaromatization with/without H_2. Second derivatives of XANES spectra are also shown in Fig. 2. After the reaction with CH_4 (denoted as [A]), Mo_2C-like species are formed, indicating a reduction and carbinding of Mo ions. Because of partially oxidized (due to coexistence of Mo^{4+} or others), spectral feature is slightly different from that of Mo_2C. [2] It indicates that highly active Mo species are consist of Mo2C (in major) and partially oxidized species such as oxycarbide species. After the reaction with CH_4+H_2 (denoted as [B]), the spectrum is quite similar to that of CH_4 reaction. Thus H_2 coexistence brings about depression of coaking but be independent on reduction of active Mo species. In case of H2 reduced catalysts in a pretreatment, the spectrum (denoted as [C]) is quite similar to bare Mo_2C. In this case, low dehydroaromatization activity is shown. It is concluded that excess reduction enhance the formation of Mo2C species, and low activity is brought about at the same time.

[1] H. Aritani et al., UVSOR Activity Report, **33**, (2006) 92.
[2] H. Aritani et al., Chem. Lett. **35** (2006) 416.

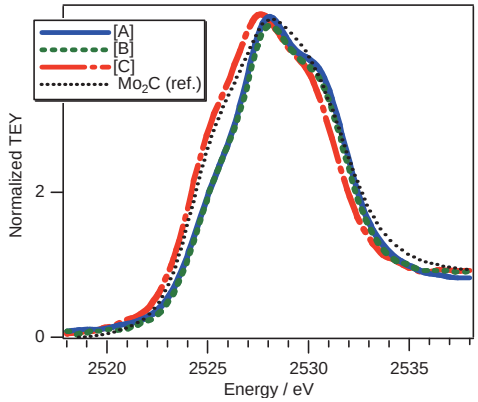

Fig.1 Mo L_{III}-edge XANES of 5wt% MoO_3/H-MFI (Si/Al_2=40). [A] After reaction with CH_4(20%)+He.; [B] After reaction with CH_4(20%)-H_2(1%)-He.; [C] After pretreatment with H_2 and reaction with CH_4 (20%)-H_2(1%)-He.

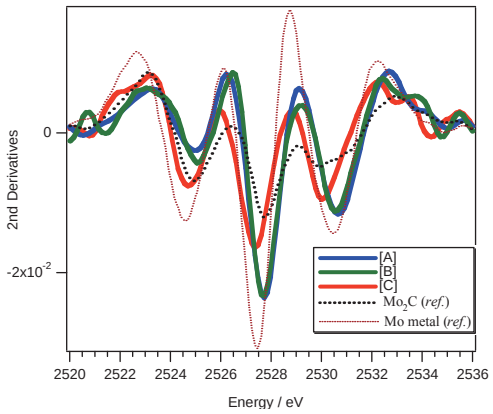

Fig. 2 Mo L_{III}-edge XANES of 5wt% MoO_3/H-MFI (Si/Al_2=40). [A] After reaction with CH_4(20%)+He.; [B] After reaction with CH_4(20%)-H_2(1%)-He.; [C] After pretreatment with H_2 and reaction with CH_4(20%)-H_2(1%)-He.

Unoccupied Electronic States of Inner Organic Thin Films: Soft X-ray Absorption Spectra of Pentacene Derivative Films

H.S. Kato[1], R. Hirakawa[1,2], F. Yamauchi[1,2], M. Kawai[1,2], T. Hatsui[3], N. Kosugi[3]
[1]*RIKEN (The Institute of Physical and Chemical Research), Wako 351-0198 Japan*
[2]*Dept. of Advanced Materials Science, Univ. of Tokyo, Kashiwa 277-8651 Japan*
[3]*Dept. of Vacuum UV photoscience, Institute for Molecular Science, Okazaki 444-8585 Japan*

Introduction

In order to extend new functionality of electronic devices, the molecular devices have recently been investigated with great efforts. In most of the devices, the properties of organic molecules are controlled by the applied electric field and charge injection. The organic field effect transistor (OFET) is the typical molecular device that controls of electric conductivity by injection of carriers into the organic thin film under the applied electric field. Based on the knowledge of inorganic semiconductor transistors, the conductive mechanism has generally been understood with a scheme of band bending of electronic states. However, the energy diagram may not be the same between inorganic and organic materials, because of more localized orbitals of the organic molecules. It is also important to elucidate the difference of electronic states for using the noble characters of organic molecular materials for the future advanced devices. Therefore, the direct observation of electronic state changes in the organic thin films under the applied electric field has been required.

In this study, we aim to establish a new experimental method that elucidates the electronic state change in organic molecular thin-films under the electric field, using model OFET devices. In general, X-ray absorption spectroscopy (XAS) is measured by the detection of Auger electrons emitted after X-ray absorption. However, the mean free path of the electrons, typically less than 1 nm, in bulk is too short for detection of the electronic states of inner organic thin films, of which typical thickness is about 100 nm. Thus, we attempted the fluorescence yield detection for XAS.

Experimental

The XAS measurements were carried out at BL4B and BL3U of UVSOR facility in IMS. We fabricated 6,13-dihydrodiazapentacene thin films on the SiO_2-covered Si substrates using a deposition system in RIKEN. Then, the samples were set in the measurement chamber at BL3U through ambient conditions. The typical base pressure at the XAS measurements was less than 10^{-5} Pa. Both the Auger electron yield and the fluorescence yield were observed using a retarding-field detector equipped with MCP plates.

Results and Discussion

The N K-edge XA spectra of the same 6,13-hydrodiazapentacene film (t = 100 nm) on SiO_2-covered Si substrate by detecting both the Auger electron yield and the fluorescence yield, as shown in Figs. 1(a) and 1(b), respectively. In both measurements, the photon energies of each component are almost the same, while the relative intensities are different.

One of the obvious differences is the detection of a peak at 398 eV. The intense peak is characteristic in the Auger electron yield spectra that are surface sensitive. Since its relative intensity increased with increasing time of ambient gas exposure, the origin of the peak would be an attachment of any impurities or surface oxidation. Thus, we concluded that the fluorescence yield spectra show the intrinsic electronic state of 6,13-dihydrodiazapentacene, which has also been supported by a molecular orbital calculation of the isolate molecule. In the fluorescence spectra, the observed π^* and σ^* peaks have clear incidence angle dependence. These evidence a good oriented structure of the molecules in the inner thin film, as the pentacene thin films on flat substrates.

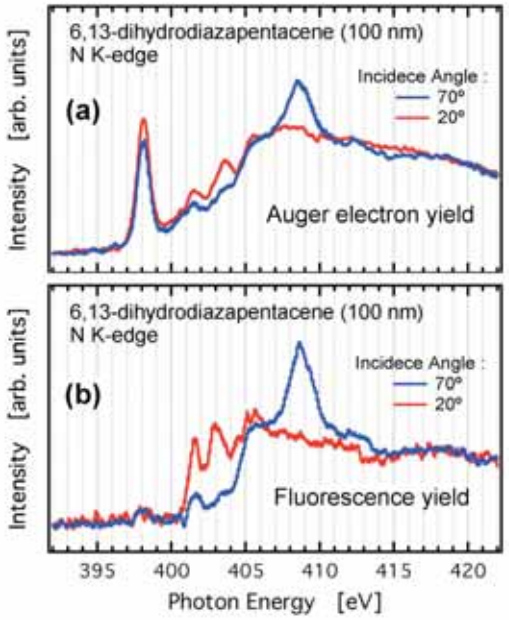

Fig. 1. N K-edge XA spectra of a 6,13-dihydrodiazapentacene film (t = 100 nm) on SiO_2-covered Si substrate: (a) Auger electron yield spectra, (b) fluorescence yield spectra. In both measurements, incidence angle dependence was performed at 70° and 20° from the surface normal, and then the intensity of the spectra was normalized by a height at around 420 eV in photon energy.

BL4B

Study on the Surface and Bulk Structures of the Positive Electrode for Li-Ion Battery Cells with High Power-Type

H. Kobayashi, M. Shikano

Research Institute for Ubiquitous Energy Devices, AIST, Ikeda, Osaka, 563-8577 Japan

Several of the requirements of rechargeable batteries for hybrid electric vehicles (HEVs) are quite different to those of portable electronic devices. In particular, high specific power and long calendar life are very important requirements of HEV applications. Much effort has been applied to understanding the mechanisms that limit the calendar life of high power Li-ion cells. Until now, although the deterioration in the performance of currently available lithium batteries is thought to result from problems with the positive electrodes, the mechanism of deterioration of the electrodes is still poorly understood. Detailed information on the changes taking place in both the cathode and anode on cycling is essential in order to determine the origin of the degradation of performance. In this study, $LiNi_{0.8}Co_{0.2}O_2$-based positive electrodes from cells that had undergone power fading through cycling tests were examined by XANES analysis to obtain information on their surfaces. The relationship between power fade and the surface state of the positive electrode will be studied.

Experimental

We used cylindrical battery cells of capacity 400 mAh for this study, which were designed to have a rate capability of more than 10 C. The positive and negative electrode was comprised of $LiNi_{0.8}Co_{0.2}O_2$ -based oxides and hard carbon, respectively. Each cell was characterized using the standard battery test procedure given in PNGV Battery Test Manual. The change in DC resistance was checked every few cycles. After completion of the degradation test, the SOC of the cell was adjusted to 0% immediately before disassembling it, since the chemical and physical properties of the active materials are influenced by the SOC. After disassembly of the SOC-adjusted cell, the surface of the positive electrode was examined by XANES in order to study the surface film or phase transitions in particles of the active material. The O K-edge XANES spectra of the samples were measured on the BL4B beamlines of the UVSOR Facility. Data were obtained in the total electron yield (TEY) and fluorescence yield (FY) modes.

Results

Figure 1 shows the cycle dependence of the DC resistance. DC resistance increased from 1.08 to 1.74 on increasing the test temperature from 20 ºC to 80 ºC. Above 80 ºC, an abrupt increase in DC resistance was observed. Figure 2 shows the O K-edge XANES spectra of 0% SOC samples before and after test. In TEY mode, O K-edge XANES spectra provide information on the surface structure. The spectrum measured before cycle testing contained peak A, corresponding to oxygen originating from the layered structure, and peaks B and C. After the cycle tests, the intensity of peak A clearly decreased at 80 ºC, while the intensities of peaks B and C showed no significant changes. The position of peak B was close to that of the NiO spectrum, indicating the existence of a cubic phase on the surface, and the position of peak C was close to that of Li_2CO_3, or to conductive materials such as AB (data not shown). When measured in FY mode, O K-edge XANES spectra provide information on the bulk structure. Here, essentially the same spectra were observed before and after the cycle tests for both samples. The strong peak A originating from the layered structure of the positive electrode was observed in FY mode. However, peak B was absent and peak C was much lower in intensity. These results indicate that the surface structure is different to that of the bulk in this system. Furthermore, it is clear that part of the layered structure at the surface of the $LiNi_{0.8}Co_{0.2}O_2$ -based positive electrode was transformed to a cubic structure at 80 ºC, although the layered structure was retained in the bulk.

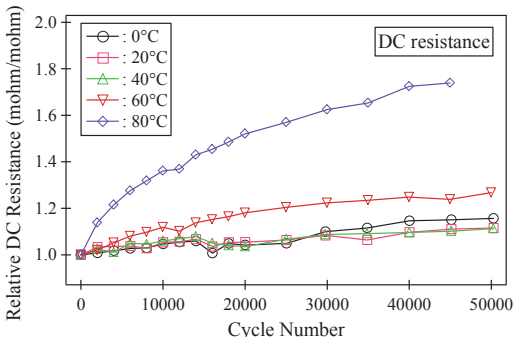

Fig.1 Cycle dependence of retention of DC resistance.

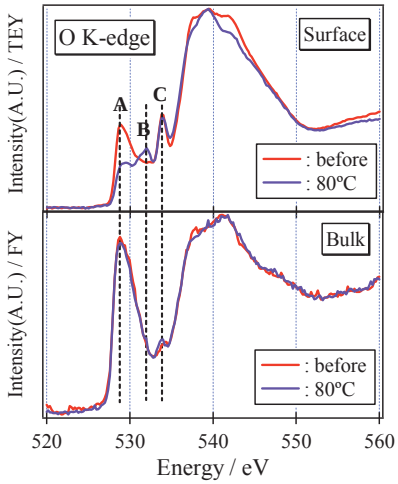

Fig.2 O K-edge XANES spectra for the positive electorrode after 45000 cycle test at 80 ºC.

BL5U

Core-Level Photoemission Study of Alkyl-Passivated Si Nanoparticles

A. Tanaka[1,2,3], T. Kamikake[2], K. Tomio[1], N. Takashima[4], M. Imamura[3], Y. Murase[2]
[1]*Department of Mechanical Engineering, Faculty of Engineering, Kobe University, Kobe 657-8501, Japan*
[2]*Department of Mechanical Engineering, Graduate School of Science and Technology, Kobe University, Kobe 657-8501, Japan*
[3]*Department of Mechanical and Systems Engineering, Graduate School of Science and Technology, Kobe University, Kobe 657-8501, Japan*
[4]*Department of Physics, Faculty of Science and Engineering, Konan University, Kobe 658-8501, Japan*

Introduction

Recently, the various Si nanostructures have a great interest, since it has been reported that they show a strong visible photoluminescence and a possibility of future integrating electronic devices with optical sensing technique is suggested. However, the interplay to their optical properties between the intrinsic quantum confinement effects and extrinsic surface/interface properties is still controversial. In order to understand the intrinsic properties of Si nanostructures, it is indispensable to characterize their surface chemical properties. In this work, we have carried out the core-level photoemission studies of alkyl-passivated Si nanoparticles synthesized by the solution routes in order to characterize their surface electronic structures.

Experiment

Synthesis procedure of *n*-butyl-passivated Si nanoparticles used in this work is described elsewhere [1]. Core-level photoemission measurements were performed at BL-5U of UVSOR II Facility.

Results and Discussion

Figure 1 shows the Si 2*p* core-level photoemission spectrum of *n*-butyl-passivated Si nanoparticle with mean diameter of 1.4 nm. As shown in Fig. 1, it is found that the present Si 2*p* core-level spectrum is reproduced by two components fairly well. From the analogy with the previous results of alkyl-terminated bulk-Si(111) surfaces [2], the lower- and higher-binding-energy features originate from the inner Si atoms of Si nanoparticles (bulk component) and surface Si atoms of Si nanoparticles bonded to surface-passivants of *n*-butyl groups (surface component), respectively. As shown in Fig. 1, this surface component accompanies with the chemical shifts to higher binding energies relative to the bulk components. This indicates the different chemical states in the surface Si atoms bonded to *n*-butyl groups with the inner Si atoms and existence of a chemical reaction (chemisorption) between the surface-passivants of *n*-butyl groups and Si nanoparticles. It has been reported in the previous work [2] that the chemical shifts for surface Si atoms of methyl- (CH_3-), pentyl- (C_5H_{11}-), and decyl- ($C_{10}H_{21}$-) terminated bulk-Si(111) surface are 0.27, 0.21, and 0.21 eV, respectively. On the other hand, the chemical shift of *n*-butyl-bonded Si atoms of the present Si nanoparticles is 0.33 eV. An important point to note is that the chemical shift of the surface component in the present Si nanoparticle is significantly larger than those of surface components of alkyl-terminated bulk Si surfaces. This indicates that the interfacial features between the surface Si atoms and surface passivants of alkyl groups, and therefore the bonding natures between the surface-passivants of alkyl groups and surface Si atoms, such as a coordination number and configuration of surface-passivants, are different among the bulk Si surface and Si nanoparticle surface.

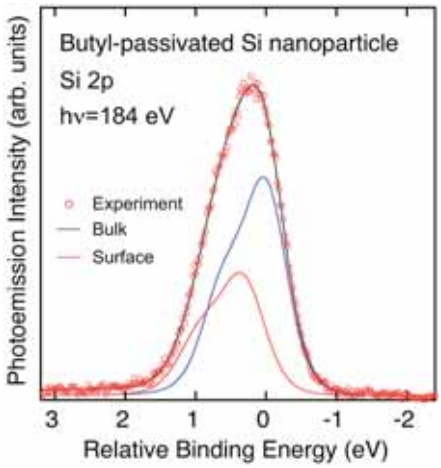

Fig. 1. Si 2*p* core-level photoemission spectrum of *n*-butyl-passivated Si nanoparticle with mean diameter of 1.4 nm measured with $h\nu$=184 eV. Result of line-shape analysis is also shown. Observed spectrum is decomposed into bulk component (blue line) and surface component bonded to surface *n*-butyl molecules (red line).

[1] A. Tanaka *et al*., Solid State Commun. **140** (2006) 400.
[2] J. Terry *et al*., J. Appl. Phys. **85** (1999) 213.

BL5U(FEL)

Threshold Photoemission Magnetic Circular Dichroism using Free Electron Laser

T. Nakagawa, T. Yokoyama, M. Hosaka, M. Katoh
Department of Electronic Structure, Institute for Molecular Science, Okazaki 444-8585 Japan
UVSOR Facility, Institute for Molecular Science, Okazaki 444-8585 Japan

Introduction

Magnetic circular dichroism (MCD) in the x-ray regions (XMCD) has widespread over the synchrotron radiation facilities because of its high sensitivity to the element specific magnetism. On the other hand, MCD in the regions from infrared to ultraviolet (UV) is also a useful tool for the study of ferromagnetic ultrathin films. The magneto-optical Kerr effect (MOKE) detects the rotation and distortion of the polarization of reflected lights from magnetic materials. The Kerr effect in valence bands in thin films usually rotates the polarization and changes the ellipticity only by 10^{-2}-10^{-6}rad. In the valence band photoemission, nevertheless, extensive works have been performed using circularly polarized synchrotron radiation and angle-resolved measurement, showing high (~30%) asymmetry. [1,2]

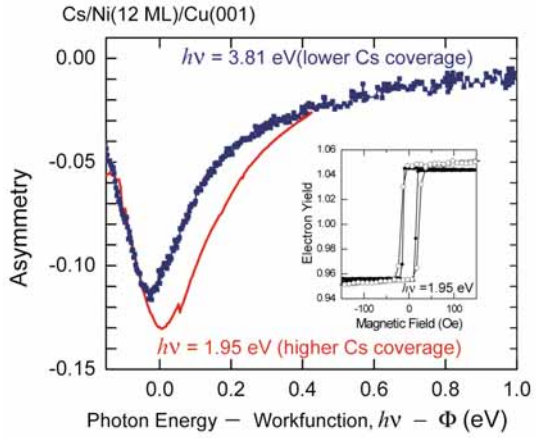

Fig. 1 MCD asymmetry as a function of maximum kinetic energy(photon energy–work fuction) on perpendicularly magnetized Ni(12ML)/Cu(001). The photon energies used are 1.95 eV and 3.81 eV. The inset shows magnetization hysteresis curves by MCD and MOKE measurements, which are identical to each other.

We have investigated the observation of enhanced MCD near the Fermi level using visible and ultraviolet lasers in a total yield mode. [3] More than 10% MCD asymmetry is achieved on perpendicularly magnetized 12 ML Ni film on Cu(001), and magnetization curves are obtained. By changing the work function with the aid of cesium adsorption, the laser experiments show that the MCD asymmetry is enhanced only near the photoemission threshold, and that the asymmetry drops to 0.1% for photon energy larger than the work function by 0.6 eV. A theoretical calculation also shows enhanced dichroism near the photoemission threshold, in agreement with the experimental result.

To obtain the high MCD asymmetry we have to tune the photon energy a little higher than the workfunction. We have used tunable free electron laser from UVSOR-II, which can deliver lower energy than $h\nu$ = 6.3 eV, close to typical workfunction for transition metal surfaces without surface modification such as alkali metal adsorption. Thus FEL at UVSOR-II is a suitable source to threshold photoemission MCD measurements. Fig. 2 shows a magnetization hysteresis curve on Ni(8 ML)/Cu(001) using $h\nu$ = 5.37 eV, where the photoemission threshold for Ni is ~5.3 eV. As is expected from the result shown in Fig. 1, the asymmetry is high, ~6%. This result clearly evidences that the clean Ni surface also shows high asymmetry near the photoemission threshold.

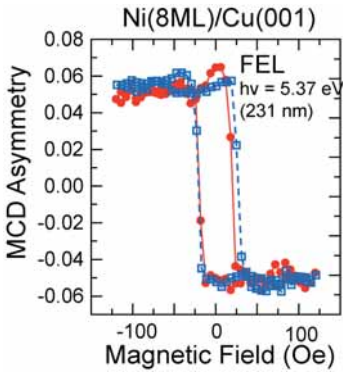

Fig. 2 Magnetization hysteresis curves on a clean eight monolayer Ni film grown on Cu(001) obtained by FEL-MCD and MOKE. The photon energy of FEL is 5.37 eV.

[1] C. M. Schneider, *et al*., Phys. Rev. B **44** (1991) R12066.
[2] W. Kuch and C.M. Schneider, Rep. Prog. Phys. **64**(2001) 147.
[3] T. Nakagawa, and T. Yokoyama, Phys. Rev. Lett. **96**(2006) 237402.
[4] T. Nakagawa, T. Yokoyama, M. Hosaka, and M. Katoh, Rev. Sci. Instrum. **78** (2007) 023907.

Adsorpiton of Benzene on Au(111) Surface by Angle-Resolved Ultravoilet Photoemission Spectroscopy

L. Wang[1], D. Qi[1], A. T. S. Wee[1], T. Mochizuki[2], H. Miyazaki[2], T. Ito[3], S. Kimura[3], J. Yuhara[2], K. Soda[2]

[1]*Department of Physics, National University of Singapore, Singapore 117542*
[2]*Graduate School of Engineering, Nagoya University, Nagoya 464-8603 Japan*
[3]*UVSOR Facility, Institute for Molecular Science, Okazaki 444-8585 Japan*

Introduction

Molecules have been shown to operate as Coulomb blockade structures, diodes, switching devices with high negative differential resistance (NRD) and conductance switches, making the nascent field of molecular electronics very promising[1]. The central issue in molecular electronics is the characteristics of the molecule-metal interface which strongly influences the transport properties in the molecular device[2]. Benzene/Au system is chosen as testbed since benzene is a typical molecule with delocalized π orbitals and gold is one of the most widely used substrate. In this study, the adsorption of benzene on Au(111) surface have been investigated by angle-resolved photoemission spectroscopy.

Experimental

Au(111) surfaces were prepared by cycles of Ar^+ ion bombardment at 1 KeV and annealing at 800 K in an ultrahigh vacuum system. The (1x1) reconstruction was clearly observed on clean Au (111) surface by low energy electron diffraction. Benzene (99%, company name) was *in situ* evaporated onto Au(111) surface which was cooled down to 5 K. One monolayer of benenze on Au was achieved by introducing the dosage of 1 Lagmuir assuming the stick coefficient =1. Angle-resolved photoelectron spectra were recorded under 2.7×10^{-8} Pa with a high-resolution energy analyzer at BL5U. The total energy resolution was 14 meV with the excitation photon energy of 29.3 eV at 5 K.

Results and Discussion

Figures 1 show the photoemission intensity of surface state on clean Au(111) along [$\bar{1}$10] direction. A dispersion near the Fermi edge with the maximum binding energy of 430 meV at Γ point can be clearly observed, which is consistent with that for Shockley-type surface state on Au(111) [3].

Figure 2 shows the angle-integrated valence band spectra for benzene mononlayer adsorbed on Au(111) at the various temperatures. After the adsorption, some noticeable features, which are originated from benzene molecules[4], emerge in the binding energy range from 8-14 eV. On the other hand, the Shockley-type surface state of Au(111) is immediately extinguished, indicating the presence of a strong interaction between the benzene molecules and the gold surface. This interaction can not be described only as purely physical interaction.

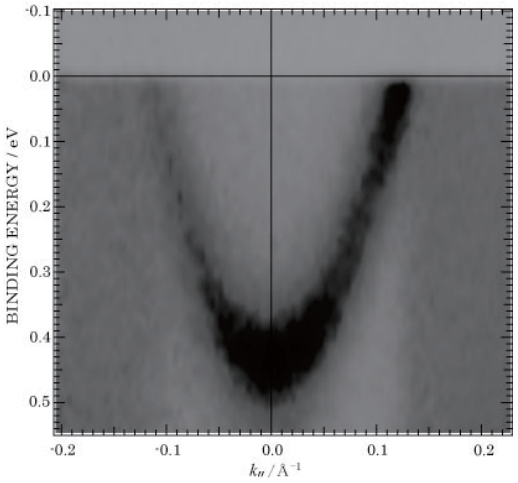

Fig.1 Photoemission intensity of Schockely-type surface state on clean Au(111) along [$\bar{1}$10] direction as a gray scale.

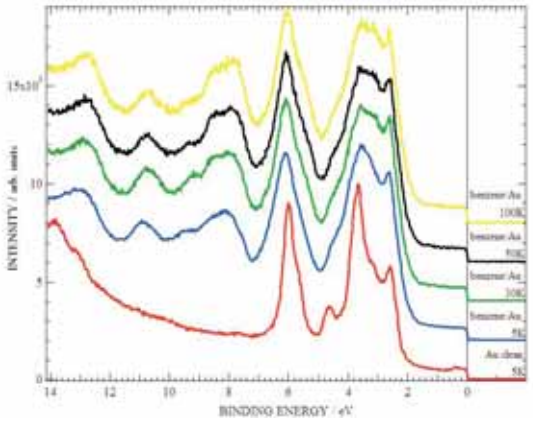

Fig.2 Angle-integrated valence band spectra for clean Au(111) and benzene/Au(111) at various temperatures.

[1] M. A. Reed *et al*., Science **278** (1997) 252; Z. J. Donhauser *et al*., Science **292** (2001) 2303.
[2] J. G. Kushmerick *et al*., Phys. Rev. Lett. **89** (2002) 086802; L. Wang *et al.*, J. Am Chem. Soc. **128** (2006) 8003.
[3] S. D. Kevan *et al*., Phys. Rev. B **36** (1987) 5809; R. Paniago *et al.*, Surf. Sci. **336** (1995) 113.
[4] Y. K. Kim *et al.,* Phys. Rev. B **71** (2005) 115311.

BL5U

Electronic Structure and Stability of the Pd-Ni-P Bulk Metallic Glass

T. Takeuchi[1], D. Fukamaki[2], H. Miyazaki[3], K. Soda[3]
T. Itoh[4], S. Kimura[4]

[1]*EcoTopia Science Institute, Nagoya University, Nagoya 464-8603 Japan*
[2]*Department of Applied Physics, Nagoya University, Nagoya 464-8603 Japan*
[3]*Department of Quantum Mechanics, Nagoya University, Nagoya 464-8603 Japan*
[4] *Institute for Molecular Science, Okazaki 444-8585 Japan*

Bulk metallic glasses (BMGs) have attracted a great deal of interests because of their ability in practical usage, such as mechanical parts of high strength, surface coating materials with high degree of hardness, soft-magnetic materials, etc. In order to design the BMGs suited for each practical usage, stabilization mechanism of the BMG's has to be revealed from microscopic viewpoints; the local atomic arrangements and the electronic structure. Since it is naturally considered that the highly-stable BMGs possess a low free-energy, the stabilization mechanism of BMG's should be discussed in terms of free-energy, which is mostly determined by the electronic structure.

We investigate, in this study, the electronic structure of the Pd-Ni-P BMG, that is one of the most famous, stable BMGs obtained in metal-metalloid systems, by employing the relevant crystals with the first principle cluster calculation, band calculation, and high-resolution photoemission spectroscopy. By calculating electronic structure of the relevant crystals, in which the structure units of the BMG (trigonal prism clusters with a phosphorus atom in the center) are formed, we found that the these units (trigonal prism clusters) possess covalent nature and highly stable. The formation of the covalent bonds in the clusters (relevant crystals) was further confirmed by observations of the bonding bands in the high-resolution photoemission spectra.

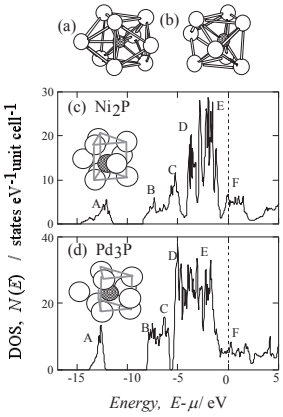

Figure 1 (a)Trigonal prism cluster and (b)tetragonal dodecahedron cluster (deformed trigonal cluster) exist in the Pd-Ni-P bulk metallic glass. Electronic density of states of the relevant crystals, (c) Ni2P, and (d) Pd3P calculated by the FLAPW-GGA method (Wien2K). The density of states of the relevant crystals are commonly characterized by possession of the narrow bands marked as A - F. The bands A-C are bonding bands, while the corresponding anti-bonding bands exist far above E_F. The bands D and E are nearly non-bonding d-bands. These configurations provide a strong covalent nature.

We also calculated the cluster-orbitals of large clusters consisting of two trigonal clusters with different inter-cluster-connections, and found that the electronic structure does not significantly altered by the inter-cluster connection with keeping the bonding-bands far below the Fermi level. This characteristic leads to flexible connections of the clusters. The trigonal clusters, therefore, are able to construct a random network to form the bulk metallic glass without significantly increasing their internal energy. The enhanced entropy and the small internal energy result in the very low free-energy of the BMG.

We conclude, therefore, that the Pd-Ni-P BMG is stable because of the random cluster network of the rigid, stable, large structure unit (cluster) of covalent nature. This stabilization mechanism is applicable for the Zr-based BMG's and even for the silica glasses, and, therefore, commonly acceptable for highly-stable amorphous solids.

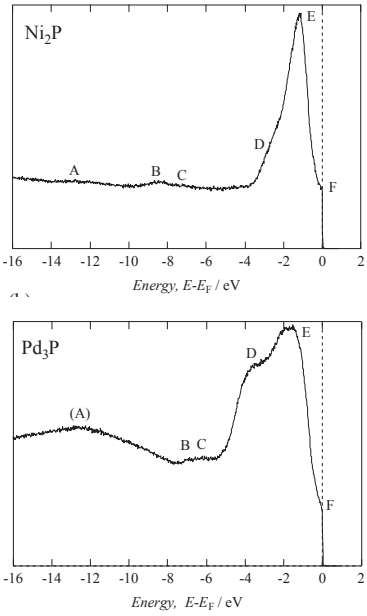

Figure 2 High-resolution photoemission spectra of the (a)Ni2P and (b)Pd3P measured with an incident energy of 40eV. The characteristics of electronic structure expected from band-calculation and cluster-calculation are qualitatively reproduced in the spectra.

BL5U

Electronic Structure of Pd-Ni-P Bulk Metallic Glass

S. Ota[1,2], T. Suzuki[1], H. Miyazaki[1,2], K. Soda[1,2], T. Takeuchi[3],
M. Hasegawa[4], N. Nishiyama[5], H. Sato[6], U. Mizutani[7], T. Ito[2], S. Kimura[2]
[1]*Graduate School of Engineering, Nagoya University, Nagoya 464-8603 Japan*
[2]*Institute for Molecular Science, Okazaki 444-8585 Japan*
[3]*EcoTopia Science Institute, Nagoya University, Nagoya 464-8603 Japan*
[4]*Institute for Materials Research, Tohoku University, Sendai 980-8577 Japan*
[5]*R&D Institute of Metals and Composites for Future Industries, Sendai 980-8577 Japan*
[6]*Aichi University of Education, Kariya 448-8542 Japan*
[7]*Toyota Physical and Chemical Research Institute, Nagakute-cho, Aichi-gun 480-1192 Japan*

Introduction

Bulk metallic glasses (BMG) possess excellent mechanical, physical and chemical properties, which come from their amorphous structure. In spite of their thermodynamical metastability, Pd-based BMG have large glass forming ability (GFA) [1]. In order to understand the mechanism of their large GFA, we have studied the electronic structure of $Pd_xNi_{80-x}P_{20}$ BMG by photoemission spectroscopy (PES) and theoretical calculation for local clusters expected in BMG.

Experimental

The PES measurement was carried out at 25 K under 2×10^{-8} Pa. $Pd_xNi_{80-x}P_{20}$ specimens were prepared by a casting method and their clean surfaces were obtained by *in situ* scraping with a file.

The theoretical calculation was performed by the DV-$X\alpha$ method with a code SCAT [2] for a Pd_3Ni_6P cluster in a form of a capped trigonal prism, which is derived from a crystalline $PdNi_2P$ [3].

Results and Discussion

Valence-band spectra of $Pd_xNi_{80-x}P_{20}$ recorded at excitation photon energies $h\nu$ are shown in Fig.1. They were normalized by the integrated intensity up to the binding energy E_B of 10 eV. There are three bands at $E_B \sim 0.8$, 2.2, and 3.9 eV, which are ascribed to the Ni 3*d*-, Pd 4*d*-, and Pd 4*d*-derived states, respectively, judging from the $h\nu$-dependence of their photoionization cross sections [4]. The spectral shape for $x = 45$ is not so much different from one for $x = 40$, while the Ni 3*d* band is relatively large for $x = 35$. There is almost no peak shifts for these bands.

In Fig.2, a spectrum recorded at $h\nu = 40$ eV is compared with the density of states calculated for the cluster in the inset, where a black sphere represents P at the center, green and blue ones for Pd at corners of the prism and a top of the cap, and yellow and pink ones for Ni at the corners and the tops, respectively. Taking account of the difference in photoionization cross sections [4], both results agree very well with each other. This suggests that the cluster may be a dominant form in $Pd_{40}Ni_{40}P_{20}$. The calculation also shows a strong P-(Pd, Ni) bonding. In the Pd-Ni-P BMG, the network of such clusters may be formed by sharing their vertices and sides with large flexibility in the inter-cluster bond direction, as in the silica glass.

[1] A. Inoue, Acta Mater. **48** (2000) 279.
[2] H. Adachi *et al*., J. Phys. Soc. Jpn. **45** (1978) 875.
[3] M.Vennstrom *et al*., J. Sol. Stat. Chem. **177** (2004) 1449.
[4] J. J. Yeh and I. Lindau, Atom. Data and Nucl. Data Tables **32** (1985) 1.

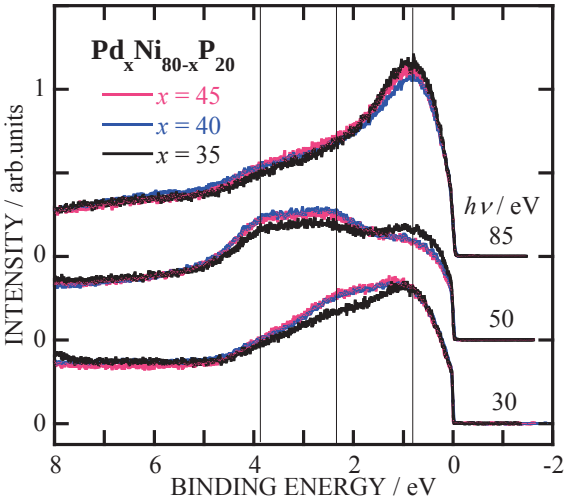

Fig.1 Valence-band spectra of $Pd_xNi_{80-x}P_{20}$.

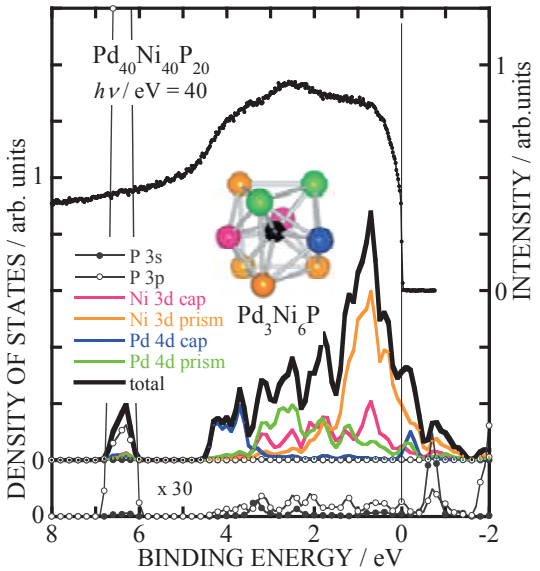

Fig.2 Valence-band spectrum of $Pd_{40}Ni_{40}P_{20}$ and calculated density of states for Pd_3Ni_6P cluster.

Electronic Structure of $(Fe_{1-x}Re_x)_2VAl$ and $Fe_2(V_{1-y}Ti_y)Al$

K. Yamamoto[1], H. Miyazaki[2,3], T. Mochizuki[2], T. Suzuki[2], S. Ota[2]
M. Kato[2], S. Yagi[2], Y. Nishino[4], K. Soda[2,3]
[1]*School of Engineering, Nagoya University, Nagoya 464-8603 Japan*
[2]*Graduate School of Engineering, Nagoya University, Nagoya 464-8603 Japan*
[3]*Institute for Molecular Science, Okazaki 444-8585 Japan*
[4]*Graduate School of Engineering, Nagoya Institute of Technology, Nagoya 466-8555 Japan*

Introduction

Heusler-type Fe_2VAl and its related alloys have attracted much attention because Fe_2VAl shows remarkable enhancement of thermoelectric power on partial substitution by the forth element [1]. In this paper, we will report results on the Fe and V 3*p*-3*d* resonance photoemission study of *p*-type alloys $(Fe_{1-x}Re_x)_2VAl$ and $Fe_2(V_{1-y}Ti_y)Al$ in order to clarify the relation between changes in their thermoelectric properties and electronic structure on the substitution.

Experimental

Photoelectron spectra were recorded at 20 K under 1.8 x 10^{-8} Pa. The origin of the binding energy E_B, the Fermi level E_F, and total energy resolution were determined by measuring the Fermi edge of a gold film. The total energy resolution was 63 meV at the photoexcitation energy $h\nu$ = 80 eV. Specimens used in this study were polycrystalline alloys of Fe_2VAl, $(Fe_{1-x}Re_x)_2VAl$ and $Fe_2(V_{1-y}Ti_y)Al$. Clean surfaces for the measurement were prepared by *in situ* fracturing the specimens.

Results and Discussion

Figure 1 shows typical valence band spectra recorded at $h\nu$ = 80 eV together with a bulk-sensitive one of Fe_2VAl at $h\nu$ = 900 eV [2]. In Fe_2VAl, there are a shoulder structure A near E_F and four bands B, C, D and E at E_B = 0.4, 0.8, 1.6 and 3.0 eV, respectively. The overall features agree well with those in theoretical density of states [3] and the bulk-sensitive spectrum except for the feature around E_F: the large intensity of the shoulder A observed in this study is attributed to surface states appearing in a pseudogap across E_F in the bulk electronic structure. On the partial substitution of Ti or Re, the shoulder A becomes indistinct with increase in the intensity at E_F and the valence band shifts to the low binding energy side as a whole, as expected in a rigid band model. This rigid-band-like shift results in the enhancement of their thermoelectric power.

Partial densities of Fe and V 3*d* states of Fe_2VAl and $(Fe_{0.95}Re_{0.05})_2VAl$, which were estimated by the 3*p*-3*d* resonance photoemission, are compared in Fig. 2 together with their valence-band spectra. By the Re substitution, the V 3*d*-derived band D shifts to the low binding energy side due to the interaction with the Re 5*d* states, while the Fe and V 3*d*-derived band C shows no shift and the intensity near E_F is relatively increased by the Fe 3*d* states: the band width of the Fe 3*d* states seems to be extended by the interaction between the Re 5*d* and Fe 3*d* states.

[1] Y. Nishino, The Science of Complex Alloy Phases (Ed. by T. B. Massalski and P. E. Turchi, TMS, Warrendale, 2005) p.325.
[2] K. Soda *et al.*, Phys. Rev. B **71** (2005) 245112.
[3] G. Y. Guo *et al.*, J. Phys.: Condens. Matter. **10** (1998) L 119.

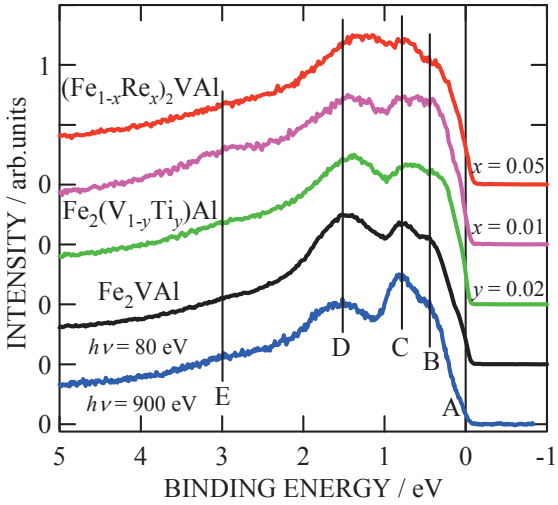

Fig.1 Valence band photoelectron spectra.

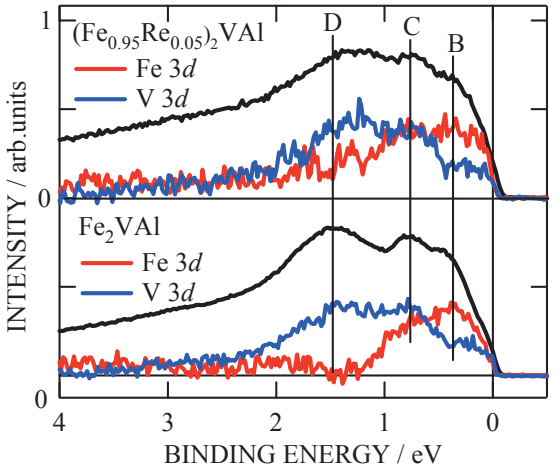

Fig.2 Partial densities of Fe 3*d* and V 3*d* states in Fe_2VAl and $(Fe_{0.95}Re_{0.05})_2VAl$.

Electronic Structure and Glass Forming Ability of Zr-Cu-Al Bulk Metallic Glasses

T. Suzuki[1], H. Miyazaki[1,2], S. Ota[1,2], M. Inukai[1], M. Kato[1], S. Yagi[1], K. Soda[1,2]
H. Kato[3], M. Hasegawa[3], T. Takeuchi[4], H. Sato[5], U. Mizutani[6], T. Ito[2], S. Kimura[2]
[1]*Graduate School of Engineering, Nagoya University, Nagoya 464-8603 Japan*
[2]*UVSOR, Institute for Molecular Science, Okazaki 444-8585 Japan*
[3]*Institute for Materials Research, Tohoku University, Sendai 980-8577 Japan*
[4]*EcoTopia Science Institute, Nagoya University, Nagoya 464-8603 Japan*
[5]*Aichi University of Education, Kariya 448-8542 Japan*
[6]*Toyota Physical and Chemical Research Institute, Nagakute-cho, Aichi-gun 480-1192 Japan*

Introduction

Bulk metallic glasses (BMG's) possess the large glass forming ability (GFA) and show physical, chemical and mechanical properties, which are superior to crystalline materials [1]. In order to understand the origin of their large GFA from the microscopic point of view, we have systematically studied electronic structure of Zr-Cu-Al BMG's using photoelectron spectroscopy.

Experimental

Photoelectron spectra were recorded under 2 x 10^{-8} Pa at 25 K at BL5U. Total energy resolution and the origin of the binding energy E_B, *i.e.* the Fermi level E_F, were determined by the Fermi edge of an evaporated Au film.

Specimens were ternary Zr-Cu-Al BMG's in a size of ϕ 1~2 mm x 3 mm. These compositions are shown in Fig.1 by symbols A ~ H with a counter map of their reduced glass temperatures T_g/T_l (T_g: glass transition temperature, T_l: liquidus temperature), which is regarded as one of parameters representing GFA. Clean surfaces for the photoelectron measurement were prepared by *in situ* scraping the specimen with a diamond file.

Results and Discussions

Figure 2 shows typical Zr 4*d* spectra of Zr-Cu-Al recorded at the excitation photon energy of 40.5 eV. These spectra are normalized with their Cu and Zr compositions so that the spectral intensity may be proportional to the density of occupied Zr 4*d* states per Zr atom. Arrows indicate peak positions of the Zr 4d bands. There is a tendency recognized that the peak binding energy and integrated intensity of the Zr 4*d* bands are increased with the Zr composition increasing from H to A. This may suggest the increase in the covalent interaction around Zr atoms with increasing the Zr composition.

The peak position (●) and integrated intensity (■) of the Zr 4*d* band are plotted as a function of T_g/T_l in Fig.3. As seen in the figure, they decrease as T_g/T_l increases: the covalent nature of Zr is relatively weak for Zr-Cu-Al with the large GFA. According to Nakano *et al.* [2], there are two typical local atomic arrangements appearing in Zr-Cu-Al: the Zr-centered covalent cluster and the Cu- or Al-centered metallic clusters, which have relatively low and high structural degree of freedom, respectively. Thus, the present results suggest that the weakening of the covalent nature of Zr and the increase in the structural degree of freedom may lead to the large GFA.

[1] M. Telford, Mater. Today **7** (2004) 36.
[2] S. Nakano *et al.*, *private communication.*

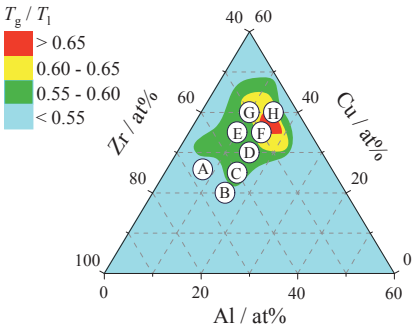

Fig.1 Compositional dependence of T_g/T_l

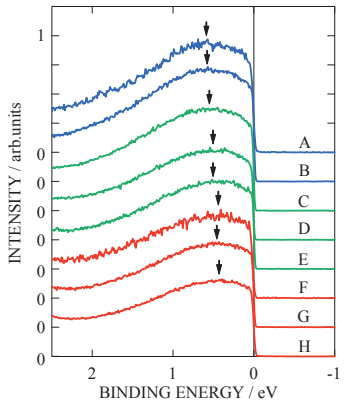

Fig.2 Typical spectra of Zr 4*d* band of Zr-Cu-Al BMG's.

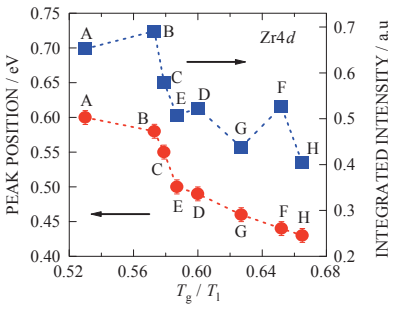

Fig.3 Peak position and integrated intensity of Zr 4*d* band as a function of the reduced glass temperature T_g/T_l.

BL5U

Three-Dimensional Angle-Resolved Photoemission Study on EuO Thin Films

H. Miyazaki[1,2], T. Ito[2,3], S. Ota[1,2], H. J. Im[4], S. Yagi[1], M. Kato[1], K. Soda[1,2], S. Kimura[2,3]

[1]*Graduate School of Engineering, Nagoya University, Nagoya 464-8603, Japan*

[2]*UVSOR Facility, Institute for Molecular Science, Okazaki 444-8585, Japan*

[3]*School of Physical Sciences, The Graduate University for Advanced Studies, Okazaki 444-8585, Japan*

[4]*Department of Physics, Sungkyunkwan University, Suwon 440-746, Korea*

EuO is a ferromagnetic (TC ~ 70 K) semiconductor. In Eu excess case (Eu-rich EuO), it shows a metal insulator transition (MIT) near the TC ~ 150 K [1, 2]. To clarify the origin of MIT and enhancement TC mechanism of Eu-rich EuO from the microscopic electronic structure view, we investigated the fundamental electronic structure of EuO and Eu-rich EuO. In this report, we have performed in situ three-dimensional angle-resolved photoemission spectroscopy (3D-ARPES) on single crystalline EuO thin films.

EuO thin films have been grown by a molecular beam epitaxy (MBE) method. To obtain high-quality single-crystalline films, we evaporated Eu onto BaO buffered Nb-doped SrTiO3 substrates at 350 °C under oxygen pressure of 8 x 10-6 Pa. Epitaxial growth of single-crystal EuO thin films has been confirmed 1 x 1 EuO (100) patterns by LEED and RHEED methods. The sample was transferred to the 3D-ARPES chamber in situ and then the photoemission spectra were measured at UVSOR-II BL5U. Sample temperature was set at 20 K (< TC ~ 70 K).

Figure 1 shows the photon-energy dependence of the ARPES spectra of EuO at normal emission ($k_{//} = 0$ Å^{-1}). Observed spectra mainly show two structure at the binding energy E_B = 1.3 ~ 3.7 eV and 3.7 ~ 8.0 eV. From the comparison with the calculated photo ionization cross section of Eu 4*f* and O 2*p* [3], the lower binding energy side is attributed to Eu 4*f* states and the other is O 2*p* states. Eu 4*f* and O 2*p* bands show small dispersion about 0.2 and 0.3 eV, respectively. Here, we use the dispersion relation

$$(h/2\pi)k_{\perp} = \sqrt{2mE_K}\cos^2\theta + V\ ,$$

where V is the inner potential, E_K is the kinetic energy at the Fermi level E_F and θ = 0 degree. We determined the inner potential V = 13 eV from the symmetry of the dispersive features.

Figure 2 shows the high-resolution ARPES spectra of Eu 4*f* around Γ point (a) recorded at $h\nu$ = 76 eV and X points (b) at $h\nu$ = 38 eV, respectively. Sizable energy dispersion of the Eu 4*f* states is observed at the Γ and X point. The observed dispersive features are the direct evidence for the 3D-lattice effect due to the Eu 4*f* and O 2*p* hybridization. However the dispersion around X point is larger than Γ point. This indicates that the hybridization between Eu 4*f* and O 2*p* states at the X point is stronger. This result is not consistent with the band calculation [4]. The detailed analysis and the further study for temperature dependence ARPES are in progress.

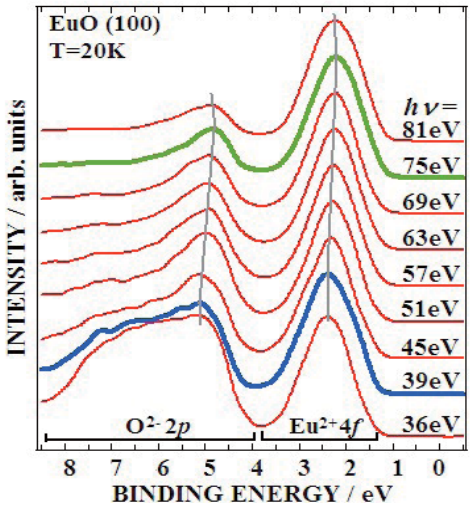

Fig. 1 Photon-energy dependence of the normal emission photoemission spectra of EuO (100).

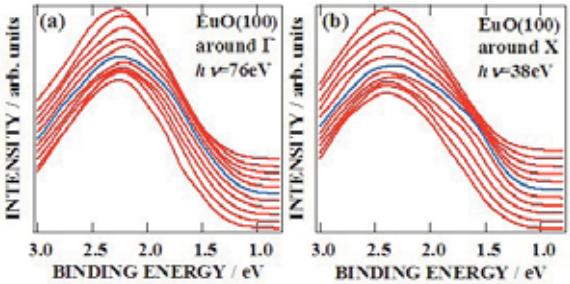

Fig. 2 ARPES spectra of Eu 4*f* around Γ (a) and X (b) points, respectively. The blue lines indicate the spectra at the Γ and X points.

[1] A. Mauger *et al.*,J. Phys. (paris) **39** (1978) 1125..
[2] M. R. Oliver *et al.*, Phys. Rev. B **5** (1972) 1078.
[3] J. J. Yeh and I. Lindau.Atomic Data and Nucl. Data Tables **32** (1985) 1.
[4] S. J. Cho. Phys. Rev. B **1** (1970) 4589.

BL8B1

Characterization of Lithium Compounds by an XAFS Method

T. Kurisaki[1], Y. Inoue[1], H. Wakita[1,2]

[1]*Department of Chemistry, Faculty of Science, Fukuoka University, Nanakuma, Jonan-ku, Fukuoka 814-0180, Japan*

[2]*Advanced Materials Institute, Fukuoka University, Nanakuma, Jonan-ku, Fukuoka 814-0180, Japan*

Lithium compounds are generally used in industrial and commercial applications such as lithium batteries, lithium glasses and other materials. Therefore, it is very interesting to investigate the chemical bonding condition of lithium compounds. However, there are a few reports about Li-K XANES spectra [1].

In this work, we applied the X-ray absorption near edge structure (XANES) spectroscopy to lithium compounds. X-ray absorption spectra of near Li K absorption edges were (XAFS) measured at BL8B1 of the UV-SOR in the Institute of Molecular Science, Okazaki [2]. The energy of the UVSOR storage ring was 750MeV and the stored current was 110-230 mA. The absorption was monitored by the total electron yield using a photomultiplier. We employed the discrete variational (DV)-Xα molecular orbital (MO) method to perform calculated spectra, and compared observed spectra with calculated spectra.

The Li *K* XANES spectra for four lithium halides are shown in Fig. 1. The energy position of each first peak should depend on halide ion. According to the increase in the atomic number of halide ion, the energy of the first peak shifts toward low energies.

The observed and calculated Li K XANES spectra for lithium chloride are shown in Fig. 2. The calculated transition peaks (bars) are convoluted by the Gaussian function of 1.0 eV full width at half maximum (FWHM). The first peak is estimated to the electron transition (mainly Li 1s to unoccupied mixed orbital consisting of Li 2s, Li2p and Cl 3d).

[1] J. Tsuji, K. Kojima, S. Ikeda, H. Nakamatsu, T. Mukoyama and K. Taniguchi, J. Synchrotron Rad. **8** (2001) 554-556

[2] S. Murata, T. Matsukawa, S. Naoè, T. Horigome, O. Matsuodo, and M. Watanabe, Rev. Sci. Instrum. **63** (1992) 1309.

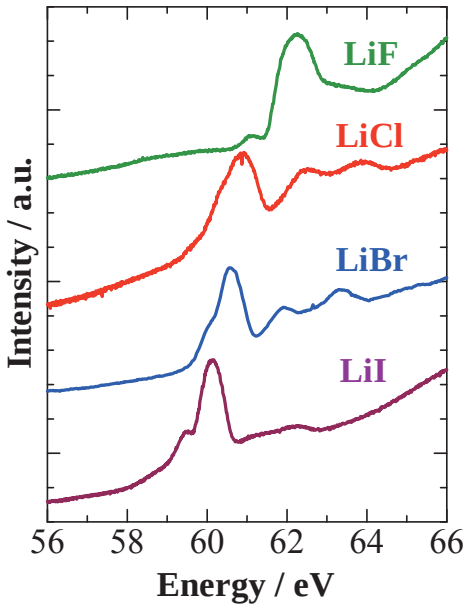

Fig. 1 Li K-edge XANES spectra of lithium halides

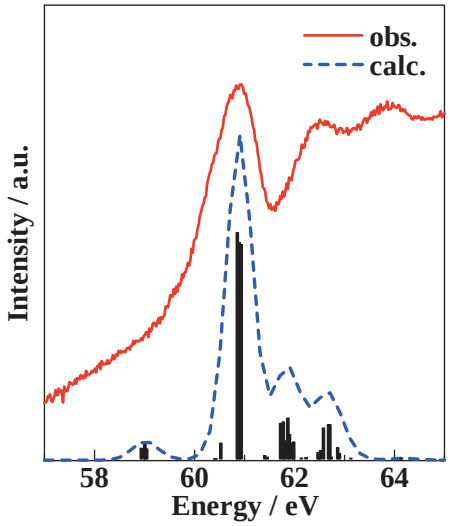

Fig. 2 Calculated transition peaks (vertical bars) and curves (broken line). The solid line is the observed Li K-XANES spectrum for lithium chloride

BL8B1

Comprehensive Classification of DLC Films Formed by Various Methods Using NEXAFS Measurement

A. Saikubo[1], N. Yamada[1], K. Kanda[1], S. Matsui [1], H. Saitoh[2]

[1] Laboratory of Advanced Science and Technology for Industry, University of Hyogo, Kamigori 678-1205 Japan,

[2]Department of Materials Science and Technology, Nagaoka University of Technology, Nagaoka 940-2188, Japan

Introduction

Various diamond like carbon (DLC) thin films have been applied to a large number of industrial fields according to the development of nanotechnology. Recently, classification and standardization of various DLC films are demanded for the expansion of further usage and applications of DLC films. Mechanical, electronic, chemical and optical properties of DLC films are strongly dependent on the elementary composition and the coordination of carbon atoms in films. Near edge X-ray absorption fine structure (NEXAFS) spectroscopy using synchrotron radiation was utilized as an efficient method of sp^2 content for DLC films [1,2]. The sp^2 content can be extracted from the NEXAFS spectrum with a high sensitiveness and a high quantitativeness, because the isolated peak corresponding to the resonance transition from carbon 1s to π* orbital can be observed. In the present study, the 55 kinds of DLC films, which were provided by the enterprises and academic organizations, were discussed by the measurement of NEXAFS spectra.

Experiment

The NEXAFS measurement was performed at the BL8B1 stage of UVSOR in the Institute for Molecular Science. The C K-edge NEXAFS spectra were measured in the energy range 275-320 eV. The energy resolution is estimated to be less than 0.5 eV FWHM. The detection of electrons coming from sample was performed in the total electron yield (TEY) mode. The $sp^2/(sp^2+sp^3)$ ratio in the film can be extracted by normalizing the area of the resonance transition to π* at 285.3 eV with the area of a large section of the spectrum. The absolute $sp^2/(sp^2+sp^3)$ ratio was determined by the comparison with that estimated from the NEXAFS spectrum of graphite. Density of DLC film was measured with X-ray reflectivity method at Nagaoka University of Technology.

Result and Discussion

Determined $sp^2/(sp^2+sp^3)$ ratio populated in the range of 0.1-0.9. Observed samples could be classified roughly to 4 kinds of group by $sp^2/(sp^2+sp^3)$ ratio and density. Group A was characterized by high density, 2.7-3.4 g/cm^3, and low $sp^2/(sp^2+sp^3)$ ratio, ≈0.4. This group consists merely of the sample formed by PVD method. The DLC thin films in this group can be estimated to have high hardness. Group B was characterized by low density, 1.3-2.6 g/cm^3, and high $sp^2/(sp^2+sp^3)$ ratio, 0.8-0.9. This group consists also of the sample formed by PVD method. Group C was characterized by medium density, 1.8-2.4 g/cm^3, and medium $sp^2/(sp^2+sp^3)$ ratio, 0.4-0.6. Most number of samples includes this group and this group consists of samples formed by both PVD and CVD methods. For group A-C, density of DLC film increases with decreasing of $sp^2/(sp^2+sp^3)$ ratio. It is interpreted that the density of DLC film increases with the ratio of sp^3 component in the film. Group D was characterized by low $sp^2/(sp^2+sp^3)$ ratio, 0.2-0.6, in spite of low density, 1.2-2.0 g/cm^3. This group consists almost of the sample formed by CVD method. The peak at ≈288 eV was observed in the several NEXAFS spectra of this group. The presence of this peak indicates the containing hetero-atom, such as nitrogen, and oxygen etc. [3]. These hetero-atoms were considered to reduce π-bonding in the DLC film. Therefore, DLC films with low density were formed in spite of low $sp^2/(sp^2+sp^3)$ ratio.

[1] K. Kanda, T. Kitagawa, Y. Shimizugawa, Y. Haruyama, S. Matsui, M. Terasawa, H. Tsubakino, I. Yamada, T. Gejo and M. Kamada, Jpn. J. Appl. Phys. **41** (2002) 4295.

[2] K. Kanda, Y. Shimizugawa, Y. Haruyama, I. Yamada, S. Matsui, T. Kitagawa, H. Tsubakino and T. Gejo, Nucl. Inst. Meth. B **206** (2003) 880.

[3] K. Kanda, J. Igaki, Y. Kato, R. Kometani and S. Matsui, New Diamond Frontier Carbon Tech. **15** (2005) 123.

BL8B2

The Electronic Structure and the Energy Level Alignment at PTCDA / Metal Interfaces

E. Kawabe[1], H. Yamane[1], K. Koizumi[1], R. Sumii[2], K. Kanai[1], Y. Ouchi[1], K. Seki[1,3]
[1]*Graduate School of Science, Nagoya University, Furo-cho, Chikusa-ku, Nagoya 464-8602 Japan*
[2]*Research Center for Materials Science, Nagoya University,*
[3]*Institute for Advanced Research, Nagoya University*

In recent years, extensive research has been carried out for applying organic materials to electronic devices such as organic light emitting diodes, organic solar cells and organic field effect transistors. It is important to understand how the energy levels align at organic/metal (O/M) interfaces for understanding the mechanism of such devices and for improving their performance, since these factors strongly affect various phenomena such as charge injection. However, the detailed mechanism of the energy level alignment at O/M interface is not yet well understood even for nonpolar molecules. We investigated the electronic structure and the energy level alignment at the interfaces formed by vacuum-depositing perylene -3,4,9,10-tetracarboxylic dianhydride (PTCDA, molecular structure shown in Fig. 2(a)) on polycrystalline vacuum-deposited films of metals (Au, Cu and Co) by ultraviolet photoelectron spectroscopy (UPS).

In the case of PTCDA/Au interface, the apparent interface states or charge transfer (CT) states were not observed in its UPS spectra (not shown here), which indicates that the interaction between Au and PTCDA is very weak, and that PTCDA molecule physically adsorbed on Au surface. The vacuum level (VL) showed sudden shift toward Fermi level (E_F) of Au at the interface, as shown in Fig. 1, indicating the formation of an interface dipole. The possible origins of such interface dipole have been proposed by Ishii *et al.* [1], and we can ascribe the presently observed change at PTCDA/Au interface to the push-back of the electron cloud spilled out from the metal surface (push-back effect) by the adsorption of PTCDA molecules. The interface dipole (Δ) for this lowering of the VL was 0.52 eV.

The UPS spectra at PTCDA/Cu interface are shown in Fig. 2(b). The highest occupied molecular orbital (HOMO) of PTCDA is observed at binding energy (E_B) of 2.47 eV at the film thickness d = 5 nm. At d = 0.4 nm, an additional spectral feature is observed at E_B = 0.2 ~ 1.2 eV. This interface specific structure may be due to the CT from Cu to PTCDA. Actually, the upward VL shift shown in Fig. 1 with Δ = -0.29 eV is consistent with the picture that CT from Cu to PTCDA leading to the rise of VL overwhelmed the push-back effect which tends to lower the VL.

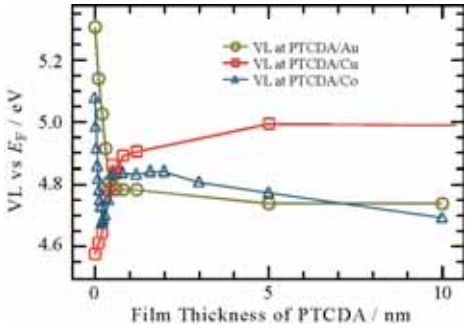

Fig. 1 The film thickness dependence of VL at PTCDA/Au, Cu and Co interfaces.

At PTCDA/Co interface, VL showed upward shift after the initial abrupt downward shift (Fig. 1). Although this upward shift indicates the CT from Co to PTCDA, CT states were not observed in the UPS spectra (Fig. 2(c)), possibly because the amount of the transferred charge is too small to appear as a new state in the spectra. The estimated amount of transferred charge at PTCDA/Cu and PTCDA/Co interfaces by the electrostatic theory [2] for explaining the VL shift are one electron per about two and five PTCDA molecules, respectively.

The schematic energy diagrams of these interfaces are summarized in ref. [3]. We found an interesting behavior at PTCDA/Co interface, so we focus attention on the effect of the d electrons on the energy level alignment.

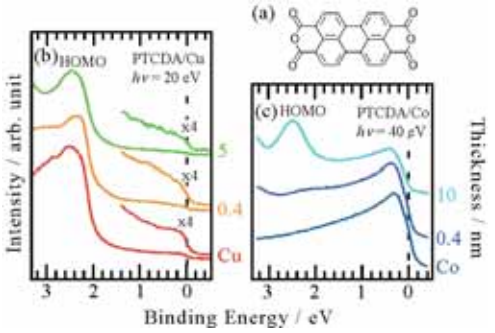

Fig. 2 (a) The molecular structure of PTCDA. (b) and (c) The UPS spectra of PTCDA/Au and PTCDA/Co interfaces, respectively.

[1] H. Ishii, K. Sugiyama, E. Ito and K. Seki, *Adv. Mater.* **11** (1999) 605.
[2] H. Ishii, N. Hayashi, E. Ito, Y. Washizu, K. Sugi, Y. Kimura, M. Niwano, Y. Ouchi and K. Seki, Phys. Stat. Sol. (a) **201** (2004) 1075.
[3] E. Kawabe, H. Yamane, K. Koizumi, R. Sumii, K. Kanai, Y. Ouchi and K. Seki, Mater. Res. Soc. Symp. Proc. **965** (2006) S09-28.

BL8B2

Photoelectron Angular Distribution of 3d-orbital Derived Bands in Mn-Phthalocyanine Monolayer

S. Kera[1], H. Fukagawa[1], T. Kataoka[1], T. Hanatani[1],
R. Sumii[2], S. Nagamatsu[1], N. Ueno[1]
[1]*Graduate School of Science and Technology, Chiba University, Chiba 263-8522 Japan*[#]
[2]*IMS and Graduate School of Science, Nagoya University*
Furo-cho, Chikusa-ku, Nagoya 464-8602, Japan

Angle-resolved ultraviolet photoelectron spectroscopy (ARUPS) has been known as a powerful technique to obtain crucial information on electronic band structure for various kinds of materials. Moreover, for organic thin films, information on the geometrical structure of the thin films can be also discussed in accordance with a quantitative analysis of the ARUPS intensity using photoelectron scattering theory. However, it is noteworthy that the experimental results are still limited to describe the relationships between the distribution of the molecular orbital (MO) and the ARUPS intensity due to a lack of a standard/simple theoretical model and well-ordered organic thin films [1].

We measured the take-off angle (θ) dependences of 2p- and 3d-orbital derived bands in ARUPS spectra for well-ordered Mn-phthalocyanine (Pc) monolayers to clarify the MO distribution affecting to the angular distribution.

Experiments

ARUPS spectra were measured at photon incidence angle $\alpha=45^{o}$, photon energy (hν) of 20 eV and 28 eV, and at a sample temperature T=295 K. The purified MnPc molecules were carefully evaporated onto the graphite (HOPG:ZYA) substrate.

Results and Discussion

Figure 1(a) shows the θ dependence of ARUPS of annealed-MnPc monolayer (0.3nm) on HOPG. The intensity is normalized to the incidence photon flux (I_R). A lowest lying feature appeared at 0.65 eV, where the binding energy is observed lower than previous metal-Pc monolayers on HOPG [2], could be ascribed to HOMO band of MnPc. The next feature at 1.2 eV is assigned to a single π MO (HOMO-1) that corresponds to HOMO of other Pc molecules [2]. DFT-MO calculation suggests that the HOMO band of the MnPc is related to Mn-3d-derived state. However, we are in progress to conclude the assignment which character of 3d MOs is responsible to this state because of a variety in the spin configuration.

Figure 1(b) shows the observed θ dependences of HOMO and HOMO-1 intensities obtained at hv =20eV. Both patterns show a similar distribution to give a maximum around $\theta=50^{o}$, though the intensity is slightly different around $\theta=25^{o}$. Figure 1(c) shows the θ dependences of HOMO and HOMO-1 intensities at hv =28eV. The patterns are different significantly between HOMO and HOMO-1. The intensity shows maximum at $\theta=8^{o}$ for the HOMO and $\theta=30^{o}$ for the HOMO-1. The difference in the θ distributions might be related to the different orbital distribution, that is, 3d-orbital for HOMO and 2p-orbital for HOMO-1.

Now we are trying to simulate the patterns by taking into account the characteristics of 3d-orbitals with theoretical calculations, multiple-scattering approximation combined with MO calculation [1]. ARUPS results would be helpful for making assignments of complex electronic structure such as a mixed valence and spin configuration of organometalic compounds.

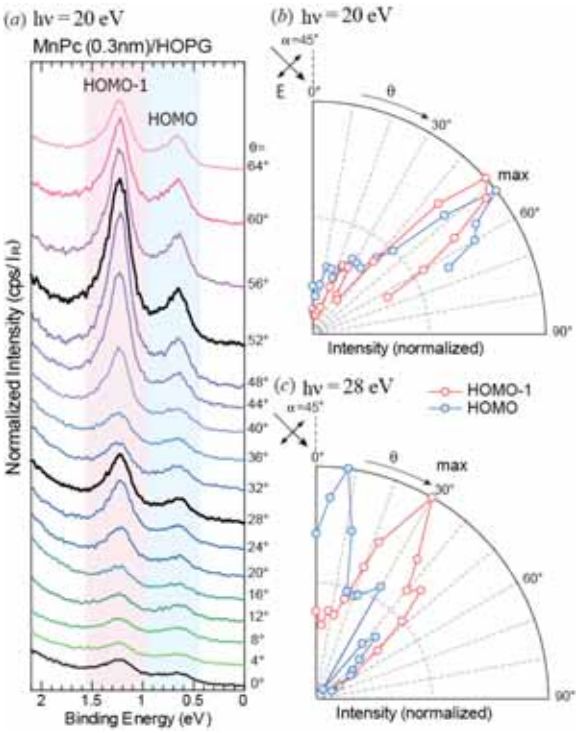

Fig. 1.(a) θ dependence of ARUPS of 1-ML(0.3nm) MnPc on HOPG measured at hv=20eV. Observed θ patterns of the HOMO band (blue circles) and HOMO-1 band (red circles) obtained by hv=20 eV (b) and hv=28eV (c).

[1] S. Nagamatsu et al, e-J. Surf. Sci. Nanotech. **3** (2005) 461.
[2] H. Fukagawa et al, Phys. Rev. B **73** (2005) 041302(R).
[#]Present add: Graduate School of Advanced Integration Science, Chiba University

BL8B2

Electronic Structure of Lithium Phthalocyanine Thin Film

S. Tanaka[1, 2], K. Watanabe[3], Y. Yoshida[3], I. Hiromitsu[3], K. Yoshino[2]
[1] *Center of Integrated Research in Science, Shimane University, Matsue 690-8504 Japan*
[2] *Research Project Promotion Institute, Shimane University, Matsue 690-8504 Japan*
[3] *Faculty of Science and Engineering, Shimane University, Matsue 690-8504 Japan*

Introduction

Phthalocyanine (Pc) and metal phthalocyanines have attracted much interest for their semiconducting properties implying many interesting applications including photovoltaics, photoconductors and sensors. Lithium phthalocyanine (LiPc) is known as a stable neutral radical and is one of a few intrinsic semiconducting molecules [1, 2]. The chemical structure of LiPc is shown in Fig. 1. It is known that LiPc has rather high conductivity and a peculiar UV-VIS absorption spectrum as compared to other metal phthalocyanines such as ZnPc, CuPc or TiOPc. Thus, the structures of LiPc and those properties are interesting, and these have been the subject of many studies [2-4]. In this work, we investigate the electronic structures of thin films of LiPc on an Au substrate. The energy level alignment at the LiPc/Au interface is revealed from the photoelectron spectra as a function of the LiPc thickness.

Experimental

LiPc was synthesized by electrochemical oxidation of dilithium phthalocyanine (Li_2Pc) following the synthesis procedure described in literatures [1]. The purification of LiPc was done by vacuum sublimation. LiPc was deposited on an Au substrate. Evaporation of LiPc was performed using a glass-cell evaporator after careful outgassing, keeping the pressure of the preparation chamber at less than 4×10^{-6} Pa. All the photoelectron measurements were carried out at photon incident angle of 45°, $h\nu = 40$ eV, and sample temperature of about 295 K. Photoelectron spectra of metal-free phthalocyanine (H_2Pc) were also measured for comparison.

Results and Discussion

Figure 2 shows the photoelectron spectra of LiPc grown on Au as a function of thickness. The abscissa is the binding energy relative to the Fermi energy of Au. The energy difference between the HOMO of LiPc and Fermi level of Au at the interface is about 0.3 eV. This suggests that the energy barrier height for hole injection from Au to LiPc is relatively small. From the secondary electron cutoff, it was observed that the energy of the vacuum level sharply decreases by about 0.4 eV within the thin-layer region up to around 1 nm (not shown here). The abrupt lowering of vacuum level at metal/organic interfaces is ascribed to the formation of the interface dipole [5]. The downward of the vacuum level caused by the LiPc deposition suggests the formation of interfacial dipole layer with LiPc side positively charged. In the thick-layer region (10 – 30 nm), no obvious shift was observed at the HOMO peak and the secondary electron cutoff. These results indicate that the thermal equilibrium condition of the LiPc layer is achieved in the thin-layer region (~ 10nm).

The HOMO peak of LiPc appears at around 1.1 eV. The binding energy and the intensity of the LiPc HOMO peak were smaller than those of the H_2Pc HOMO peak. The ionization potential of the LiPc thin film and that of the H_2Pc thin film were estimated at about 5.1 eV and 5.2 eV, respectively, from the secondary cutoff and the lower cutoff of the HOMO peak. The HOMO peak intensity of LiPc was smaller than that of H_2Pc, reflecting a characteristic of the unpaired electron of LiPc.

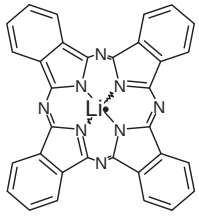

Fig. 1 Chemical structure of lithium phthalocyanince.

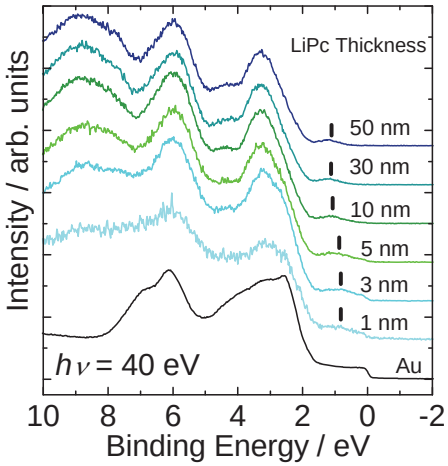

Fig. 2 Photoelectron spectra of LiPc film incrementally deposited on Au.

[1] P. Turek *et al.*, Chem. Phys. Lett. **134** (1987) 471.
[2] M. Brinkmann *et al.*, Thin Solid FIms **324** (1998) 68.
[3] T. Kimura *et al.*, Chem. Phys. **253** (2000) 125.
[4] N. Sato *et al.*, Appl. Surf. Sci. **212-213** (2003) 438.
[5] H. Ishii *et al.*, Adv. Mat. **11** (1999) 605.

BL8B2

Structural Change in Lithium Phthalocyanine/Poly(3-hexylthiopehne) Interface Caused by Annealing

S. Tanaka[1, 2], K. Watanabe[3], Y. Yoshida[3], I. Hiromitsu[3], K. Yoshino[2]

[1] *Center of Integrated Research in Science, Shimane University, Matsue 690-8504 Japan*

[2] *Research Project Promotion Institute, Shimane University, Matsue 690-8504 Japan*

[3] *Faculty of Science and Engineering, Shimane University, Matsue 690-8504 Japan*

Introduction

The conjugated polymers are promising material for organic semiconductor devices. Poly (3-hexyl -thiophene) (P3HT) is one of π–conjugated polymers. P3HT is used widely in polymer field-effect transistors, photovoltaic cells, and light-emitting diodes because of its characteristic properties such as solubility for various organic solvents, fusibility at relatively low temperature, and relatively high carrier mobilities. [1] The control of electrical properties in the conjugated polymers is a major issue for further device applications. Doping is the one way to control the electric property of the conjugated polymers.

We have recently studied an effective molecular doping for the P3HT film. Lithium phthalocyanine (LiPc) molecule is a candidate of the molecular dopant for P3HT. In this work we measured the variation of the photoelectron spectra of the P3HT films caused by annealing following a deposition of LiPc molecules.

Experimental

The molecular structure of P3HT and LiPc are shown in Fig. 1. The P3HT sample was prepared with a chloroform solution of P3HT casting on a clean Au foil. The sample was immediately introduced into the vacuum chamber. The annealing of the sample was done in the preparation chamber *in situ*.

Results and Discussion

Figure 2 shows the photoelectron spectra of (a) P3HT, (b) LiPc (3nm) on P3HT, and (c) LiPc (3nm) on P3HT after annealing at 373 K. The abscissa is the binding energy relative to the Fermi energy of Au. It is expected from the shape of the spectrum that the P3HT sample was slightly charging because of the thickness of the P3HT film. In the P3HT spectrum, the intense feature extending from 12 to 5 eV contains the levels associated to the alkyl groups and the π-electrons of the thiophene rings contributes to the region below 5 eV [3]. The LiPc layer with 3 nm thickness was deposited on to the P3HT layer by vacuum evaporation, and the photoelectron spectrum (Fig. 2. (b)) was measured *in situ*. The feature of the photoelectron spectrum showed the electronic structure almost only of LiPc; hence, the surface of the P3HT layer was fully covered with the LiPc molecules. After the measurement of the photoelectron spectrum, the sample of LiPc (3 nm) on P3HT was annealed at 373 K (100 min) *in situ*. The spectrum of fig. 2 (c) is the photoelectron spectrum after the annealing. As seen in fig. 2 (c), the spectrum showed not the LiPc electronic structures but the P3HT electronic structures. Because of the surface sensitivity of the photoelectron spectroscopy, these results indicate that there were few LiPc molecules on the sample surface after annealing. A possible reason of the drastic change caused by annealing is that the LiPc molecules were diffused into the P3HT layer with the conformation change by the annealing. The Li 1s spectra showed peak shift and the splitting caused by annealing (not shown). To investigate the relations between the doping mechanism and the variations of the photoelectron spectra, further studies are now in progress.

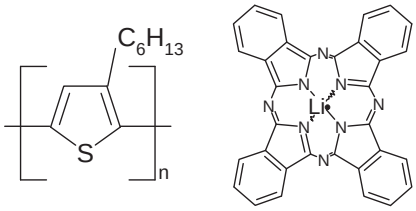

Fig. 1 Chemical structures of (a) poly(3-hexyl -thiophene) and (b) lithium phthalocyanince.

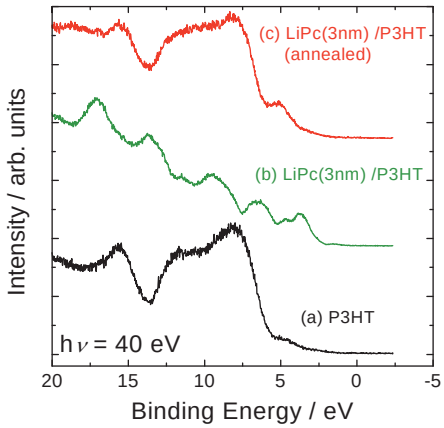

Fig. 2. The photoemission spectra of (a) P3HT, (b) LiPc (3 nm) on P3HT, and (c) LiPc (3 nm) on P3HT after annealing at 373 K.

[1] K. Yoshino, M. Onoda, Polymer Electronics, Corona, Tokyo, (1996) (in Japanese).

[2] M. Brinkmann *et al.*, Thin Solid Films **324** (1998) 68.

[3] R. Lazzaroni *et al.*, J. Chem. Phys. **93** (1990) 4433.

BL8B2

Electronic Structure of Singlet Biradical Hydrocarbon Ph_2-IDPL Thin Film

K. Kaname, T. Kubo[1], H. Yamane[2], R. Sumii, K. Nakasuji[3], Y. Morita[1], K. Seki[2,4]

Research Center for Materials Science, Nagoya University, Furo-cho, Chikusaku Nagoya 464-8602 Japan

[1]Department of Chemistry, Graduate School of Science, Osaka University, Machikaneyama 1-1, Toyonaka, Osaka 560-0043, Japan

[2]Department of Chemistry, Graduate School of Science, Nagoya University, Furo-cho, Chikusa-ku, Nagoya 464-8602, Japan

[3] Fukui University of Technology, Gakuen 3-6-1, Fukui-shi, Fukui 910-0028, Japan

[4] Institute for Advanced Research, Nagoya University, Furo-cho, Chikusa-ku, Nagoya 464-8602, Japan

Realization of the columnar stackings of planar molecule on the substrate by intermolecular interaction between extended π-systems is widely interested matter in surface physics and organic device technology. Diphenyl derivative of s-indacenodiphenalene (Ph_2-IDPL) was isolated and characterized as a singlet biradical hydrocarbon by T. Kubo *et al* [1]. Ph_2-IDPL was reported to have strong intra- and intermolecular interaction leading to π- π stacking distance (3.137 Å) for the crystal, which is substantially shorter than the van der Waals contact of carbon atoms (3.4 Å). In Ph_2-IDPL crystal, staggered stacking of the molecules forms ideal one-dimensional molecular chain. Such strong intermolecular interaction in the ground state of Ph_2-IDPL molecule is caused from the interaction between unpaired electrons characteristic of biradical molecule. It is expected that tendency of Ph_2-IDPL molecules to undergo facile self-association on the substrate and form highly oriented film with π- π stacking originated form the strong intermolecular interaction.

In this report, the electronic structure of Ph_2-IDPL film deposited on single crystal GeS(100) surgface were investigated by angle-resolved ultraviolet photoemission spectroscopy (ARUPS).

ARUPS measurements were performed in UVSOR BL-8B2. Base pressure of the experimental chamber was under 5×10^{-8} Pa. Clean surface of GeS substrate was obtained by cleaving the surface in vacuum. Thickness of the Ph_2-IDPL film was monitored by quartz microbalance.

Figure 1 shows UPS spectra of Ph_2-IDPL film with the thickness of 0.4 nm on GeS(100) surface. θ stands for take-off angle of photoelectron. Dependence of the spectral shape on θ was clearly observed. Based on ARUPS measurements as shown in Fig. 1 the momentum $k_{//}$ dependences of the energy of each spectral features labeled A, B, C, D and E are presented in Fig. 2. Those features show clear energy dispersion characteristic of one-dimensional system, which indicates the formation of well-ordered Ph_2-IDPL film with anisotropy on GeS(100) surface. Such one-dimensional energy dispersion was predicted in the framework of extended Hueckel (EH) theory [1]. Especially, the behaviors of A and B are qualitatively well explained by the energy band calculation by using EH theory. However, observed energy width of the dispersion (*e.g.* about 0.1 eV and 0.5 eV for A and B, respectively) is smaller than that estimated by energy band calculation [1].

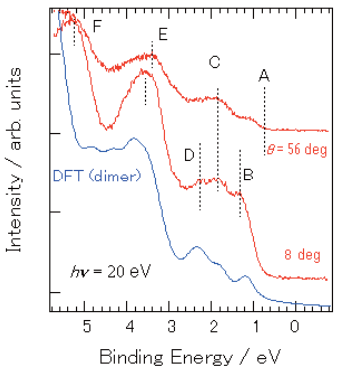

Fig. 1 UPS spectra of Ph_2-IDPL film on GeS(100) surface. The normal emission is origin of θ.

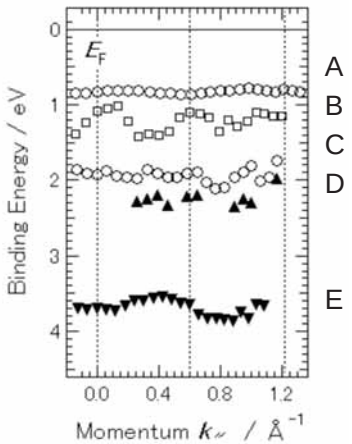

Fig. 2 Momentum dependence of the energy of the spectral features labeled in Fig. 1. Dotted vertical bars represents the boundary of Brillouin zone calculated by lattice constant along the molecular stacking in crystal.

[1] T. Kubo, K. Nakasuji *et al.*, Angew. Chem. Int. Ed., 44 6564 (2005).

BL8B2

Ultraviolet Photoelectron Spectra of $(YC)_2@C_{82}$ and $Y_2@C_{82}$*

S. Hino [1†], N. Wanita[1], K. Iwasaki[1], D. Yoshimura[2,3], T. Akachi[4],
T. Inoue[4], Y. Ito[4], T. Sugai[4], H. Shinohara[4]

[1] *Chiba University, Inage-ku, Chiba 263-8522 Japan*
[2] *Institute for Molecular Science, Okazaki 444-8585 Japan*
[3] *Research Center of Material Science, Nagoya University, Nagoya 464-8602 Japan*
[4] *Faculty of Science, Nagoya University, Nagoya 464-8602* Japan

Recently, encapsulation of multiple atoms, such as metal clusters [1, 2], metal nitrides [3] and metal –carbon clusters [4] inside the cage has been reported. These metallofullerenes are considered a different class from mono-metal atom encapsulated metallofullerenes from the view point of electron transfer from the encapsulated atoms to the fullerene cage. This is thought to be because encapsulated atoms may form chemical bonds among them as well as they may form bonds to the carbon atoms that constitute the cage.

Recently, numerous yttrium and carbon atoms encapsulated metallofullerenes ($(YC)_2@C_{82}$) have been reported, and three isomers were isolated [4]. Yttrium atoms have also been reported to be encapsulated into the fullerene cage, and three $Y_2@C_{82}$ isomers were identified [4]. NMR spectra of a $(YC)_2@C_{82}$ (III) isomer [4] and $Y_2@C_{82}$(III) revealed that their cage structures are exactly the same and, their absorption spectra resemble each other, suggesting their analogous electronic structures.

Figure 2 shows the UPS of $(YC)_2@C_{82}$ (III). The intensity of each structure in the UPS of $Y_2@C_{82}$ (III) labeled A – I changes upon tuning the incident photon energy, which is typical spectroscopic behavior of fullerenes. The USP of $(YC)_2@C_{82}$ (III) resemble those of $Y_2@C_{82}$ (III). To clarify the difference between these two metallofullerenes, their UPS obtained with 30 eV photon are shown in Fig.2

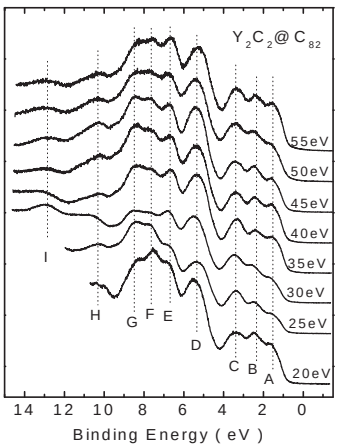

Fig. 1 Incident photon energy dependence of the UPS of $(YC)_2@C_{82}$ (I).

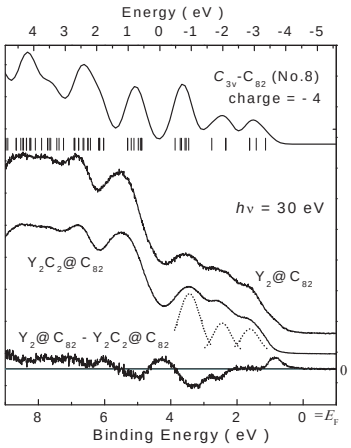

Fig.2 Comparison of the UPS of $(YC)_2@C_{82}$ and $Y_2@C_{82}$ isomers. Difference spectrum between them (bottom) and simulation spectra (top) obtained by MO calculation.

The first three structures of $(YC)_2@C_{82}$ (III) can be deconvoluted into three components with intensity ratio of 4 : 5 : 9. This is well reproduced by a simulation spectrum (top in Fig. 2) calculated using geometry of C_{3v}-C_{82} (No.5) [5] with additional 4 electrons on the cage. This finding indicates $(YC)^{2+}{}_2@C_{82}{}^{4-}$ is the plausible oxidation state.

Onset energy of $Y_2@C_{82}$ (III) is slightly smaller than that of $(YC)_2@C_{82}$ (III). Difference spectrum between them (bottom in Fig. 2) reveals two additional electrons on $Y_2@C_{82}$ (III). Thus, the oxidation state of this metallofullerene might be $Y^{3+}{}_2@C_{82}{}^{6-}$. Since the oxidation state of Y must be + 3, probably two electrons in $(YC)_2@C_{82}$ (III) might be used either to form the bonds between Y and C or to donate electrons to acetylide.

* This work was published in Phys. Rev. B **72** (2005) 195424.

† present address, Ehime University, Matsuyama, Ehime 790-8577.

[1] M. Takata *et al*., Phys. Rev Lett. **83** (1999) 2214.
[2] C.-R. Wang *et al*., Nature **408** (2000) 426.
[3] S. Stevenson *et al. ibid*. (1999) 55.
[4] T. Inoue *et al*., Chem. Phys. Lett. **382** (2003) 226 and J. Phys. Chem. B **108** (2004) 7573.
[5] P. W. Fowler, "An atlas of Fullerenes", Oxford Press, Oxford, 1995.

BL8B2

Ultraviolet Photoelectron Spectra of Three Tm@C_{82} Isomers*

S.Hino [1†], N. Wanita[1], K. Iwsaki [1], D. Yoshimura[2,3], N. Ozawa[4],

T. Kodama[4], K. Sakaguchi[4], H. Nishikawa[4], I. Ikemoto[4], K. Kikuchi[4]

[1]*Chiba University, Inage-ku, Chiba 263-8522 Japan*
[2]*Institute for Molecular Science, Okazaki 444-8585 Japan*
[3]*Research Center of Material Science, Nagoya University, Nagoya 464-8602 Japan*
[4]*Faculty of Science, Tokyo Metropolitan University, Hachioji, Tokyo 192-0397* Japan

Up to now a lot of metallofullerenes have been synthesized [1] and among them the most abundantly obtainable metallofullerene seem to have C_{82} cage. There are nine isolated pentagon rule (IPR) satisfying cage structures for C_{82}. While it seems that trivalent metal atom accommodates only in C_{2v} and C_s cages, divalent metal atoms prefer more cages. Tm atom is entrapped inside the C_{82} cage and three Tm@C_{82} isomers have been reported [2, 3]. We present the UPS of three Tm@C_{82} isomers and compare them with previously reported one [4] and those of two Ca@C_{82} isomers [5] and discuss the correspondence among these metallofullerenes. Cage structures of three Tm@C_{82} isomers are also proposed with an aid of molecular orbital calculation.

Figure 1 shows the valence band UPS one of three Tm@C_{82} isomers, isomer (I) obtained with hν = 20 – 55 eV photon energy. Spectral onsets of three isomers are 0.85 eV (I), 0.75 eV (II) and 0.9 eV (III). The onset energies of Tm@C_{82} isomers are relatively large compared with those of La@C_{82} and Gd@C_{82} but almost the same as those of Ca@C_{82} isomers [4].

Figure 2 shows the UPS of three Tm@C_{82} isomers and two Ca@C_{82} isomers. The UPS of Tm@C_{82} (II) and Ca@C_{82} (III) are essentially the same which indicates that these two metallofullerenes have the same electronic structure derived from the same cage structure. The UPS and MO calculation proposed C_2(c) cage structure for the geometry of Ca@C_{82} (III) [6] and this deduction was later supported by the NMR measurements [7]. Further the NMR on Tm@C_{82} (II) predicts the same C_2 symmetry. On the other hand,

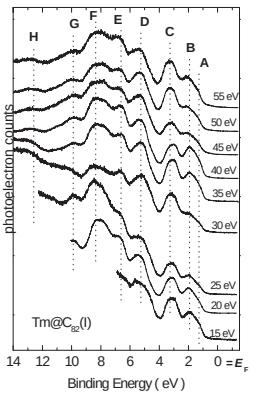

Fig. 1 Incident photon energy dependence of the UPS of Tm@C_{82} (I).

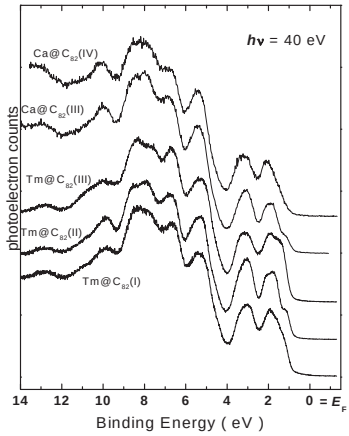

Fig.2 Comparison of the UPS of two Ca@C_{82} isomers and three Tm@C_{82} isomers.

these spectra correspond with the HeI and HeII excited spectra reported by Pichler's group who claimed that they measured C_{3v}-Tm@C_{82} [4]. That is, the metallofullerenes that we and Pichler's group have measured are the identically the same species and Pichler's claim of symmetry definition was wrong.

The UPS of three Tm@C_{82} isomers were compared with MO calculation and it was found that their cage structures are C_s(c) cage structure for Tm@C_{82} (I), C_2(c) for Tm@C_{82} (II) and C_{2v} for Tm@C_{82} (III)

* This work was published in Chem. Phys. Lett. **402**, 217 (2005).

† present address : Ehime University, Matsuyama, Ehime 790-8577 Japan

[1] for example, H. Shinohara, Rep. Prog. Phys. **63** (2000) 843.
[2] U. Kirbachet al., Chem. Int. Ed. Engl. **35** (1996) 2380.
[3] T. Kodama et al., J. Ame. Chem. Soc. **124** (2002) 1452.
[4] T. Pichler et al., Appl. Phys. A**66** (1998) 281
[5] S. Hino et al., Chem. Phys. Lett. **230** (1994) 165.
[6] S. Hino et al., Chem. Phys. Letts. **227** (2001) 65.
[7] T. Kodama et al., Chem. Phys. Letts. **377** (2003) 197.

BL8B2

Electronic Structure at Highly Ordered Pentacene/Cu(110) Interface: Energy-Level Splitting and Energy-Band Dispersion

H. Yamane [1], E. Kawabe [1], R. Sumii [2], K. Kanai [2], Y. Ouchi [1], K. Seki [1,2]
[1] *Department of Chemistry, Nagoya University, Nagoya 464-8402 Japan*
[2] *Research Center for Materials Science, Nagoya University, Nagoya 464-8602 Japan*

Introduction

The electronic structure at organic/metal interfaces, in particular the energy positions of the highest-occupied and lowest-unoccupied molecular orbital (HOMO and LUMO) levels relative to the Fermi level (E_F) of metal electrodes, plays a crucial role in determining the charge injection barrier in (opto) electronic devices using organic semiconductors. Therefore it is natural that many research groups have been investigating the energy-level alignment at organic-related interfaces in order to elucidate the energetics at the interfaces. For deeper understanding of the energetics at organic/metal interfaces, a more pertinent experimental approach to this issue would be the use a well-characterized system in quantitative electron spectroscopic measurements. In this work, we studied the electronic structure of highly-ordered monolayer of pentacene prepared on Cu(110) surface by angle-resolved UV photoemission spectroscopy (ARUPS) using synchrotron radiation. We observed a distinctive electronic structure at the interface, which is completely different from those of the gas- and bulk-phase pentacene.

Experimental

The purified pentacene was carefully evaporated onto the clean Cu(110) surfaces, which was kept at 500 K during the deposition.

The azimuthal angle (ϕ) dependence of ARUPS spectra was measured at the photon energy ($h\nu$) of 20 eV, the photon incidence angle (α) of 60°, take-off angle (θ) of 58° from the surface normal, and the temperature of 300 K. The origin of the azimuthal angle ϕ = 0° was defined so that the electric-field vector of the incident photon is on the incident plane containing the substrate [1-10] direction and the surface normal.

Results and Discussion

The ϕ dependences of the ARUPS spectra with a step of 3° for the clean Cu(110) substrate and the pentacene monolayer on the Cu(110) substrate are shown in Fig. 1. The abscissa is binding energy (E_b) relative to the substrate E_F, and the spectra are normalized to the incident photon flux. As a reference, we also show the UPS spectrum of the gas-phase pentacene [1], which is shifted to align the lowest-E_b peak to that of the pentacene monolayer on Cu(110) at ϕ = 0°. For the Cu(110) substrate, the peak S due to the direct s,p-band transition appears at 1.9 eV when ϕ = 0° and gradually shifts toward the low-E_b side until ϕ reaches 30°. Upon formation of the pentacene monolayer on the substrate, the intensity of this substrate peak S decreases, and the new peaks A, B, and C appear with the continuous change in the peak positions with ϕ. We note that the separation between A and B is about 0.7 eV, while the E_b difference between the HOMO and HOMO-1 peaks in the gas-phase spectrum is much larger (1.4 eV) [1]. This discrepancy is in contrast to the case of the physisorbed pentacene monolayer on highly oriented pyrolytic graphite, where the relative energies of the peaks correspond well with those in the gas phase [2]. Thus we can consider that the peaks A and B are formed by the strong molecule-substrate interaction.

From the consideration of symmetry selection rules and the θ dependences of the ARUPS spectra [3], we can deduce that (i) the peaks A and B originate from the energy-level splitting of the original HOMO level and that (ii) the continuous change in the peak position with ϕ originates from the intermolecular energy-band dispersion. In this system, the intermolecular interaction via direct contact is considerably weak, and these findings may originate from the intermolecular interaction via the substrate due to the significant hybridization of the MOs and the substrate.

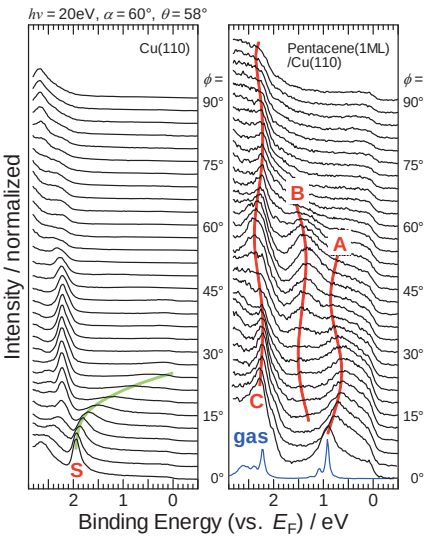

Fig. 1 Azimuthal angle (ϕ) dependence of the ARUPS spectra for the Cu(110) substrate (left) and the pentacene monolayer on Cu(110) (right).

[1] V. Coropceanu *et al.*, Phys. Rev. Lett. **89**, (2002) 275503.
[2] H. Yamane *et al.*, Phys. Rev. B **72** (2005) 153412.
[3] H. Yamane *et al.*, UVSOR Activity Report 2005 (2006) 113.

6
Surface science, photochemistry and Others

BL4A

Development of Differential Pump System for Studies the Effects of XeF_2 Etching of Si and SiO_2 Induced by Synchrotron Radiation

T. Y. Chiang[1], T. Makimura[2], K. Murakami[2], N. Nakai[3], H. Uno[1], R. Tero[1,3], T. Urisu[1,3]

[1]*Dept. of Vacuum UV photo-science, Institute for Molecular Science, Okazaki 444-8585 Japan*

[2]*Institute of Applied Physics, Tsukuba Univ., Tsukuba 305-8577 Japan*

[3]*Graduate University for Advanced Studies, Okazaki 444-8585 Japan*

An etching system was constructed to clarify the difference between synchrotron radiation (SR) -induced reaction and dark reaction in XeF_2 etching of Si experiment at the beam-line BL4A1 in the UVSOR last year, and an etching rate of 0.9 μm/min on Si surface was achieved. A XeF_2-flow chamber isolated and evacuated independently with a LiF window is installed in the end-station beam chamber, in order to avoid the damage of vacuum pressure and evacuation instruments in the beam-line. However, the LiF window is damaged easily owing to the violent collision of photon. So an apparent result can not be observed at long-time performances that escape the balance of selective and non-selective reactions of XeF_2 Etching on Si.

In order to eliminate the constraint imposed by the damage on the entrance window of the reaction cell, a differential pump apparatus system has been developed. The entrance window is replaced by an aperture and a sequence of pressure stages which reduce a pressure of 0.5 Torr in the reaction cell to 10^{-9} Torr in the pre-mirror chamber as shown in Fig.1 and Fig. 2. By means of this technology a higher energy resolution and a beam size of 1 mm in the energy direction can be obtained.

The non-condensed beam spot of incident beam after pre-mirror chamber is about 10×10 mm^2. In order to focus the beam trajectory to pass through the aperture, a paraboloid mirror is designed to condense the divergent incident beam. As illustrated in Fig. 3, the horizontal beam profile far from pre-mirror is expected to be condensed at sample position.

A part of the beam condensed apparatus was fabricated and an extremely high etching rate and spacial resolution was obtained from a performance test of Teflon etching. After the setting up of new etching chamber, we are planning to study the SR irradiation effects on the material selectivity of etching between Si and SiO_2, to find whether there exist an anisotropic character in desorption reaction of XeF_2 etching induced by synchrotron radiation.

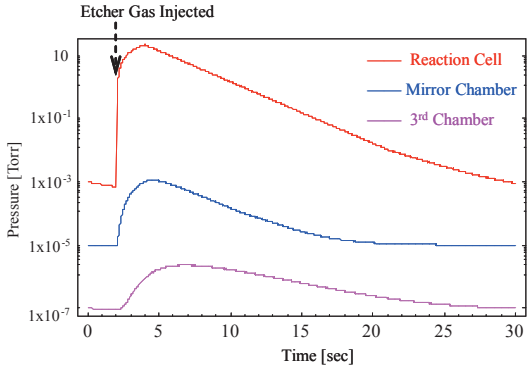

Fig. 2 Characteristic of the pressure variation in differential pump system after etcher gas injected by simulation - The system restrains the variation of pressure from etcher injection, and obtains achievement of experiment pressure.

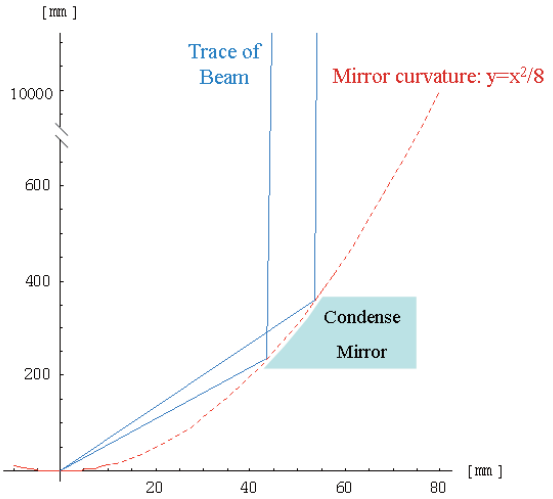

Fig. 3 Schematic optical layout of beam condenser system

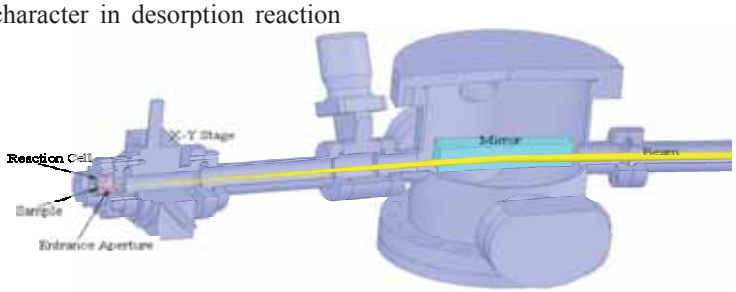

Fig. 1 Schematic section view of the etching chamber, beam converged on the sample surface by moving the position of the condenser mirror.

BL8B2

Electronic Structure of Pentacene Thin Film Converted from IBM Type Precursor and Vacuum Deposit

R. Sumii [1], A.Takahara [2], K. Kanai [1] , K. Seki[1,3]

[1] *Research Center for Materials Science, Nagoya University, Nagoya 464-8602, Japan*

[2] *Institute for Materials Chemistry and Engineering, Kyushu University, Fukuoka 812-8581, Japan*

[3] *Department of Chemistry, Nagoya University, Nagoya 464-8602, Japan*

Introduction

Pentacene has high hole mobility, and many studies have been performed on it. Pentacene film can be fabricated only by vacuum deposition due to its poor solubility to solvent. But recent study reported highly soluble pentacene precursor shown in Fig.1 (IBN type precursor), which can be spin-cast to form a film [1]. A retro Diels-Ader reaction caused by heating converts this precursor to a pentacene. In this study, we performed a UPS study of the change of the pentacene precursor film to pentacene, showing that the same electronic structure are that for a vacuum deposited film was actually observed.

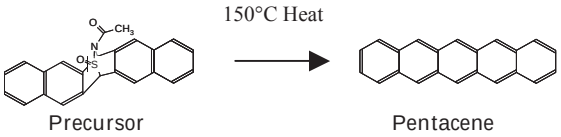

Fig. 1 IBM type pentacene precursor

Experimental

The pentacene vacuum deposition film was deposited on a Au/Si substrate. The pentacene precursor film was prepared by the spin coating of the precursor solution of chloroform. Spin coated film was heated at 150°C under nitrogen atmosphere about 10 minutes. UPS measurements were performed for these films at BL-8B2 of UVSOR facility.

Results and discussion

Figure 2 shows the UPS spectra of pentacene precursor film before and after heating. The binding energy in this figure is given with respect to the Au Fermi level. We see a clear change between pentacene precursor and heated film can see at the region of the HOMO peak. Heated precursor film show the HOMO peak at 1.5-1.6eV while the precursor film does not show such peak at this energy. The simulated spectra by molecular orbital calculations for these spectra also show good agreement with the observed spectra.

Figure 3 shows the UPS spectra of vacuum deposited pentacene film and the heated pentacene precursor film. These spectra are very similar, except that the peak intensity is a little different at around 0-4eV. This structure is ascribed to the combined contribution from σ and π orbitals. Supplemental penning ionization electron spectroscopy (PIES) study indicated that this difference of intensity around 3eV comes from the film structure. Similar structure difference between spin-coat and evaporated film are reported for other compound [2].

Moreover, XPS study at the S_{2p} region also showed that the adduct part is completely removed from the film by heating. These results indicate that the IBM type pentacene precursor can give high quality pentacene film from the view point of electronic structure.

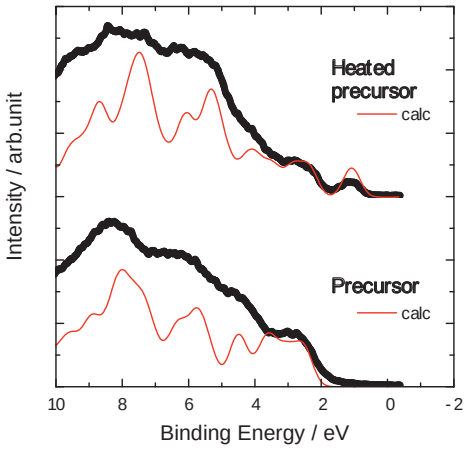

Fig. 2 UPS spectra of pentacene precursor film before (bottom) and after (top) heating compared with the theoretically simulated results.

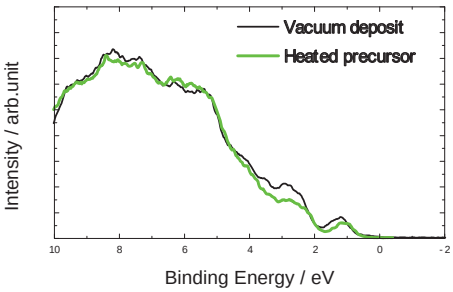

Fig. 3 UPS spectra of vacuum deposited pentacene film and heated pentacene precursor film.

[1] A. Afzali, C. D. Dimitrakopoulos, T. L. Breen, J. Am. Chem. Soc. **124** (2002) 8812

[2] H. Ozaki, J. Chem. Phys. **113** (2000) 6361

BL4B

X-ray Magnetic Circular Dichroism of Co Nanorods Grown on Cu(110)-(2×3)N surface

X.-D. Ma[1], T. Nakagawa[1,2], F. M. Leibsle[3], T. Yokoyama [1,2]

[1] *Department of Structural Molecular Science, The Graduate University for Advanced Studies (Sokendai), Okazaki, Aichi 444-8585, Japan*

[2] *Department of Molecular Structure, Institute for Molecular Science (IMS), Okazaki, Aichi 444-8585, Japan*

[3] *Department of Physics, University of Missouri at Kansas City, 5110 Rockhill Road, Kansas City, Missouri 64110, U. S. A.*

Magnetic properties of nanorods are hot subjects in recent years. York *et al*. [1] discovered self-assembled Co nanorods on Cu(110)-(2×3)N that are ~1 nm thick and well separated with each other up to as much as ~2 ML (monolayer). In the present work, we have investigated the magnetic properties of the Co nanorods by combining x-ray magnetic circular dichroism (XMCD) with the magneto-optical Kerr effect (MOKE) measurements.

The experiments were performed at soft X-ray varied line monochromator station Beamline 4B. The Co nanorods on Cu(110)-(2×3)N were grown along the [1-10] direction. The Co $L_{III,II}$-edge XMCD were taken with the polarization factor of 0.70 at ~90 K.

Figure 1 shows the Auger electron spectra (AES) and the LEED patterns. The N-KLL AES intensity is found to be kept constant on Co deposition, implying that the N atoms are located always at the surface even after deposition of Co. On the contrary, the Cu-MNN AES is reduced quickly with the Co deposition, suggesting that Cu does not migrate on/in the Co rods so significantly. On the other hand, the LEED patterns show (1×6) superstructure as in Figs. 1(d) and 1(e), consistent with the previous STM observation. This implies successful preparation of the Co nanrods.

Figure 2(a) depicts the anisotropic magnetization curves taken by MOKE. The hysteresis accompanied by remanent magnetization can be seen only along the [001] direction, implying that the magnetic easy axis is [001] that is perpendicular to the rod axis. The shape anisotropy does not determine the magnetic easy axis. Figure 2(b) shows the anisotropic XMCD. The inset of Fig. 2(b) gives the XMCD normalized with the edge jump. The [001] spectrum yields the most intense XMCD among the three directions of [001], [1-10] and [110], confirming that the present magnetic anisotropy is derived from the anisotropic spin-orbit interaction. Moreover, one can note that the orbital magnetic moment is rapidly enhanced on the formation of nanorods (<2 ML), as shown in Fig. 2(c).

[1] S.M York *et al*., Phy. Rev. B **64** (2001) 033411.

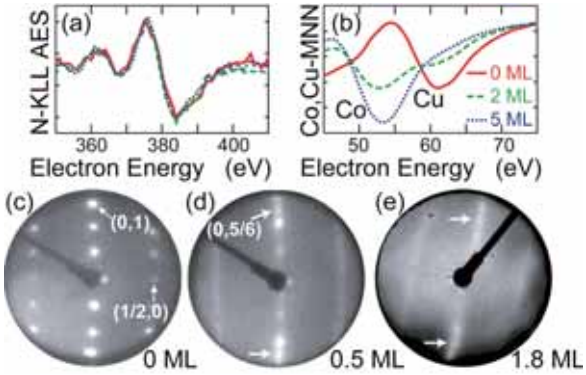

Fig. 1 (a) N-KLL and (b) Co, Cu-MNN AES and LEED (c-e) of the Co nanorods on Cu(110)-(2×3)N.

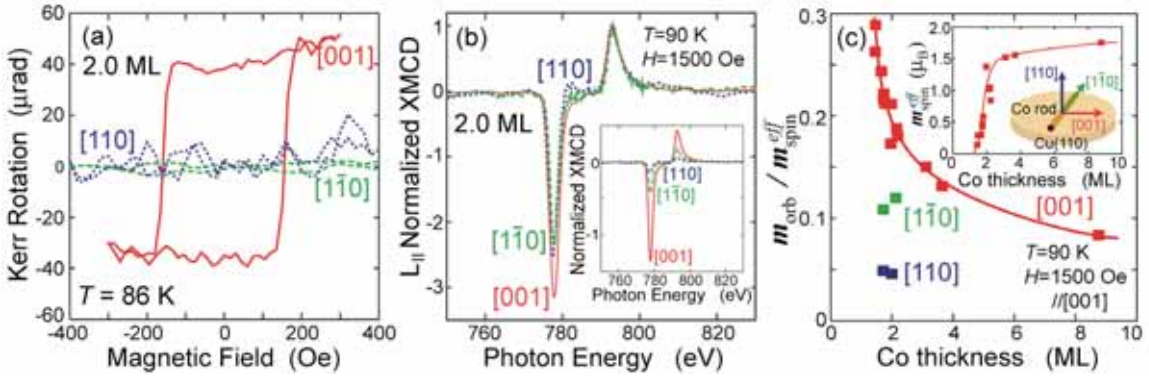

Fig. 2 (a) Magnetic curves taken by MOKE. (b) Co L-edge XMCD normalized with the L_{II} peak, together with those normalized with the edge jumps in the inset. (c) Ratio of the orbital/spin magnetic moment as a function of the Co thickness, together with the thermally averaged spin magnetic moment in the inset.

BL6B

Terahertz Spectroscopy of Protein Powder

X. Jin [1], J. Li [1], M. Shinjo [1], S. Kimura [2], H. Kihara [1]

[1] *Department of Physics, Kansai Medical University, 18-89 Uyama-Higashi, Hirakata 573-1136, Japan*

[2] *UVSOR Facility, Institute for Molecule Science, and School of Physical Sciences, The Graduate University for Advanced Studies (SOKENDAI), Myodaiji, Okazaki 444-8585, Japan*

Biological polymers are expected to exhibit broad vibrational spectral features in terahertz regime corresponding to functionally relevant, global and subglobal collective modes on the picosecond timescale. This is supported by theoretical molecular dynamics studies and normal mode calculations [1,2]. Due to the strong frequency-dependent terahertz attenuation of water, these studies should have dry, or partially hydrated samples. Here we report the terahertz spectra of representative proteins having various secondary structures, myoglobin, lysozyme, α-synuclein, β-lactoglobulin and src-SH3 domain.

All experiments were done at terahertz beam line BL6B at UVSOR-II. The thickness of the samples was around 0.1 mm. The wavenumber range we monitored was 10-250 cm^{-1}. Each spectrum was accumulated 100 times. The final spectra were divided by cell spectrum in order to subtract influence of the cell. All measurements were accumulated five times to get good S/N ratio.

Myoglobin is rich in α-helices. Figure 1 shows its terahertz spectrum. β-Lactoglobulin is rich in β-sheets (Figure 2). Lysozyme is one of α/β proteins (Figure 3). α-synuclein does not form any secondary structures and takes only random coil (Figure 4). Src-SH3 forms β-sheets mostly (Figure 5).

Results show significant difference between α-synuclein and other proteins at around 20 – 130 cm^{-1}.

[1] Brooks, B. and Karplus, M. (1983) Proc. Natl. Acad. Sci. 80: 6571-6575

[2] Tama, F., Gadea, F.X., Marquues, O., and Sanejouand, Y.H. (2000) Proteins 41: 1-7

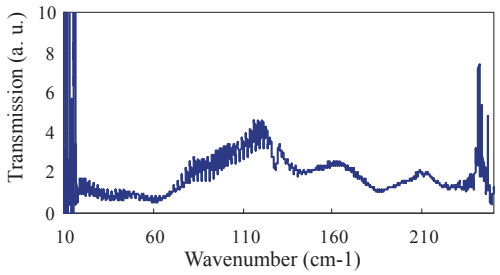

Fig.1 Terahertz spectroscopy of myoglobin

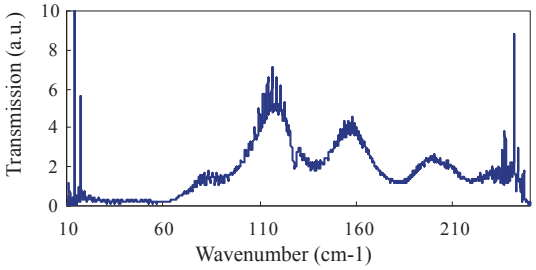

Fig.2 Terahertz spectroscopy of β–lactoglobulin

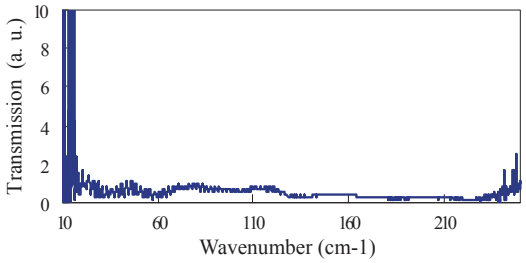

Fig.3 Terahertz spectroscopy of lysozyme

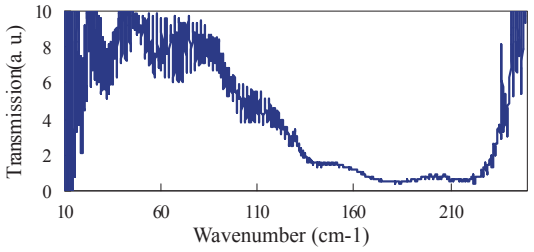

Fig.4 Terahertz spectroscppy of α–synuclein

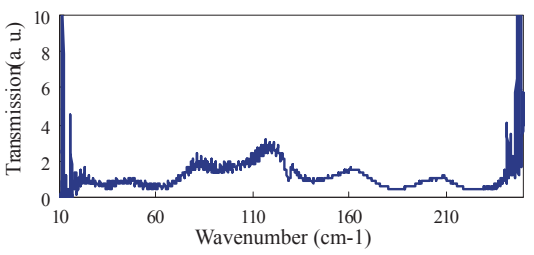

Fig.5 Terahertz spectroscopy of src-SH3 domain

Publication List

List of Publication 2006

J. Azuma, M. Itoh, M. Koike, M. Kamada, and M. Endo
Infrared Absorption Change in Single-walled Carbon Nanotubes Observed by Combination Spectroscopy of SR and Laser
Journal of Synchrotron Radiation 13 (2006) 464.

K. Chong, T. Hirai, T. Kawai, S. Hashimoto, and N. Ohno
Optical Properties of Bi^{3+} ions Doped in $NaYF_4$
J. Lumin. **122-123** (2007) 149.

J. Ding, B.H. Sun, T.X. Fan, D. Zhang, M. Kamada, H. Ogawa, and Q.X. Guo
EXAFS Study on Dynamic Structural Property of Porous Morph-genetic SiC
Nucl. Instrum. Methods Phys. Res. B 238 (2005) 138.

T. Ejima, T. Harada, and A. Yamazaki
Phase Change Observation in Reflection Multilayers by Total Electron Yield and Reflection Spectra
Appl. Phys. Lett. **89** (2006) 021914.

J. Fujioka, S. Miyasaka, and Y. Tokura
Doping Variation of Orbitally Induced Anisotropy in the Electronic Structure of $La_{1-x}Sr_xVO_3$
Phys. Rev. Lett. **97** (2006) 196401.

K. Fukui, Y. Kugumiya, N. Nagagawa, and A. Yamamoto
Infrared Reflectance Measurement for InN Thin Film Characterization
Phys. Stat. Sol. (c) **3** (2006) 1874.

K. Fukui, S. Naoe, K. Okada, S. Hamada, and H. Hirayama
Band-to-band and Inner Shell Excitation VIS-UV Photoluminescence of Quaternary InAlGaN Alloys
Phys. Stat. Sol. (c) **3** (2006) 1879.

M. Furukawa, H.S. Kato, M. Taniguchi, T. Kawai, T. Hatsui, N. Kosugi, T. Yoshida, M. Aida, and M. Kawai
Electronic States of the DNA Polynucleotides Poly(dG)-poly(dC) in the Presence of Iodine
Phys. Rev. B **75** (2007) 045119.

M. Hasegawa, T. Takeuchi, K. Soda, H. Sato, and U. Mizutani
Electronic Structure and Phase Stability of Glassy Alloys
Mater. Sci. Forum **539-543** (2007) 2048.

M. Hasegawa, K. Soda, H. Sato, T. Suzuki, T. Taketomi, T. Takeuchi, H. Kato, and U. Mizutani
Stability and Electronic Structure of Zr-based Ternary Metallic Glasses and Relevant Compounds
Journal of Alloys and Compounds **434-435** (2007) 149.

Y. Hikosaka, T. Kaneyasu, and E. Shigemasa
Ion Pair Formation in the Vacuum Ultraviolet Region of NO Studied by Negative Ion Imaging Spectroscopy
Journal of Electron Spectroscopy and Related Phenomena **154** (2007) 43.

T. Hirai, N. Ohno, S. Hashimoto, and S. Sakuragi
Luminescence of $NaGdF_4$:Tb^{3+},Eu^{3+} under Vacuum Ultraviolet Excitation
J. Alloys and Compounds **408-412** (2006) 894.

T. Hirai, H. Yoshida, S. Sakuragi, S. Hashimoto, and N. Ohno
Transfer of Excitation Energy from Pr^{3+} to Gd^{3+} in YF_3:Pr^{3+},Gd^{3+}
Jpn. J. Appl. Phys. **46** (2007) 660.

K. Ichimura, T. Fuyuki, T. Kawai, S. Hashimoto, T. Hirai, and N. Ohno
Luminescence Properties of Tl^+ Centers doped in KH_2PO_4
Phys. Stat. Sol. (c) **10** (2006) 3607.

T. Ito, H.J. Im, S. Kimura, and Y.S. Kwon
Three-dimensional Fermi-surface of $CeTe_2$ Studied by Angle-resolved Photoemission
J. Mag. Magn. Matar. **310** (2007) 431.

T. Ito, S. Kimura, H.J. Im, E. Nakamura, M. Sakai, T. Horigome, K. Soda, and T. Takeuchi

BL5U at UVSOR-II for Three-dimensional Angle-resolved Photoemission Spectroscopy

AIP Conf. Proc. **879** (2007) 587.

T. Ito, H.J Im, S. Kimura, and Y.S. Kwon

Angle-resolved Photoemission Study on $CeTe_2$

Physica B **378-380** (2006) 767.

B.P. Kafle, H. Katayanagi, and K. Mitsuke

Photofragment Imaging Apparatus for Measuring Momentum Distributions in Dissociative Photoionization of Fullerenes

Am. Inst. Phys. **CP879** (2007) 1809.

K. Kanda, K. Mitsuke, K. Suzuki, and T. Ibuki

Photodissociation of Butyl Cyanides and Butyl Isocyanides in the Vacuum UV Region

Am. Inst. Phys. **CP879** (2007) 1817.

T. Kaneyasu, T. Aoto, Y. Hikosaka, E. Shigemasa, and K. Ito

Coster-Kronig Decay of the 2s Hole State in HCl Observed by Sub-Natural Linewidth Auger Electron Spectroscopy

Journal of Electron Spectroscopy and Related Phenomena **153** (2006) 88.

T. Kaneyasu, Y. Hikosaka, and E. Shigemasa

Development of Auger-Electron-Ion Coincidence Spectrometer to Study Decay Dynamics of Core Ionized Molecules

AIP Conf. Proc. **879** (2007) 1793.

T. Kaneyasu, Y. Hikosaka, and E. Shigemasa

Electron-Ion Coincidence Spectrometer for Studies on Decay Dynamics of Core-Excited Molecules

Journal of Electron Spectroscopy and Related Phenomena, in press.

M. Katoh, E. Shigemasa, S. Kimura, and N. Kosugi

Present Status of UVSOR-II

AIP Conf. Proc. **879** (2007) 192.

M. Katoh, M. Hosaka, A. Mochihashi, M. Shimada, S. Kimura Y. Takashima, and N. Kosugi
Coherent Terahertz Radiation at UVSOR-II
AIP Conf. Proc. **879** (2007) 71.

E. Kawabe, H. Yamane, K. Koizumi, R. Sumii, K. Kanai, Y. Ouchi, and K. Seki
The Electronic Structure and the Energy Level Alignment at the Interaface Between Organic Molecules and Metals
Mater. Res. Soc. Symp. Proc. **965** (2007) 0965-S09-28

S. Kimura, and T. Mizuno
Application of Terahertz Synchrotron Radiation at UVSOR-II
AIP Conf. Proc. **902**, 67 (2007).

S. Kimura, T. Nishi, T. Takahashi, T. Mizuno, K. Miyagawa, H. Taniguchi, A. Kawamoto, and K. Kanoda
Pressure Dependence of Phase Separation in Deuterated κ-$(ET)_2Cu[N(CN)_2]Br$ at the Mott Boundary
J. Magn. Magn. Mater **310** (2007) 1102.

S. Kimura, T. Ito, E. Nakamura, M. Hosaka, and M. Katoh
Design of a High-Resolution and High-Flux Beamline for VUV Angle-Resolved Photoemission at UVSOR-II
AIP Conf. Proc. **879** (2007) 527.

S. Kimura, Y. Sakurai, E. Nakamura, and T. Mizuno
Terahertz Microspectroscopy and Infrared Reflection-Absorption Spectroscopy Apparatuses at UVSOR-II
AIP Conf. Proc. **879** (2007) 595.

S. Kimura, J. Sichelschmidt, J. Ferstl, C. Krellner, C. Geibel, and F. Steglich
Optical Observation of Non-Fermi-liquid Behavior in the Heavy Fermion State of $YbRh_2Si_2$
Phys. Rev. B **74** (2006) 132408.

S. Kimura, E. Nakamura, T. Nishi, Y. Sakurai, K. Hayashi, J. Yamazaki and M. Katoh

Infrared and Terahertz Spectromicroscopy Beam Line BL6B(IR) at UVSOR-II

Infrared Phys. Tech. **49** (2006) 147.

S. Kimura, H.J. Im, Y. Sakurai, T. Mizuno, K. Takegahara, H. Harima, K. Hayashi, E. Matsuoka, and T. Takabatake

Infrared Study on Electronic Structure of SrT_4Sb$_{12}$ (T = Fe, Ru)

Physica B **383** (2006) 137.

S. Kimura, T. Mizuno, H.J. Im, K. Hayashi, E. Matsuoka, and T. Takabatake

Iron-Based Heavy Quasiparticles in $SrFe_4Sb_{12}$: An Infrared Spectroscopic Study

Phys. Rev. B **73** (2006) 214416.

M.Kitaura, N.Fujita, M.Itoh, and H.Nakagawa

Origin of Photocarrier Traps in Photorefractive α-$LiIO_3$ Crystals by Optical Measurement and Cluster Calculation

Phys. Rev. B **73** (2006) 115110.

H. Kobayashi, Y. Arachi, S. Emura, K. Handa, and K. Tatsumi

Observation of Valence State Change in Layered $Li_{1-y}Ni_{1/3}Mn_{1/3}Co_{1/3}O_2$

AIP Conf. Proc. **882** (2007) 478.

Y.S. Kwon, K.E. Lee, M.A. Jung, E.Y. Song, H.J. Oh, H.J. Im, and S. Kimura

Hybridization Gap Collapse at a Quantum Critical Point of $CeNi_{1-x}Co_xGe_2$

J. Magn. Magn. Mater. **310** (2007) 310.

Y.S. Kwon, J.B. Hong, H.J. Im, T. Nishi, and S. Kimura

Infrared Absorption in Heavy Fermion System $CeNi_{1-x}Co_xGe_2$

Physica B **378-380** (2006) 823.

M. Labat, M. E. Couprie, M. Hosaka, A. Mochihashi, M. Katoh,
and Y. Takashima
Longitudinal and Transverse Heating of a Relativistic Electron Bunch Induced by a Storage Ring Free Electron Laser
Phys. Rev. ST Accel. Beams **9** (2006)100701.

K. Mitsuke, T. Mori, J. Kou, Y. Haruyama, Y. Takabayashi, and Y. Kubozono
Photoion Yield Curves of Dy@C_{82} in the Vacuum UV Region
Int. J. Mass Spectrom. **243** (2005) 121.

K. Mitsuke, H. Katayanagi, J. Kou, T. Mori, and Y. Kubozono
Fragmentation Mechanism of Highly Excited C_{70} Cations in the Extreme Ultraviolet
Am. Inst. Phys. **CP811** (2006) 161.

H. Miyazaki, K. Soda, S. Yagi, M. Kato, T. Takeuchi, U. Mizutani,
and Y. Nishino
Surface and Bulk Electronic Structures of Heusler-type Fe2VAl
J. Vac. Sci. Technol. A **24** (2006) 1464.

A. Mochihashi, M. Katoh, M. Hosaka, Y. Takashima, and Y. Hori
Touschek Lifetime Measurement with a Spurious Bunch in Single-bunch Operation in UVSOR-II Electron Storage Ring
Nucl. Instrum. Methods Phys. Res. A **572** (2007) 1033.

T. Nakagawa, T. Yokoyama, M. Hosaka, and M. Katoh
Measurements of Threshold Photoemission Magnetic Dichroism Using Ultraviolet Lasers and a Photoelastic Modulator
Rev. Sci. Instrum. **78** (2007) 023907.

S. Nakano, T. Takeuchi, K. Soda, M. Hasegawa, U. Mizutani, H. Sato, K. Itoh,
and T. Fukunaga
Investigation of Stability of the Zr-Ni-Al Bulk Amorphous Phase from Local Atomic Arrangements of the Relevant Crystals
J. Jpn. Soc. Powder Powder Metallurgy **53** (2006) 100.

T. Nishi, S. Kimura, T. Takahashi, H.J. Im, Y.S. Kwon, T. Ito, K. Miyagawa, H. Taniguchi, A. Kawamoto, and K. Kanoda
Magnetic-field-induced Superconductor-insulator-metal Transition in an Organic Conductor: An Infrared Magneto-optical Imaging Spectroscopic Study
Phys. Rev. B **75** (2007) 014525.

H. Okamura, T. Watanabe, M. Matsunami, N. Tsujii, T. Ebihara, H. Sugawara, H. Sato, Y. Onuki, Y. Isikakwa, T. Takabatake, and T. Nanba
Universal Scaling in the Dynamical Conductivity of Heavy Fermion Ce and Yb Compounds
J. Phys. Soc. Jpn. **76** (2007) 023703.

H. Okamura, T. Michizawa, T. Nanba, and T. Ebihara
Infrared Study of Valence Transition Compound $YbInCu_4$ Using Cleaved Surfaces
J. Phys. Rev. **B** 75 (2007) 041101.

Y. Sakurai, T. Nishi, S. Kimura, Y.S. Kwon, M.A. Avila, and T. Takabatake
Optical Study on Clathrates $Sr_8Ga_{16}Ge_{30}$ and β-$Eu_8Ga_{16}Ge_{30}$
Physica B **383** (2006) 122.

T. Suzuki, H. Miyazaki, K. Soda, T. Takeuchi, M. Hasegawa, H. Sato, and U. Mizutani
Electronic Structure of Zr-TM-Al (TM = Ni, Cu) Bulk Metallic Glasses
J. Jpn. Soc. Powder Powder Metallurgy **53** (2006) 107.

T. Takeuchi, S. Nakano, K. Soda, H. Sato, M. Hasegawa, U. Mizutani, K. Itoh, and T. Fukunaga
Local Atomic Arrangements and Electronic Structure of the Zr-Ni-Al Bulk Metallic Glass - Analysis by Use of the Relevant Crystals -
Materials Science and Engineering A **449-451** (2007) 599.

T. Takeuchi, D. Fukamaki, H. Miyazaki, K. Soda, M. Hasegawa, H. Sato, U. Mizutani, T. Ito, and S. Kimura
Electronic Structure and Stability of the Pd-Ni-P Bulk Metallic Glass
Materials Transactions, **48**(6) (2007) in press.

A. Tanaka, M. Imamura, and H. Yasuda
Interface Electronic Structures of Alkanethiolate-passivated Au Nanoparticles Studied by Photoelectron Spectroscopy
Phys. Rev. B **74** (2006) 113402.

A. Tanaka, R. Saito, T. Kamikake, M. Imamura, and H. Yasuda
Nanoparticles
Solid State Commun. **140** (2006) 400.

K. Watanabe, A. Kokalj, H. Horino, I.I. Rzeznicka, K. Takahanshi, N. Nishi, and T. Matsushima
STM and NEXAFS Studies of N_2O Orientation on Pd(110)
Jpn. J. Appl. Phys., **45** (2006) 2290

M. Yamaga, E. Hayashi, N. Kodama, K. Itoh, S. Yabashi, Y. Masui, S. Ono, N. Sarukura, T.P.J. Han, and H.G. Gallagher
Vacuum Ultraviolet Spectroscopy of Ce^{3+}-doped $SrMgF_4$ with Superlattice
J. Phys. : Condens. Matter **18** (2006) 6033.

T. Yoshida, T. Tanabe, S. Takahara, and H. Yoshida
Measurement of Luminescence from Silica Glasses : an Optical X-ray Absorption Fine Structures Study at Si K-edge
Physica Scripta **T115** (2005) 528.

T. Ejima
Phase Measurement Method of EUV Reflection Multilayer Combining Reflection and Total Electron Yield Spectra
Journal of the Spectroscopical Society of Japan **55** (2006) 259 (in Japanese).

H.S. Kato, M. Furukawa, T. Hatsui, M. Taniguchi, T. Kawai, N. Kosugi, and M. Kawai
Charge Migration Mechanism in DNA Strands Elucidated by Electronic Structure Examinations
Journal of the Surface Science Society of Japan **27** (2006) 35 (in Japanese).

Appendix

3rd JSSRR Wakate Workshop on Next Generation Light Sources
~ Future Science Developed by Advanced Ring-type Light Source ~

Okazaki Conference Center

August 7, 2006

13:00 - **(I) Interim report of the advanced ring-type light sources committee**

Y. Amemiya (Univ. Tokyo)

13:30 - **(II) Project of the advanced ring-type light source – ERL project in Japan**

Coordinator:	N. Kumagai (JASRI)
Outline:	H. Kawata (KEK-PF)
Machine:	S. Sakanaka (KEK-PF)
Electron gun:	R. Hajima (JAEA)
Superconducting RF cavity:	T. Furuya (KEK)

15:00 - **Coffee Break**

15:20 - **(III) Science developed by advanced ring-type light source**

III-1 Life science

Coordinator:	S. Wakatsuki (KEK-PF)
Speaker:	S. Takeda (National Cardiovascular Center)
	G. Kurisu (Univ. Tokyo)
	M. Yamamoto (RIKEN)

Topics ~FEL~

17:00 -	**Present status of SCSS**	T. Ishikawa (RIKEN)
17:15 -	**Present status of FEL - UVSOR-II**	M. Hosaka (UVSOR)
18:00 -	**Banquet**	

August 8, 2006

9:00 - **III-2 Materials science**

Coordinator:	H. Kawata (KEK-PF)
Speaker:	Y. Inada (KEK-PF)
	S. Shimomura (Keio Univ.)
	S. Koshihara (Tokyo Inst. Tech)

10:30 - **III-3 Imaging**

Coordinator:	Y. Kagoshima (Univ. Hyogo)
Speaker:	A. Momose (Univ. Tokyo)
	K. Hirano (KEK-PF)

12:00 - **(IV) Overall discussion**

Coordinator:	Y. Amemiya (Univ. Tokyo)
Panelist:	N. Kumagai (JASRI)
	N. Igarashi (KEK-PF)
	H. Kawata (KEK-PF)
	Y. Kagoshima (Univ. Hyogo)

The workshop was organized by The Japanese Society for Synchrotron Radiation Research and was sponsored by UVSOR.

The 66th Okazaki Conference
International Workshop on Soft X-ray Raman Spectroscopy and Related Phenomena (IWSXR)

Okazaki Conference Center

Advisory Committee Members:
Hiroki Nakamura, Director General of IMS, Japan
Joseph Nordgren, Councilor of IMS, Uppsala University, Sweden
Marc Simon, LCP-MR, France

Local Organizing Committee:
Nobuhiro Kosugi, IMS, Japan (Chair)
Hiromi Okamoto, IMS, Japan (Vice Chair)
Eiji Shigemasa, IMS, Japan
Takaki Hatsui, IMS, Japan

August 17, 2007

13:00 -	**Registration & Coffee**	
14:00 -	**Opening Remarks**	
Session 1. Fundamental Aspects		Chair: Nobuhiro Kosugi
14:10 -	**Resonant Soft X-ray Emission for Materials Science and Chemical Physics**	Joseph Nordgren Uppsala Univ., Sweden
15:00 -	**High resolution soft X-ray emission spectroscopy of transition metal compounds and heme proteins**	Shik Shin Univ.Tokyo/RIKEN/SPring-8, Japan
	Coffee Break	
16:20 -	**Advances in X-ray Raman Spectroscopy in both Resonant and Non-Resonant Applications**	Uwe Bergmann Stanford Univ., U.S.A
17:10 -	**Visualizing and controlling picometric quantum ripples in molecules**	Kenji Ohmori IMS, Japan
18:10-20:00	**Get-Together Party**	

August 18, 2007

8:10 - 9:00	**Breakfast (Poster Room)**	
9:00 -	**Welcome Address**	Hiroki Nakamura Prof., Director-General of IMS

Session 2. Molecules & Raman effects Chair: Takaki Hatsui

9:10 -	**Resonant inelastic X-Ray scattering around the chlorine K shell of the HCl molecule: role played by the nuclear dynamics in the tender X-Ray region**	Marc Simon LCP-MR, France
9:50 -	**Theoretical Simulations of Resonant Inelastic X-Ray Scattering Spectra in K-shell Cl Core-Excited Chlorinated Molecules**	Stephane Carniato LCP-MR, France
10:30 -	**Resonant X-ray Raman scattering: Doppler effect versus scattering, role of the detuning and the shape of the spectral function**	Victor Kimberg IMS, Japan
11:10 -	**Vibrational and thermal effects in resonant inelastic X-ray scattering**	Alexander Föhlisch Hamburg Univ., Germany

11:50-12:00 **Conference Photo**

August 18, 2007
Session 3. Poster Session
12:00-14:00 **with lunch and coffee (Poster Room)**

Session 4. Materials Science and Experimental Techniques Chair: Eiji Shigemasa

14:00 -	**Resonant inelastic soft-x-ray scattering studies of nanostructured strong correlated materials**	Jinghua Guo ALS, LBNL, U.S.A.
14:50 -	**Theory of Resonant Inelastic X-ray Scattering at Transition Metal L2,3 edge: dd Excitation, Charge-Transfer Effects and Their Interplay**	Munetaka Taguchi RIKEN/SPring-8, Japan
15:30 -	**Resonant inelastic x-ray scattering spectroscopy for advanced XAFS studies**	Hisashi Hayashi Japan Women's Univ. Japan
	Coffee Break	
16:50 -	**Development of a high performance slit-less spectrometer and a liquid flow cell for soft X-ray emission spectroscopy**	Takashi Tokushima RIKEN/SPring-8, Japan

17:20 -	**Development and performance of a transmission-grating spectrometer for soft X-ray emission studies**	Takaki Hatsui IMS, Japan
18:00 -	**Preparing for resonant soft x-ray Raman spectroscopy at SOLEIL**	Coryn Hague LCP-MR, France

18:50-20:30 **Conference Dinner**

August 19, 2007

8:10 - 9:00 **Breakfast (Poster Room)**

Session 5. Water and Solutions Chair: Hiromi Okamoto

9:00 -	**Theoretical and experimental x-ray investigations of liquid water structure**	Lars G.M. Pettersson Stockholm Univ, Sweden
9:50 -	**Theoretical study of two-dimensional Raman spectroscopy: Anharmonic dynamics and local hydrogen bond network structure in liquid and solid water**	Shinji Saito IMS, Japan
10:30 -	**A molecular dynamics study of vibrational relaxation of solute molecule in solution**	Susumu Okazaki IMS, Japan
11:10 -	**Non-linear ultrafast X-ray spectroscopy; Theoretical challenges**	Shaul Mukamel Univ. California, Irvine, U.S.A.

11:50-12:00 **Closing Remarks**

Workshop on Research for VUV Luminescence

Institute for Molecular Science

November 17, 2006

#	**Chairperson:**	A. Yoshikawa (Tohoku Univ.)
1.	**Opening Remarks (Research for VUV Luminescence)**	M. Itoh (Shinshu Univ.)
2.	**UV/VUV Luminescence Measurements in UVSOR**	K. Fukui (Fukui Univ.)
3.	**EUV Light Source Excited by High-Power Laser**	H. Komori (EUVA)
#	**Chairperson :**	Y. Kayanuma (Osaka Pref. Univ.)
4.	**Deep-UV Luminescence in Alkali Chlorides Doped with Iodine Ions**	I. Akimoto (Wakayama Univ.)
5.	**Soft-X Ray Luminescence of Titanium Oxides**	Y. Tezuka (Hirosaki Univ.)
6.	**Ultra Fast Relaxation Dynamics in Condensed Matter Induced by Core Excitation: Competition between Localization and Non-Localization**	S. Tanaka (Osaka Pref. Univ.)

Short Tour to UVSOR and Banquet

November 18, 2006

#	**Chairperson :**	N. Sarukura (Osaka Univ.)
7.	**Amorphous VUV Transparent Materials**	K. Kajiwara (ERATO-SORST)
8.	**Single Crystal Growth of Fluorides for VUV Luminescent Materials**	A. Yoshikawa (Tohoku Univ.)
9.	**Development of Nano-Strip Gas Counter and Its Application to VUV Region**	H. Takahashi (Tokyo Univ.)
#	**Chairperson :**	K. Fukui (Fukui Univ.)
10.	**Evaluation of Materials Using Electronic Transitions by VUV Light Excitation**	M. Ohta (Niigata Univ.)
11.	**Development of On-Axis Discharge-Excitation-Type UV/VUV Laser and Rare-Gas Dimer Laser**	T. Kanno (Osaka Univ.)
12.	**Prospect of VUV Luminescent Materials**	N. Sarukura (Osaka Univ.)
13.	**Concluding Remarks**	M. Itoh (Shinshu Univ.)

UVSOR Mini-Workshop on

"Present status and future perspective of research and development for free electron lasers (FEL)~ attitudes towards practical utilization of XFEL ~"

Institute for Molecular Science, March 13. 2007

First Session 13:00 - 15:15

	Coordinator	E. Shigemasa (UVSOR)
13:00 -	**Preface**	N. Kosugi (UVSOR)
13:35 -	**Beam characteristic of prototype accelerator and present status of fundamental design for the XFEL machine at SPring-8**	H. Tanaka (RIKEN)
14:05 -	**Seeding FEL experiments using the prototype accelerator at SPring-8**	T. Hara (RIKEN)
14:35 -	**Property of FEL light, and current/future aspect of FEL beamlines**	M. Yabashi (JASRI)
14:55 -	**Transfer of high-stability timing signal in XFEL and its measurement system**	K. Tamasaku (RIKEN)
15:15 -	**Coffee Break**	

Second Session 15:30 - 17:45

	Coordinator	N. Kosugi (UVSOR)
15:30 -	**Outline of joint project proposal for utilization of XFEL, submitted by four research groups in IMS**	E. Shigemasa (UVSOR)
15:45 -	**Present status of research and development for FEL at UVSOR**	M. Katoh (UVSOR)
16:15 -	**Anticipation for pump-probe experiments with ultra short X-ray pulses**	T. Hatsui (IMS)
16:45 -	**Tracking of ultrafast photochemical reaction with high harmonic generation laser pulses: present situation and future outlook**	A. Hishikawa (IMS)
17:15 -	**General discussion on the XFEL project**	
18:00 -	**Banquet**	

Organic Thin Films Studied by Synchrotron Radiation

" Histrical Review of BL8B2 and Future Prospects"

Institute for Molecular Science

March 22, 2007

09:20 -	**Opening remarks**	
	Chairman	S. Kera (Chiba Univ.)
09:25 -	**Construction and early days of BL8B2**	K. Seki (Nagoya Univ.)
09:40 -	**Electronic structure of organic functional thin films and their interfaces studied by angle resolved ultraviolet photoelectron spectroscopy: Previous output from the Nagoya university group**	H. Ishii (Chiba Univ.)
	Coffee break	
11:00 -	**Observation of the electronic structure at the organic insulator / metal interface with XAFS**	M. Kiguchi (Hokkaido Univ.)
11:30 -	**Possibility of the Fermi Level Control by VUV-Induced Doping of an Organic Thin Film**	M. Ono (Chiba Univ.)
	Lunch	
	Chairman	H. Yamane (Nagoya Univ.)
13:00 -	**Quantitative determination of molecular orientation for organic thin film : ARUPS and IAC approximation**	K. Okudaira (Chiba Univ.)
14:00 -	**Anisotropic distribution of photoemission intensity from valence states of well-ordered organic films**	S. Kera (Chiba Univ.)
14:30 -	**NEXAFS Spectroscopy As an Analytical Tool : Examples of NEXAFS analysis at SR Center of Ritsumeikan Univ.**	H. Oji (JASRI)
15:20 -	**Photoelectron spectroscopy of fullerenes, from the dawn to now**	S. Hino (Ehime Univ.)
	Get together party	

March 23, 2007

	Chairman	H. Yamane (Nagoya Univ.)
09:00 -	**Transport and spectroscopic measurements of interfaces between magnetic electrodes and organic semiconductors**	T. Shimada (Tokyo Univ.)
09:30 -	**Angle resolved X-ray photoemission studies of metal/organic interfaces: depth profiles and diffusion coefficients**	H. Yoshida (Kyoto Univ.)
10:00 -	**Photo- and thermo-responsive effect on the characteristics of organic thin films studied by photoelectron spectroscopy**	S. Tanaka (Shimane Univ.)
	Coffee break	
10:50 -	**Development of new inverse photoemission spectroscopy system for organic materials and study on electronic structure of ionic liquid**	K. Kanai (Nagoya Univ.)
11:20 -	**Undulator soft-x-ray beamline BL3U and the soft x-ray emission spectrometer: Present Status**	T. Hatsui (IMS)
	Lunch	
	Chairman	R. Sumii (UVSOR)
13:00 -	**Photoemission study of quasi-one-dimensional organic molecular solids**	T. Ito (UVSOR)
13:30 -	**Intramolecular energy-band dispersion in the oligomer films of polyethylene and polytetrafluoroethylene studied by angle-resolved photoemission with synchrotron radiation**	D. Yoshimura (SAGA-LS)
14:00 -	**Intermolecular energy-band dispersion in oriented films of organic semiconductors**	H. Yamane (Nagoya Univ.)
14:30 -	**Electronic structure of a Pentacene ultra-thin film**	K. Sakamoto (Chiba Univ.)
	Coffee break	
15:20 -	**Panel discussion**	

UVSOR Lunch Seminar

FY2006

June 14 Mr. Norikazu FUSE, Graduate School of Science and Engineering, Waseda University
Characterization of polymer nanocomposites by photoluminescence

Oct. 4 Prof. Toshihiko YOKOYAMA, Department of Molecular Structure, Institute for Molecular Science
Ultraviolet threshold photoemission magnetic circular dichroism using UVSOR-II FEL for photoemission electron microscopy

Oct 11 Dr. Masahito HOSAKA, UVSOR Facility, Institute for Molecular Science
FEL experiments at UVSOR-II

Oct. 18 Dr. Shigeru KODA, Saga Light Source (SAGA-LS)
Present Status of SAGA-LS

Mar. 28 Dr. Yoko SAKURAI, UVSOR Facility, Institute for Molecular Science
Infrared reflection absorption spectroscopy using synchrotron radiation

Mar. 28 Mr. Yusuke SUZUMURA, Graduate School of Engineering, Nagoya University
Orbit stabilization at UVSOR-II